UAB
Universitat Autònoma de Barcelona

Nanomaterials for Cell Actuation at Low Light Intensities of Near Infra-Red Light

Nour al hoda Al Bast

ADVERTIMENT. L'accés als continguts d'aquesta tesi queda condicionat a l'acceptació de les condicions d'ús establertes per la següent llicència Creative Commons: https://creativecommons.org/licenses/?lang=ca

ADVERTENCIA. El acceso a los contenidos de esta tesis queda condicionado a la aceptación de las condiciones de uso establecidas por la siguiente licencia Creative Commons: https://creativecommons.org/licenses/?lang=es

WARNING. The access to the contents of this doctoral thesis it is limited to the acceptance of the use conditions set by the following Creative Commons license: https://creativecommons.org/licenses/?lang=en

UAB
Universitat Autònoma de Barcelona

Nanomaterials for Cell Actuation at Low Light Intensities of Near Infra-Red Light

Nour al hoda Al Bast

Universitat Autònoma de Barcelona

Nanomaterials for Cell Actuation at Low Light Intensities of Near Infra-Red Light

Nour al hoda Al Bast

Doctoral Thesis

Directors:

Dra. Maria-José Esplandiu

Dra. Carme Nogues

Dr. Borja Sepulveda

Department of Chemisrty

Doctoral Program in Materials Science

Barcelona, February 2024

This work entitled ‘Nanomaterials for cell actuation at low light intensities of Near Infra-Red light’ presented by Nour al hoda Al Bast to acquire the degree of Doctor in Materials Science from Universitat Autonoma de Barcelona (UAB), was accomplished at the Magnetic Nanostructures Group in the Catalan Institute of Nanoscience and Nanotechnology (ICN2) and the Departament de Biologia Cel·lular, Fisiologia i Immunologia (UAB) under the supervision of Maria-José Esplandiu, Borja Sepulveda and Carma Nogues.

I. Abstract

Electrical stimulation of tissues has a wide range of biomedical applications. However, current wired electro-stimulators are bulky and invasive. Wireless cell stimulation with opto-electric devices can be an alternative to generate local actuation with minimal invasiveness. However, most opto-electronic devices for cell electro-stimulation use visible light, limiting the applications to superficial tissues. Therefore, new wireless opto-electronics devices optimized to work under low intensity near infrared (NIR) light within the first or second biological spectral windows, in which light penetration in tissues is maximized, are highly demanded.

NIR light is also used in cancer photodynamic therapies. However, typical photodynamic molecules have low efficiency in the NIR and poor stability. To solve this problem, novel nanomaterials are currently being explored to generate therapeutic reactive oxygen species with NIR light. In this line, the narrow bandgap, outstanding photocatalytic activity, and biocompatibility of MoS_2 nanostructures position them as promising photodynamic agents.

Within this framework, we have focused on the development of different opto-electronic devices for wireless cell stimulation and photodynamic therapy operated with low-intensity, safe, and high penetration NIR light.

The first opto-electronic device was based on Si/Au nanowires with an in-built pn junction. Short and long nanowire arrays were fabricated through a cost-effective/scalable colloidal lithography technique. The short-Si/Au nanowires device, featuring a protected pn junction buried in the silicon structure, showed a very good opto-electrical performance under 810 nm illumination (first biological window). The Si/Au nanowires enhanced light absorption through hybrid plasmonic metal/dielectric resonances. These devices exhibited similar photovoltages, but much higher photocurrents compared to the standard flat Si pn junction, thus enabling cell stimulation through combined capacitive/faradaic processes.

Si/Au nanowires exhibited high biocompatibility for osteoblast cells. Under very low intensity of 810 nm light (4.5 $\mu W/mm^2$), cells demonstrated enhanced proliferation over 21 days compared to dark conditions. Photo-induced signals triggered calcium influxes through activation of voltage-gated Ca^{2+} channels, even at 1 $\mu W/mm^2$. Differentiation studies revealed increased alkaline phosphatase levels and calcium deposit formation under light actuation compared to dark conditions. Although, short-Si/Au nanowires produced lower photovoltages and photocurrents in the second biological window (1050 nm), they are promising for future experiments.

In contrast, long-Si/Au nanowires with exposed pn junction to the electrolyte experienced a large drop in photovoltage/photocurrent. Protection strategies of the pn junction improved opto-electrical signals, showing potential for future studies. Long-Si/Au nanowires easily released from the silicon support to a liquid phase, which can be exploited for direct nanowire injection inside tissues or to develop soft implantable devices with minimal invasiveness.

The second opto-electronic device was based on Si/Pt nanoneedle arrays, featuring Schottky junctions for cell stimulation within the second biological window. They exhibited good photo-

electrical response although optimization is required for enhanced performance. Similar response was obtained by activation from the nanoneedles or flat silicon sides due to the high transparency of Si, being advantageous for biomedical applications. Osteoblast cells grew well attached on the nanoneedle surface. Although only 17% of the cells were activated upon illumination (3.4-fold increase compared to dark condition), the biocompatibility and potential improvement capacity of the Si/Pt nanoneedle devices make them promising for further studies.

Finally, $SiO_2/MoS_2/Cu_2O$ nanoreactors were explored as photodynamic platform in the first biological window for cancer therapy. The immobilized and dispersed nanoreactors demonstrated biocompatibility. Upon low intensity NIR illumination (660/808nm) a remarkable decrease in the viability of bone tumoral cells was observed due to the photogenerated reactive oxygen species. An apoptotic mechanism of cell death was detected. Internalization of the dispersed nanoreactors was low, requiring further optimization. This work offers promising avenues for advanced NIR photodynamic agents.

II. Table of Contents

I. Abstract 4

II. Table of Contents 6

III. List of Abbreviations 9

1. Introduction 7

1.1 Importance of light in biological processes and medicine 7

1.1.1 Light in Biology 7

1.1.2 Light in Biomedicine 8

1.1.3 Importance of the NIR Biological Windows 11

1.2 Light for Cell Electrostimulation 13

1.2.1 Importance and Basics of Cell Electrostimulation 13

1.2.2 Opto-Electrical Cell Stimulation 22

1.3 Light for ROS Generation 38

1.3.1 Importance of ROS in Biology and Biomedicine 38

1.3.2 PDT with Molecules 40

1.3.3 PDT with Nanoparticles 42

1.3.4 Transition Metal Dichalcogenides for ROS Generation 44

IV. Motivation 46

V. Aims and Objectives 48

VI. Outline 49

2. Si/Au Nanowires with integrated pn junction for Wireless Opto-Electrical Stimulation of Bone Cells with Ultralow Intensity NIR Light 51

2.1 Introduction 51

2.2 Results and Discussion 55

2.2.1 Design of Si/Au NWs with pn junction 55

2.2.2 Fabrication of Si/Au NW System 58

2.2.3 Opto-electric Analysis 59

2.2.4 Biocompatibility of the Short Si/Au NWs Device 62

2.2.5 Response of Osteoblasts to NIR Opto-Electric Stimulation under Ultra Low Light Intensities 65

2.2.6 Towards Injectable Si/Au NW for Cell Electrostimulation 71

2.2.7 Conclusion 74

2.3 Materials and Methods 75

2.3.1 Fabrication and Characterization of Au/Si NWs 75

2.3.2 Opto-Electric Tests 76

2.3.3 Osteoblast Cell Culture 76

2.3.4 Cell Viability Analysis 76
2.3.5 Cell Attachment Analysis 77
2.3.6 Actin Cytoskeleton Distribution 77
2.3.7 Intracellular Calcium detection 77
2.3.8 Cell Proliferation Quantification 78
2.3.9 ALP Quantification 78
2.3.10 Calcium Deposit Detection 78
2.3.11 Immunodetection of Collagen I 79
3 Si/Pt Schottky junction Nanoneedles for Cell Stimulation 81
3.1 Introduction 81
3.2 Results and Discussion 83
3.2.1 Fabrication of Si/Pt Schottky junction Nanoneedles 83
3.2.2 Opto-Electric Analysis 84
3.2.3 Biocompatibility and Interaction of Si/Pt Nanoneedles with Cells 88
3.2.4 Osteoblast -like Cells Response to Stimulation 90
3.3 Conclusion 91
3.4 Materials and Methods 91
3.4.1 Fabrication and Characterization of Si/Pt Nanoneedles 91
3.4.2 Opto-Electric Tests 91
3.4.3 Osteoblast Cell Culture 92
3.4.4 Cell Viability Analysis 92
3.4.5 Cell Attachment Analysis 92
3.4.6 Actin Cytoskeleton Distribution 92
3.4.7 Intracellular Calcium Detection 93
4. Silica/MoS_2/Cu_2O Nanoreactors for Photodynamic Therapy with NIR Light in the First Biological Window 94
4.1 Introduction 94
4.2 Results and Discussion 96
4.2.1 Fabrication and Characterization of the Nanoreactors 96
4.2.2 Synthesis of Mesoporous Silica Nanoparticles 96
4.2.3 Self-assembly of the Silica Nanoparticles 97
4.2.4 Modification of Silica Nanoparticles with MoS_2/Cu_2O 98
4.2.5 Evaluation of ROS Generation 99
4.2.6 Cell Viability Analysis 100
4.2.7 Apoptosis Detection 104
4.2.8 Nanoreactors Internalization Assessment 106

4.3 Conclusion 108
4.4 Materials and Methods 108
4.4.1 Synthesis of Mesoporous Silica Nanoparticles 108
4.4.2 Self-assembly Process 109
4.4.3 Synthesis of MoS_2/Cu_2O on Silica 110
4.4.4 ROS Quenchers 110
4.4.5 Cell Viability Analysis 110
4.4.6 Apoptosis Detection 111
4.4.7 Internalization Assessment 111
5. Conclusions 112
6. Future Perspectives 115
7. References 117
Appendix 130

III. List of Abbreviations

ALP	**Alkaline Phosphatase**
AP	**Action Potential**
APTES	**(3-Aminopropyl) triethoxysilane**
BSA	**Bovine Serum Albumin**
CDT	**Chemo-dynamic Therapy**
CTAB	**Cetyltrimethylammonium bromide**
DOT	**Diffuse Optical Tomography**
DRG	**Dorsal Root Ganglion**
DMF	**Dimethylformamide**
ECM	**Extracellular Matrix**
Ef	**Fermi Level**
ELISA	**Enzyme-linked immunosorbent assay**
EPR	**Enhanced Permeability and Retention Effect**
ES	**Electrical Stimulation**
FBS	**Fetal Bovine Serum**
FDTD	**Finite-difference time-domain**
HF	**High Frequency Power**
ICP	**Inductively Coupled Plasma Power**
MSN	**Mesoporous Silica Nanoparticles**
MPE	**Maximum Permissible Exposure**
ND	**Nanodiscs**
NIR	**Near infra-red**
NPs	**Nanoparticles**
NW	**Nanowires**
OCT	**Optical Coherence Tomography**
PDT	**Photodynamic Therapy**
PC	**Photocurrents**
PTT	**Photothermal Therapy**
PBS	**Phosphate Buffer Saline**
PDDA	**Poly Diallyldimethyl ammonium chloride**

PECVD	**Plasma-enhanced chemical vapor deposition**
PFA	**Paraformaldehyde**
PV	**Photovoltage**
QDs	**Quantum Dots**
ROS	**Reactive Oxygen Species**
RIE	**Reactive Ion Etching**
SEM	**Scanning Electron Microscopy**
TMDs	**Transition Metal Dichalcogenides**
TMB	**Trimethyl benzene**
UV	**Ultraviolet**
VGIC	**Voltage-Gated Ion Channels**

1. Introduction

Light plays a crucial role in the dynamic realms of biology and biomedicine, guiding innovation beyond conventional methods of biological interrogation. This introduction seeks a comprehensive overview of the pivotal role that light assumes in these domains, with a specific emphasis on its application in cell electrostimulation and photodynamic therapies (PDT). The adoption of light as a wireless modality for cell electrostimulation signifies a notable departure from historical electrostimulation techniques. The introduction will also address the opto-electronic principles and the underlying physical fundamentals behind opto-electronic devices. Then, the interaction of opto-electronic devices with the bio-interface will be covered. An exhaustive examination of the processes and required nanoplatforms for probing cells will be made, focusing on the use of Near-Infrared (NIR) sources inside the biological windows for in-depth actuation. Additionally, this introduction covers the role of light in photodynamic approaches, specifically reviewing the state of the art on the generation of therapeutic reactive oxygen species (ROS), and the emergence of novel nanomaterials with refined properties, tailored to address biological systems through the use of safe and highly penetrating light sources. Thus, this comprehensive introduction aims to contextualize the development of the doctoral thesis within the broader landscape of light-driven advancements in biomedicine.

1.1 Importance of light in biological processes and medicine

1.1.1 Light in Biology

Light plays a crucial role in biology, exerting significant influence on processes at both the biomolecular and cellular levels. It serves as an essential energy source for many organisms and impacts the behavior of plants and animals.

When light interacts with the surface of biological tissue, an array of optical phenomena comes into play. This includes absorption, where photons are taken in by molecules, scattering, wherein light changes direction due to interactions with the tissue's structure, luminescence, involving the re-emission of absorbed light, and reflection, where light bounces off the surface. Moreover, this interaction can lead to crucial photothermal effects, involving a rise in local temperature, and photochemical/photomechanical effects, resulting in chemical reactions or mechanical responses. Most of these intricate processes are essential for sustaining life in biological systems[1]. For instance, light absorption is crucial for plant photosynthesis, converting solar energy into chemical energy and serving as the foundational process sustaining ecosystems and supporting diverse forms of life. In biomolecules, light absorption activates or fine-tunes numerous biological processes by exposing them to specific light frequencies. Absorption at certain wavelengths can enhance enzyme performance. Red photons can promote cellular differentiation, restore cell activity, facilitate healing processes, and possess

immunomodulatory properties[2]. Conversely, blue photons can exert cytostatic or bactericidal effects[2] (e.g., inactivation of *Escherichia coli* and *Staphylococcus aureus).* Light can also influence proliferation of cells as in yeasts and bacteria[3] .

The interaction of light at the biomolecular level triggers vital behavioral responses in living systems. Phototaxis, involving movement toward or away from light, is crucial for energy acquisition, protection, resource location, reproduction, and environmental awareness in some organisms. Light interacting with photoreceptors is essential for animal vision, seasonal adjustments, and daily biological rhythms, influencing gene expression, aligning the biological clock, and impacting physiological and behavioral processes. Moreover, bioluminescence and light reflection on photonic crystal structures in living systems enhance survival and reproduction tactics. All these examples highlight the profound connection between light and biology and underscore its role as a determinant and driving force of natural evolution.

On the other side, the different light interacting processes driven at specific wavelengths have facilitated the widespread adoption of light-based techniques and the development of innovative optical setups for researching biological systems. For instance, fluorescence spectroscopy provides an unparalleled level of precision in exploring cellular processes[1,4]. In cases where photon-tissues interaction depends on absorption and scattering, it becomes possible to measure significant diagnostic markers by analyzing absorbed and scattered light from constituents of the tissues[2,4]. Additionally, dynamic light scattering techniques have enabled rapid assessments of microvasculature functionality. Light microscopy imaging, enzyme-linked immunosorbent assay (ELISA) and flow cytometry are additional examples of light-based techniques used in laboratories for biological assessment[4] .

In this context, light has emerged as an indispensable tool for visualizing, probing, and manipulating biological structures at the cellular and molecular level, revolutionizing the field of biomedical research and applications, and significantly contributing to the development of innovative medical diagnosis, treatments, and interventions, as will be introduced below.

1.1.2 Light in Biomedicine

Medical technologies leverage diverse interactions between light and tissue to develop tools for imaging, diagnosis, therapy, and surgery. Physical processes such as light absorption, scattering, and luminescence play a crucial role in medical imaging and diagnosis, offering valuable insights into tissue composition and identification of pathological changes. Additionally, the photoexcitation of endogenous or exogenous light-sensitive agents can lead to effects like heat generation (photothermal), chemical reactions (photochemical), and biological processes (photo-biological or optogenetic), or the production of sound waves/mechanical forces (photomechanical effects). These effects have been primarily utilized to create innovative therapeutic treatments and surgical interventions[4].

Light-based diagnostic and therapeutic/surgical techniques rely on precise control and understanding of light interactions with biological tissues. In diagnostics, the choice of light

wavelength is crucial, as different wavelengths interact differently with tissues. For example, NIR light excels at penetrating deeper into tissues (as discussed later on). Conversely, visible light is useful for surface-level examinations, revealing details such as skin conditions and surface abnormalities. Additionally, the intensity and duration of light exposure play pivotal roles. Diagnostic procedures often require specific light doses to achieve optimal contrast and resolution. In therapy, light intensity becomes a critical factor, particularly in treatments where light-activated compounds target and destroy diseased cells. The choice of wavelength is tailored to the absorption characteristics of the therapeutic agent, ensuring precise targeting while minimizing damage to surrounding healthy tissue[5]. Balancing these parameters ensures that light-based techniques can provide accurate diagnosis and effective therapy with minimal impact on healthy tissues.

Below, some examples of diagnosis, therapy, and surgical intervention techniques in modern medicine where light plays a leading role will be briefly indicated.

Light based imaging and diagnosis tools

Several optical approaches have significantly enhanced tissue imaging, rapidly becoming a relevant modality in the field of diagnosis. This is due to their non-invasive nature, remarkable resolution, and diverse contrast mechanisms. They enable tissue characterization, visualization of superficial and deeper blood vessels, the examination of internal organs, as well as screening for certain types of cancer. For instance, Optical Coherence Tomography (OCT) employs low-coherence light, typically in the NIR spectrum, to generate high-resolution cross-sectional images of tissues. Diffuse Optical Tomography (DOT) uses NIR light to measure the absorption and scattering of photons in tissue, offering insights into hemoglobin concentrations, water content, and lipid levels, which is particularly useful for cancer cases[4]. Super-resolution microscopy enables visualization of structures with the aid of fluorescent labels or nanomaterials to highlight specific cellular elements and processes[6]. Raman spectroscopy analyses inelastic scattering of light to gather molecular information about tissues, aiding in the identification of various biochemical compounds and potentially contributing to the diagnosis of diseases, like cancer. Photoacoustic Imaging, which generates ultrasound signals from tissue absorption of pulsed laser light, allows for high-resolution, depth-penetrating imaging, particularly valuable in visualizing vasculature and detecting tumors. Endoscopy using visible optical fibers provides direct visualization of internal organs and tissues, widely applied in gastroenterology, urology, and gynecology for early detection and monitoring of abnormalities[4].

Light activated Therapies

In addition to its effectiveness in diagnostics and imaging, light plays a crucial role in disease treatment[2], giving rise to a wide range of phototherapies using wavelengths from ultraviolet (UV) (commonly used for certain dermatological diseases) to NIR light (currently employed

for anti-inflammatory effects, pain treatment, wound healing, stimulation of cellular processes, etc.).

Due to its minimal invasiveness and notable clinical safety, phototherapy is considered a promising modality in cancer treatment[7]. PDT and Photothermal Therapy (PTT) are two widely used forms of phototherapy for targeting tumoral cells. PDT involves the use of photosensitizing agents (molecules, nano-photocatalysts) that, when activated by light of a specific wavelength, generate ROS from nearby oxygen. These ROS species are cytotoxic and can be employed to kill tumoral cells, treat skin diseases, inactivate viruses, or combat bacteria, among other applications. However, the limited penetration depth of light required for photosensitizer activation has restricted the clinical use of PDT, which is presently reserved for treating superficial lesions or lesions accessible during surgery or endoscopy[8,9]. To expand the therapeutic range, activation with NIR light is essential, which necessitates the development of photosensitizers that can be directly activated by NIR. This is a task that presents certain challenges but can be addressed with the support of nanotechnology and the emergence of new nanomaterials.

PTT uses light-absorbing agents to induce hyperthermia or thermal ablation[10]. In more recent years, plasmonic nanoparticles (NPs) are being employed to generate heat and selectively destroy cancer cells or other targeted tissues. Notably, PTT provides an effective approach for treating hypoxic tumors, as it operates independently of oxygen availability. As mentioned earlier, NIR light is preferred due to its greater penetration depth; therefore, nanomaterials activated by NIR are in high demand. PTT can also stimulate an immune response, as the heat-induced cellular stress prompts the immune system to recognize and attack the damaged cells. This immune activation can enhance the therapeutic effects of the treatment[8].

From this discussion, it is evident that nanomaterials and nanotechnology are profoundly influencing PTT and PDT therapies, contributing to the field of nanomedicine. Apart from their impact on PPT and PDT, nanotechnology can provide a wide range of NPs made from various materials with customizable size and shape, and therefore, tailored properties, capable of releasing drugs in response to light, enabling precise and controlled administration. It can also offer theranostic NPs, which combine diagnostic and therapeutic functionalities, holding great promise in precision medicine. The potential applications of light-activated NPs extend beyond imaging and drug administration, as they can also be endowed with light-controlled robotic properties to perform more complex tasks, such as non-invasive surgeries.

A more in-depth discussion of the physical and chemical processes underlying PDT and PTT in the context of nanomedicine will be covered in the subsequent sections to provide additional context for the experimental outcomes of this thesis.

Another related topic in light-based therapies is the development of implantable opto-electronic devices. These devices can be used for cellular stimulation in treatment and rehabilitation and as cellular activity sensors. For instance, prosthetic retinas show potential for vision restoration in patients with degeneration of retinal photoreceptor cells, driven by advances in opto-electronic technologies[11]. There is an expectation of emerging implantable devices based on light functionalities due to progress in bio-optic interface technology. In the following sections,

a broader overview of the state-of-the-art in opto-electronic devices and nanomaterials for cell stimulation will be covered due to their close relation to the experimental results of this thesis.

Laser Surgery

The advent of laser technology has transformed the therapeutic and surgical applications of light, surpassing the well-established effects of traditional lamps. With lasers, emission intensities can reach magnitudes several orders higher than that of sunlight. Moreover, generation of short pulses and precise selection of wavelengths are enabled[4]. Currently, medical lasers find extensive use across diverse fields, including ophthalmic surgeries, skin ailment treatment, and the application of fiber-optic delivery for tissue ablation within internal organs. Various lasers operate within different wavelength ranges, spanning from UV to Infrared[12]. It is important to note that the choice of laser wavelength, laser intensity (beam power/targeted area) and the use of pulsed laser depends on factors such as the type of tissue being treated, the specific surgical procedure, and the desired interaction with the tissue (e.g., cutting, vaporizing, coagulating, lithotripsy, etc.).

1.1.3 Importance of the NIR Biological Windows

The penetration depth of light in biological tissues—meaning how deeply light can travel through different types of tissues before it is absorbed, scattered, or otherwise attenuated—is a very important concept in medical therapy and imaging. The penetration depth depends on the wavelength of light. Shorter wavelengths (such as UV light) are absorbed more quickly and have shallower penetration depths, while longer wavelengths (such as red or NIR light) penetrate deeper. The composition and structure of biological samples play a significant role in determining penetration depth. Hemoglobin and water content, which absorb light at specific wavelengths, along with scattering events occurring when light interacts with cellular and subcellular structures, substantially influence this depth. Managing incident light energy is another vital concern, crucial for minimizing tissue injury and heat damage[13].

For instance, in cancer treatment, phototherapies have been utilizing visible and UV light sources, which as previously mentioned, exhibit low penetration depth[7] and high light absorption, often resulting in tissue damage[13]. This limitation confines the effectiveness of these therapies to superficial cancerous tissues[7]. Moreover, in the realm of biological marker detection and diagnostic imaging, the prevailing strategies revolve around fluorescent probes based on organic molecules. These molecules typically necessitate stimulation by high-energy light, such as UV and visible light, eliciting a response of visible light emission. Nevertheless, UV light comes with certain drawbacks in the imaging process. It induces photobleaching of organic molecules, thereby restricting their duration of use[14]. Furthermore, the use of UV light leads to autofluorescence in biological tissues, subsequently diminishing image contrast due to background interference[13,14]. Moreover, UV rays exert a phototoxic effect on biological substances. These considerations highlight the complexity and nuances involved in selecting

appropriate wavelengths and techniques for optimal outcomes in medical imaging and therapies.

Consequently, achieving deep photon penetration to reach the target with minimized absorption and scattering effects from the surroundings and reduced tissue injury is a paramount goal in optical imaging and light-based therapies for medical and biological applications[13,14]. Accordingly, the NIR range offers a balance between sufficient penetration depth and lower light energy levels, thus minimizing the risk of biological tissue damage during diagnostic or therapeutic procedures. Within the NIR range, there are specific "biological windows" or spectral regions where light penetration and interaction with biological tissues are particularly favorable: the first biological window (NIR I, 700-900 nm), the second biological window (NIR II, 1000-1350 nm) and the third biological window (NIR III, 1600-1870 nm) as shown in ***Figure 1a***. NIR I limits with the visible band and an absorption band at 980 nm due to the absorption of water. NIR II exhibits higher penetration depths into the tissues due to the lower scattering of cell organelles at longer wavelengths and weaker absorption of other biomolecules[13]. In the NIR III, water absorption limits substantially the final light penetration[5].

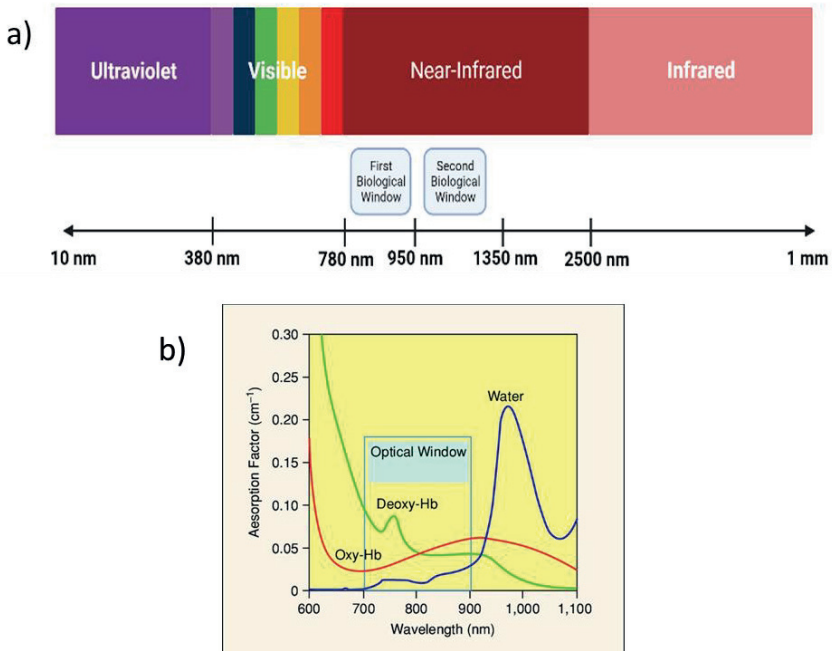


Figure 1 a) Electromagnetic spectrum ranging over different frequencies with their corresponding wavelengths showing the first and second biological windows in the NIR. b) An illustration depicting the absorption spectrum of water and hemoglobin, along with the first optical window range where the absorption characteristics of these compounds are minimized. Adapted from reference 15[15].

Understanding these biological windows is crucial for designing and optimizing devices and techniques that utilize NIR light or nanomaterials with therapeutic properties. For instance, in medical imaging, the careful selection of the appropriate wavelength range significantly influences the depth of penetration and the quality of the resulting images. Similarly, in therapeutic applications like PDT or PTT, which rely on exogenous materials, choosing the correct wavelength range to activate these materials and carry out their therapeutic function

without affecting adjacent healthy tissue is imperative for achieving the desired outcomes. All this underscores the necessity to explore, design, and tailor nanomaterials capable of harnessing their properties effectively within these biological windows.

1.2 Light for Cell Electrostimulation

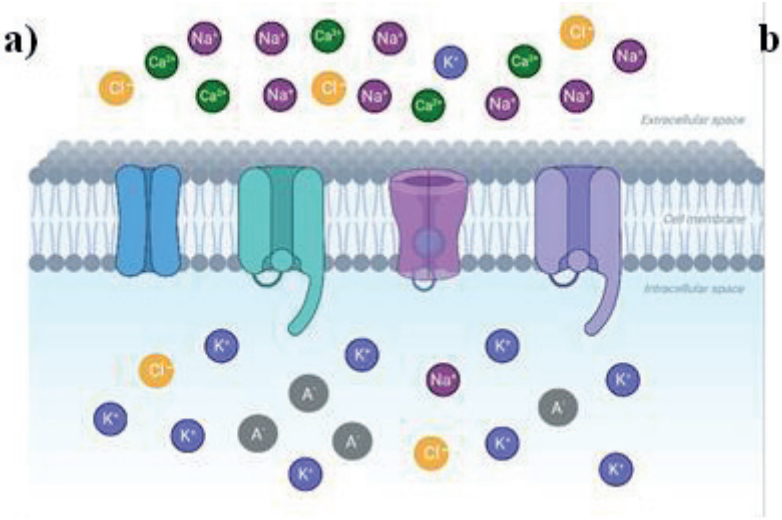
1.2.1 Importance and Basics of Cell Electrostimulation

1.2.1.1 Membrane Potential

Cell membranes are composed of a lipid bilayer which has an outer polar and inner non-polar parts. Even though this bilayer is very thin, it forms a good barrier against the diffusion of some molecules along the cell. Basically, the inner part of the bilayer is composed of the phospholipids hydrocarbon tails making it hydrophobic and consequently preventing the passage of charged and polar molecules[16]. However, membranes are more than a simple phospholipid bilayer. Several types of proteins are integrated in the lipid bilayer assisting in accomplishing the roles of a cell membrane. Among these proteins, some examples are pumps, transporters, and ion channels. Their main role is to facilitate the movement of ions and other molecules across cell membrane[16].

Besides identifying a proper shape for the cells, the plasma membrane serves as a barrier between intracellular and extracellular fluids. Both fluids are rich in various positively and negatively charged molecules and ions. The cytoplasm is rich in potassium ions (K^+), negatively charged amino acids such as aspartate and glutamate, phosphates, and nucleic acids. While the extracellular fluid is rich in sodium ions (Na^+) and chloride anions (Cl^-) (***Figure 2a)***. Calcium ions (Ca^{2+}) are also predominant in the solution outside the cell, but have storages in some organelles inside the cell, such as: endoplasmic reticulum, mitochondria, and calciosome[17]. This unequal distribution of ions across the cell membrane leads to the formation of a concentration gradient, allowing the movement of ions down the gradient, besides the emergence of a voltage difference denoted as the membrane potential [16–18]. Membrane potential can be defined as the potential difference between the internal and external faces of the membrane, which results mainly from the passive diffusion of ions[17]. In excitable cells as neurons and muscle cells, for example, resting membrane potential ranges between -70 and -80 mV[19]. V_m is maintained through the differential permeability of cell membrane to ions[20]. Typical concentrations of ions in extracellular and intracellular environments are shown in ***Figure 2b***.

a)



b)

Ions	Intracellular Concentration (mM)	Extracellular Concentration (mM)
K^+	140	3
Na^+	14	140
Cl^-	14	146
Ca^{2+}	1*10^-4	1.5

Figure 2 a) Illustration showing the distribution of ions across the cell membrane. At resting state, ions like sodium, calcium and chloride are mainly concentrated outside the cell. While potassium and other anions are concentrated inside the cell. b) Table constituting the concentrations of ions in the intracellular and extracellular solutions across the plasma membrane.

Thus, the movement of ions in physiological solutions is controlled by an electrochemical gradient which includes both concentration and electrical gradients of ions[17,21]. Due to this unequal distribution, ions will pass through the membrane until they reach an equilibrium. When an electrochemical equilibrium is achieved, it does not mean that concentration is equal on both sides of the membrane. Instead, a concentration gradient persists, but it is counteracted by the opposing electrical gradient[21]. As a result, membrane potential plays a major role in determining the direction and amplitude of ions movement across the membrane[17]. The role of membrane potential is not only restricted to excitable cells. Research studies have shown that, although smaller in magnitude compared to excitable cells, membrane potential is important in non-excitable cells as well, playing various roles in cellular functions, such as cell proliferation, cell cycle, wound healing, and contraction of muscles[20]. Membrane potential in excitable cells will be discussed later.

As mentioned before, the intricate regulation of ion flux is assisted by a diverse array of proteins located within the cell membrane. These proteins serve as molecular gatekeepers, meticulously controlling the passage of ions in and out of the cell as will be described below.

1.2.1.2 Ion Channels

Ion Channels are integral membrane proteins exhibiting a three-dimensional structure that spans the membrane from one side to the other forming a hydrophilic narrow pore across the membrane[16,17]. They allow the diffusion of millions of ions per second down their electrochemical gradient, without need of energy[22]. As their name depicts, ion channels facilitate and control the movement of inorganic ions down their electrochemical gradient across the membrane based on two main factors that specialize them: ion permeation and ion

selectivity[16,17,22]. Being selective, these channels favor specific ions with the appropriate charge and size to pass through them[23]. Compared to simple aqueous pores, ion channels are not always open; however, they are gated channels that open and close upon response to a certain stimulus[24]. Based on this, ion channels could be divided into three types as shown in ***Figure 3***: a) Voltage-gated, which open in response to membrane potential changes; b) Ligand-gated open upon ligand binding, and c) Mechanical-gated due to a mechanical stress[25]. Animal and plant cells and microorganisms as well, all express many types of ion channels which play different roles in different cells, mainly in excitable ones. For instance: they are responsible for the electrical excitation of muscle cells and participate in electrical signaling mediation of the nervous system[26]. Non-surprisingly, a single nerve cell expresses more than 10 types of ions channels.

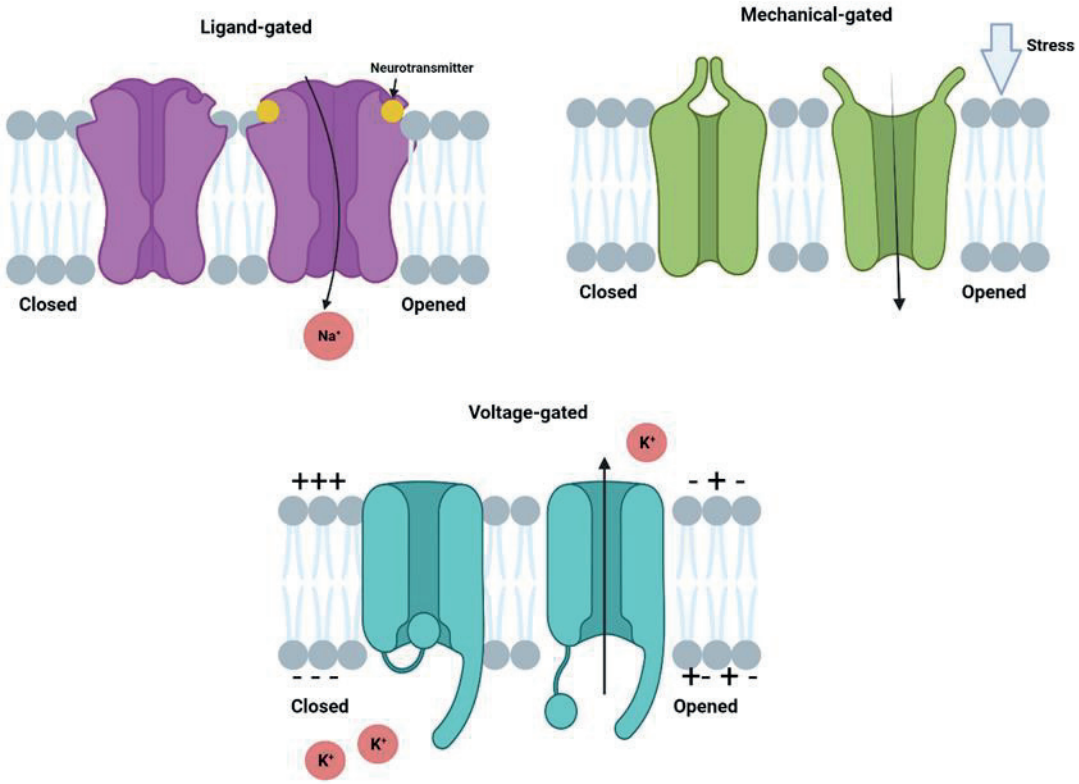


Figure 3 Different types of channels based on gate type. a) Ligand-gated ion channel which opens upon binding of a ligand like neurotransmitters in neural cells. b) Mechanical-gated ion channel that opens in response to stress. c) Voltage-gated ion channels open due to changes in the membrane potential.

Voltage-gated Ion Channels (VGICs)

The superfamily of Voltage-Gated Ion Channels (VGICs) is among the largest groups of signaling proteins, ranking in size after G protein-coupled receptors and protein kinases in terms of the number of members within the family[27]. VGICs are activated by alterations in the electrical potential across the cell membrane. Even though they are predominantly located in excitable cells and tissues, they can also be expressed in non-excitable cells[28]. There are three primary families of VGICs that can be differentiated depending on the specific cation that they allow to pass through them: potassium (K_V), sodium (Na_V) and calcium (Ca_V)[29]. VGICs can efficiently convert subtle changes in membrane voltage, ranging from as little as 1 mV up to 100 mV during an action potential, into a fast, effective, and specific movement of one of the three primary ions (Na^+, K^+, and Ca^{2+}) across cell membranes[29]. This feature specializes VGICs from other types of ion channels[29].

Voltage-gated Ca^{2+} Channels

Calcium ions serve as a secondary messenger for signal transduction activating various cellular processes which differ with cell types (***Figure 4***). Therefore, there are different subtypes of calcium channels. In terms of calcium conductance, calcium channels are subdivided into the following types: L-, N-, PQ-, R- and T-type, which were previously classified as high- and low-voltage activated currents[30,31]. Since a variety of functions can be accomplished through the opening of the calcium channels, different types of channels become activated at varying voltages and exhibit distinct kinetics[3232]. For instance, the L-type is a long-lasting calcium channel which is characterized by a high voltage of activation[30]. Compared to L-type, T-type channel requires a lower voltage to be activated, however it undergoes a rapid inactivation[30].

Typically, neurons, muscle cells and certain endocrine cells are recognized as excitable cells[31,33]. However, other cell types also exhibit some fluctuations in the voltage[31]. Upon cell membrane depolarization, action potentials or subthreshold depolarizing signals are generated, thus triggering the opening of calcium channels which are expressed in many cell types[30,31]. The cytoplasm of cells maintains a relatively low level of free intracellular Ca^{2+} ranging from 10 to 100 nM in comparison to the extracellular environment[31]. When calcium channels open, Ca^{2+} move down their electrochemical gradient, leading to an increase in the cytosolic Ca^{2+} concentration[30,31,34]. Depending on the cell type, this calcium elevation mediates different responses. It facilitates the secretion of hormones in endocrine cells, initiates contraction in smooth and cardiac muscle cells and transmission of signals between neurons[30,32]. Moreover, it plays a regulatory role of various biochemical processes including enzyme activity and gene expression[30]. In summary, on the cell membrane, electrical signals of action potential are transformed into a transient increase in intracellular calcium concentration driving various cellular processes. Here, voltage-gated Ca^{2+} channels play a key role in electrical excitability through the facilitation of calcium entry into the cells[30].

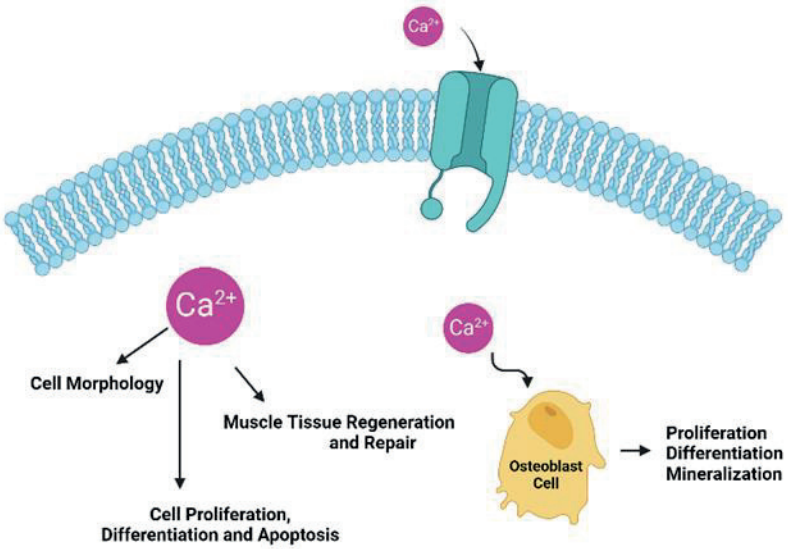


Figure 4 Illustration showing some of the cellular processes activated in response to Ca^{2+} flow into the cells. Various cellular processes are affected such as proliferation, morphology, differentiation, and regeneration depending on the cell type and signaling pathway triggered by the calcium inflow serving as a secondary messenger.

1.2.1.3 Excitable Cells and Action Potentials

In terms of electrical activity in our body, excitable cells are the key players as they can be electrically excited and elicit action potentials (AP). Excitable cells include a diverse group: neurons, muscle cells (skeletal, smooth, and cardiac) and some endocrine cells (pancreatic β cells). In response to a certain stimulus (mechanical stress, signaling molecules…), the membrane potential depolarizes to positive potential, followed by a rapid repolarization back to resting membrane potential. This change in the membrane potential is mediated by the opening and closing of certain ion channels such as Na^+ and K^+, ending up firing an AP.

To explain it in more detail, when the membrane potential exceeds a specific threshold, depolarization is triggered through the opening of voltage-gated sodium channels leading to an influx of Na^+ into the cells, followed by a rapid closing of these channels and activation of voltage-gated potassium channels. At this point, membrane repolarization is induced due to the efflux of K^+. After reaching resting potential, some of potassium channels remain open which causes a hyperpolarization state where the membrane potential becomes more negative. This state remains until potassium channels close, thus restoring resting membrane potential as shown in ***Figure 5***[16].

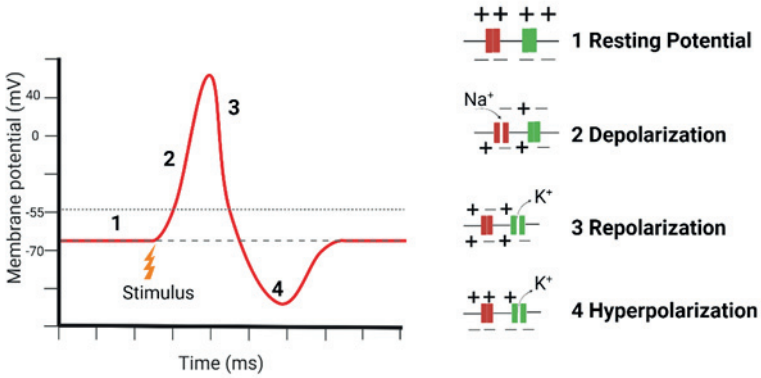


Figure 5 Graph portraying the different stages before and after an action potential is elicited upon stimulation.

APs serve different roles in different excitable cells. For instance, they are needed for the transmission of signals along the whole length of a nerve cell, allowing cells to communicate with one another through neurotransmitters release[16,20,21]. In cardiac and skeletal muscles, AP generation is coupled to excitation-contraction of muscles besides an increase in the Ca^{2+} level inside the cells[16,20]. Hence, they play a fundamental role in transmitting information and facilitating communication, especially within nervous and muscular systems. Therefore, studying AP and excitable cells is not merely important for physiological purposes, it also sheds light on vital clinical cases. Impairment of cells and malfunction of VGICs lead to abnormal excitable cells ending up in a wide range of diseases affecting especially the nervous and muscular systems. For instance, studies showed that cancer could be associated with extra functioning of VGICs in excitable cells[28]. Alzheimer, Parkinson and cardiac arrythmia are among the illnesses associated to impairment of neurons and cardiac cells[35,36]. Moreover, when the electrical activity of β-pancreatic cells is slower, it leads to abnormal secretion of insulin, thus resulting in higher glucose levels and leading to diabetes[37].

On the other hand, cells that do not elicit AP are termed as non-excitable cells, although they also undergo changes in the membrane potential, but without exceeding the threshold. Besides not generating AP, they neither generate nor conduct electrical impulses. Yet, non-excitable cells constitute various types of cells that play crucial roles in the body contributing to structural support, immune responses, secretory functions, in addition to communication and signaling (***Figure 6***).

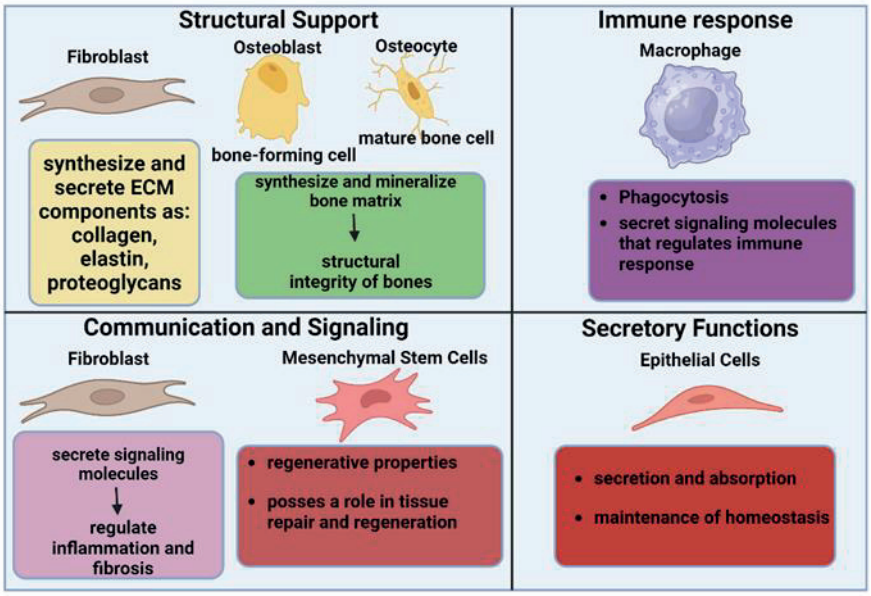


Figure 6 Portrait of different types of non-excitable cells and their roles in the body.

An example of non-excitable cells are bone cells. Osteoblasts, known as bone-building cells, play a vital role in bone formation through three processes: osteogenesis (Extracellular Matrix (ECM) synthesis), modeling and remodeling. Osteoblasts are responsible for ECM synthesis by secreting bone matrix proteins, including collagen type I, alkaline phosphatase (ALP) and osteocalcin. Performing and regulating these processes is important to ensure proper bone development, facilitate fracture repair, and maintain a healthy skeleton throughout our lives. In cases where bone matrix gets depleted, osteoblasts are activated. Bone defects also trigger the activation of osteoblasts to fix these issues, promoting bone regeneration. Due to their role in bone regeneration, osteoblasts become a target for advanced bone therapies[38,39].

Osteoblasts descend from mesenchymal progenitors, which differentiate into pre-osteoblasts, that subsequently differentiate into osteoblasts in a three-stages process: 1) Proliferation. where cells proliferate and secrete fibronectin, osteopontin and collagen, 2) Matrix maturation in which cells starts differentiating and enriching the matrix with ALP and collagen, 3) Matrix mineralization where osteocalcin is secreted and enrich the scaffold enhancing mineral deposition[39].

Different approaches as electrical cell stimulation have been reported as possible ways to restore the function of impaired cells. While it is true that non-excitable cells do not generate AP, some of them express VGICs and possess electrical activity, although to a lesser extent than excitable cells. In this thesis, our focus is on non-excitable cells, specifically bone cells. Therefore, in the following part, we will discuss/present some applications for electrical stimulation (ES) of both excitable and non-excitable cells.

Typical Applications of Electrostimulation and Wired Methods

In response to the disorders resulting from malfunctioning of excitable cells, various treatments have emerged. Historically, for several years, ES has been standing at the forefront of biomedical technologies, offering various applications that cover different fields such as neuroscience and tissue engineering. ES, in principle, is based on the employment of electrical signals which leads to a variation in certain components of the cells, such as ion channels. Consequently, APs are triggered in excitable cells. This leads to modulation in cellular behavior and restoration of their function[40]. In the field of tissue engineering, ES is used for the replacement of damaged tissues. Its efficacy in the modulation of cellular proliferation, differentiation, and morphology as well as ECM formation and mineralization has been also demonstrated[40,41]. Despite the complexity of neural system and its regeneration, ES was successfully employed to activate axon growth and trigger neural differentiation[40]. With the help of ES, it is possible to investigate neural pathways and to study the effects of electrical impulses on biological processes. Studies have demonstrated that ES affects signal transduction proteins, influencing cellular behavior related to differentiation, migration, and proliferation[42]. Conversely, some studies have also shown that ES could suppress cellular proliferation. For instance, applying direct current to mesenchymal stem cells was shown to halt proliferation and instead induce their differentiation into neuron-like cells[42]. Furthermore, ES can reduce pain and boost blood circulation[43].

While it is true that most applications of ES are predominantly associated with excitable cells, such as neurons and muscle cells, it has also demonstrated a role in non-excitable cells. Non-excitable cells express VGICs enabling a change in the membrane potential which can trigger cellular processes, thus rendering them responsive to ES as well. Although glial cells are part of the central nervous system, they are classified as non-excitable cells. However, they express voltage-gated channels and communicate through ion flows. It has been shown that glial cells respond to ES through calcium waves generation. Moreover, signaling between glial cells can be promoted in response to ES[44]. Likewise, low-level alternating electric fields have facilitated the mineralization of bones and induced osteogenic differentiation[41]. While bone cells can naturally regenerate, this ability is limited to small defects. ES has shown efficiency in fostering bone formation, thereby promoting bone healing[41,45].

In general, several factors play a role in the response to ES, including cell type, frequency, voltage or current amplitude, and duration of the stimulation in addition to the material used[40,41]. These parameters can be easily tuned to achieve the desired outcomes and maximize the repair effects[43].

Clinically, ES has proven to be both highly effective and widely adopted in therapies related to excitable cells. Implantable devices as electronic pacemakers, cochlear and retinal implants show a successful combination between ES and medical practices (***Figure 7a-c***). These devices can aid in fixing the failure in electrical conduction of the heart and restore auditory as well as visual functions, respectively[36,46,47]. Furthermore, deep brain stimulation and nerve stimulation have been shown to improve the life quality of Parkinson disease patients and those suffering from epilepsy and rheumatoid arthritis[48,49].

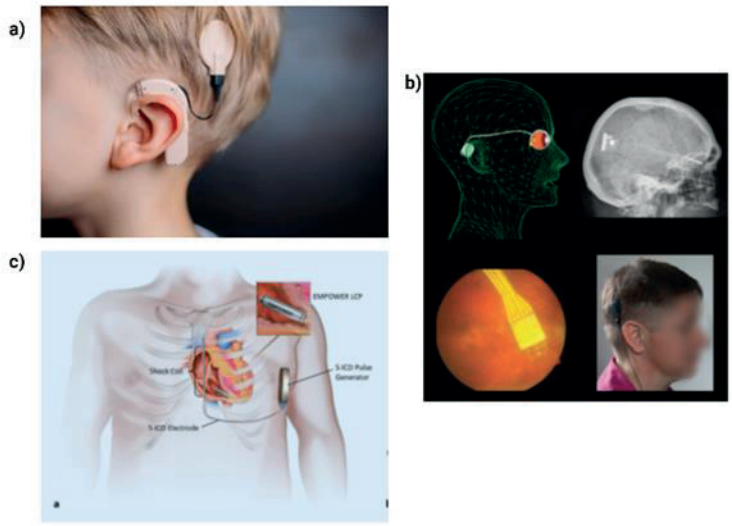


Figure 7 Different wired electrical stimulation applied clinically. a) Cochlear implant to stimulate nerve endings of ears for auditory restoration. b) Alpha-IMS subretinal implant[50]. c) Molecular cardiac rhythm management implanted system, image adapted from reference 51[51].

However, in these applications, ES has been achieved through implantable devices involving wired electrodes and battery supply, denoted as Wired ES. Despite the great success achieved, it is still facing serious limitations. Wired ES is bulky and invasive, requiring surgery to insert the electrodes, which can increase the possibility of infection and inflammation at the interface between tissue and device[36,40,49]. Unexpected electrochemical reactions could also be generated[36]. Spatial resolution, as well as treatment location have been limited by the necessity of wired devices, resulting in asymmetrical activation/inhibition of cells. For instance, neural ES has partially failed in targeting specific neurons, leading to a collective response which can affect the clinical outcome of the stimulation[36,52]. In seeking improvement of clinical outcomes and overcoming these limitations, research has been directed towards abandoning electrodes and using other stimulations instead. This has led to the development of wireless stimulation, where optical, magnetic, and acoustic signals become useful and non-invasive tools to efficiently stimulate cells with less tissue damage.

The selection of wireless techniques hinges on the specific needs of the application, considering factors such as the desired target tissue depth, required spatial and temporal precision, and safety considerations. Each technique possesses distinct advantages and disadvantages. For example, magnetic and acoustic approaches offer impressive penetration depths but face challenges in achieving fine spatial resolutions due to inherent difficulties in focusing their respective operating fields. They also exhibit moderate temporal resolutions. While ongoing efforts in each wireless technology aim to mitigate limitations and enhance synergies by complementing one another, optical techniques for inducing electrical signals stand out as the only approach capable of combining subcellular spatial and sub-millisecond temporal resolutions. Despite ongoing efforts to address limitations in penetration depth, optoelectronic

biomodulation is anticipated to play a pivotal role in advancing the frontier of electroceuticals in the upcoming era.

1.2.2 Opto-Electrical Cell Stimulation

1.2.2.1 Basics of Opto-electronic Processes

Semiconductors are essential for developing opto-electronic devices and it is important to consider various aspects that govern their final performance. The photoelectronic conversion involves four distinct stages, each requiring optimization of different parameters and relevant materials. The first step is light absorption to generate charge carriers in the valence and conduction bands. The second step is the separation of the photo-induced charge carriers minimizing recombination processes. In this part, interfacial junctions and the generation of built-in electric fields play a key role. It is this charge separation that allows the independent movement of positive and negative charges, a relevant factor for achieving high-performance devices. Once separated, the charge carriers should move within the semiconductor material. Along this route, trapping and recombination of charge carriers can occur. Therefore, optimizing transport paths is vital to maximize the efficiency of the photoconversion process. The culmination of the conversion process lies in the injection of charge carriers into a circuit, an electrolyte interface, bio-interface, or the charge accumulation at the interfaces. This step ensures that the converted electrical signal is directed towards its intended destination, where it can be harnessed for a wide variety of purposes[53,54]. In the context of bio-interfaces, the output electrical signal has the potential to induce capacitive effects by charging interfacial layers, or elicit faradaic currents, subsequently influencing cellular processes. Further details on these processes will be provided later.

Firstly, we will focus on the fundamental characteristics of interfacial material junctions in opto-electronic devices, namely, pn junctions and Schottky junctions. These elements exert a significant influence on electronic properties, especially in charge injection and separation and play a fundamental role in achieving multifunctionality and property tuning for opto-electronic stimulation. They are key for the development of self-powered actuators operating under illumination.
Then, more insights of the other processes involved in the photoconversion will be given in connection to the different materials used for opto-electronic devices.

Interfacial Junctions: pn junction and Schottky junctions

Silicon material will be used as a model system to establish the fundamental principles underlying both pn junctions and Schottky junctions, which will be useful for understanding the performance of devices integrating such junctions in biological cell stimulation. Here, a brief overview of the fundamentals of these junctions will be provided.

i) pn junctions

Silicon's conductivity can be tailored through chemical doping, allowing it to become either an n-type or p-type semiconductor. In n-doped silicon, impurities like phosphorus or arsenic (Group V) introduce an energy level near the conduction band, adding extra electrons to the material at the conducting band. These additional electrons are free to move around, creating a surplus of charge carriers. Conversely, p-doping involves elements from Group III, such as boron, which introduce vacancies (holes) in the valence band . These holes act as acceptors for electrons, resulting in an excess of positive charge carriers. In doped silicon, the number of electrons in the conducting band and the number of holes in the valence band are unequal, leading to a shift in the Fermi level (E_f) towards either the conduction or valence band for n-doped and p-doped silicon, respectively.

The transport of charge carriers in these materials is governed by diffusion (driven by concentration gradients) or drift (driven by electric field) and with their lifetime being affected by hole/electron recombination processes. Tailoring carrier transport is a pivotal aspect of semiconductor device engineering, and these junctions are useful tools to accomplish that. In particular, pn junctions are crucial for generating electronic and opto-electronic diodes. They exhibit rectifying properties, wherein a forward applied voltage leads to an exponential current-voltage relationship, while a reverse voltage blocks current flow. Moreover, under light illumination an overall current flow across the junction can be established, depending on their concentration and mobility. To better understand the system, it is better to start describing the pn characteristics in absence of any external perturbation, that is, when n Si and p Si are connected and reach an equilibrium. As mentioned, the n-side possesses an excess of mobile electrons whereas the p-side an excess of holes, induced by dopants. When these sides are brought together, mobile electrons diffuse from the n-side towards the p-side, creating a positive charge on the dopant at the n-side. Conversely, the p-side, with dopants deficient in one electron compared to silicon, generates mobile holes that diffuse towards the n-side, resulting in a negative charge on the dopant of the p-side. The charged region is restricted to the interfacial part (since beyond such region recombination processes neutralize the charges). This charged interface generates an electric field pointing from the n-side to the p-side (***Figure 8a***).

This charge exchange process can be explained in terms of the energy band model, that is in terms of the valence band, conducting band and bandgap of the semiconductor. That facilitates the visualization of the impact of the in-built electric field from another perspective (***Figure 8b-e***). Initially, before contact, the n-doped region has a high concentration of electrons in the conduction band (Ec) and with the Fermi level close to the conducting band, while the p-doped region has a high concentration of holes in the valence band (Ev), with the Fermi level close to the valence band (***Figure 8b***). Upon contact, electrons diffuse from the n to the p-region, and holes diffuse in the opposite direction. This diffusion makes the Fermi level at the n-doped material shift down, and that of the p-doped material shift upwards, with both Fermi levels coming together and becoming equalized when reaching equilibrium (***Figure 8c***). This process produces a charged interface and the band bending phenomenon at the semiconductor bands. The bending of the bands while keeping their connection at the pn junction is a consequence

of addressing two critical considerations: i) ensuring that, despite the interface being charged by the carrier exchange, the original electronic and doping properties beyond the interfacial region are preserved [a], and ii) maintaining the basic rule that the Fermi level of the system should not exhibit slopes or discontinuities in equilibrium. In this way a flat Fermi energy level is ensured. The band bending covers the charged interface, creating a depletion zone of mobile carriers (holes and electrons), affecting the charge transport. The electrons in the conducting band of the n-doped region encounter an energy barrier at such bend region when attempting to diffuse into the p-region. Only very few carriers could have enough energy to overcome this barrier. The same happens on hole diffusion at the valence band. Very few holes could have energy enough to diffuse to the other side. Additionally, the slope of the band bending is the signature of a built-in electric field, with a direction pointing from the n to the p-region. Consequently, only electrons from the p-region (minority carriers) can drift into the n-region at the conducting band. Likewise, only holes from the n-region (minority carriers) can be driven towards the p-region at the valence band. This results in a balance between diffusion and drift currents, reaching an equilibrium state (***Figure 8d and e***)[55,56].

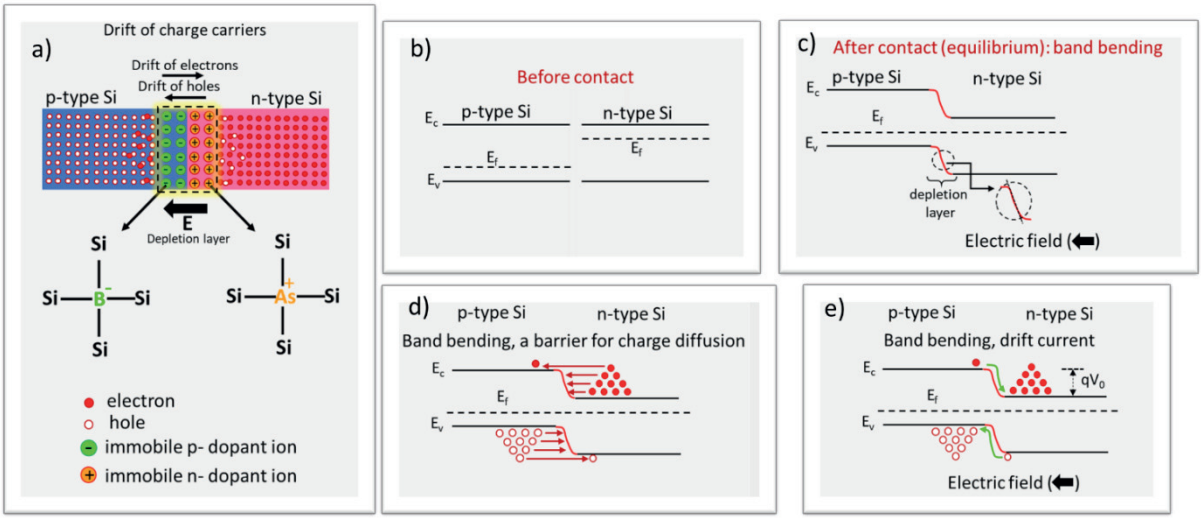


Figure 8 Physical scheme of a pn junction showing the built-in electric field (a). Band diagram models depicting the pn system before contact (b), after contacting (c) and the diffusion (d) and drift currents (e) that are balanced at equilibrium.

An external perturbation, like exposing the pn junction to light, breaks the charge balance affecting carrier transport. When uniformly illuminated, the pn junction generates an excess of

[a] That means that the position of the Fermi level with respect to the valence band (p-doped region) or the Fermi level with respect to the conduction band (n-doped region) and the bandgap beyond the interfacial region will be kept the same as before contacting.

hole and electron pairs throughout, including in the depletion region, its vicinity, and the bulk n and p-sides. However, the most significant processes predominantly occur within or close to the depletion region. The surplus carriers generated at the depletion layer are swept out away by the in-built electric field, initiating a drift current. Electrons will be drifted towards the n side and holes towards the p side. This process is unique to the pn junction, as it lacks in simple p-type or n-type semiconductors. Notably, the drift current impacts not only carriers within the depletion region but also those nearby, in what is called diffusion length (L_p or L_n). Minority carriers within the diffusion length experience random motion but it's their own stochastic movement that may lead them into the depletion region, and them swept them out of the depletion region towards the opposite side, and thus contributing to the interfacial current (***Figure 9a-b***).

The photocurrent is determined by factors including area, generation rate of carriers, diffusion lengths, and depletion region width. The drift process of carriers at the junction creates an excess of electrons in the n-side and excess holes in the p-side of the device respectively, which splits the Fermi levels at both doped sides generating a voltage drop across the pn junction. If the pn junction is at open circuit, the developing voltage due to the light illumination (photovoltaic effect) is referred to the open circuit voltage (Voc). The Voc is a very important parameter to characterize the photodiode performance. More explicitly the open circuit photovoltage is the maximum voltage that can be measured across the terminals of a photovoltaic device when there is no external load connected to it (that is in conditions of high impedance conditions, no current) (***Figure 9c***). In other words, it is the voltage generated by the pn junction when it is not being used to deliver current to any external device. The other important parameter for characterizing light activated devices for generating power is the short circuit photocurrent, which is the maximum current that can flow through a photovoltaic device when its terminals are connected together (***Figure 9d***). In this case, the np device acts as a short circuit device, and the photogenerated current flows through a low impedance circuit, from the n side to the p side. The product of these two parameters is known as the *theoretical* maximum power output of the device, which is a measure of its efficiency (***Figure 9e***). The efficiency of an optoelectronic device can be increased by optimizing the properties of the pn junction, using materials with a suitable energy bandgap, and improving the device design. In the scope of this thesis and as mentioned, both photovoltages (PV) and photocurrents (PC) will be the ones playing the crucial roles in stimulating biological cells[57,58].

It is also important to mention that, under electrolyte contact, the photodiode/electrolyte interface can additionally influence the device performance. In general, the n-side and p-side silicon terminals in contact with the electrolyte exhibit band bending in different directions. This band bending creates barriers that influence the movement of charge carriers, thus impacting the photodiode's behavior. When exposed to light, these potential barriers can be dynamically modified, affecting the flow of current across the interface.

Additional junctions can be found at the photodiodes if they have metal contacts forming ohmic or Schottky junctions as discussed below.

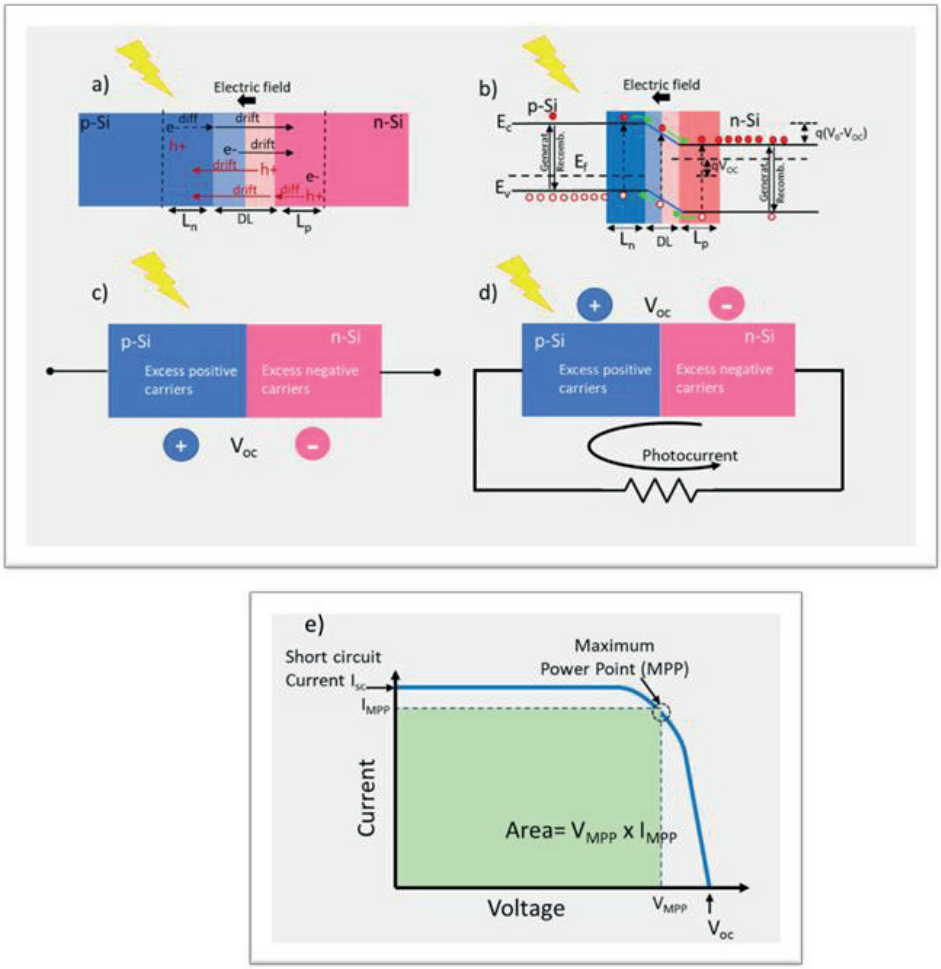


Figure 9 Physical and band diagram models of a pn junction under light illumination (a and b) (DP, denotes depletion layer and L_n and L_p are the diffusion lengths for electrons and holes). Schemes of the pn junction with their photogenerated carriers accumulated at the terminals of the n and p-side, giving rise to the maximum output voltage in open circuit (under high impedance connections) or depicting a short circuit photocurrent (under conditions of very low impedance connections) (c and d). Scheme showing the maximum power output of the device, which is roughly the area below the I/V curve (e) (I_{sc}= short circuit current; V_{oc}= open circuit voltage; MPP= maximum power point; I_{MPP}= current at the maximum power point; V_{MPP}= voltage at the maximum voltage point).

ii) Schottky Junction

In this section, the influence of Schottky junctions will be explored, as devices based on this type of junction are also addressed in this thesis. A Schottky junction is formed by bringing a metal into contact with a semiconductor material. This junction exhibits properties akin to those of a diode. The Schottky junction's behavior depends on the type of semiconductor (n or p) and the work function of the metal in relation to that of the semiconductor[b]. The work function Φ

[b] The work function, the vacuum energy level (E_o) and electron affinity (χ, as the difference of energy between the conduction band and E_o) of a solid could have also been introduced earlier in the section on pn junctions, as they are related to the Fermi level and the conduction band. For simplicity, the pn junction was explained solely in terms of the Fermi level and the semiconductor bands. However, in the case of Schottky junctions, these parameters are important to consider for a better understanding of the process.

is the energy needed to remove an electron from the Fermi level of a solid to a point in the vacuum immediately outside the solid surface (E_o). To create a Schottky barrier with an n-type semiconductor, the metal's work function (Φ_m) must be higher than that of the semiconductor (Φ_s). When these materials come into contact, there is a rapid diffusion of charges between them, leading to equilibrium. Electrons from the semiconductor's conducting band move towards the metal (lower energy levels), causing a shift in the Fermi level of the n-doped material to align with that of the metal[57].

The instantaneous charge diffusion up to reaching equilibrium generates a charged interface and induces a shift in the vacuum energy levels of both the metal and semiconductor. This ensures the retention of their electronic and doping characteristics (bandgap, Φ, electron affinity χ, and hence the position of E_f with respect to Ec) beyond the charged interface region. As mentioned before, to maintain these parameters unchanged as well as to keep the Fermi levels aligned and ensure no discontinuity at the energy levels in the vacuum, both the conduction and valence bands should bend at the interface. The band bending only takes place at the semiconductor side, generating a region depleted of electrons at the interface, which is evident by the relatively larger position of E_f from the conducting band at the interface compared to the one in the bulk semiconductor. Once equilibrium is reached, electron diffusion over the metal side ceases. The band bending results in a potential barrier that hinders electron flow from the semiconductor side to the metal, creating an electric field directed towards the metal (slope of the band bending). This field restricts electron drift from the n-side and from the metal side (***Figure 10a-c***). It does only allow for a small number of holes to drift from the semiconductor to the VB of the metal, but their concentration is so low that the effect is negligible.

On the other side, to create a p-type Schottky barrier, the semiconductor's work function must be higher than that of the metal ($\Phi_s > \Phi_m$). When they come into contact, holes (majority carriers in the p-type semiconductor) diffuse from the semiconductor to the metal up to align the Fermi levels of both materials. This creates a band bending at the semiconductor interface in the opposite direction to the one of the n-doped Si. Accordingly, an interfacial hole depletion at the semiconductor interface and a hole accumulation at the metal surface are induced. Once equilibrium is reached, the band bending, and consequent positive electric field built into the semiconductor block hole diffusion and drift from the semiconductor to the metal (***Figure 10d-f***).

The Schottky barrier functions like a one-sided diode, with the depletion region only forming on the n- or p- side of the semiconductor, not in the metal. The built-in potential at the semiconductor side is actually the barrier that electrons (at the conducting band of n-doped Si) or holes (at the valence band of p-doped Si) see trying to move into the metal. Such potential barrier is defined as $V_o = (\Phi_m - \Phi_s)$. In turn, the Schottky barrier height is the barrier that charge carriers see to move from the metal to the semiconductor and is defined as the energy difference

between the Fermi level of the metal and the conducting band edge of the semiconductor and given by $\Phi_B = \Phi_m - \chi$, as shown in ***Figure 10b***. For p-type semiconductor, the barrier height is given by the difference between the valence band edge and the Fermi energy in the metal, $\Phi_B = E_v - \Phi_m$ (***Figure 10e***).

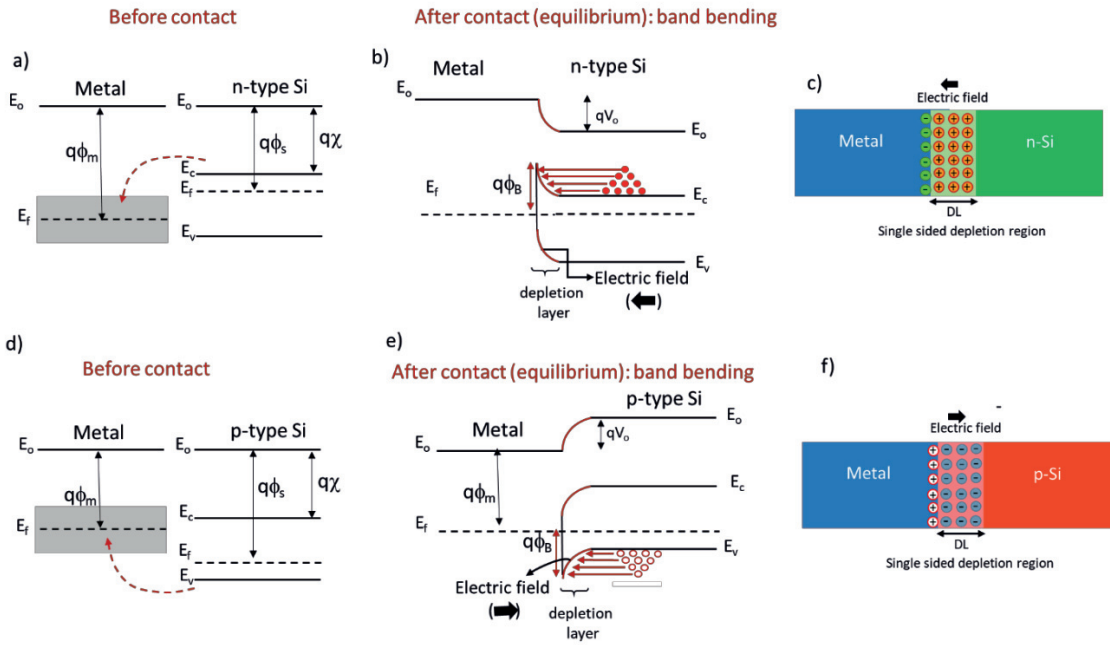


Figure 10 Band diagrams model for a n-doped Si/metal Schottky junction before (a) and after contact (b) together with the physical model (c). Band diagrams model for a p-doped Si/metal Schottky junction before (d) and after contact (e) together with the physical model (c).

For a Schottky junction at equilibrium, the net current is zero, but an external perturbation can modify substantially the barrier potential at the semiconductor side and induce a current (e.g. a bias potential), while the Schottky barrier can remain essentially constant in ideal conditions. Light illumination can also shift the equilibrium conditions inducing a PC. Different possibilities exist regarding the direction of charge flow at the junction under light exposure. For instance, electrons from the metal can be injected into the semiconductor with light. Light illumination can induce hot electrons on the metal side with enough thermal or kinetic energy to surpass the Schottky barrier height[59–61] (***Figure 11a***). Another possibility could be that light illumination populates the conducting band with more electrons (e.g. n-doped Schottky junction), allowing a higher number of electrons with enough kinetic energy to be injected into the metal than the number of electrons drifting into the semiconductor[62] (***Figure 11b***). While the former process has been frequently observed in many applications, the latter one has also been reported in some studies, highlighting the bidirectional characteristics of charge flow depending on the light wavelength, intensity, exposure time and semiconductor doping[63–65].

Various mechanisms of charge transport can contribute to the total current, including diffusion (due to concentration gradient across the depletion layer), thermionic emission (where energetic charge carriers with sufficient thermal energy surpass energy barriers), drift (driven by the built-in electric field), or tunnelling (predominantly for very thin barrier thicknesses,

especially in heavily doped semiconductors). While all these mechanisms play a role in the overall current within a junction, the dominance of one process over the others depends on device conditions. Typically, thermionic emission is the most likely dominant mechanism[61,66–68]. Drift currents are rather negligible restricted to the minor carriers in the semiconductor. The plasmonic characteristics of some metals can assist in the thermionic injection of hot electron from the metal into the semiconductor provided by enhanced electromagnetic field at the metal interface via surface plasmon resonances.

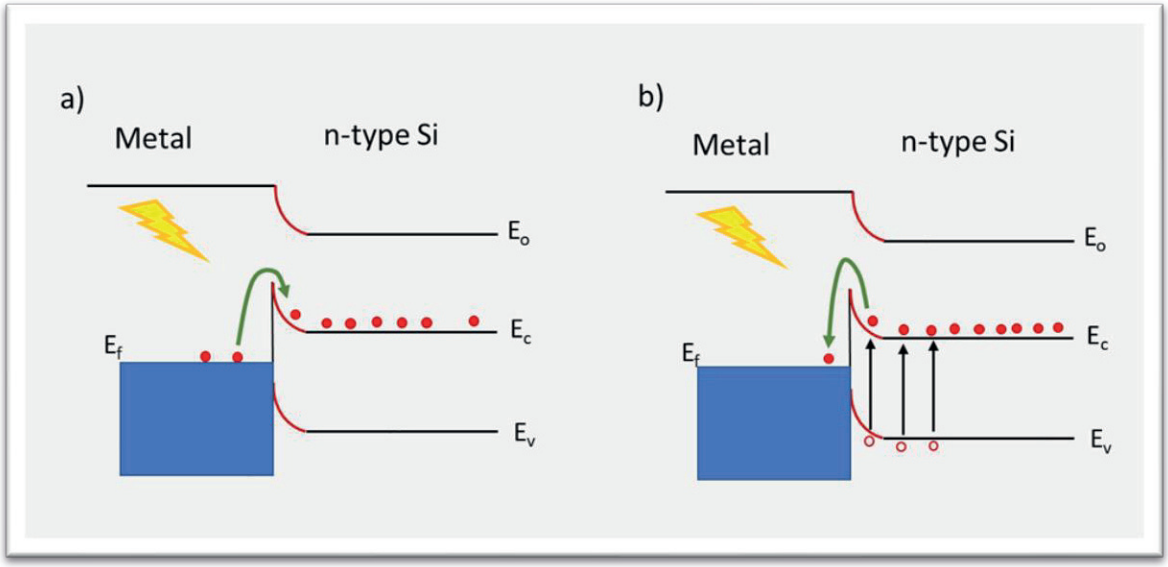


Figure 11 Band diagram models of a n-doped/metal Schottky junction under light illumination. (a) Light illumination can activate hot electrons at the metal side overcoming the Schottky barrier height and being injected into the semiconductor, a process that can be enhanced by the plasmonic characteristics of the metal and has been frequently observed with particularly longer wavelength sources. (b) Light illumination can also favor the injection of electrons from the semiconductor side into the metal, especially when illuminating with shorter wavelengths, creating significant hole/electron pairs at the semiconductor side. The photogenerated electrons at the conducting band, although influenced by the junction electric field, can also acquire enough kinetic energy to flow towards the metal side.

1.2.2.2 Materials for Opto-Electric Stimulation and their Limitations

In the preceding section, the different processes behind an opto-electronic actuation were indicated: light absorption and photogeneration of charge carriers, charge carrier separation, transport and charge accumulation/injection into a circuit, electrolyte, or bio-interface. Emphasis was placed on the pivotal role of interfacial junctions in efficiently separating charges through the creation of in-built potentials, a key factor in the development of wireless opto-electronic actuators. This section further delves into these processes, exploring the properties of materials utilized in such opto-electronic architectures and offering insights into potential new materials to address existing shortcomings[53,54].

Maximizing **light absorption** to increase the concentration of photogenerated electrons has conveyed the involvement of different materials and strategies. For instance, maximized light absorption can be achieved with semiconducting nano-structuring, increasing the surface area exposed to light. Nanostructures on the device surface enhance photon capture and decrease retroreflection. The textured surface allows for more interactions between incoming photons and the semiconductor material, effectively capturing a higher percentage of the incident light and therefore improving light absorption. Nano-structuring can also change the bandgap of the material due to quantum confinement effects and thus the wavelength absorption range for photocarrier generation. Doping can also tune light absorption and the generation of photocarriers. The introduction of dopants into semiconductors modifies their band structure, shifting absorption edges towards longer wavelengths. Although doping can promote photoelectric properties, excessive doping can create charge trapping and recombination centers. Another strategy to maximize light absorption and charge carriers is by combining semiconductors with plasmonic metals (gold, silver, and copper) through their resonant surface plasmons (collective oscillations of the metal free electrons). When the incident light matches the resonant frequency of these plasmons, the material can absorb light more efficiently. This is because the plasmons enhance the local electromagnetic field around the metal surface. Furthermore, the absorption and scattering cross-sections across a wide range of wavelengths of metal nanostructures can be tailored by adjusting parameters such as size, shape, composition, and environment. This means that through careful engineering of these factors, light absorption at specific wavelengths can be optimized. Additionally, resonant surface plasmons can generate hot electrons that can be injected into the semiconductor system, increasing PC. Furthermore, charge carriers can be increased through multiple excitons effect. Semiconductor nanocrystals or quantum dots (QD) can generate multiple electron-hole pairs from a single photon absorption, with very high conversion efficiency when the photons have energy greater than twice the bandgap energy of the semiconductor[53].

From the point of view of the typical semiconductor materials used for optimizing light absorption, nanostructured semiconductors with high absorption coefficients such as TiO_2, ZnO, and SnO_2 have been commonly used. However, they have the disadvantage of having wide bandgaps activated mainly by UV light. The demand for light-activated semiconductors with narrow bandgaps, particularly in the visible light or preferably in the NIR region, is crucial for advanced biomedical applications, where deep tissue penetration is essential. Under this context silicon continues to be a very relevant low bandgap material that can be activated in the visible-NIR region. Nevertheless, novel 2D layered materials (e.g., MoS_2, WS_2, $MoSe_2$) are now emerging and offering promising alternatives due to (i) small bandgap for efficient solar conversion energy; (ii) significant photon absorption, (iii) bandgap tunability via modulation of the valence band and conducting band with the number of stacked layers. In the same line, although being a zero-bandgap semiconductor, graphene has shown to efficiently convert light into electricity via a hot-carrier multiplication process on a femtosecond time scale over a wide range of light frequencies with special performance in the NIR range. This makes graphene very attractive for emerging applications in opto-electronics[69].

With respect to the strategies and materials used to improve **charge separation**, homojunctions based on silicon have already been reviewed. However, there are numerous other junction strategies. Heterojunctions formed between different semiconductor materials also create built-in electric fields at the interfaces, efficiently separating photogenerated electron–hole pairs and regulating carrier transportation. Heterojunctions of n-n type, involving semiconductors A and B, offer notable improvements (e.g., ZnO-$CdMoO_4$, which enhances photo-electric properties of ZnO). Nanostructured pn junctions as well as p–insulating–n junctions have also been studied, many of them combining typical n-ZnO or n-TiO2 with p-doped carbon nanotubes, p-doped transition metal dichalcogenides, p-NiO, p-CuO, among others. Other heterojunctions, combining inorganic with organic counterparts have been also addressed. Organic materials offer advantages such as facile large-scale fabrication, absorption range in UV-visible, and the capacity to elastically modulate semiconductor characteristics. Charge separation has been achieved with heterojunctions made of p-type polyaniline, polypyrrole, or polyvinyl alcohol, etc., paired with n-type semiconductors (e.g., TiO_2). Other metal oxide semiconductors and perovskites have also been used in organic–inorganic hybrids to increase charge separation. Under the same context, Schottky junctions have been used not only with typical metals but also with n-doped oxide semiconductors in conjunction with graphene[53,54,70].

In terms of **charge transport**, there are several crucial factors at play. One key aspect is charge mobility, an intrinsic property of materials that measures how fast a charge carrier (holes or electrons) moves through a material when subjected to an electric field. In general, charge mobility is far superior in inorganic materials than in organic ones. 2D layered inorganic semiconductors based on transition metal dichalcogenides (e.g., MoS_2) are gaining prominence due to their good carrier mobility besides their tunable bandgap. Nevertheless, standout examples can be found in low-dimensional carbon-based materials, particularly carbon nanotubes and graphene. Material crystallinity is another related parameter affecting charge transport, which is determined by the fabrication process and subsequent treatments. An excess of defects, grain boundaries, or doping in semiconductor crystals can result in the trapping and recombination of charge carriers, weakening the photo-response. To counter this, precise preparation methods and suitable treatments are necessary to produce high-quality semiconductor crystals with enhanced crystallinity and fewer defects. Additionally, semiconductor dimensionality (ranging from 0D to 3D) is also an important parameter affecting charge transport. Different nanostructures of semiconductors can be employed, influencing the transport of photogenerated charge carriers. For example, 1D semiconductor nanostructures like nanowires (NW), nanobelts, nanorods, and nanotubes have garnered considerable research interest. Specifically, 1D nano-structuring can provide long path length for photon absorption while short channels for carrier transport, leading to increased light absorption and fast carrier transit. Additional parameters influencing charge transport encompass temperature, surface effects, among others[53,54].

For the **charge injection** into to the targeted system to be stimulated, the contact junctions at such interfaces are important issues to be considered. When injecting electrical power to an external circuit, ohmic or Schottky barriers are commonly involved. The characteristics of these barriers can be customized by carefully selecting the metals. Ohmic junctions offer low-resistance contact, while Schottky diodes provide rectifying and self-powering properties.

On the other hand, when the targeted system involves an electrolyte or a bio-interface surrounded by an electrolyte, the semiconductor undergoes a junction with this interface, also resulting in band-bending at the semiconductor surface. For instance, when a semiconductor is immersed in an electrolyte containing ions and redox species, a natural process of charge flow occurs between the solid and liquid phases to reach equilibrium in terms of Fermi levels (that of the semiconductor and that of the redox species, which define the redox potential of the species). This leads to band bending on the semiconductor surface. Depending on the type and doping level of the semiconductor, this process creates a depletion region and a charged interface. The alignment of the semiconductor's Fermi levels with respect to the solution's redox potentials influences the electrochemical or photoelectrochemical reactions occurring at the semiconductor surface. When a semiconductor is illuminated in an electrolyte, it produces different energy distributions for the photogenerated carriers. Guided by the built-in electric field, photocarriers can be injected into the solution, driving photoelectrochemical reactions, which can be harnessed for different applications such as in cellular stimulation[53,54].

So far, we have reviewed the different steps behind an opto-electronic stimulation process and the materials and properties that are important to tune to achieve a relevant photo-response. In summary, it has been seen that semiconductor materials play a crucial role in the design of optoelectronic devices, being the interfacial junctions key to achieve wireless remote activation with light. Although different inorganic or organic semiconductor materials can be used, inorganic semiconductors stand out for their great ability to adjust their bandgap and light absorption by modifying their dimensionality or size. This aspect has been reinforced with the appearance of new narrow bandgap materials with the ability to extend the photo-response towards the NIR range. Inorganic semiconductor devices can be processed in a scalable manner due to the availability of well-established technologies for integrated circuit manufacturing. Furthermore, they can be precisely fabricated into various nanoscale architectures to maximize light absorption and to match the size of subcellular and molecular components for stimulation. They also have high carrier mobility, unlike their organic counterparts, which provides them with rapid responses and high sensitivity. On the other hand, organic semiconductors also have several important ingredients to be used in this field, such as better mechanical compliance, easier solution processability, intrinsic flexibility, stretchability, and printability that open possibilities for portable and cost-effective devices[53,54].

In this context, silicon-based materials still meet the requirements to achieve a high photo-response. Silicon's narrow bandgap makes it competent to absorb light within the visible to NIR spectrum. Furthermore, its ability to synergize its response with plasmonic materials, along with its good carrier mobility, reinforces its status as an exemplary option. The perfect compatibility of silicon with standard micro/nanofabrication techniques for precise nano-structuring, along with its versatility for chemical modification to enable personalized adjustments of its stability and for doping to easily create pn/Schottky junctions further strengthen their attributes. These distinctive qualities collectively underline the role of silicon as still a highly relevant model system in the optoelectronics landscape[71].

1.2.2.3 Materials for Opto-Electric Stimulation of Excitable and Non-excitable Cells

Opto-electronic modulation offers a less invasive and appealing tool for biological purposes, overcoming limitations associated with bulky wired electrical devices. It is of significant interest due to their properties and closer proximity to clinical applications, ensuring subcellular spatial and temporal resolution, features lacking in conventional electrical devices[72].

This section focuses on the opto-electronic stimulation of both excitable and non-excitable cells, along with an examination of the materials used for this purpose. Before diving into the specifics, it is important to outline the processes involved in wireless opto-electronic stimulation for the specific case of biological cells. The opto-electric process converts light into either a voltage or a current signal, which can induce capacitive effects or initiate faradaic currents at the bio-interface (as shown in ***Figure 12***). Capacitive effects involve storing photoelectrical charge at the interface between the device and the surrounding medium, forming double layers. This means that photogenerated charge carriers, like electrons, accumulate at the device-electrolyte interface, altering the concentration distribution of ions in the surrounding electrolyte. This leads to the accumulation of counter ions, such as cations, at the electrolyte side of the device, creating a capacitor at the interface and expelling anions from the device, which accumulate at the external side of the membrane. This, in turn, influences the cell's membrane potential, resulting in cell membrane depolarization and the initiation of AP in excitable cells. In non-excitable cells, it can alter ion permeability, triggering signaling cascades that impact cell processes. Alternatively, the generation of PC leads to Faradaic currents at the device/electrolyte interface, creating an ionic imbalance in the extracellular medium. This can also lead to membrane depolarization, affecting cellular activity. Although both processes can be present, the capacitive process is generally preferred, as redox reactions can sometimes have unintended consequences that may be detrimental or lead to degradation of biological components[54,73].

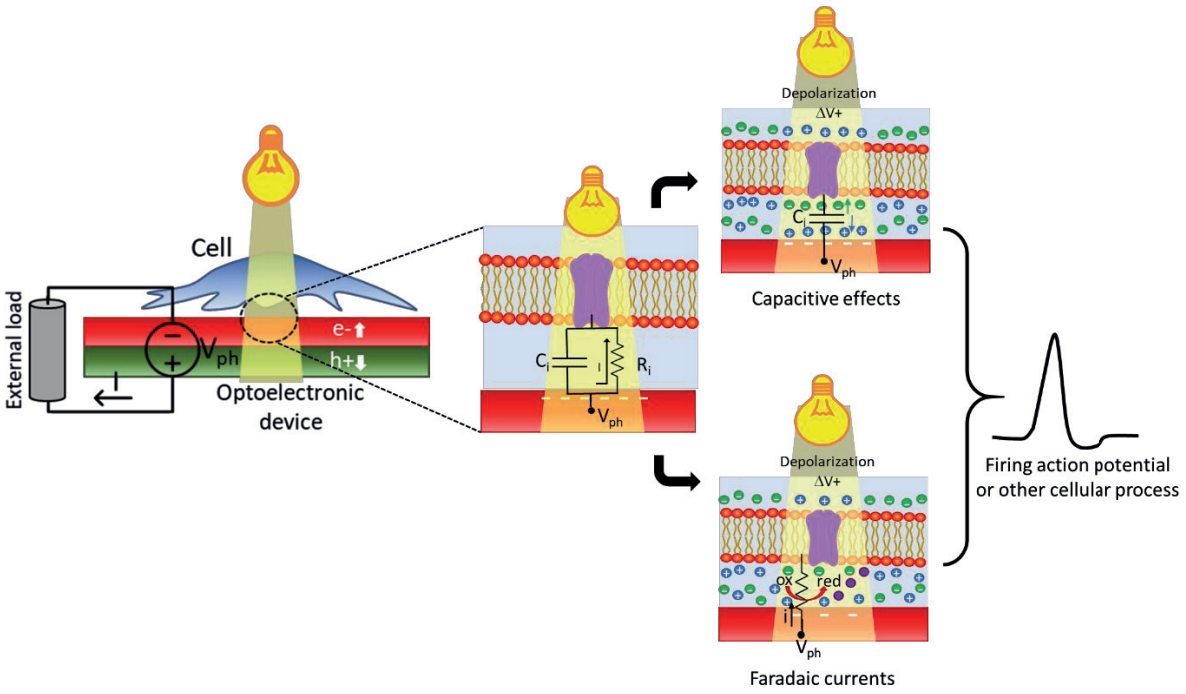


Figure 12 Different opto-electronic stimulation mechanisms. When exposed to light, a photovoltage (Vph) and photocurrent (I) are generated, which are then utilized by the external load (in this case, the electrolyte/cell medium) for inducing its stimulation. The stimulation process can take place through capacitive effects or faradaic reactions, leading to cell membrane depolarization and the initiation of cellular processes, including firing action potentials.

Accordingly, the primary goal of optoelectronic devices is to induce a change in membrane potential significant enough to elicit AP in excitable cells or to prompt an appropriate cellular response in non-excitable cells. Achieving this requires the use of suitable materials in the opto-electronic device that can convert optical energy into an electrical output, while also being biocompatible. Additionally, the opto-electronic device must be capable of using safe wavelengths, avoiding shorter wavelengths and high powers, all while ensuring deep tissue penetration. This also underscores the importance of employing NIR light within the biological windows. As seen, semiconductors possess properties that make them well-suited for integration into opto-electronic devices. Below, different materials used in photoelectrical modulation of biological cells will be discussed.

i) Inorganic Materials

Silicon remains highly relevant for biological stimulation due to its favorable optical properties. In contrast, semiconductors like InP and GaP, while similar to silicon, entail higher fabrication costs and more sophisticated instrumentation. Silicon possesses unique properties, such as tunable electrical and chemical characteristics, biocompatibility, and bioresorbability without toxic by-products, low bandgap, and absorption in the NIR range (especially in the biological windows), enabling deep tissue penetration. Additionally, silicon exhibits a moderate heating/thermal effect, which can be fine-tuned by integration with plasmonic nanomaterials. Moreover, the mature infrastructure and fabrication know-how associated with silicon-based

devices offer flexibility in creating various nano/microstructures for use at different biological levels. These attributes have positioned silicon as a top choice for extensive examination in bioelectronic approaches. Furthermore, the dispersibility and modifiability of silicon NW enhance cell targeting and spatial specificity, particularly as they have been demonstrated to accumulate in cells through phagocytosis.

Silicon has been extensively studied and offers a vast potential for further exploration. For example, free-standing coaxial doped silicon NW (p-Si/intrinsic Si/n-Si denoted as p-i-n), and also decorated with gold nanoclusters, have been used to modulate neuronal activity. These NW could induce AP in rat dorsal root ganglion (DRG) neurons. Similar coaxial configuration of silicon NW (p-i-p) but supported on polymers, has been employed to convert low-radiance light into stimulatory signals for cardiac cells[74]. Moreover, various rational designs of silicon structures have also been developed for optically controlled multiscale bio-interfaces using Si (p-i-n) diodes, resulting in enhanced capacitive currents[75]. Additionally, integration of metal components has led to increased capacitive and Faradaic currents for cell stimulation. For instance, at a subcellular level, Si (p-i-n) NW were employed to stimulate intracellular calcium modulation. Progressing to a cellular level, extracellular photo-stimulation induced AP in DRG neurons, achieved through a planar p-i-n junction in a Si diode. At a tissue level, photo-stimulation was applied to generate excitatory postsynaptic currents in ex-vivo brain slices, employing an array of p-i-n junctions in a mesh architecture. Finally, at an organism level, neural activity in the live mouse brain was photo-stimulated using a metal-coated (Au) p-i-n Si mesh array[75].

Furthermore, silicon junctions composed of p-doped nano-porous Si and p-doped non-porous Si have demonstrated a robust photoelectrochemical response for stimulating cardiac cells and sciatic nerves. The disparity in porosity within the p-doped silicon structures can create a diode-like band alignment, similar to the typical one formed with p-doped Si/n-doped Si. This p-doped homojunction has shown strong photoelectrochemical properties without the need for dopant modulation[76].

Moreover, micro-photodiode arrays based on silicon have been employed to stimulate retinal ganglion cells via NIR light. This integrated wireless implant holds promise for restoring functional vision in individuals affected by degenerative retinal diseases[75,77].

Although less common, non-excitable cells have also been targeted using Si-based devices. Bone cells exhibit voltage gated channels that open in response to changes in membrane potential. They are among the few cells with a self-regenerative capacity when minor damage occurs. Three-dimensional biomimetic scaffolds based on silicon microstructures have shown enhanced bone regeneration under light illumination. The 3D hybrid structure was composed of a biodegradable porous collagen/hydroxyapatite/polymer matrix with embedded thin-film Si patterns, including mesh, pillar, and pyramid Si structures at multiple scales. These Si-based structures guided cell growth and regulated cell behavior through the photoinduced electrical signals. Additionally, Si photovoltaic microcell arrays, featuring planar pn junctions, have been also used for opto-electronic stimulation of osteoblast cells, eliciting intracellular calcium transients[45,71].

Apart from silicon, there have been limited studies involving other inorganic semiconductors. TiO_2 nanoparticles, while primarily responsive to UV light due to their higher bandgap, have been tailored for visible light photoactivation through decoration with gold nanostructures. The plasmonic effect of gold induces charge injection into the titania NW upon light exposure, allowing the conversion of light into electrical signals[78]. This approach has been applied in the activation of degenerated retinas. Additional research has explored the use of films based on semiconducting HgTe nanoparticles for neural stimulation under visible light excitation[79]. However, further studies are necessary, particularly in assessing the long-term toxicity of these nanomaterials.

ii) Organic Materials

Organic semiconductors offer benefits like flexibility, light weight, and biocompatibility for light-mediated stimulation of neuronal cells and tissues. However, they face challenges compared to inorganic materials, including issues like water-induced swelling, degradation, and delamination when implanted in the body. Additionally, organic semiconductors used in photovoltaic bioelectronics often have limitations like low photoconversion efficiency, reduced charge mobility, and high sensitivity only in the visible spectrum, limiting their use with NIR light.

Successful examples in visible range opto-electrical stimulation involve polymer blends utilizing an electron donor-acceptor mechanism. For instance, a blend of poly(3-hexylthiophene) (P3HT) as the donor and phenyl-C61-butyric-acid-methyl ester (PCBM) as the acceptor has been effective in stimulating neurons. It has also been demonstrated that using only the donor component (P3HT) on supported Indium tin oxide (ITO) can efficiently stimulate neurons and restore light sensitivity in damaged retinas, provided by the capability of ITO to aid in the charge separation[11,80].

Optoelectronic devices based on a thin trilayer of metal and pn semiconducting organic nanocrystals have also been employed to electrically stimulate neurons. The p-type organic semiconductor, a phthalocyanine acting as a donor, combined with a perylene derivative acting as an acceptor, shows promise for retinal implants and for stimulating electrogenic tissues or for oocyte stimulation[81,82]. Other polymer blends, such as PEDOT:PSS (poly(3,4-ethylenedioxythiophene)-poly(styrenesulfonate)) or PCBM blended with a copolymer of cyclopenta dithiophene and benzothiadiazole (PCPDTBT), have exhibited strong performance, with the latter one approaching the NIR range[83].

Lastly, despite not being a true semiconductor, graphene-based platforms also show promise for opto-electronic cell stimulation. Studies have demonstrated its effectiveness in optically stimulating heart muscle cells, or cardiomyocytes[69]. The potential of graphene-based opto-electronic devices for cellular stimulation is vast, thanks to their exceptional conductivity, biocompatibility, broad light absorption, fast response rate, and ability to create flexible devices. However, challenges remain, including the need to improve absorption efficiency through integration with other nanomaterials like QD, as well as the complexities involved in fabrication and device integration.

All these studies highlight the potential of opto-electronic approaches in cellular applications, providing ample room for exploration and addressing key challenges. Further work is needed to enhance the optical performance of existing nanomaterials, enabling stimulation at very low light intensities for potential clinical use in the future, and to contribute more effectively to therapies.

1.2.2.4 Other Optical Stimulation Methods

Apart from opto-electronics, other light-based techniques can be used for cell stimulation such as optogenetics, photothermal or photoacoustic strategies.

Optogenetics is based on the use of light-sensitive proteins, called opsins, to control the activity of specific cells within living tissue[84]. These opsins are encoded genetically and can be introduced into target cells using viral vectors or other genetic engineering techniques. Once these genes are expressed, opsins are produced and integrated into the cell membrane. When exposed to light, these opsins undergo conformational changes that enable the flow of ions (e.g., sodium, calcium) across the cell membrane, thereby altering the cell's membrane potential.

Optogenetics has been extensively applied to stimulate various types of cells, including neurons, cardiac cells, muscle cells, immune, and endocrine cells, among others. As an illustrative example, this technique has enabled the introduction of channel rhodopsin into cardiac cells. Upon blue illumination, this allows for the activation of cardiomyocytes, leading to alterations in calcium homeostasis and cardiomyocyte beating[85]. Although it requires genetic engineering, this technique offers the advantages of cell specificity and temporal precision.

The photothermal stimulation is based on laser-induced heating of cells or tissues, where absorption of light generates heat to stimulate cellular responses[86–88]. Traditionally, this technique has operated in the NIR range, relying on the generation of transient heat through intense laser beams, primarily absorbed by water in the tissue, capitalizing on the absorption water overtones. However, this water absorption limits the depth to which light can penetrate the tissue, often requiring relatively high energy for effective stimulation. With the advent of nanotechnology, tailored plasmonic nanomaterials have emerged, exhibiting excellent photothermal attributes[89,90]. For instance, semiconductors or metal nanostructures are being used in conjunction with lasers, significantly enhancing photothermal effects. This approach offers the advantage of utilizing low power sources while concentrating the photothermal conversion on the nanomaterial itself, as the primary agent, rather than relying on water absorption.

These techniques find applications in both extracellular and intracellular studies, enabling diverse applications such as neuronal stimulation and modulation of intracellular calcium concentration. In general, temperature-induced reversible changes in membrane capacitance

occur due to perturbations in the distribution of ions adjacent to the cell membrane, as well as activation of temperature-sensitive ion channels[86].

Among the absorbing nanomaterials, gold nanostructures serve as excellent photothermal agents, customizable to strongly absorb laser light in NIR range through adjustments in size, shape, and surface dielectric properties of the nanoparticles. For example, gold nanorods have been utilized to efficiently stimulate primary auditory neurons in the NIR range[91]. Another illustrative example involves the use of textured silicon NW, which exhibit enhanced photothermal efficacy compared to smooth NW. These have been employed to induce calcium wave propagations both intracellularly and intercellularly[92].

By precisely tuning the generated heat, these techniques extend beyond cell stimulation, impacting various biological processes. They enable controlled drug release from nanomaterials, providing a targeted approach for therapeutic agent delivery. Moreover, through temperature modulation, photothermal methods can induce protein denaturation and disrupt cell membranes, offering a potent strategy for tumor eradication[8].

Photoacoustic stimulation involves the use of pulsed laser light to generate acoustic waves within tissue, creating pressure gradients. These waves have the capacity to stimulate cells and tissues. In contrast to ultrasound stimulation, which relies on sound waves with greater penetration depths, optoacoustic stimulation employs laser-induced acoustic waves, providing enhanced temporal precision due to the pulsed nature of laser light. This innovation has led to the development of miniaturized tapered fiber optoacoustic emitters capable of generating an ultrasound field with high spatial resolution[93]. Through such emitters, researchers have significantly improved the precision of optoacoustic neuron stimulation, enhancing both spatial and temporal resolution. Optoacoustic stimulation, being a relatively recent technique, is currently under exploration for applications not only in neural modulation, but also in drug delivery, and tissue engineering.

1.3 Light for ROS Generation

1.3.1 Importance of ROS in Biology and Biomedicine

ROS are highly reactive molecules containing oxygen atoms and unpaired electrons, capable of triggering oxidative chemical pathways. ROS encompasses various species such as superoxide radicals (O_2•−), hydroperoxyl radical (HO_2•), singlet oxygen, and hydroxyl radical (•OH), with the latter being the more potent oxidant. ROS can be produced endogenously in cells, via ionization/UV radiation or through Fenton or Fenton-like reactions (***Figure 13***).

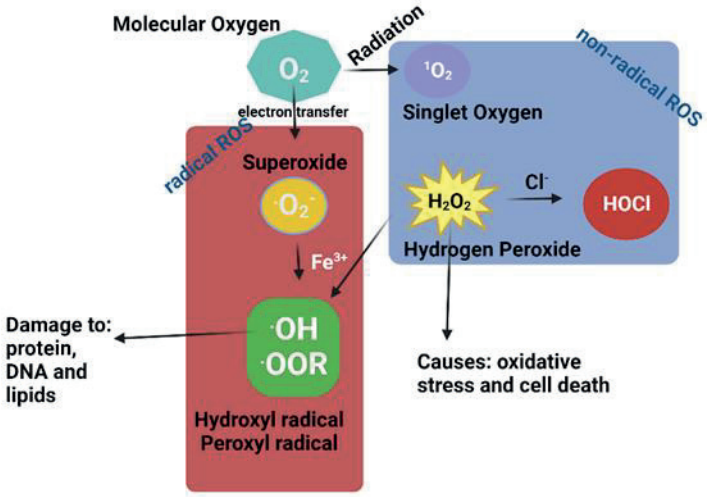


Figure 13 Schematic representation of different pathways for reactive oxygen species production.

ROS are produced in the cells as metabolic by-products via various mechanisms including the electron transport chain in mitochondria, enzymatic reactions mediated by NADPH oxidases and Fenton reactions[94–97]. Usually, antioxidant mechanisms in cells, such as scavenging enzymes (SOD, CAT...) and antioxidant molecules (vitamin E, Glutathione...) are activated to maintain ROS levels in homeostasis[97,98]. An alteration in the balance between ROS production and antioxidant mechanism can lead to high levels of ROS which are believed to cause cell cycle arrest, oxidative stress, and cell death[97,99] through the activation of certain signaling pathways, in addition to cell metabolism inhibition[95]. Moreover, protein, lipid and DNA damage are additional consequences of elevated ROS levels[95,96]. Conversely, modulation of ROS and their maintenance at normal levels activate signaling pathways that correlates with cell proliferation and differentiation[95]. Furthermore, apart from their messenger and mediatory role in intracellular signaling, ROS also play a role in protecting organisms from infections [96].

Studies have consistently demonstrated the significant role for ROS in several pathologies, such as in cancer, diabetes, and neurodegenerative diseases[95,96,100]. Tumors are characterized by high ROS levels which induce/activate several factors and pathways, consequently promoting cancer cell proliferation, survival, and enhancing cell migration and invasion[95]. However, above a certain threshold, ROS becomes toxic to cancer cells and can induce cell death through oxidative stress[95,101]. Hence, there is a current focus on therapies aimed at targeting cancer cells by increasing ROS levels, and these approaches are undergoing extensive studies. Conversely, strategies aimed at reducing ROS levels are also growing to suppress cancer proliferation.

With the emergence of nanotechnology and leveraging the physical and chemical characteristics of nanomaterials, their application in biological and medical applications has been growing very fast. Targeting ROS generation is highly used in the treatment of various diseases such as cancer, wound healing, stem cell differentiation, etc. Different types of nanoparticles such as iron or copper particles have been used as ROS inductors to treat cancer

cells [101]. However, there are still challenges, such as exploring if ROS effectiveness is consistent across all types of tumors, or how to increase specificity of ROS inductors for cancer cells[78]. In order to attain superior results while preventing harm to normal cells, it is crucial to optimize and improve ROS delivery systems. More details on the impact of nanotechnology on ROS based therapies will be discussed in the next sections.

1.3.2 PDT with Molecules

As evident from the aforementioned, modulating ROS levels holds significant promise as an alternative strategy for addressing infectious and cancerous diseases. This approach has the potential to provide a universal and cost-effective therapy, irrespective of tumor type, heterogeneity, or state, with the added benefit of enhanced delivery directly to the tumor region. In fact, chemo-dynamic therapy (CDT) is an antitumor therapy based on Fenton and Fenton-like reactions[c] producing ROS to destroy tumor cells in the tumor microenvironment characterized by relatively elevated levels of H_2O_2 and slightly acidic pH.

PDT is a non-invasive related treatment, involving the utilization of light activated molecules, termed photosensitizers. These photosensitizers undergo a photochemical reaction to produce ROS. In principle, upon exposure to light, photosensitizers are excited from their singlet ground state to a singlet excited state. The excited photosensitizer can then undergo transition to the first triplet excited state via intersystem crossing. From there, the excited photosensitizer interacts with nearby molecules such as molecular oxygen to transfer either protons or electrons forming ROS radical ions (Type I), or by direct energy transfer to oxygen to generate predominantly singlet oxygen ($^1O_2$) (Type II)[102] (***Figure 14***). In the overall process, singlet oxygen is considered the primary and most significant ROS responsible for the therapeutic effects of PDT, leading to degradation of biological molecules and cell structures, ultimately resulting in cell death. Apoptosis, necrosis and even autophagy have been suggested as mechanisms of death in response to PDT[9]. Moreover, microvasculature decrease was also reported as a possible outcome and is a main reason for the decrease in the oxygen level in tumors (hypoxia)[103,104]. In addition, unlike chemotherapy and radiotherapy, PDT has the capacity to induce an immune response[103]. All these effects attracted the attention toward PDT as a possible efficient therapy, and throughout the years, it has been involved in several diseases including malignant and non-malignant ones. However, still PDT is restricted clinically to superficial applications due to some limitations involving photosensitizer molecules, light source, and oxygen availability in tumor tissue[4].

[c] In a Fenton reaction, hydrogen peroxide reacts with transition metal ions, typically iron (Fe^{2+}), to produce hydroxyl radicals (•OH)

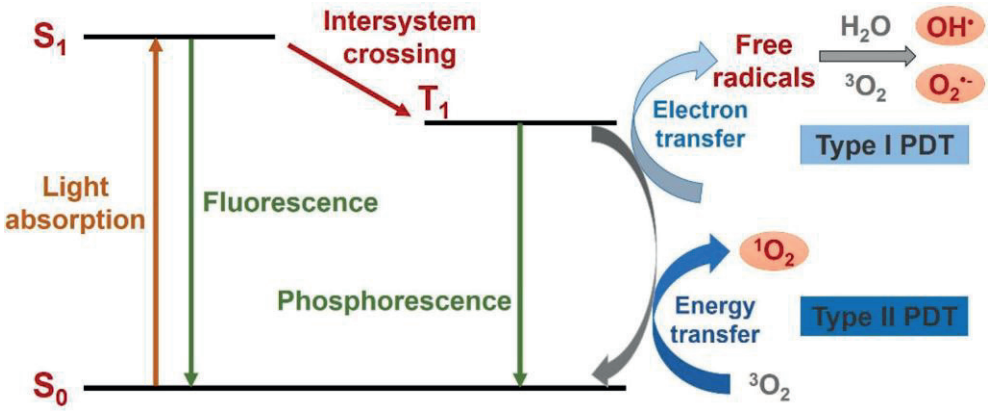


Figure 14 Molecular mechanism of ROS generation (Adapted from reference 82).

To be clinically useful in PDT, a photosensitizer should exhibit a high quantum yield of ROS production, high photochemical stability, low dark toxicity, and selective accumulation within targeted pathologies. In addition, the PDT photosensitizer must minimally meet a number of photo-physical/chemical criteria, including substantial photon absorption at longer wavelengths (beyond the visible light) to ensure a more effective light penetration into tissues, and a high probability of intersystem crossing between the excited singlet and triplet states to guarantee ROS activation.

At present, the majority of clinical PDT photosensitizers are based on porphyrins and phthalocyanines. These molecules consist of aromatic macrocycles acting as anionic pockets with the capability to bind metals and form complexes, enabling customization and improved properties. While these photosensitizers, initially used in PDT have shown very good ROS yield generation, they predominantly absorb visible light thus limiting their effectiveness to superficial tissues[9,103,104]. Besides, factors like photobleaching, hydrophobicity, low solubility and aggregation tendency further constrain their efficiency [9,103,104]. The low accumulation of photosensitizers in the tumor tissues also contributes to limited PDT clinically[104]. Because of the very short half-life of singlet oxygen varying between 0.01-0.04 µs, these species can span through few nanometers of the tissue (0.01-0.02 µm). This results in an immediate effect restricted to the location of the photosensitizers[9,103,105]. Modifications on the structures of photosensitizers have improved PDT but toxicity in dark conditions was a serious issue faced with the second generation of these molecules[104]. Various approaches towards more efficient, soluble, photostable, and less toxic photosensitizers have been reported. Nonetheless, efforts need to be invested to meet the key requirement of finding NIR-excited photosensitizers to enhance the prospects of PDT with molecules for wider use[4].

1.3.3 PDT with Nanoparticles

With the emergence of nanotechnology and its fast progress, several approaches were developed to boost the therapeutic efficiency of PDT. Benefiting from the unique characteristics of nanomaterials which exhibit a good response in phototherapies[105], various nanostructures for different purposes were developed in a way to overcome the limitations of photosensitizers mentioned above.

Due to the special microenvironment of the tumor tissue, NPs can accumulate in tumor cells with the enhanced permeability and retention effect (EPR), however since some tumors do not exhibit the EPR effect and blood vessel permeability is not uniform, this keeps passive delivery less efficient[105,106]. At this level, the principle of targeting NPs)with special ligands that can bind to receptors on cancer cells has arisen and is denoted as active targeting. This would ensure the delivery of NPs selectively to cancer cells without any damage to adjacent normal ones[105]. Therefore, NPs have been used either as carriers for photosensitizers or as photosensitizers themselves[104].

NPs as carriers: Given the poor solubility and stability exhibited by molecular photosensitizers, their incorporation into nanoparticles is believed to enhance delivery efficiency and also offers the potential to control photosensitizer release through a specific stimulus (***Figure 15a***)[104,105]. A wide range of NPs have been used, including gold NPs, mesoporous silica, upconversion NPs, micelles, metal-organic frameworks (MOFs), etc. For instance, upon exciting upconversion NPs with NIR light, visible light is emitted which is used to activate the carried photosensitizer[d4]. Also, photosensitizers loaded in lipid nano-capsules have shown an improved solubility and good ROS production[105]. Despite the development of various nanoparticle-photosensitizer systems and extensive research, the potential of PDT is also limited due to the challenge of simultaneously optimizing ROS production while ensuring precise delivery to intracellular organelles to induce potent cytotoxic effects [104]. Besides, most of the NPs used are not biodegradable, leading to their accumulation in the body. Therefore, biodegradable NPs endowed with high phototherapeutic properties are required[104].

[d] Upconversion refers to a process where lower energy photons are absorbed by semiconducting NPs and then converted into higher energy photons. This phenomenon, although counterintuitive, makes the NP absorbs multiple lower energy photons in a stepwise manner, each photon elevating an electron to a higher energy level. Once a sufficiently high-energy state is reached, the electron can return to a lower energy state, releasing the accumulated energy in the form of a higher energy photon. This photon has a shorter wavelength than the absorbed photons. In bioimaging, it enables the use of low-energy, safer excitation sources like NIR, which can penetrate tissues more deeply. In photodynamic, the emitted higher-energy photons can then be used to drive photocatalytic or photoredox reactions to generate ROS.

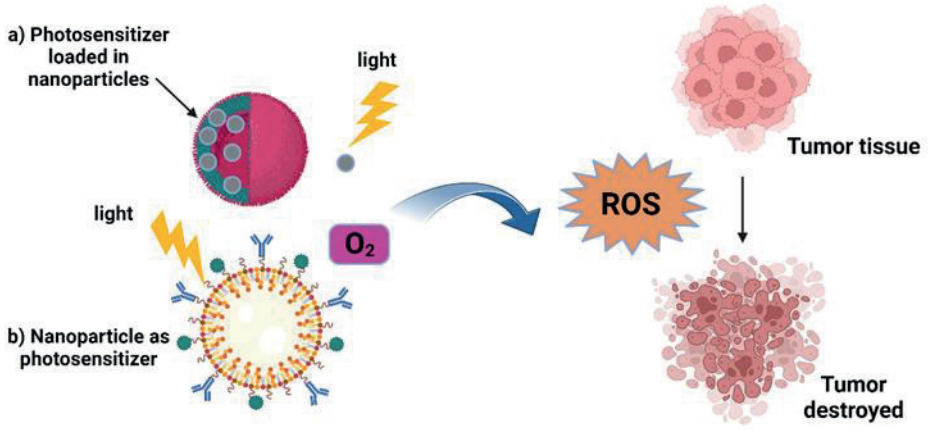


Figure 15 Schematic representation of the models of nanoparticles (NPs) used in PDT for ROS generation. a) NPs employed as carriers for photosensitizer molecules which when released in target site and exposed to light, they cause the production of ROS from oxygen molecule. b) NPs act as photosensitizers themselves, when irradiated by light, ROS is generated. The outcome in both systems is the destruction of tumor tissues.

NPs as Photosensitizers: ROS generating particles are of great interest for their capability to respond to light stimulation, a characteristic that enabled the birth/discovery of the latest generation of photosensitizers (***Figure 15b***). Semiconducting NPs are commonly used in this role. They rely on absorbing photons with energy similar to their bandgap to promote electrons from the valence band to the conducting band, creating electron-hole pairs. These pairs act as redox agents, triggering chemical pathways that lead to ROS production. Typical semiconductor NPs that can serve as photosensitizers include fullerenes, organic semiconducting NPs, and inorganic semiconductor NPs. While fullerenes show promise as photosensitizers, they require functionalization to overcome their hydrophobic nature and avoid aggregation [9,104]. Organic semiconductor NPs, which exhibit high biocompatibility, are beginning to be explored[107]. They are based on conjugated polymers, which mainly induce singlet oxygen species. Although their activation can be tailored for visible/NIR light, these nanomaterials have lower quantum yield and lower resilience to the produced ROS compared to their inorganic counterparts. Inorganic semiconductor NPs are ideal candidates due to their good stability, broad absorption band, narrow and intense emission spectra, high quantum yield, and unique physical and chemical properties[106,108]. However, they still face some limitations. A critical one is related to the semiconductor bandgap width. For instance, semiconductors like TiO_2, ZnO, CeO_2[109] are efficient photosensitizers in PDT, but they have large bandgaps, requiring UV or higher energy visible excitation and consequently rather limited to superficial tissues[9,110]. Efforts have been made to lower the bandgap of the particles, which has shown promise in improving their photoexcitation properties to enable NIR activation, as demonstrated in the case of TiO_2. However, it has been observed that this did not significantly enhance the ROS phototoxic effect on cancer cells[110].

To overcome this problem, upconversion nanomaterials were also included. However, the emitted UV-visible light can be harmful to adjacent normal cells[106] Additionally, upconversion strategies tend to be associated with high costs and low efficiency due to the energy losses in the conversion steps, in contrast to one-step absorption approaches. Therefore, to ensure light reaching deep tumor tissues, semiconductors with low bandgap energy and high absorption yield are highly required as they can be NIR excited [111].

1.3.4 Transition Metal Dichalcogenides for ROS Generation

Since the discovery of graphene, two-dimensional materials have been widely explored and garnered the attention of scientists for their fascinating properties compared to their bulk material. A special class of these 2D materials includes the Transition Metal Dichalcogenides (TMDs) which are grabbing great attention in nanotechnology due to their extraordinary properties. TMDs are semiconductors exhibiting a layered structure which consists of a core of transition metals (Mo, W) laying between two layers (monoatomic) of chalcogen atoms (S, Se, Te)[112,113]. TMDs usually have a formula of MX_2 (M: transition metal, X: chalcogen atom), where various combinations of elements can be designed yielding a wide range of properties[114]. In general, TMDs are characterized by a high surface area to mass ratio which enables high efficiency of drug loading. In addition, biocompatibility, low cytotoxicity, tunable bandgap, multifunctionality, superconductivity and photoelectric properties have favored the involvement of TMDs in applications of different fields such as biomedical (biosensing, bioimaging, therapies), catalysis, optoelectronics, energy storage and water remediation[112,114].

MoS_2 for ROS generation

Molybdenum disulfide MoS_2, a 2D layered material falling within the TMDs class, has garnered significant attention due to its unique properties. It is a semiconductor material with a bulk bandgap of 1.2 eV (1033nm), which increases with the decrease of stacked layers reaching a value around 1.8 eV (689 nm) for a typical MoS_2 monolayer. The low bandgap allows this material to exhibit strong absorption in the NIR region, making it suitable for various environmental or biomedical applications. Its tunable bandgap with the number of stacked layers, high extinction coefficient, versatile surface chemistry with active catalytic sites at the layer edges, as well as thermal and structural stability, enhance its utilization as bioimaging probes, drug delivery platform and phototherapeutic agents[114,115]. In addition to its biocompatibility and physiochemical properties, its low-cost synthesis favors its use over other 2D material in biomedical applications.

MoS_2 materials are indeed promising candidates for ROS generation under visible/NIR light. A common strategy to enhance the photocatalytic activity of MoS_2 and generate more ROS is to increase the number of active sites, such as edges. Researchers have prepared various MoS_2 nanomaterials with different sizes or morphologies, including MoS_2 QDs, porous MoS_2, holey MoS_2 nanosheets, few-layered vertically aligned MoS_2, and pyramid-shaped MoS_2[116–119]. Furthermore, other functional materials like metals, metal halides, or metal oxides can be combined with MoS_2 to create nano-heterostructures. These structures demonstrate improved

photocatalytic performance due to their larger specific surface area, appropriate band alignment, and enhanced separation of electron-hole pairs.

Some studies using different MoS_2 nano-systems, have also proven their efficiency in PTT and PDT at the same time, providing added value, since antitumor activity can be significantly improved by combining both strategies [115].

Moreover, MoS_2 offers alternative strategies for ROS generation. One strategy involves using MoS_2 as nanozymes[e]. Particularly, MoS_2 NPs with small sizes or fewer layers exhibit peroxidase (POD)-like activity, effectively converting H_2O_2 into ·OH. In this line, Fenton like reactions where MoS_2 interacts efficiently with H_2O_2 and Fe^{2+}/Fe^{3+} to produce hydroxyl radical have been also demonstrated, rendering it highly useful in therapies based on Fenton reactions[119]. MoS_2 can decompose H_2O_2 as well producing O_2, thus helping to overcome the hypoxic environment in tumors[112]. Furthermore, MoS_2 ROS generation can be achieved through permonosulfate activation[f] or via its piezoelectric activity[g 119].

[e] Nanozymes refer to those nanomaterials (e.g. inorganic NPs) with enzyme-like catalytic properties.

[f] In this process peroxymonosulfate molecules generate highly reactive sulfate radicals (SO_4•−) for various oxidative reactions using MoS_2 as catalyst.

[g] When subjected to external mechanical stress, MoS_2 exhibit a piezoelectric effect, where electric charges accumulate internally, leading to the separation of electron-hole pairs and the generation of reactive radicals. This phenomenon has been demonstrated to enable direct water splitting and hydroxyl radical generation in single- and few-layered MoS_2 nanoflowers.

IV. Motivation

Light-based therapies have made outstanding achievements in the field of healthcare, becoming a fundamental pillar in modern medicine. Leveraging the notable light properties, it is possible to treat a wide range of diseases including neurodegenerative disorders and cancer. The joint action between light and exogenous light-responsive nanoplatforms or nanomaterials can be harnessed to selectively stimulate cells or facilitate the release of therapeutic payloads. This capability allows for the modulation of cellular processes, screening for abnormal signaling pathways, and inducing cytotoxic effects in tumoral cells.

With light stimulation, non-invasive and targeted therapies are possible to achieve a considerable milestone towards more precise treatments. External stimulation of both excitable and non-excitable cells is an appealing strategy for therapeutic purposes. In this context, biomedical devices activated by ES have a long history with an important relevance for treating various disorders involving a wide range of cell types. However, the clinical application of these devices has encountered limitations due to health concerns like inflammation and rejection of the probes, as well as challenges in achieving spatial resolution. Among the approaches to overcome these limitations, opto-electronic devices emerge as a promising alternative. The generation of an electrical signal from a light source helps in establishing wireless stimulation through minimally invasive methods.

Silicon is a well-known semiconducting material that has been incorporated in different fields such as telecommunications, energy, electronics, and biomedical fields. Taking advantage of its biocompatibility, and optoelectronic properties, silicon is a remarkable candidate for being the backbone of optoelectronic devices. Notably, its capability for absorption in the biological windows allows for increased penetration depth, a crucial factor in various biomedical applications. Silicon's special characteristics in opto-electronics arise from its exceptional versatility, enabling precise doping and the formation of pn and Schottky junctions. These junctions play a crucial role in adjusting silicon conductivity, allowing for the development of self-powered actuators when exposed to light. Silicon's ability to synergize its response with metals or plasmonic materials further enhances its suitability for opto-electronic applications. Moreover, the well-established fabrication expertise associated with silicon-based devices provides a high level of adaptability in crafting silicon nano/microstructures, which can be used for optimizing light absorption and researching bio-interfaces at various biological levels.

In addition to the inherent advantages of silicon nanomaterials in light-induced processes, nanotechnology offers the prospect of creating novel hybrid nanomaterials with tailored bandgaps. These hybrids can facilitate the in-situ production of therapeutic species, like ROS, within the visible-NIR region, presenting a promising avenue for targeted cancer cell destruction. Biocompatible layered TMDs, in particular, stand out as potential game-changers in the realm of PDT, promising an encouraging future in advancing the precision and effectiveness of cancer treatment.

Achieving a precise and deep stimulation or treatment for targeted cells with high efficiency displays a great improvement in the field and holds great promise for clinical applications. At the same time considering optical safety limits is vital to avoid any side-effects. In this context, the exploration of limits in light power for probing bio-interfaces gains relevance, as it is desired to minimize power incidence into biological tissues without compromising therapeutic effectiveness. Therefore, in this thesis, our interest is addressed towards the fabrication of advanced wireless silicon-based opto-electronic devices that could induce a cellular response at a very low light intensity within the biological windows. In addition, a promising nanoplatform of layered $SiO_2/MoS_2/Cu_2O$ for cancer treatment, based on ROS generation, is also proposed.

V. Aims and Objectives

Wireless stimulation of cells has transferred therapies into another level, overcoming different limitations and opening the way for efficient and long-lasting devices in the biomedical field. Opto-electronic materials, especially Si-based ones, have been demonstrated to be a highly desirable material due to its exceptional properties and versatility. While silicon currently holds a prominent position, ongoing exploration, and refinement of its attributes for opto-electronics imply that there is untapped potential for further advancements and innovations with this relevant material. Therefore, this thesis will focus on the fabrication of nanostructured silicon-based devices to enhance the opto-electric wireless cell stimulation, using a cost effective and scalable nanofabrication strategy, with the ultimate goal to stimulate bone cells using minimal light intensities within the NIR biological window.

On the other hand, ROS generation for cancer treatment is of great interest especially with the ability to target specific cells without harming normal ones. Light-responsive material biocompatibility and the optical safety within NIR wavelengths of the laser source are basic elements in the development of a system that can produce ROS and induce cell death. In line with this, the thesis will explore novel approaches involving nanostructured TMDs semiconductors for efficient light-induced ROS production within the NIR biological window to enhance therapeutic efficacy in cancer treatments.

To achieve the main goals, three different light-activated systems are designed.

1. A Si/Au nanowire-based device with in-built pn junctions to enhance its opto-electrical properties, enabling efficient cellular responses in bone cells upon stimulation in the first biological window.

2. A Pt/Si nanoneedle-based device integrating Schottky junctions, as an easier and faster fabrication opto-electrical platform to stimulate bone cells, enabling exploration of the second biological window for deeper light penetration.

3. An efficient hybrid low bandgap semiconductor 2D-MoS_2/Cu_2O system supported on mesoporous silica nanoparticles to enhance surface area and hence photochemical reactivity for the efficient ROS production and with the capability to be activated with NIR light to induce effective cancer cell death.

VI. Outline

The results of the thesis have been collected into 4 chapters which are summarized below, starting from chapter 2 as the first chapter was devoted for the introductory part.

1. The second chapter describes the rational design and application of the opto-electronic device based on Si/Au nanowires with built-in pn junctions to stimulate bone cells (osteoblasts) within the NIR first biological window.

2. The third chapter describes the nanofabrication and characterization of Silicon based nanoneedles integrating Schottky junctions to stimulate osteoblasts within the NIR second biological window.

3. The fourth chapter addresses the fabrication and application of 2D MoS_2-Cu_2O on mesoporous silica supports for the photogeneration of therapeutic ROS for cancer treatments with NIR light.

4. The fifth and sixth chapters compile the summary of the conclusions obtained from this thesis and the future perspectives respectively.

5. Appendix contains information about additional work accomplished in other fields by exploiting the different nanofabricated nanostructures presented in this thesis.

2. Si/Au Nanowires with integrated pn junction for Wireless Opto-Electrical Stimulation of Bone Cells with Ultralow Intensity NIR Light

Stimulation of cells can be achieved through opto-electrical devices which convert light into an electrical output. This electrical signal exerts an impact on various cellular processes. For instance, in the case of osteoblast cells, ES can induce proliferation, differentiation, and ECM mineralization via activation of voltage-gated Ca^{2+} channels. This study focuses on NIR light, emphasizing its safety and increased tissue penetration within the first or second biological windows, making this spectral range noteworthy for applications in clinical therapies. In this study, an efficient Si/Au NW device integrating a pn junction was fabricated through a scalable colloidal lithography technique. Upon exposure to NIR in the first biological window and at very low light intensity (below 10 $\mu W/mm^2$), these NW devices proved their capacity to generate high photovoltage values (over 300 mV) and substantially higher photocurrents (ca. 3-fold) compared to the flat pn Si wafer. Being biocompatible, they provided an adequate surface for cell attachment and proliferation over 21 days. Furthermore, a significant influx of Ca^{2+} was detected with light stimulation at ultra-low light intensity, even for 1 $\mu W/mm^2$. The opto-electric stimulation enabled enhanced proliferation, differentiation and promoted an increased formation of calcium deposits. These results highlight the potential of the nanostructured Si/Au device for highly efficient cell stimulation at ultra-low intensity levels of high penetration NIR light.

2.1 Introduction

The emergence of wireless cell stimulation techniques is an important step towards overcoming the limitations encountered when ES is used. Being invasive, bulky and with high possible risk of infection, wired ES has clinical restrictions[36,40,49]. To address these challenges, different types of energies (optical, magnetic, acoustic) capable of being converted into electrical or thermal outputs can be applied to stimulate cells[69]. With light stimulation, non-invasive and targeted therapies are possible, achieving a considerable milestone towards more precise treatments. That is possible due to the easy control of the size, intensity, and pattern of the light beam, allowing it to target cells as well as tissues. Therefore, development of implantable devices that can be controlled by light becomes an appealing solution to overcome the problems associated with ES. These devices possess the potential to wirelessly stimulate cells with high spatiotemporal resolution, thus presenting them as promising alternatives for therapeutic applications[79,120].

Emerging studies based on silicon, organic semiconductors and gold nanostructures have shown significant progress towards implantable opto-electric cell stimulation devices (***Table 1***). Visible light actuation in mesostructured Si[121] and coaxial p-type/ intrinsic/n-type (p-i-n) Si

NW[122] have been able to extracellularly elicit action potentials in a single neuron, and Au-decorated Si mesh have been effective for light-controlled modulation of mouse brain activity *in vivo*[123]. Ligand-conjugated Au NPs have been targeted to neurons for triggering action potentials and exciting activity in mouse hippocampal slices by exploiting photothermal effects[124]. Organic semiconductors offer advantages such as flexibility and biocompatibility for light-mediated stimulation of neuronal cells, but challenges like water-induced swelling, progressing degradation, delamination and limited photoconversion efficiency exist. However, successful performance has been shown by using poly-3-hexylthiophene (P3HT)-based devices. Polymer blends with donor-acceptor polymers, like P3HT/phenyl-C61-butyric-acid-methyl ester (PCBM), poly(3,4-ethylenedioxythiophene) PEDOT/poly(styrenesulfonate) PSS or PCBM/cyclopenta dithiophene benzothiadiazole (PCPDTBT), have exhibited strong performance under visible light, with the latter one approaching stimulation in the NIR range.[83] These organic based opto-electronic devices have induced neuronal firing and restored light sensitivity in explanted rat retinas with photoreceptor degeneration[125]. However, these opto-electric stimulators usually employ low penetration visible light and high light intensities, which limit their application to superficial implants and might even cause tissue damage due to excessive thermal heating[126,127]. Moreover, the used light intensities are much higher than the ocular safety limit for continuous exposure to visible light (107 $\mu W/mm^2$ at 532 nm)[128] or even skin safety limits (2000 $\mu W/mm^2$ and 3000 $\mu W/mm^2$ for 532 nm and 808 nm, respectively)[129] thus hampering their clinical application. Therefore, there is still a need to drastically increase the actuation efficiency of implantable devices in the NIR biological windows for achieving safe and maximized actuation in deeper tissues.

In addition, the majority of these wireless stimulation systems have been applied to excitable cells (e.g., neurons, cardiomyocytes) via induction of action potentials[83,124,130]. Table 1 collects an overview of the different studies addressing optical cell stimulation, indicating the different parameters used, usually requiring visible light and high light intensities as previously mentioned.

Table 1 Optical cell stimulation materials and employed light conditions.

Materials	Wavelength (nm)	Intensity ($\mu W/mm^2$)	Light Parameters	Stimulated cells or tissues	Refs
Lipid-supported mesoporous Si	532	$6.7 \cdot 10^7$	5.32 mW, spot size 10 µm	DRG neuron	[121]
Coaxial p-i-n Si nanowires	532	$8.6 \cdot 10^5$	6.75 mW, focused spot, assumed spot size 100 µm	DRG neuron	[122]
Au-decorated p-i-n Si mesh	473	$1.3 \cdot 10^5$	5 mW, spot size 216 µm, 100 ms	Mouse brain in vivo	[123]
Nano-crystalline Si nanowires	592	$3.3 \cdot 10^5$	14.4 mW, spot size: 237nm, 1 ms	Glial cells	[123]
Nano-crystalline Si nanowires	592	$1.8 \cdot 10^5$	2.1 mW, spot size: 211 nm, 1 ms	HUVECs	[123]
Textured i-Si nanowires	592	$2.8 \cdot 10^6$	22.3 mW, focused spot, assumed spot size 100 µm	Neuron, glial cell	[131]

Supported p-i-n Si nanowires	514	$3{\cdot}10^6$	0.6 µW, spot size 500 nm	Cardiomyocyte	132
Si photodiode array	905	800	Duration 4 ms	Rat retina	133
Si photodiode array	915	550	10 ms pulses	Rat retina in vivo	134
Hybrid organic film P3HT: PCBM	532	10^4	50 ms	Neuron	135
P3HT film	532	$1.5{\cdot}10^4$	20 ms pulses	Neuron	125
Metal/ H_2Pc/ PTCDI film	600	$4.8{\cdot}10^3$	5 ms pulses	Neuron	136
PTCDI/ H_2Pc/ITO	660	$6{\cdot}10^3$	1 ms pulses	Xenopus laevis oocytes	137
Au nanorods	980	$1.59{\cdot}10^6$	1 ms pulses	Neuron	138
Silica-coated Au nanorods	780	$1.15{\cdot}10^7$	1 ms, aligned to cell body, assumed spot size 100 µm	Neuron	139
Au nanoparticle (20 nm)	532	$3.1{\cdot}10^8$	1 ms, 31kW/cm^2	DRG[h] neuron	124
Au nanoparticle (100 nm)	800	2.7		Neuron	130
Au nanoparticle	532	$8{\cdot}10^3$	10 ms	cardiomyocyte	140
Au-decorated TiO_2 nanowires array	375/ 546	133/ 470	0.24 s	Blind rat retina	141
Si photovoltaic microcell array	488	15.8	Every second for 15 min	Saos-2	71
Photovoltaic organic implant (bulk heterojunction)	730	47	10 ms pulses	Retinal ganglion cells	83
p-i-n Si mesh	473	$7.8{\cdot}10^5$	2mW, spot size: 57 µm, 1 ms	Mouse brain slices	142
Nanoporous Si pillars	532/808	$4.10^4/8.7.10^4$		Heart ex vivo	76
Nanoporous Si pillars	532/808	$6.8{\cdot}10^4/2.1{\cdot}10^5$	10 ms	Sciatic nerve in vivo	76
PEDOT/PSS	626	80	20 ms	X.laevis oocytes	82
PCPDTBT: $PC_{60}BM$	565/730/780	$1\ 10^3$ (565 nm), $6{\cdot}10^3$ (730 nm), $7.5{\cdot}10^3$ (780 nm)	10 ms	Mice retina	83
Thin film Si:mesh, pillars, pyramid/porous collagen/HA/PCL	808	$2{\cdot}10^3$-10^4	3 s or 8 s (depends on the assay)	hBMSCs[i]	45

However, non-excitable cells can be also electrically activated by stimulation of the voltage-gated ion channels, which can be found in a very wide range of cells, such as epithelial cells, pancreatic beta cells, fibroblasts, some immune cells, or even osteoblasts and osteoclasts.[33,143] Although, ES in non-excitable cells is much less explored than in excitable cells, it can also modulate very diverse biological processes, ranging from regulation of electrolyte balance, cell migration, wound healing, and tissue repair. For bone cells in particular, ES has been proven to influence cellular behavior at different levels, including proliferation, morphology, and

[h] DRG neuron: Dorsal Root Ganglion, it emerges from the dorsal root of the spinal nerves.
[i] hBMSCs: human Bone marrow Mesenchymal Stem Cells.

differentiation[144,145], therefore highlighting their potential for healing upon ES. However, the opto-electric stimulation of bone cells is barely unexplored. A recent study has shown the enhanced proliferation, and osteogenic differentiation in bone marrow stromal cells by 3D Si-based microstructures upon NIR illumination. However, the regeneration of bone defects was promoted with a very high light intensity (10^4 $\mu W/mm^2$)[45]. Another study has used Si photovoltaic microcell arrays, featuring planar pn junctions, for opto-electronic stimulation of osteoblast cells. This approach elicited intracellular calcium transients using visible light (488 nm)[71].

Due to the lack of opto-electronic studies with non-excitable cells, the present study focuses on the development of an opto-electronic device based on nanostructured Si/Au with integrated pn junctions for wireless stimulation of bone cells. The study also leverages silicon's biocompatibility and remarkable opto-electronic properties of the hybrid nanostructured device, particularly in the NIR spectrum, which enable high penetration depth actuation within the first and even second biological windows.

Therefore, this chapter compiles the design of Si/Au NW combined with pn junctions, their effectiveness in producing high PV and PC, and their application in the stimulation of osteoblast cells under ultra-low light intensities ($\mu W/mm^2$) in the first NIR biological window. The proposed device platform merges silicon pn junctions, Au/Si Schottky junctions and surface nano-structuration to enhance photon capture. The nano-structuration is achieved through scalable and cost-effective lithography techniques. Firstly, the electronic and optical properties of the Si/Au nanostructured surfaces, aimed at maximizing the light trapping efficiency, the photogenerated carrier separation and charge injection into the electrolyte solution, are described. Next, the opto-electronic performance of Si/Au nanostructured surfaces is presented in comparison with other silicon based opto-electronic devices under different illumination conditions to fully understand and maximize their optical response at ultralow light levels. Finally, the optimized structures and illumination conditions are employed to demonstrate the efficient opto-electric actuation in osteoblasts. This involves triggering an influx of Ca^{2+} (most probably through voltage-gated Ca^{2+} channels) and the monitoring of differentiation markers induced by the stimulation. This approach presents a promising route for the actuation in bone tissue with high penetration and safe low intensity NIR light.

2.2 Results and Discussion

2.2.1 Design of Si/Au NWs with pn junction

To fabricate a highly efficient opto-electronic device, which in turn, requires minimum light intensity, attention must be devoted to three fundamental aspects which include: enhancement of photon absorption efficiency, precise separation, and transport of photogenerated carriers, and efficient injection of charges into the electrolyte solution. Hence, it is essential to tailor the materials to fulfil these requirements, particularly for the specific objective of this work, which involves their utilization in the first biological window of the NIR. Accordingly, the proposed opto-electronic platform consists of monocrystalline silicon with a buried pn junction and a surface nanostructured by an array of silicon NW capped with gold nanodiscs. The special characteristics of silicon combined with gold will help fulfil the three specified requirements. Silicon is known for its low bandgap, which enables opto-excitation in the visible-NIR range. Additionally, achieving efficient separation of photocarriers requires the creation of a customized pn junction, a process facilitated by the silicon's mature technology in micro/nanoelectronics that allows for precise manipulation of doping levels and band structure. In parallel, a Schottky junction is created through the direct conjugation of n-side silicon with the gold nanodiscs, effectively promoting the injection of photoelectrons into the electrolyte solution under stimulation. This process induces faradaic processes, with the n-Si/Au side serving as reducing agent.

Figure 1a depicts a schematic of the pn Si/Au structure. ***Figure 1b*** illustrates the band diagram of the system with the pn junction and Schottky barriers under equilibrium, with the Fermi level equalized across the different components forming the device. Under equilibrium, band bending occurs at the different interfaces of the semiconductor silicon, indicative of an in-built electric field. The band bending established at the pn junction balances the diffusion and drift of charge carriers, resulting in a net zero current. The band bending at the n-side Si/Au interface generates a Schottky junction. Electrons on the n-side encounter a potential barrier, hindering their injection into the metal side. ***Figure 1c*** illustrates the operating principle of the proposed device under light stimulation. Upon light excitation, absorbed photons generate electron-hole pairs. The photogenerated e-holes carriers are drifted and separated by the electric field at the pn junction (depletion region). Electrons, as minority carriers at the p-side, drift to the n-side, while holes, minority carriers in the n-side, drift to the p-side. The electric field, coupled with the inherent elevated doping level in the n region and the electron/holes generated at the Au/Si side, significantly reduce the potential barrier in the Schottky junction, facilitating the photocarriers transfer into the gold nanodiscs and enhancing photocurrents[53,146,147]. These processes ultimately lead to changes in capacitive charge at the Au/electrolyte side and charge injection at the electrolyte, inducing redox processes.

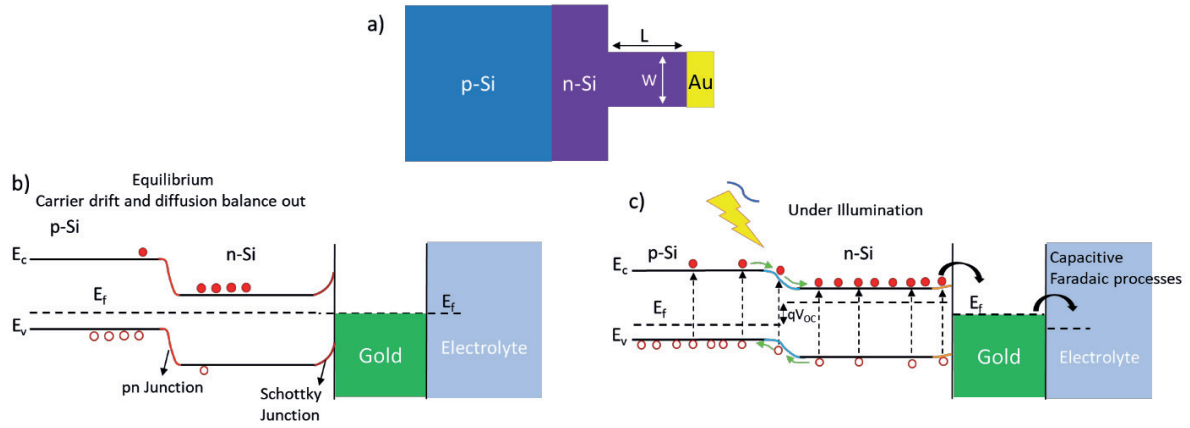


Figure 1 (a) Schematic part of the proposed silicon-based device. Band diagram of the p-Si/n-Si/Au nanostructured system in dark at equilibrium (b) and under light stimulation (c), creating a photovoltage (V_{oc}) and photocurrent.

To attain effective opto-electric responses at ultralow light intensities, it is necessary to ensure efficient photon absorption within the active region. Monocrystalline silicon exhibits different levels of absorption across the visible-NIR regions. It has significant absorption in the visible range, particularly for shorter wavelengths. However, it becomes more transparent in the NIR region, allowing longer-wavelength light to penetrate deeper. Usually, in a silicon wafer with pn junction, the PV is induced by the photocarriers generated in the initial 1,2 µm of the wafer. Under this context, light absorption percentage can decrease from 20% at 650 nm to less than 5% at 900 nm (***Figure 2a***). To improve photon absorption and accomplish relevant PVs or PCs, the contribution of the gold nanodiscs as plasmonic nanomaterials to enhance light absorption is considered. Accordingly, a theoretical finite-difference time-domain (FDTD) analysis of the absorption efficiency of silicon patterned with Au nanodiscs (Au ND), and short (Short Si/Au NW) and long nanowires (Long Si/Au NW) capped with gold nanodiscs was conducted in comparison with the non-structured flat silicon wafer (flat Si wafer). According to the calculations (***Figure 2a***), silicon patterned with Au ND or solely with short Si NW do not exhibit improved absorption efficiency in the NIR. For short Si NW samples, only a subtle increase in absorption is observed at wavelengths beyond 750 nm compared to the flat Si wafer, indicating that the dielectric Mie resonances of Si/Au NW are drastically damped by the Si substrate.

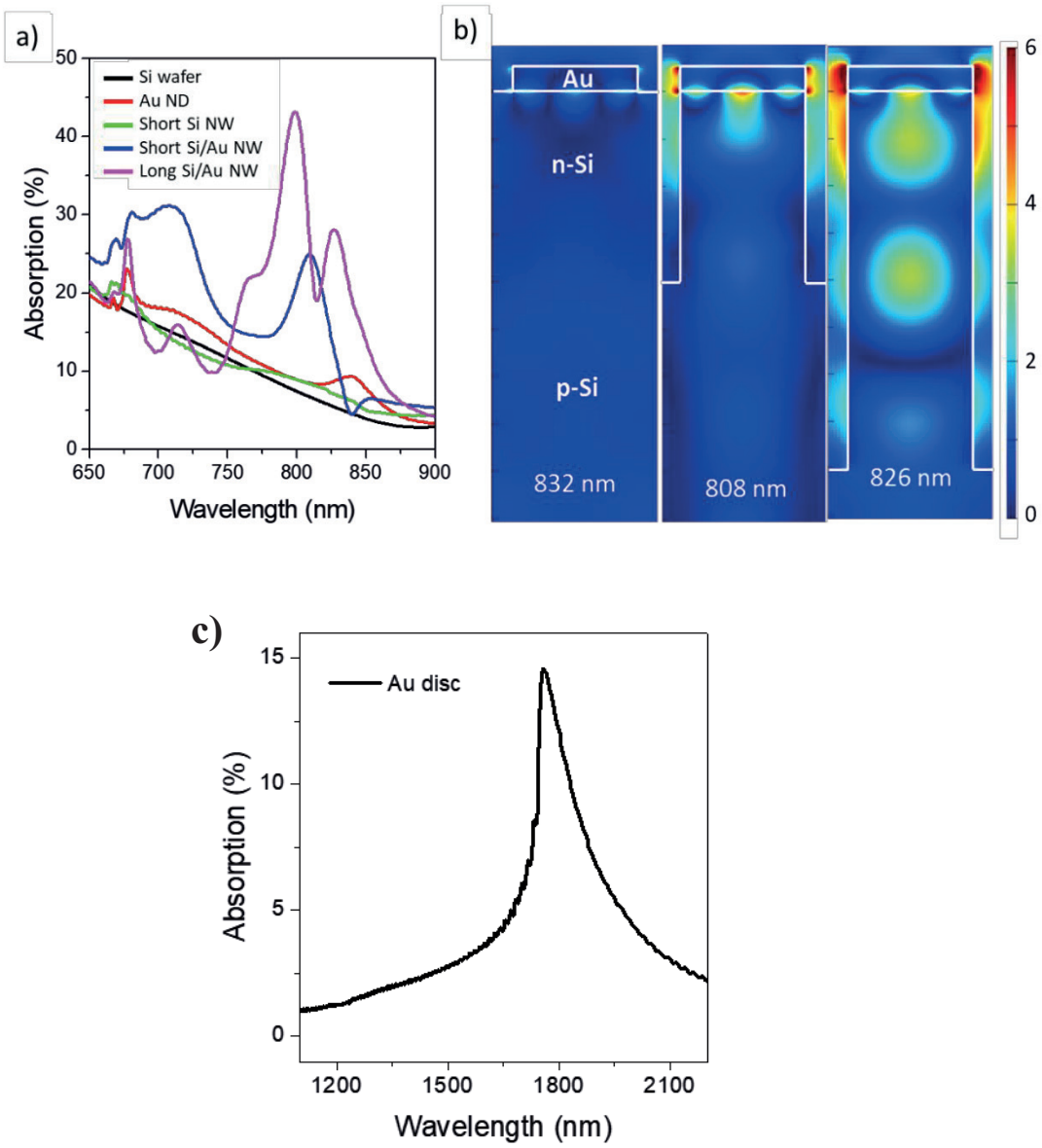


Figure 2 a) Finite-difference time-domain (FDTD) absorption spectrum after 1.2 µm light penetration inside the Si wafer for a flat Si wafer, and for nanostructured surfaces with Au nanodiscs (Au ND, diameter 230 nm, height 75 nm), Si nanowires (Si NW, diameter 230 nm, height 350 nm), and Si/Au NW (diameters 230 nm, heights 350 nm and 800 nm, for the Short Si/Au NW and Long Si/Au NW, respectively). b) Electric field (Abs [Ex]) distributions for Au ND, short and long Si/Au NW at the resonances located at 832 nm, 808 nm and 826 nm wavelength, respectively. c) Percentage of light absorption by the Au ND at longer wavelengths.

In the case of Au ND on flat Si wafer, a plasmonic resonance at around 1800 nm is expected, notably distant from the silicon bandgap energy threshold, and another small resonance peak at around 830 nm was observed, indicating a weak electromagnetic field confinement at the Si/Au interface (***Figure 2b***). Conversely, when analyzing NW that are capped with Au nanodiscs, a potent hybrid metal/dielectric resonance is produced, consequently intensifying light absorption at the pn region and at the Si/Au interface. Interestingly, the diameter and height of the NW have a relevant influence on the hybrid resonance in the first biological window of the NIR. Long Si/Au NW (with a diameter D = 230 nm and length L = 800 nm)

exhibits 6-fold enhancement in absorbed light at wavelengths 800 nm and 826 nm due to hybrid resonances. In shorter Si/Au NW (D = 230 nm, L = 350 nm), the amplification is 2-fold and 4-fold for hybrid resonances located at 710 nm and 808 nm wavelengths, respectively. Larger diameters result in red-shifted hybrid resonances (Plot available in the thesis of Yue Zhang)[148].

2.2.2 Fabrication of Si/Au NW System

Taking the theoretical analysis explained above as a reference, we fabricated Si/Au NW of both heights: short and long, using two polarities in the silicon junctions: pn Si/Au NWs and np Si/Au NWs (the latter one has been only used for calcium peak assessment as specified below). ***Figure 3*** shows different samples with the pn configuration. Just note that on the long nanowires the pn junction is completely exposed to the surrounding media as compared to the shorter ones. The opto-electric performance of the different systems was compared to a flat Si wafer with pn junction.

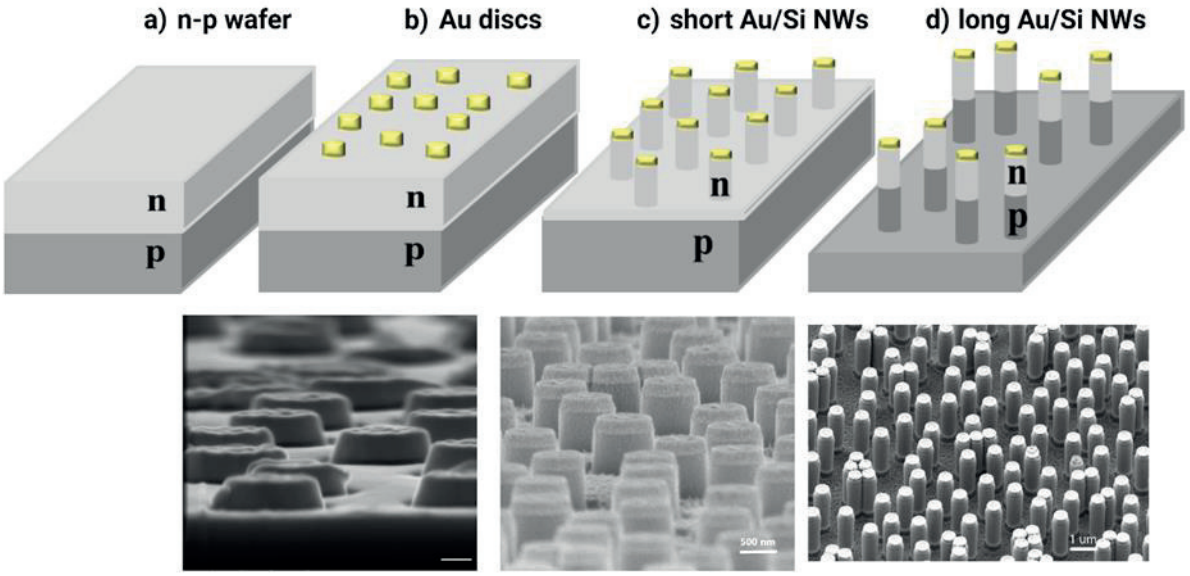


Figure 3 Schematic illustrations with respective SEM images of the different configurations used for the opto-electric analysis: (a) Flat Si photodiode with pn junction depth at 560± 10 nm; and photodiodes with various structures with (b) Au ND (D ≈ 210nm, L ≈ 75 nm), (c) Short Si/Au NWs (D ≈ 210nm, L ≈ 240 nm), and (d) Long Si/Au NWs, (D ≈ 210nm, L ≈ 1 μm).

To minimize the fabrication cost, we employed a scalable colloidal lithography fabrication process. The process started with the implantation of dopants on 4-inch silicon wafer as follows: n-dopant on p-wafer and p-dopant on n-wafer, with a depth of approximately 560 nm ± 10 nm. Then, a layer of gold with a 75 nm thickness was deposited on both sides of the wafer, followed by electrostatic colloidal self-assembly of positively charged polystyrene nanoparticles of 200 nm diameter on the polished and implanted Si/Au surface. This results in a homogenous distribution of the particles at a high density. To produce Au ND as in (***Figure 3b***), reactive ion etching (RIE) with Ar gas was employed using nanoparticles as masks. In the

last step, NWs of adjustable heights were fabricated through RIE with fluoride gases using the Au ND as masks **(*Figure 3c-d).***

2.2.3 Opto-electric Analysis

To evaluate the performance of the Si/Au NW as potential wireless opto-electronic devices in response to stimulation with the high penetrating NIR light within the first and second biological windows, the generated PV and PC were measured. To accomplish such measurements, an electrochemical cell was used with phosphate buffer saline (PBS) 1X, pH 7.4 as the electrolyte, a platinum wire as counter electrode and the NW substrate, contacted through a metal contact at its backside, serving as the working electrode (***Figure 4ab***). To have a comparative analysis, the tested samples included: pn flat Si wafer, Au ND, and short and long Si/Au NWs. To avoid shortcuts by the liquid electrolyte, samples were treated with PDMS at the edges of the chips, whose sizes were 1.5·1.5 cm^2. Then, they were exposed to square light pulses of 10 ms duration with wavelengths centered at 810 and 1050 nm, i.e., in the first and second biological window, respectively. The PV was measured under open circuit conditions (high impedance).

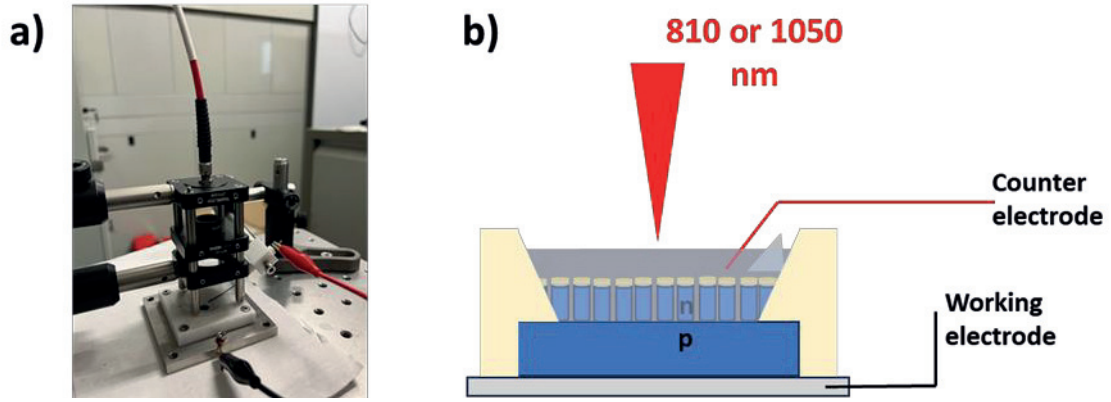


Figure 4 Setup for opto-electrical measurements. a) An image showing the setup where the measurements are carried on. b) Schematic illustration depicting the exposure of short Si/Au NW samples to 810 nm or 1050 nm with the sample covered by PBS 1X.

Figure 5a depicts the output PV for the different samples as a function of light power at a wavelength of 810 nm. The PV generated by the short Si/Au NW and the pn flat Si wafer were nearly equal, with the short Si/Au NW being slightly larger than the pn flat Si wafer and Au ND. All samples exhibited an initial steep increase of the PV at low light power reaching a saturation profile at higher power values. A high PV for the pn flat Si wafer and the Au ND samples was expected, since the response by the pn junction would be similar in both samples. In contrast, the long NWs exhibited a significantly lower PV, ca. 4-fold lower than the short NW, as shown in the same plot, despite the larger expected light absorption in the long NWs. In this case, the PV drop could be explained by the shortcut produced for exposing the pn junction to the electrolyte.

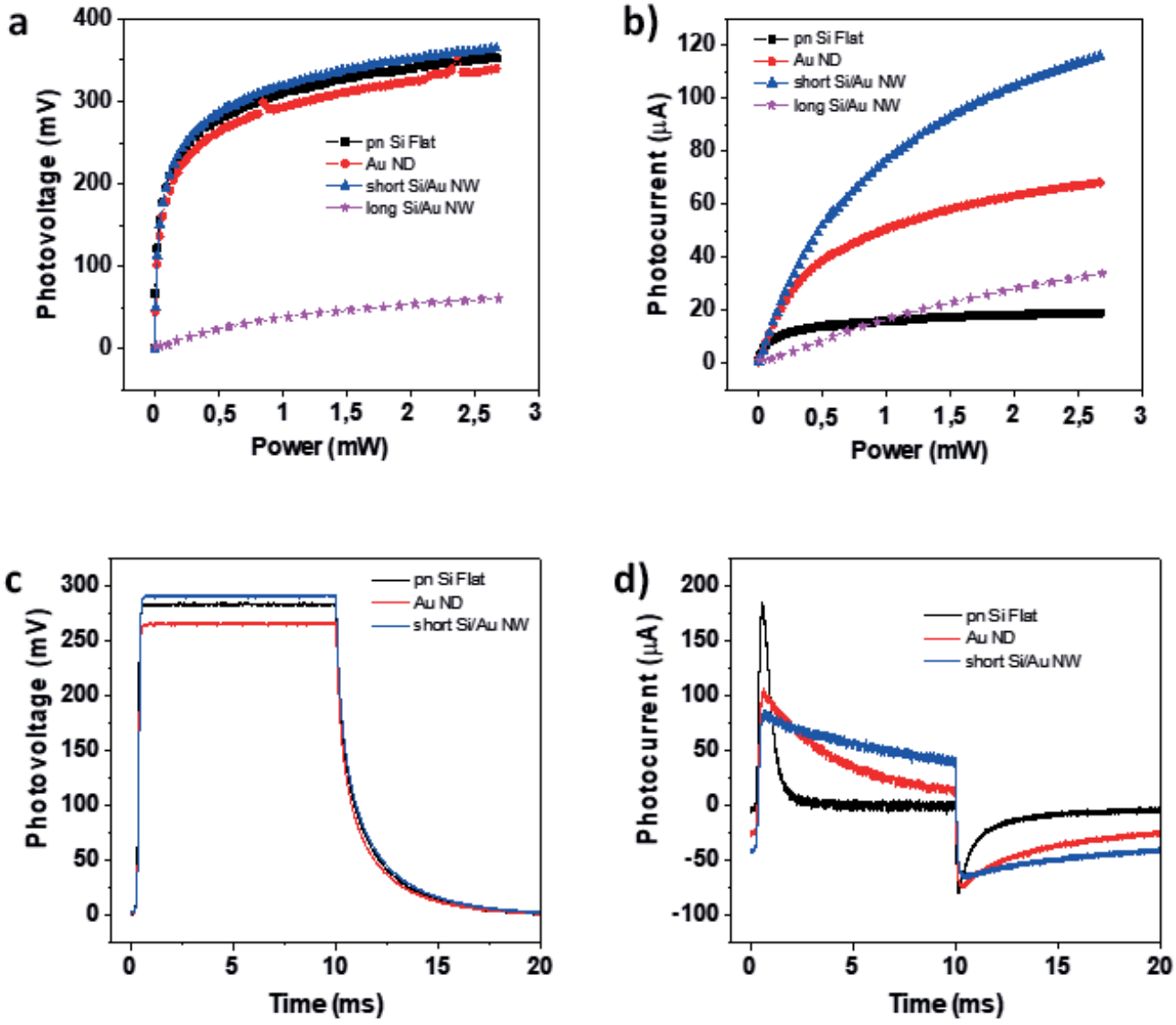


Figure 5 Opto-electrical analysis of different structures. a) and b) PV and PC obtained for the different samples in response to NIR at 810 nm as a function of the light power (beam size 6 mm diameter). c) and d) PV and PC measured in response to 810 nm light specifically at 49 μW/mm^2.

Next, we measured the average PC, by calculating the integral of the absolute value of the current over the 20 ms period, divided by the time period (20 ms). Unlike the PV, the PC exhibited a very different behavior in the four different configurations. The results show a relatively high PC generated by the short Si/Au NWs followed by the Au ND. For a light power of 2 mW and spot size of 6 mm diameter (equivalent 71 μW/mm^2), the PC of the short Si/Au NWs was ca. 6-fold higher than that of the flat Si wafer photodiode. In contrast, the long NW also produced very low PC (***Figure 5b***).

The PV and PC transients under the square light pulses of 10 ms duration and at light power of 1.3 mW (intensity 49 μW/mm^2) are shown in ***Figure 5c-d***. The temporal plots of the PV

showed square pulses that closely followed the shape of the light pulses, with very similar values for the pn flat Si wafer, Au ND and short Si/Au NWs. More differences were observed in the PC transients. The PC showed that pn flat Si wafer presented a sharp transient, with a rapid increase in current, followed by a very fast decay. That is ascribed to a capacitive current built up from the accumulation of the electrolyte ions at the silicon interface to balance light generated excessive charge carriers. However, Au ND and short Si/Au NWs exhibited a fast initial increase, but the current was sustained afterwards, instead of quickly returning to zero during the 10 ms actuation, with this effect being more pronounced for the Si/Au NWs. Such behavior suggests that the light induced both capacitive and Faradic currents. These results imply that gold nanostructures facilitate the transport and injection of the light-generated electrons to the solution, promoting reduction reactions with species in the electrolyte. Interestingly, the PCs reverse when light is off, indicating a reverse double-layer charging and reactions, further supporting the combined faradic process and photo-capacitive effect. Therefore, the presence of pn junctions in series with Schottky junctions under light illumination seems to significantly promote the potential barrier decrease for the photogenerated charge carriers, facilitating their injection into the electrolyte.

The combination of relatively high PV and PC generation by the short Si/Au NWs favors them over the other samples. This implies that they possess relevant capacitive and faradaic characteristics, making them promising for wireless stimulation under NIR light. These findings are encouraging for addressing the limitations faced with other types of cell stimulations in terms of tissue penetration depth and minimal cellular damage.

In parallel, characterization of the samples was also performed with NIR light in the second biological window, where light of 1050 nm wavelength was used. Same PV and PC measurements were conducted. Like the results obtained with 810 nm, the generated PV was quite similar for the pn flat Si wafer, the Au ND and short Si/Au NW samples (***Figure 6a***). Moreover, as in the case of the first biological window, the PC generated by the short Si/Au NWs was the highest followed by the Au ND and then the pn flat Si sample (***Figure 6b***).

In the next step, we compared the PV and PC measurements for the short Si/Au NWs at both light wavelengths. As expected, both PV and PC generated were slightly higher at 810 nm than 1050 nm (***Figure 6c-d***). The reason is due to the Si absorbance decrease with increasing wavelength approaching the bandgap threshold (1.1 μm). However, the PV and PC values remain sufficiently high, making them promising for stimulation in the second biological window.

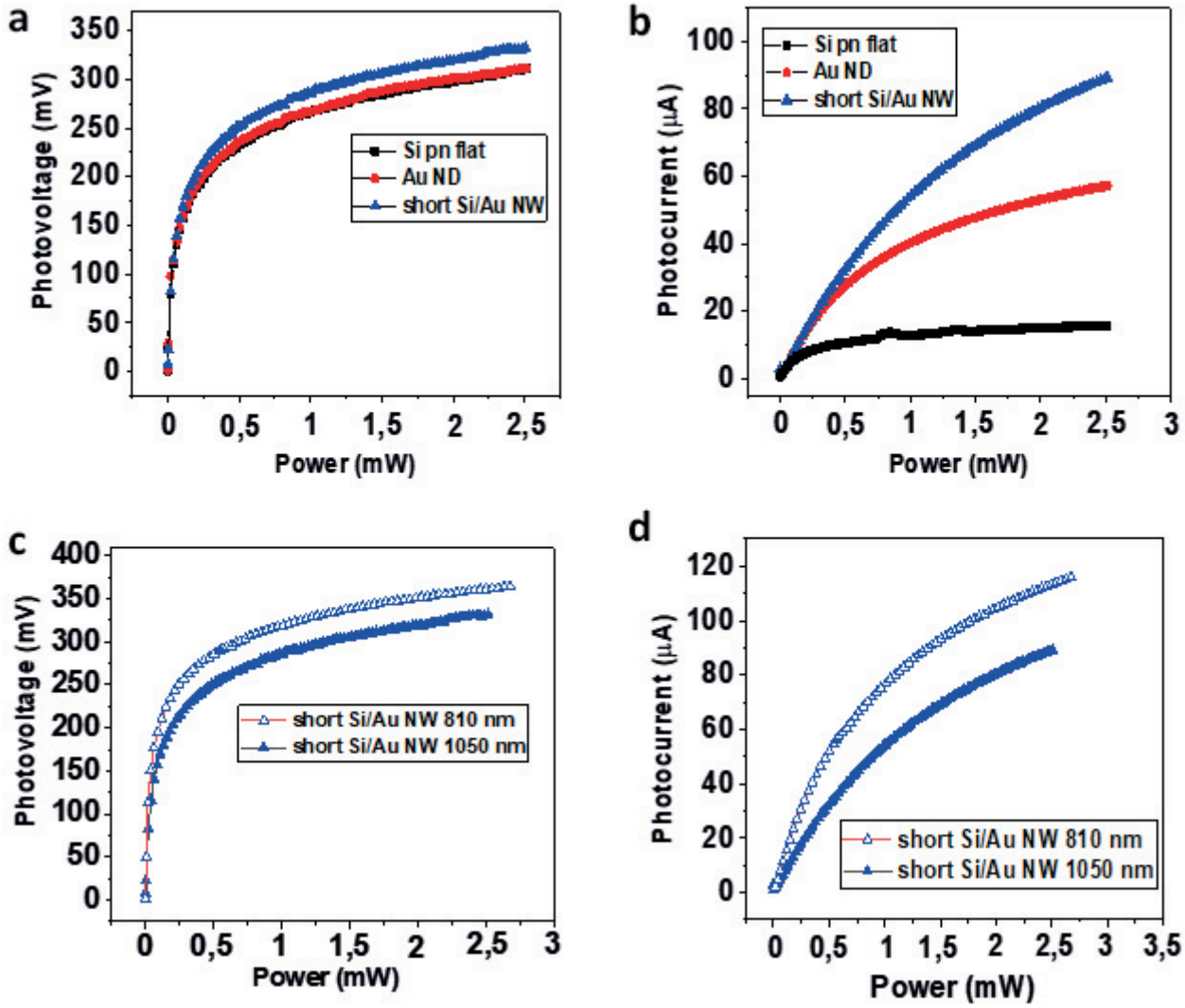


Figure 6 Opto-electrical characterization of the structures. a) and b) PV and PC generated in response to 1050 nm light. c) and d) Comparison of PV and PC measurements between short Si/Au NWs at 810 nm and 1050 nm.

2.2.4 Biocompatibility of the Short Si/Au NWs Device

These opto-electric results show the potential of the Si based devices for wireless opto-electric stimulation in the NIR biological windows, and the capacity to tune the actuation from a pure capacitive (pn flat Si wafer) to a combination of capacitive and faradaic stimulation (short Si/Au NW). Before studying the stimulation of the osteoblasts, the biocompatibility analysis of the interaction between osteoblast cells and the Si/Au NW was assessed. Firstly, the borders of the nanostructured NW sample were passivated with PDMS to prevent shortcuts. Then, the samples were subjected to an oxygen plasma treatment to enhance hydrophilicity before cells (Saos-2 cell line) were seeded. After 24 h of cells seeding, very few cells were adhered to the NW surface. Therefore, the incubation time was extended to 48 h, before light stimulation, to allow the majority of the cells attach and remain alive (***Figure 7a***). Previous studies have

consistently demonstrated the biocompatibility of silicon for cell applications[45,74,149]. Here, it was further proved that topography of the NW did not affect the viability of the cells.

Scanning electron microscope (SEM) images showed a proper attachment of Saos-2 cells on NW surfaces. Compared to glass, where cells appear in a flat shape, distinct morphologies like elongated and oval-shaped cells were observed when Saos-2 cells were cultured on the NW surface, as shown in ***Figure 7b***. In addition, nucleoli were obvious, reflecting that cells were active in transcription[71].

The light used for cell stimulation in these experiments was in the NIR first biological window, which has been previously proved to be safe for cells. To confirm its safety and check any possible influence of the light on the cells, Saos-2 cells cultured for 48 h on Si/Au NWs and on glass, as a control, were exposed to NIR light of 810 nm wavelength and intensity of 4.5 $\mu W/mm^2$ for 24 h. This low light intensity did not cause any harm to the cells grown on glass coverslips, used as control, with a viability of 98,4 ± 0,4% (***Figure 7c***), neither on cells grown on NW (***Figure 7d***) where 98,5 ± 0,5% of cells were alive.

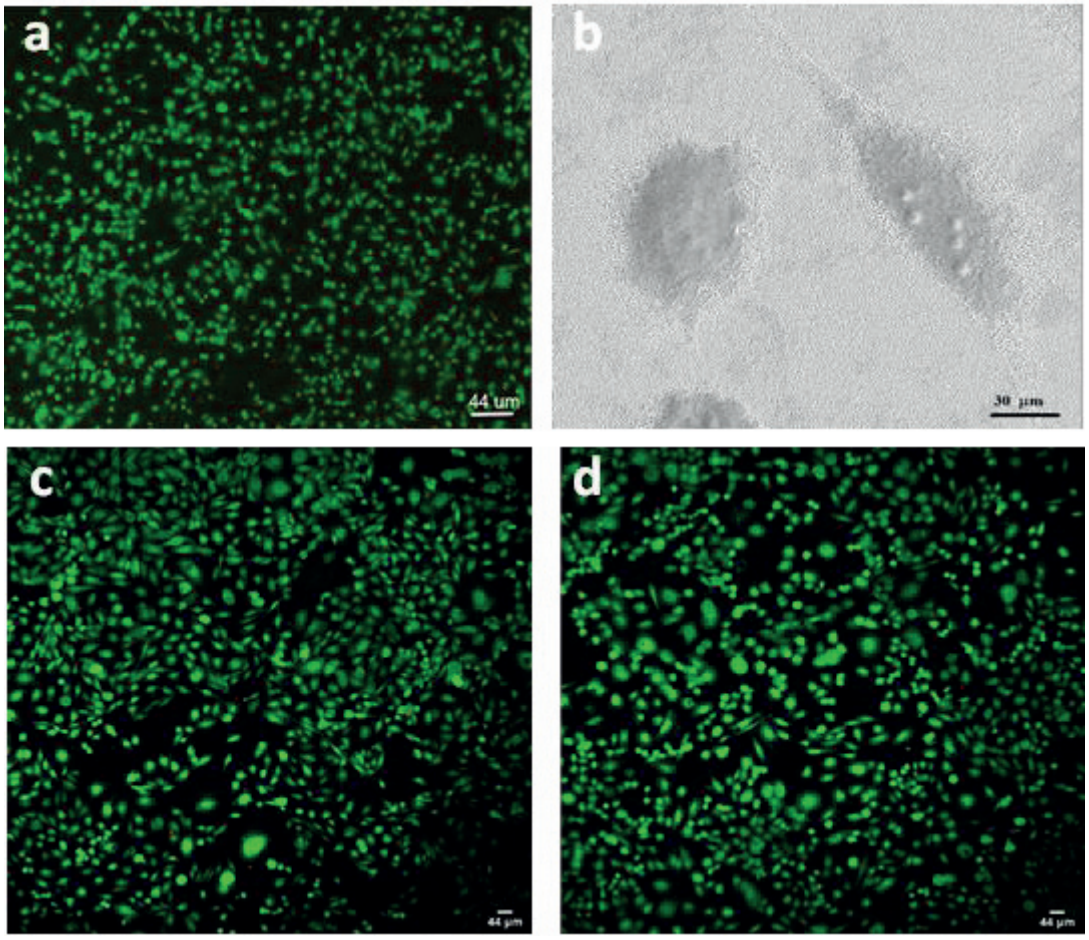


Figure 7 Viability and morphology of Saos-2 cells seeded on top of Si/Au NWs. (a) Cell viability and (b) morphology (SEM image) after 48 h of culture in the absence of NIR light. Cell viability of cells grown on NW (c) and on glass coverslip (d) after been exposed to NIR stimulation for 24 h at a light intensity of 4.5 $\mu W/mm^{2.}$ Green and red cells represent live and dead cells, respectively.

In addition, the distribution of actin cytoskeleton in Saos-2 cells grown on Si/Au NWs was analyzed. The interaction between the cells and the substrate depends on focal adhesion structures, a complex formed by integrins and other cytosolic proteins[71]. These integrin proteins, in conjunction with actin filaments influence the cell behavior on the substrate[150]. Through these focal adhesion structures, integrins activate the formation of stress fibers from actin fiber bundles[71,150]. As shown in ***Figure 8,*** 48 h post seeding, cells acquire a polygonal shape due to the compression applied by stress fibers spanning the cell's length (blue arrow). Additionally, the image illustrates slender extensions (yellow arrows), referred as protrusions, facilitating the cell's adhesion to distant NWs. These results agree with other studies that showed how cells, like mesenchymal stem cells, attach and grow on Si pillars with actin-rich membrane protrusions more effectively than when cells are cultured on plain silicon surfaces[45].

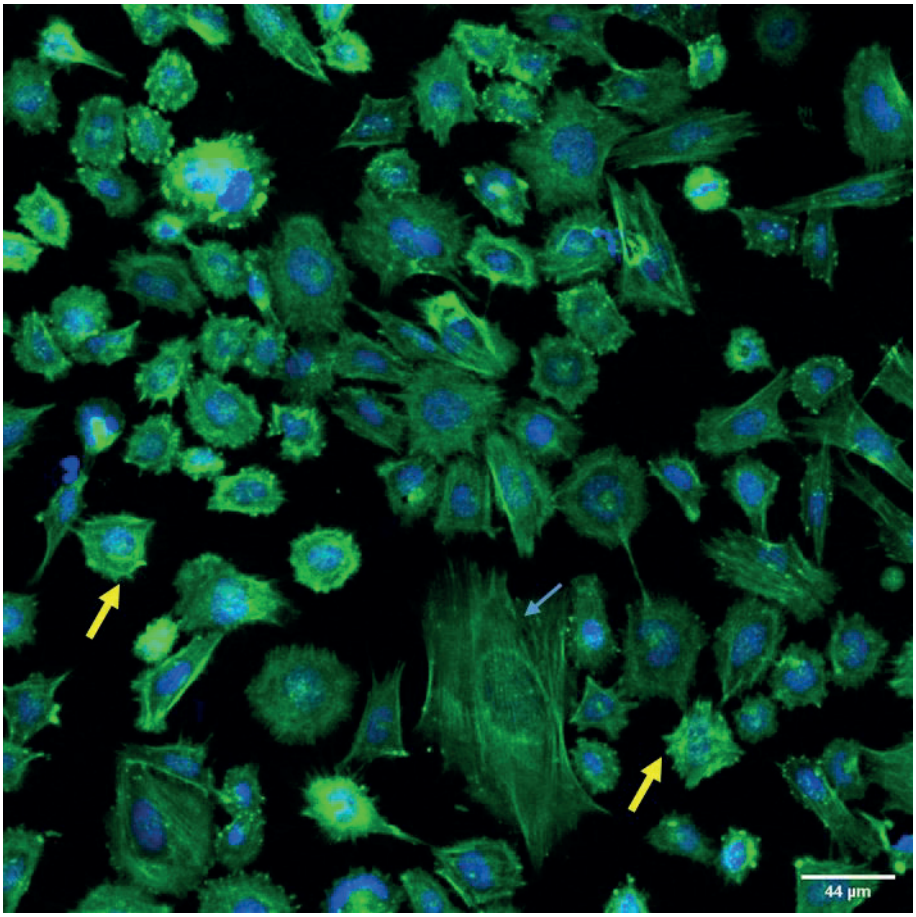


Figure 8 Actin filaments distribution (stained with Phalloidin-488 (green)) in Saos-2 cell line cultured for 48 h on the surface of Si/Au NW. The nuclei are highlighted in blue, while yellow arrows indicate a cellular protrusion utilized for attaching to a distant NW, and blue arrow shows fibers spanning the cytoplasm.

2.2.5 Response of Osteoblasts to NIR Opto-Electric Stimulation under Ultra Low Light Intensities

The potential of opto-electrical stimulation to induce the differentiation of osteoblast Saos-2 cells through the short Si/Au NWs device was evaluated by examining first the capacity to stimulate their voltage-gated Ca^{2+} channels, via detection of light induced calcium peaks. Then the changes in proliferation were assessed, and different biomarkers related to different stages of the differentiation process were analyzed. We compared the effects of the pn flat Si wafer with the short Si/Au NWs, which exhibited the highest PC response, to assess the effect of the faradaic stimulation. Although the long Si/Au NW could be interesting to develop injectable opto-electric devices, they were discarded due to their very low PV compared to the other configurations. In the last section, some alternatives are presented to achieve injectable nanodevices with higher opto-electric response.

a. Effect of Opto-Electric Stimulation in the Opening of Voltage-Gated Ca^{2+} Channels

Ca^{2+} serves as a secondary messenger that can activate various signaling pathways within the cells and affecting their behaviour[71,143]. The concentration of Ca^{2+} inside a cell is significantly lower compared to the concentration of Ca^{2+} in the extracellular fluid. There are different ways to internalize Ca^{2+} inside the cells, one of them is through the voltage-gated Ca^{2+}channels, which open in response to ES, enabling flow of $Ca^{2+}$and, consequently, the activation of different processes. To examine whether the opto-electric stimulation affects the cells and exerts an influence on Ca^{2+}entry, intracellular $Ca^{2+}$was measured using Fluo4-AM, a cell-permeable Ca^{2+}-indicator that turns fluorescent upon calcium-binding.

To determine the minimal light intensity that is necessary to stimulate the osteoblasts with NIR light in the first biological window, 810 nm NIR light pulses at a frequency of 50 Hz with very low light intensities, ranging between 11 and 1 $\mu W/mm^2$, were applied. The experiments were conducted using an inverted fluorescence confocal microscope. To integrate this setup with the opto-electronic activation process of the samples, the NW doping was inverted. In this case, n-doped silicon samples with a 560 nm p-implantation were used. The NWs capped with gold were nanofabricated at the p side, whereas the n side was flat and covered with 75 nm of Au, where cells were seeded (***Figure 9a***). This configuration was used to enable assessing the effect of the NIR light and to avoid the influence of the 488 nm confocal laser on the opto-electric stimulation. In this configuration, the NIR illumination was applied from the top through the NW side to ensure an optimal generation of PVs and PCs upon light absorption in the pn region. In contrast, the fluorescence response from cellular stimulation was captured from the opposite side of the sample, where the cells were seeded, and collected by the objective in the inverted confocal microscope (see the scheme of the ***Figure 9a***). The nearly complete reflection of the blue light by the continuous Au film, the large distance to the pn junction and the very low penetration of the confocal 488 nm light prevent the generation of opto-electric effects in the

cultured cells. To determine the effects of the surface nano-structuration, the stimulation was compared to that of pn flat Si wafers.

Saos-2 cells were stimulated for 20 min under these conditions and the percentage of cells that presented Ca^{2+} peaks are summarized in ***Figure 9b***. In the dark, the percentage of stimulated cells was nearly 20% and 15% for the Si/Au NW and the pn flat Si samples, respectively. It is worth highlighting that these numbers of activated cells in the dark with the Si/Au NW were substantially higher that those obtained on glass samples, ca. below 15%. In contrast, at the highest applied light intensity (11 $\mu W/mm^2$, 10 ms on/off), over 50% of the cells were activated, as clearly observed from the fluorescent flashes seen in the recorded video, for both Si/Au NW and np flat Si wafer. This equal percentage of activated cells in the different samples correlates with the opto-electric analysis, where both samples generated approximately equal PV around 330 mV (***Figure 5a***). To explore further, we decreased the light intensity from 11 to 4.5 $\mu W/mm^2$ to reach the region in which the PV is around 275 mV (***Figure 5a)***. Compared to 11 $\mu W/mm^2$, no change was evident in the cells activated with 4.5 $\mu W/mm^2$ using the Si/Au NW device (about 49% of the cells remaining active). However, with the flat sample, the percentage of activated cells using 4.5 $\mu W/mm^2$ decreased significantly to 28.5%. Reducing the light intensity to 2 $\mu W/mm^2$ maintained a higher number of activated cells with the NW sample than with the flat one, which has slightly increased compared to 4.5 $\mu W/mm^2$ (from 28,5% to 36%). The lowest intensity reached was 1 $\mu W/mm^2$ and at this intensity again the percentage of activated cells became approximately equal (33% for the flat, 31% for the NWs). The preservation of a high percentage of activated cells upon NIR illumination in the Si/Au NWs samples with 11, 4.5 and 2 $\mu W/mm^2$ could be explained by the faradaic effects of the device, due to the relatively higher PCs produced with the Si/Au NWs compared to the flat sample.

It has been reported that modifying certain parameters in the light actuation could enhance results. To analyse the effect of the frequency of the light in cell stimulation we decided to test two different frequencies, 50 Hz and 100 mHz, using the light intensity that provided the best results in producing Ca^{2+} peaks. In ***Figure 9c***, the plot depicts the percentage of activated cells under illumination at 4.5 $\mu W/mm^2$ with two different frequencies. No significant changes were observed when exposed the cells to a lower frequency (100 mHz) compared to the previous experiment conducted at 50 Hz, suggesting that frequency did not significantly influence osteoblast stimulation via activation of voltage-gated Ca^{2+} channels.

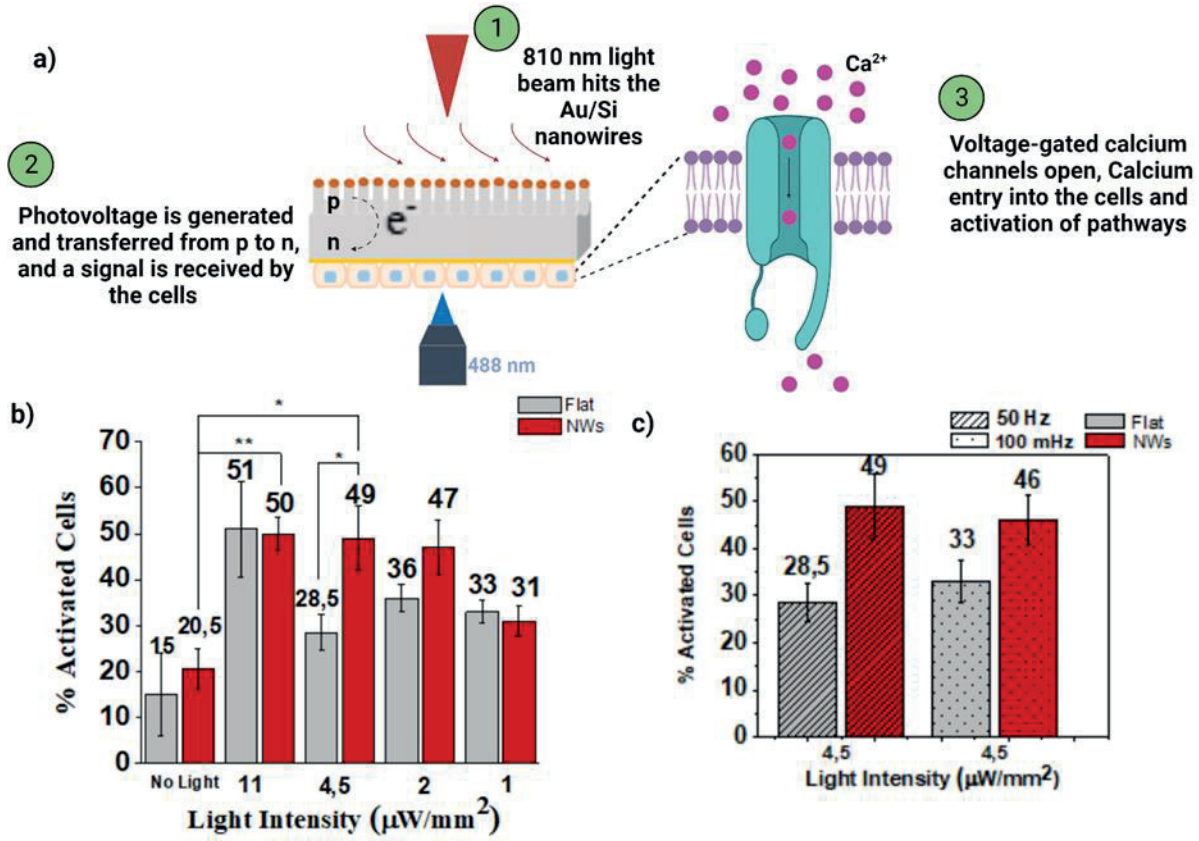


Figure 9 Intracellular Ca^{2+} flow induced by opto-electrical stimulation of Saos-2 cells. a) Schematic representation illustrating the different events occurring in response to opto-electrical stimulation. This opto-electrical stimulation facilitates the activation of Ca^{2+} channels, initiating the flow of Ca^{2+}. b) Percentage of activated cells at different light intensities in both flat (control) and Si/Au NWs samples. Asterisks indicate significant difference ($p<0,05$). c) Percentage of activated cells at the same light intensity (4.5 µW/mm^2) but different frequency (50 Hz or 100 mHz).

These results demonstrate that NIR illumination of the Si/Au NWs generates an electrical signal initiated by a flow of electrons from the p to the n part of the junction, resulting in the generation of a PV and PC. Saos-2 cells, which were cultured on the n part, receive the stimulus, causing membrane depolarization, and consequently, the opening of the voltage-gated calcium channels, allowing an influx of Ca^{2+} into the cells, as shown in ***Figure 9a***. Ca^{2+} entry into the cells is crucial for triggering pathways driving the osteogenic process of osteoblasts[45].

b. Effect of Opto-Electrical Stimulation on Osteoblast Proliferation

After confirming the capacity to stimulate the VGCCs under very low light intensity, the analysis of the proliferation of Saos-2 cells on the NW surface, upon exposure to opto-electrical stimulation, was assessed. In this case, to keep the stimulation via electrons, we used p-doped wafers and n-implantation in the region in which the short Si/Au NW were nanopatterned.

The cell stimulation effects were evaluated and quantified after 8, 14 and 21 days from the seeding, without and with light stimulation (810 nm, 4.5 µW/mm^2, 10 ms on/off cycles for one hour over the 21 days). Until day 14, cells were growing in a comparable manner in both

conditions. However, at day 21, a significant increase in the number of cells was obtained under stimulation compared to the non-stimulated sample, which suggests an induction of cellular proliferation with light stimulation (***Figure 10b***). Such significant increase in the cellular proliferation in the stimulated cells compared to non-stimulated ones is in line with previous results showing that electric stimulation can influence the behaviour of bone cells and enhance proliferation[41]. However, the effect of stimulation was highly pronounced from day 14 until day 21, in contrast to other studies where pre-osteoblast cells grew faster in the first days of stimulation, with no noticeable change over time[41]. Usually, Saos-2 cells tend to grow in a monolayer rapidly when seeded in culture plates. However, since the cell culture was done on the NW surface, and required two days for proper cell attachment, it is possible that additional time may be needed to reach confluency in an osteoblast monolayer on the Si/Au NWs substrate.

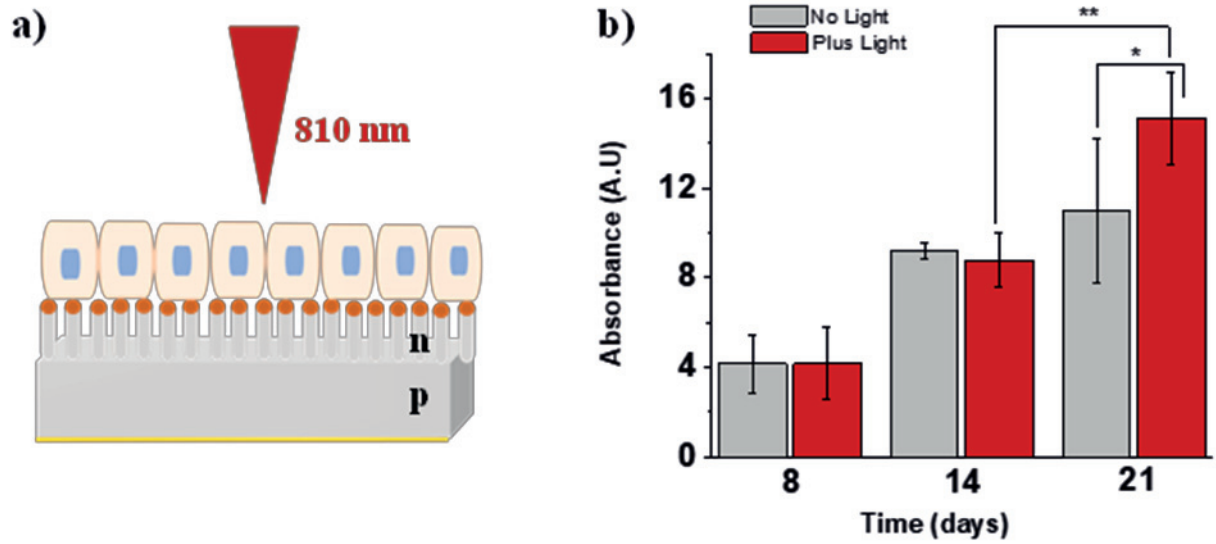


Figure 10 Saos-2 cells response to opto-electrical stimulation in terms of proliferation. a) Schematic representation of the setup used for the stimulation of Saos-2 cells seeded on the top of the Si/Au NW using 810 nm light source under the following conditions: light intensity 4.50 μW/mm^2, 50 Hz frequency, on/off cycles of 10 ms over 21 days for one hour daily. b) A graph representing the percentage of cell proliferation with and without light. Asterisks indicate significant difference ($p<0,05$) between both conditions at the same time point and at the same condition over time.

c. Effect of Opto-Electrical Stimulation on Osteoblast Differentiation

After analyzing intracellular calcium flow in response to opto-electric signals mediated by the Si/Au NWs and its impact on long-term cellular proliferation, further analysis of differentiation markers was conducted.

Osteoblasts, derived from mesenchymal stem cells, are responsible of ECM synthesis in a process called osteogenesis[39]. They undergo differentiation over three stages. The first stage is proliferation where cells continue to proliferate, accompanied with secretion of collagen I, fibronectin and osteopontin. During the second stage, termed as ECM maturation, more collagen I is secreted, and high activity of ALP is detected. After synthesizing and maturing the

ECM, osteocalcin is expressed, and calcium phosphate is deposited into the matrix to achieve its mineralization as the third stage of differentiation[39]. Then, the deposited calcium phosphates undergo maturation into hydroxyapatite which provides strength to the bone[38]. At this point, osteoblasts appear with a cuboidal shape[39].

Osteogenesis can be triggered under ES. It has been proved that stimulation exerts an impact on proliferation, migration, differentiation, ECM maturation and mineralization. More specifically, ES can enhance bone regeneration and healing. Although ES has succeeded in promoting bone healing clinically, still the mechanism is poorly understood. However, some studies refer it to the effect of ES on cellular behavior mentioned above[151]. Research studies have shown that ES can enhance differentiation markers as collagen I, calcium deposition and ALP activity[152–154].

To assess the impact of the pn Si/Au NWs device on osteoblasts differentiation, different markers were studied, including ALP activity, calcium deposit and collagen I production. For the three assays, Saos-2 cells were cultured on top of the Au/Si NWs for 21 days, exposed to stimulation (810 nm, 4.5 $\mu W/mm^2$, 50 Hz, 10 ms on/off cycles) for one hour daily. ***Figure 11*** shows the results of ALP activity, Alizarin Red Staining (ARS) for calcium deposits, and collagen I detection with and without light stimulation. First, ALP activity was analyzed, (***Figure 11b*****)** and compared to glass. ALP activity was significantly increased in cells cultured on NW with or without light stimulation, with a higher activity under stimulation. No significant change was recorded on day 8 (results not shown). In a recent study, mesenchymal stem cells cultured on Si NW were opto-electronically stimulated using NIR light (808 nm) at a high light intensity of 200 mW/cm^2. High ALP activity was detected in both stimulated and non-stimulated samples, with a significant increase in the stimulated sample at day 7[45]. Compared to our study where a much lower light intensity was used at 810 nm, ALP activity showed only a significant increase at day 21 of stimulation. As cells required two days to adhere and attach properly, this delay may have influenced the cellular behavior induced by stimulation. In addition, other studies have concluded that ALP activity can be influenced by the substrate characteristics, such as its nature, roughness, and topology[152]. These findings encourage us to perform long-term assays, extending beyond 21 days, to understand more the cell behavior and detect any possible improvements caused by the stimulation.

Next, considering that collagen I constitutes the basics of the bone matrix, its level was assessed on day 21 by immunofluorescence detection for the stimulated and unstimulated samples. ***Figure 11e-f*** show the presence of collagen I in cells without and with stimulation, respectively. Both samples show a similar level of collagen I. This is likely because the synthesis of collagen I starts to decrease after 14 days of culture.

Lastly, extracellular calcium deposit was analyzed using ARS. Alizarin red binds to the calcium deposits present in the matrix of differentiating osteoblast cells. This complex exhibits a prominent red color. At day 21 a noticeable increase in the formation of this red complex was observed in the stimulated sample compared to the unstimulated one (***Figure 11c-d***). This suggests that light stimulation enhanced the deposition of calcium into the matrix, an event that occurs in the last stage of osteoblasts differentiation. ECM mineralization provides evidence

of the efficiency of stimulation to induce the differentiation of osteoblasts. The qualitative analysis of calcium deposits through the alizarin technique revealed an increase in the red complex, indicating the effects of opto-electrical stimulation with our device. In a similar study where Si nanopillars were optically stimulated with 808 nm wavelength, an increase in the calcium deposits was observed at day 14 in response to stimulation, using a much higher intensity (200 mW/mm^2)[45] than in our study (4.5 µW/mm^2).

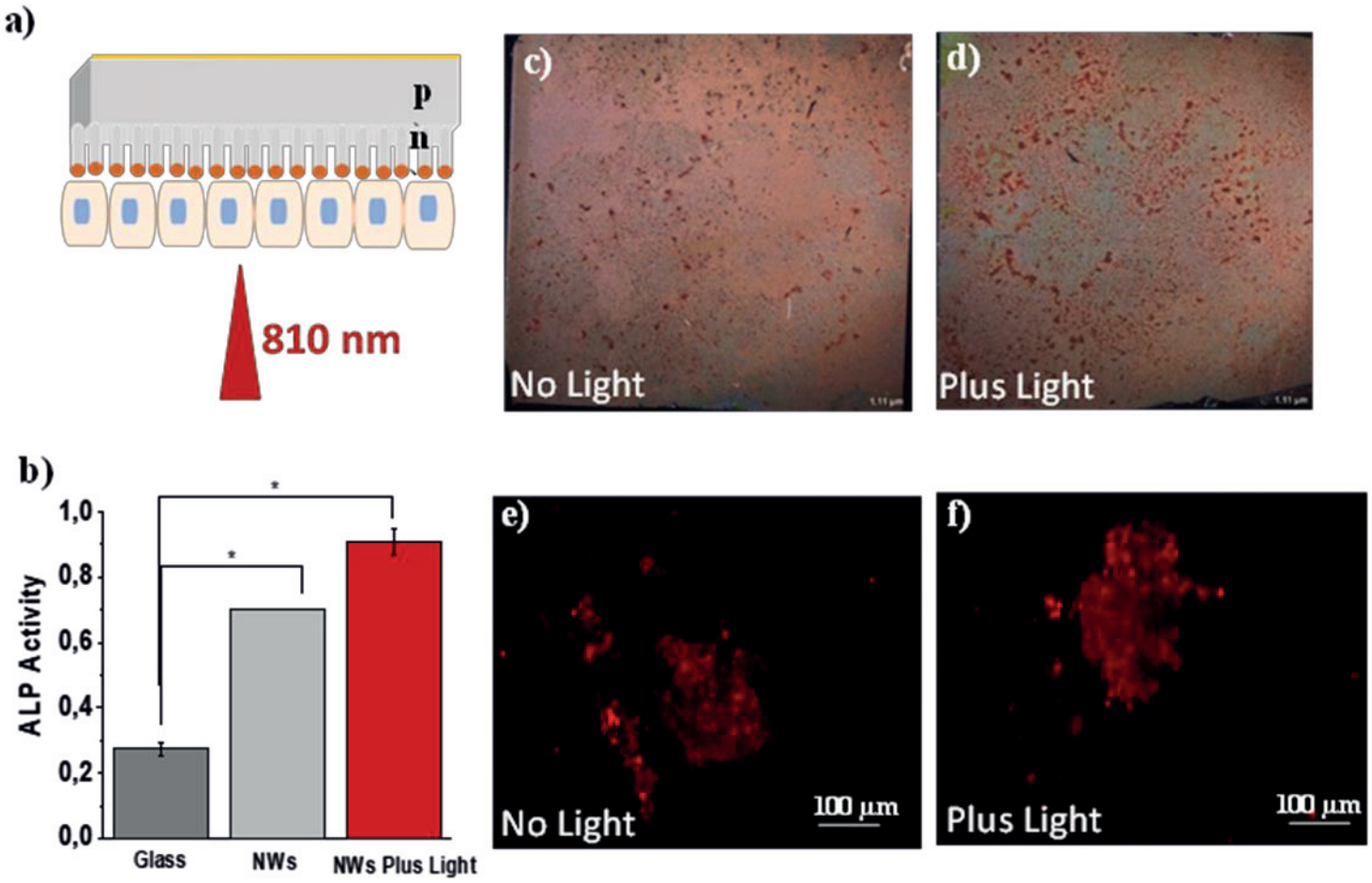


Figure 11 Osteogenic differentiation of Saos-2 cells upon opto-electric stimulation at 4.5 µW/mm^2, 50 Hz, for 1 h per day with 10 ms on/off cycles over the 21 days. a) Schematic representation of sample stimulation. b) Quantitative analysis of ALP activity on glass and Si/Au NW with and without light stimulation. Asterisks indicate significant difference ($p<0,05$). Alizarin Red staining on day 21 without (c) and with (d) light stimulation respectively. Qualitative analysis of Collagen I after 21 days without (e) and with (f) stimulation respectively.

Based on the obtained results, Si/Au NWs device showed a high efficiency in triggering a calcium flow in response to opto-electrical stimulation at very low light intensities (even at 1 µW/mm^2). Illumination with 4.5 µW/mm^2 also significantly enhanced the cell proliferation after 3 weeks of cell culture. In terms of differentiation markers, although a clear increase in ALP levels and calcium deposits were observed, studies at longer term (more than 21 days) should be conducted to measure any possible further influence of the stimulation. By contrast,

assessment of collagen I could be done at an earlier stage to detect differences during the maximum of its synthesis that occurs around day 14. Moreover, stimulation with the cells on the flat Au layer in the sample of Si/Au NW with reverse polarity could provide helpful information to determine the effect of the surface nanostructure in the proliferation and differentiation processes.

2.2.6 Towards Injectable Si/Au NW for Cell Electrostimulation

Although we have seen in the previous sections that the short Si/Au NW with the pn junction configuration can provide an efficient opto-electric stimulation of osteoblast under very low light intensities, the rigidity of the silicon chips can hamper their integration as implants in vivo, requiring invasive surgery for the implantation and inducing a complex grafting due to the very different mechanical properties with respect to the physiological tissues. Therefore, the development of injectable or soft implantable opto-electric nanostructures could significantly minimize the invasiveness of the devices and the integration into the tissues. Long Si/Au NW with a pn junction can be easily released from the Si substrate by ultrasonication, and the optical simulations showed their capacity to enhance the light absorption due to the generation of hybrid plasmonic-dielectric resonances, thereby being ideal candidates for injectable opto-electric nanodevices. However, we have shown in the previous sections that the generated PVs of long Si/Au NW with 200 nm of diameter drastically dropped when the pn junction was exposed to the electrolyte, due to the short-cut of the junction. To minimize this problem, we tried to protect the NW with a lateral oxide layer (***Figure 12***) for passivating the lateral silicon surface and protecting the pn junction. To achieve this passivation, the Si/Au NW were first covered by a SiO_2 layer of ca. 20 nm, by plasma-enhanced chemical vapor deposition. Next, the top SiO_2 layer was removed by RIE, thereby yielding the NW covered with SiO_2 only at the lateral surface. The 200 nm diameter and 2 µlong NW could be directly released to water or buffer by sonication.

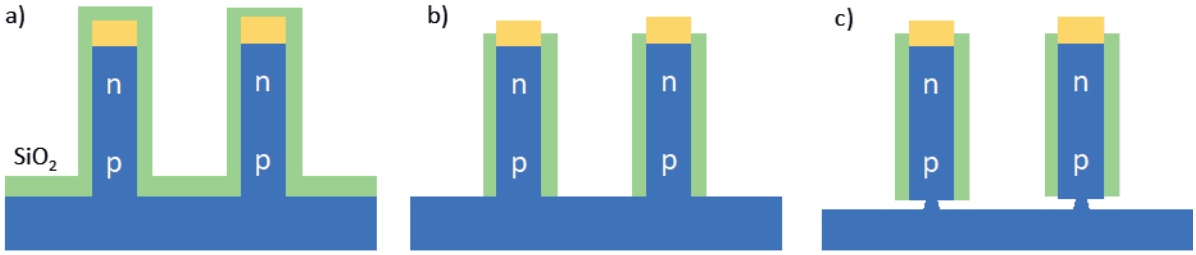


Figure 12 Schematic of the fabrication process to protect the pn junction in long Si/Au NW. a) Conformal deposition of SiO_2 by plasma enhanced chemical vapor deposition (PECVD). b) Reactive Ion Etching leaving the SiO_2 on the lateral walls of the nanowires. c) Isotropic Si etching to etch the base of the nanowires enabling easy mechanical release.

In the case of the 200 nm diameter nanowires with the protective SiO_2 layer, a substantial increase (40%) in the generated PV compared to the unprotected nanowires was observed by actuation with NIR light in both the first and second biological windows. In contrast, the PC did not exhibit an increase due to the protection, and even slightly decreased under illumination

with 1050 nm light. Therefore, in addition to the shortcut at the pn junction, the charge trapping at the interface generated by the surface defects has a very important impact on the opto-electric response, especially in the case of NW with small diameter (i.e., high surface to volume ratio). The SiO_2 layer grown by PECVD, whose quality is lower than the thermal SiO_2, was therefore not enough to passivate the defects in the lateral surface.

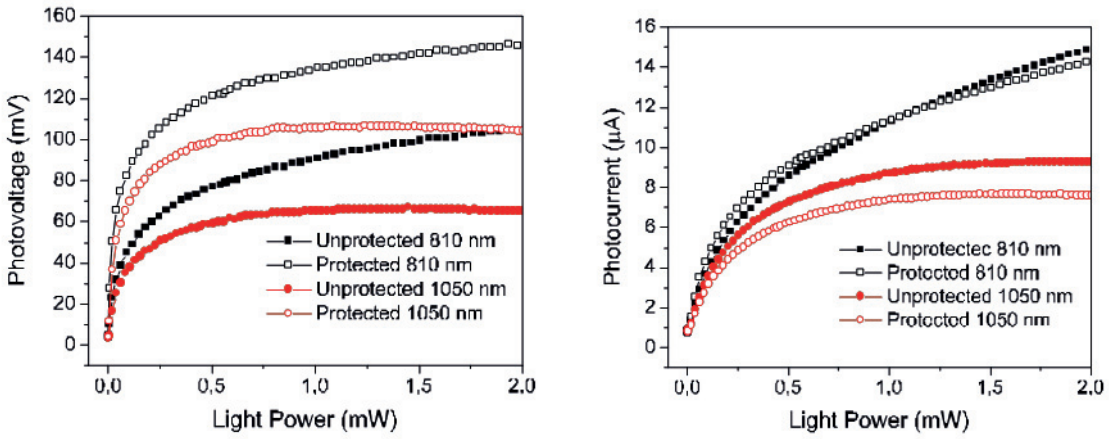


Figure 13 PV and PC of the protected long Si/Au NW compared to the unprotected ones.

To minimize this problem associated to the large surface-to-volume ratio of the NW, we decided to explore the protection of NW with larger diameter (500 nm). We followed a similar fabrication process. However, due to the difficulty to release the 500 nm diameter NW by sonication (***Figure 14***), a final RIE step was included to isotropically etch the base of the NW. After this etching step, the thick NW could be easily detached from the surface by sonication.

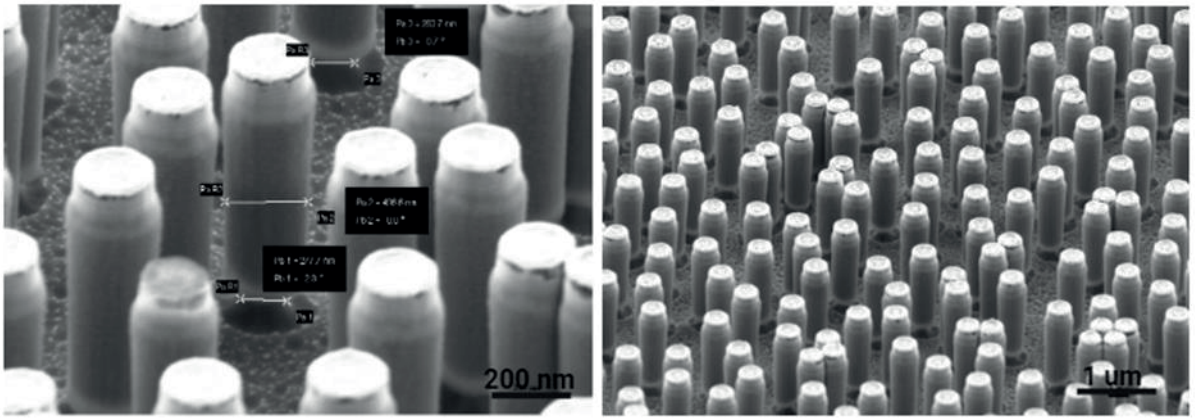


Figure 14 SEM images of 500 nm diameter protected Si/Au NW with isotropically etched base to enable easy mechanical detachment.

Preliminary results of the characterization of the 500 nm diameter Si/Au NW with SiO_2 protection showed photovoltages approaching 250 mV for a light power of 2 mW. Although the PV was still lower than that of the short Si/Au NW, it could be enough for the stimulation of the bone cells.

On the other hand, to show the capacity to integrate the long NW into soft flexible and transparent substrates, the long Si/Au NW were first released to water by sonication and then electrostatically self-assembled on Si or glass substrates previously coated with positive PDDA polyelectrolyte (***Figure 15a-b***). Then liquid PDMS was poured of the matrix of self-assembled NW and cured by temperature (80ºC for 45 min) in a hot plate. Once the PDMS was cured, the soft elastomer layer with the embedded NW was released (***Figure 15c***). As some of the NW were almost fully embedded in the elastomer, and additional SF_6 RIE step was carried out to remove the first nanometers of the PDMS film and to expose the NW to the electrolyte (***Figure 15d***).

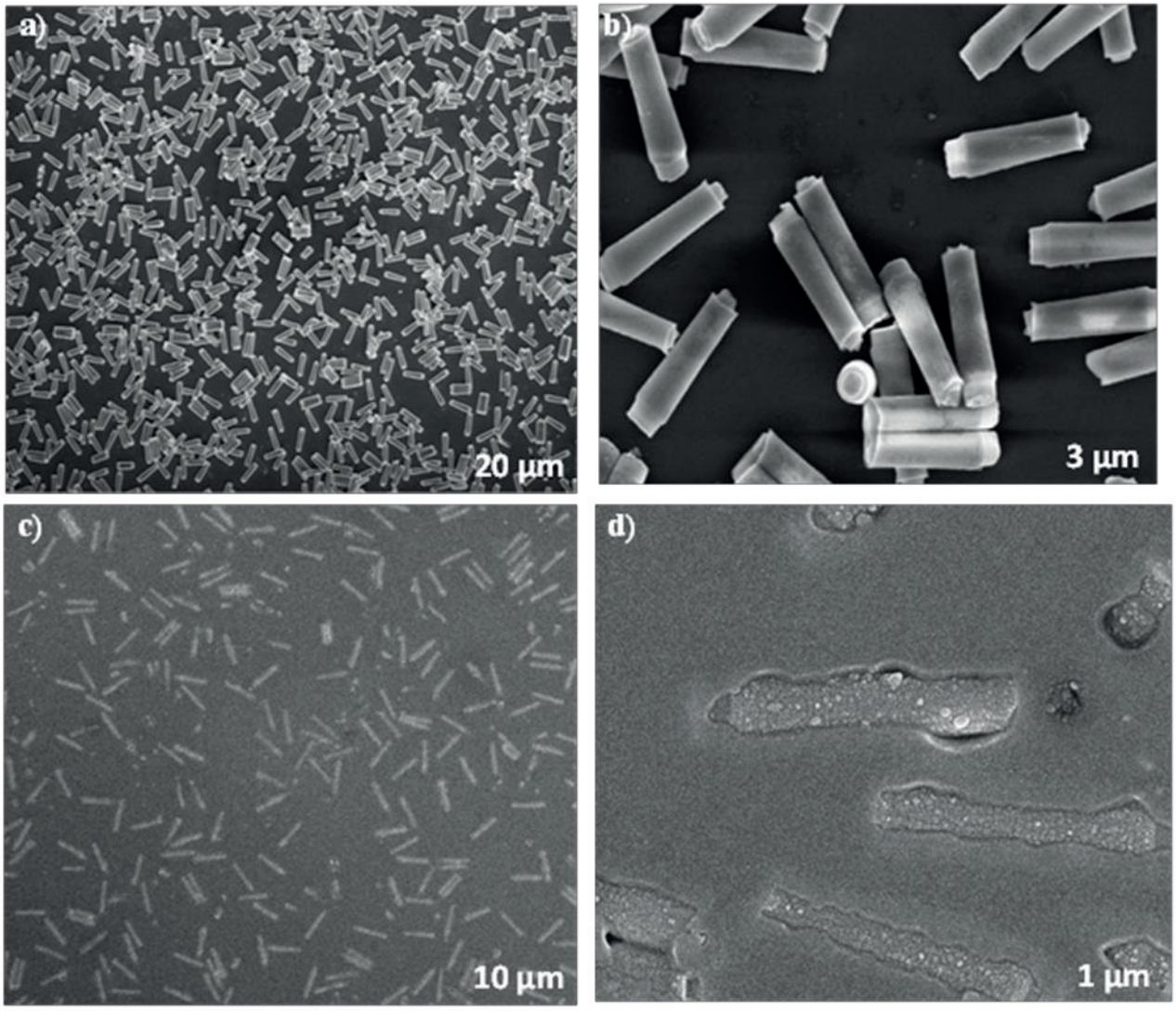


Figure 15 SEM images of the self-assembled nanowires on the Si substrate (a) and (b) and embedded on PDMS films (c) and (d).

Therefore, the thicker (500 nm) and long Si/Au NWs are a promising technology for both injectable and soft implantable opto-electric stimulators, which can be produced in large scale by combining standard microelectronics processes with colloidal nanolithography at the wafer scale.

2.2.7 Conclusion

In conclusion, this study presents the development and analysis of nanostructured Si/Au opto-electronic device for efficient cell electro-stimulation under low intensity NIR light. The Si/Au opto-electronic devices, fabricated through an easy and scalable lithography technique, have been designed to enhance their overall performance through various key features. The inclusion of silicon nano-structuration and gold nanostructures plays a relevant role in improving NIR light absorption, facilitating enhanced light capture, and benefiting from local electromagnetic field enhancement, due to the hybrid plasmonic-dielectric resonances of the gold/silicon nanostructures. The in-built silicon pn junction contributes to more efficient separation of generated photocarriers, ensuring optimized opto-electronic response. Additionally, the gold capping further enhances the device's capabilities, facilitating more efficient charge injection into the solution.

Different lengths of NW enable the development of two systems: the first involves the short NW and their utilization on supported flat Si wafers, and the second includes the long NW that can offer various applications, given their ability to be easily released from their rigid support and dispersed in aqueous solutions.

The short Si/Au NW device has shown very good opto-electrical performance, generating relatively high PV and PC in response to NIR illumination in the first biological window (810 nm wavelength). These outcomes, particularly the elevated PCs, underscore the device's features encompassing both capacitive and faradaic characteristics, significantly enhancing its efficacy as a model for cell stimulation. Analysis was also done in the second biological window of NIR (1050 nm), producing PV and PC that are lower than those obtained at 810 nm due to the decrease in silicon absorbance at higher wavelengths, but they are higher compared to the flat Si wafer and could be further exploited in future experiments.

To achieve the main purpose of this study, it was necessary to confirm the biocompatibility of the device as well as the safety of the NIR light. Si/Au NW exhibited a suitable surface for cells attachment and proliferation. Response of osteoblast cells to electrical signals under NIR illumination of the NW was also investigated. Under stimulation, cells showed an enhanced proliferation over 21 days compared to dark conditions. Moreover, opto-electric actuation stimulated voltage-gated Ca^{2+} channels, thereby triggering the influx of Ca^{2+} ions at very low light intensities, as low as 1 $\mu W/mm^2$. It is noteworthy that opto-electronic stimulation with such low light intensity has not been reported with other devices before. Furthermore, differentiation studies showed an increase in ALP in cells cultured on Si/Au NWs as compared to glass, in addition to an enhancement in the formation of calcium deposits when NWs were stimulated.

The potential of the short Si/Au NW to promote Ca^{2+} influx that activates signaling pathways, and to enhance some differentiation features at an ultralow light intensity, make them promising for further investigation and stepping forward in the field of wireless cells stimulation.

On the other hand, promising outcomes with long Si/Au NWs have also been outlined. Although a substantial drop in the opto-electronic response has been observed with these NWs due to the exposure of the pn junctions to the electrolyte, a strategy to protect the pn junction has been developed, showing a notable increase in PV, yet the charge trapping at the interface remained a challenging factor to improve, especially in the PC response of NW with small diameters (200 nm), while wider NWs (500 nm diameter) showed better outcomes.

Long NWs show promise as devices due to their easy release from rigid supports and dispersion in liquids, expanding their potential applications. A fabrication strategy has been developed for their effective dispersion in liquid, successful self-assembly on silicon wafer and easy transfer into soft elastic elastomer films. This offers the choice of developing soft implantable devices, as well as their direct injection in tissues as single entities. These options comprise more practical strategies that minimize the invasiveness of devices.

2.3 Materials and Methods

2.3.1 Fabrication and Characterization of Au/Si NWs

The fabrication process of Si/Au NWs is illustrated in ***Figure 3.*** We used an Ion Implanter IBS IMC 210RD to introduce phosphorous dopants into 4-inch p-doped silicon wafer (resistivity 1-10 Ohm.cm), with a dose of 4x 10^{15} ions/cm^2 and energy of 50 keV. For the assay of calcium detection, an opposite configuration was used. In this case, n-doped silicon wafer was used and implanted with boron species. Next, 75 nm of gold was deposited on both sides of the wafer by physical vapor deposition (AJA International Inc.). For the electrostatic self-assembly, the introduction of negative charges is needed to activate the gold surface. That was done by treating the wafer with O_2 RIE (pressure 80 mTorr, HF (radio frequency power) 100 W and flow of O_2 of 30 sccm) for 2 min. Then, a 0.1% solution of positively charged amidine latex beads (Thermo Fischer Scientific, 4% w/v, 200 nm in size) was applied on the wafer surface for 5 min. Then the wafer was cleaned by rinsing it in milli Q water to remove extra NPs and dried with a gently blow of N_2 gas. To produce Au discs, argon gas RIE with the following conditions: HF 40W, Inductively Coupled Plasma power (ICP) 1000W, pressure 8 mTorr and argon flow of 20 sccm was run. At this level, latex beads served as masks to make Au ND. Finally, to fabricate the short NW, RIE was done at a pressure of 12 mTorr, HF power 30 Watt and ICP power of 1200 Watt for 55 s with alternating cycles of C_4F_8 and SF_6 at 15 and 10 sccm flow rates, respectively. Long Si/Au NWs were obtained by applying DRIE via Bosch process, which was done at HF power of 30 W, ICP power of 500 W for 6 min. Repeated cycles of isotropic etching with SF_6 and passivation layer creation using C_4F_8 at 150 and 100 sccm flow rates were applied respectively. The height, width and morphology of the NW were characterized by SEM (FEI Magellan 400L XHRSEM).

2.3.2 Opto-Electric Tests

The PV and PC with pulsed laser illumination were measured through a homemade testing system with LabView programs. Waveform generator (SIGLENT SDG1025) was used for controlling LED signal by modulating it by LabView programs. LED controller (THORLABS, LEDD1B) was used to control the LED current, whereas photodiode amplifier (THORLABS, PDA200C), and data acquisition (NATIONAL INSTRUMENTS, NI USB-6361) were used to acquire the photovoltage and photocurrent measurements.

For PV and PC measurements, a special set-up was prepared using an electrochemical cell as shown in ***Figure 4***. On top of a metal holder, the sample (1.5x1.5 cm^2 size) to be measured was placed. For these measurements, different samples were used: pn flat Si wafer serving as a control, Au ND, short Si/Au NW and long Si/Au NW. The chips were fixed on the metal holder with a Teflon support with a round hole of 1 cm size sealed with an o-ring, to confine the electrolyte solution in just one side of the chips. A solution of 1x PBS was used as electrolyte, which was poured in the hole covering the wafer surface. A platinum wire was placed in the PBS as counter-electrode, whereas the sample was connected as working electrode via the back Au contact of the chips. LEDs of 810 nm and 1050 nm wavelength were used as light sources. A collimated light beam (diameter 6 mm) with the size equal to the size of the hole illuminated the sample. Pulses were applied with frequency at 50 Hz or 0.1 Hz and were controlled by the Labview program.

2.3.3 Osteoblast Cell Culture

Human osteoblast-like cells Saos-2 purchased form ATCC were used as tumoral cell line and maintained in a growth medium consisting of high-glucose Dulbecco´s Modified Eagle´s Medium (DMEM) (Gibco) supplemented with 10% Fetal Bovine Serum (FBS) (Gibco). Cells were maintained at 37 ^{0}C in a 5% CO_2 humidified incubator.

2.3.4 Cell Viability Analysis

Si/Au NW and flat Si wafers of 1.5*1.5 cm^2 were sterilized with UV-light for 3 min and placed in a 35 mm petri dishes. Then, 2.8*10^5 cells were seeded on top. Samples were exposed to NIR light at a wavelength of 810 nm, 450 μW, 50 Hz for 1 h per day with 10 ms on/off cycles. Glass coverslips were used as control.

The cytotoxicity of cells grown on Au/Si NWs and Si flat wafers was analyzed by live/dead viability/cytotoxicity kit for mammalian cells (Invitrogen), according to manufacturer´s instructions. Cell viability assay was performed 48 h after seeding, and after light exposure to check the effect of stimulation on cells.

Images were taken by Olympus inverted microscope equipped with epifluorescence and analyzed by Image J and cell counter plugin.

2.3.5 Cell Attachment Analysis

In parallel, attachment of cells on Au/Si NW and Si flat wafers was analyzed 48 h after seeding, cells were washed gently with 0.1 M cacodylate buffer then fixed with 2.5% of Glutaraldehyde for 15 min at room temperature (RT). Then, dehydration was carried out using a series of ethanol (50%, 70% and 90%, and twice of 100%) for 8 min each. Then, samples were dried with hexamethyldisilane reagent (Electron Microscopy Science) for 15 min at RT. Finally, samples were mounted on stubs, sputtered with a 5 nm layer of Au/Pt and visualized with SEM.

2.3.6 Actin Cytoskeleton Distribution

Cell cytoskeleton analysis of Saos-2 cells attached to the Si/Au NWs was performed by actin filaments staining. $2.8*10^5$ cells were seeded on the nanowires for 48 h, followed by two washes with 1x PBS. Then, cells were fixed by 4% paraformaldehyde (PFA) in PBS for 20 min at RT, followed by two washes with PBS. Next, cells were permeabilized with 1% tween-20 in PBS for 20 min at RT. A mixture of Phalloidin-Atto 488 (Sigma-Aldrich, Merck, Burlington, MA, USA) and Hoechst 33258 (Sigma-Aldrich) was prepared and incubated with the sample for 45 min in darkness. Last, cells were washed with PBS, air-dried and mounted on 35 mm glass-bottom dishes (Ibidi, Germany) using prolong anti-fade mounting solution (Life technologies, CA, USA). Samples were visualized with confocal microscopy (FluoView FV1000, Olympus) and images were taken from different sites of the sample.

2.3.7 Intracellular Calcium detection

At approximately 90% confluence, cells were washed with 2 ml of Hanks balanced salt solution (Gibco) followed by detachment with 1 ml of 1X trypsin/EDTA. In 35 mm petri dishes, two UV-sterilized silicon samples (pn Si flat wafer and Si/Au NWs) were placed with their golden unpolished surface facing upwards and cells seeded at a density of $2.8*10^5$ cells/dish. 48 h later, cells were washed with warm complete media and then stained with Fluo-4 AM (Invitrogen) (λexcitation= 494 nm, λemission= 506 nm) (3 µl in 1500 µl of media without FBS) for 40 min inside the incubator. After incubation time, cells were washed with media and the wafer transferred into a 35 mm glass-bottom petri dish (Ibidi) containing warm DMEM (without FBS and phenol red) with cells assembled at the flat silicon side of the device, which in turn, face the bottom of the glass support of the petri dish and nanowires facing upwards. Then, the petri dish was transferred carefully into the pre-warmed chamber of a Leica SP5 confocal microscope set at 37 ^{0}C for 10 min. Two conditions were tested: control samples referring to cells on the flat Si and Si/Au NWs wafers without light and light-activated samples where the flat Si and Si/Au NWs surfaces were exposed to NIR light in the first biological

window at 810 nm wavelength. In the former control samples videos were recorded for 15 min whereas in the latter ones, videos were recorded for 20 min in total: first 5 min without light followed by 15 min of light. Different light intensities were applied: 11, 4.5, 2 and 1 μW/mm^2. Frequency was set at 50 Hz, except at 4.50 μW/mm^2 in which 50 Hz and 100 mHz were used.

A 488 nm Argon laser was used to visualize the cells. Videos were recorded for 15 or 20 min using the xyt mode of the confocal microscope at a rate of 2 frames per second. Pinhole was set at 2 Airy disk units and image size at 512*512. Analysis was done with Image J (Fiji)12 and Microsoft Office-Excel.

2.3.8 Cell Proliferation Quantification

For cell proliferation, cells were seeded on top of the Si/Au NWs at a density of 7500 cells/well in 24-well plates. Samples were exposed to light stimulation of 4.5 μW/mm^2 for 1 h daily over 21 days. Proliferation was quantified using the alamar blue reagent. On days 8, 14 and 21 of stimulation, cells were incubated with alamar blue for 4 h and 30 min. Alamar blue interacts with living cells, as a result, resazurin is reduced to resorufin producing a violet to pink color. After incubation time, solution is collected, and fluorescence is measured by Spark multimode plate reader.

2.3.9 ALP Quantification

ALP is an enzyme that increases upon differentiation of cells. To detect its activity, Saos-2 cells were seeded on the surface of Si/Au NWs at a density of 7500 cells/well for 48 h. Samples were exposed to light stimulation of 4.5 μW/mm^2 for one hour daily over 8 and 21 days. Si/Au NWs and glass coverslip without light are referred to as control. On day 8 and 21 of light stimulation, cells were washed gently and incubated with 1-Step™ p-nitrophenyl phosphate (PNPP) for 30 min at RT in darkness. Upon the reaction of PNPP and ALP, a yellowish water-soluble product is formed. Absorbance was measured at 405 nm with Spark multimode plate reader. Data was normalized to the number of cells obtained from alamar blue assay performed before ALP.

2.3.10 Calcium Deposit Detection

For the detection of matrix mineralization, Saos-2 cells were seeded on top of Si/Au NWs at a density of 7500 cells/well for 48 h. Samples were exposed to light stimulation at an intensity of 4.5 μW/mm^2 for 1 h daily over 21 days. Cells seeded on Si/Au NWs without light were used as a control. On day 21, cells were washed gently with cold PBS two times before being fixed with 4% PFA in PBS for 30 min at RT. Then, cells were incubated with 2% alizarin red solution

for 45 min at RT in darkness. After incubation time, samples were washed with milli Q water four times to remove extra solution. Images of the red crystals were captured by stereomicroscopy.

2.3.11 Immunodetection of Collagen I

Collagen I is considered as a differentiation marker in early stages. Immunofluorescence detection was performed to visualize the presence of this marker. Saos-2 cells were seeded on the surface of a Si/Au NW at a density of 7500 cell/well in 24-well plate. After 48 h of seeding, NW samples were exposed to light stimulation with the following conditions: 4.5 $\mu W/mm^2$, 50 Hz, 10 ms duration, for 1 h every day over 21 days as shown in ***Figure 11a***. A sample without light is referred to as control. To perform immunostaining, cells were washed with 1X PBS three times gently, then cells are fixed with 4% PFA for 20 min at RT, followed by permeabilization with PBS containing 1% of Tween-20 for 20 min, then blocked with 5% bovine serum albumin (BSA) in PBS for 20 min at RT. Cells were washed and incubated with primary antibody: LB-1197 rabbit monoclonal anti-collagen I (1:200) overnight at 4 ^{0}C. On the following day, cells were rinsed twice in 1% BSA in PBS then incubated with secondary antibody Alexa Fluor 594-conjugated goat anti-rabbit (Thermo Fisher Scientific) at a dilution of 1:400 in PBS for one hour at RT accompanied with Hoechst 33258 (Sigma Aldrich) to stain the nucleus. On a glass slide, samples were set upside down on a drop of prolong anti fade for 24 h. Images from different regions of each sample were taken with fluorescence microscope. Fluorescence was quantified using Image J Fiji.

3 Si/Pt Schottky junction Nanoneedles for Cell Stimulation

The preceding chapter highlighted silicon's attributes, emphasizing its versatility and biocompatibility for opto-electronic devices with an integrated pn junction. However, its utility extends beyond conventional applications involving pn junctions to encompass the innovative use of Schottky junctions, serving as a power source to induce electrical signals. Schottky junctions are cheaper and easier to develop than the pn junction described in the previous chapter, and their use can be also exploited within the second biological window of the NIR light, which possesses higher penetration depth and thus reaches deeper tissues. Therefore, in this chapter we describe the fabrication of a simple Si/Pt nanoneedles array device integrating Schottky junctions, designed to operate under NIR light corresponding to both the first and, more importantly, the second biological window. This nanostructured system aids in balancing absorption and penetration depth. Illumination of this device with NIR in the second biological window resulted in PV generation and increased PC compared to the planar Si/Pt junctions, although both PV and PC were smaller than those observed in the case of the pn junction. Cultured osteoblasts showed good adhesion and growth on the nanoneedles surface, reflecting a good interaction between the nanoneedles and the cells. However, the pulsed light stimulation in the second biological window only induced a small percentage of activated cells compared to the control on the dark. The lower PV and PC obtained using the Schottky junction compared to the pn junction are probably behind the weaker activation of the voltage-gated Ca^{2+} channels.

3.1 Introduction

Silicon is a cornerstone semiconductor material for opto-electronic applications whose narrow bandgap has enabled efficient light absorption in the visible and NIR within the first biological window[71]. However, silicon transparency at wavelengths from 1100 nm and above, makes the development of efficient and responsive opto-electronic devices within the second NIR biological window (1000 – 1350 nm) challenging[155,156]. The interest in this window of NIR stems from its deeper penetration depth into tissues and the substantially higher maximum permissible exposure (MPE) compared to the first window (***Figure 1a-b***). For example, the MPE at 1050 nm is 1.0 W/cm^2, while it drops up to 0.33 W/cm^2 for 810 nm[157]. To solve this problem, silicon Schottky junctions, which are formed at the interface of Si and a metal have been explored. The Si based Schottky junctions have enabled the light detection even with wavelengths substantially longer than the bandgap due to the generation of hot-electrons in nanostructured metal layers or NPs[158–160]. Moreover, the fabrication of these junctions is simple and cost-effective, and they exhibit distinct electrical characteristics. In comparison to pn junctions, Schottky junctions typically feature reduced barrier heights and capacitances, enabling faster switching speeds. Schottky junctions exhibit rapid switching because their operation relies on majority carriers, avoiding the slowdown caused by the storage and recombination of excess minority carriers, as observed in pn junction diodes[57]. All these characteristics make the Schottky junctions highly promising elements for exploitation in

various opto-electronic devices such as photodetectors with diverse applications in data transmission, night vision imaging, biomedical testing, and automotive radar systems, among others[156,161]. Their simplicity and capacity of wireless light activation can also open new paths for the electrical stimulation of cells.

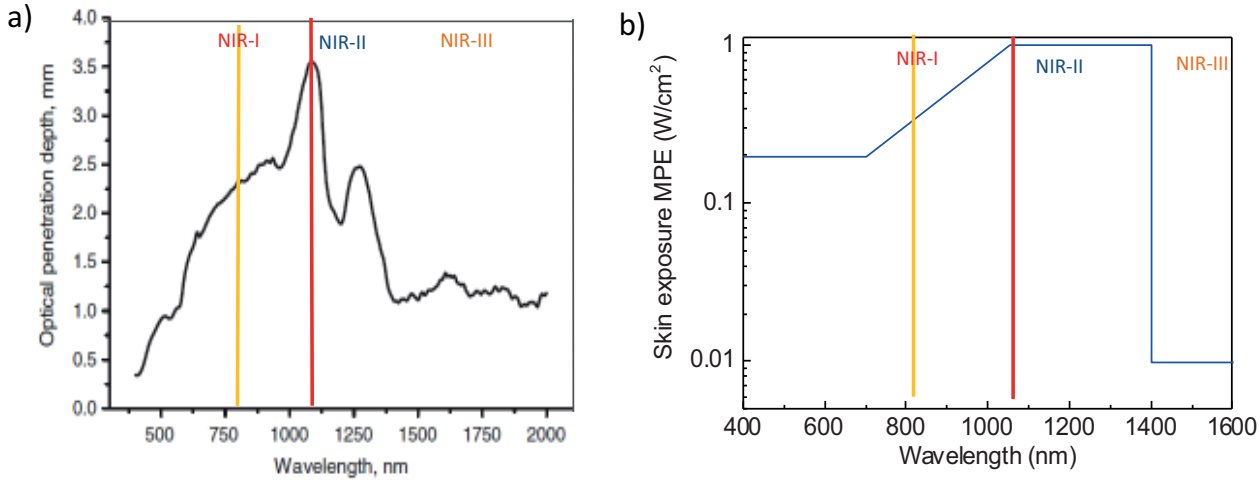


Figure 1 a) Optical penetration depth in the skin as a function of the light wavelength. b) Maximum permissible exposure (MPE) of light in the skin as a function of light wavelength. Adapted from ref 5.

The exploration of Si Schottky junctions within the second biological window could offer a promising platform for biomedical research. This combination of silicon with the corresponding metals producing a Schottky junction at their interface has been described in some studies, demonstrating an enhancement in the response of the device in the NIR. For instance, a photodetector fabricated with asymmetric Schottky junctions (Au/Si/Ag) exhibited high responsivity and proved its efficiency for NIR imaging acting as a photosensor[161]. Another photodetector, designed for high detectivity, was based on silicon with Au NPs and a graphene layer[156]. However, utilization of such devices for the electric stimulation of cells is poorly studied. Hence, in this chapter, the development of an opto-electronic device based on Si/Pt nanoneedles with Schottky junction via a simple and cost-effective process is presented as a potential system for stimulating cells in the second NIR biological window. To optimize the light responsivity[155], three Pt thicknesses were studied: 3, 5 and 10 nm. The high transparency of Si in this wavelength range made it possible to generate PV and PC by light illumination from both sides of the samples, showcasing the adaptability and versatility for diverse assays. From the in vitro results, a good interaction between the Si/Pt nanoneedles and the osteoblasts was observed, presenting them as suitable substrate for further biological studies. However, the stimulation of the cultured cells, detected by the opening of voltage-gated Ca^{2+} channels, was lower than the pn junction case, suggesting the need to optimize several parameters to improve the stimulation.

3.2 Results and Discussion

3.2.1 Fabrication of Si/Pt Schottky junction Nanoneedles

The main goal of this study is to develop cost-effective and efficient Schottky-based wireless opto-electronic stimulation devices working in the second biological window of NIR light to achieve a higher penetration depth and improve therapeutic applications. In the case of silicon, there are two possibilities to generate a Schottky junction: i) p-doped Si with low dopant concentration and a metal with low working function, such as Al, and ii) n-doped Si with low dopant concentration and a metal with high working function, such as Pt. Due to the aim of using it in biological application in a highly corrosive environment, we selected the Si-n/Pt option, which provides higher electrochemical stability than the Si-p/Al case. Moreover, n-type Schottky diodes exhibit higher potential barriers and can develop greater PV than their p-type counterparts.

On the other hand, maximizing light absorption is a crucial step for an effective opto-electronic device. This can be obtained by introducing nanostructures, which will increase the surface area, facilitating light trapping and enhancing the interaction between light and structures. Nano-structuring can also influence the spectral range of absorption for photocarrier generation[53]. In addition, the nanostructures can also improve the interaction of the cells with the substrate. Considering that in the previous case of the short pn-Si/Au NWs the cells only interacted with the cap of the NWs, here we propose arrays of Si/Pt nanoneedles for simultaneously achieving improved light absorption and cells/substrate interactions.

The fabrication methodology, as in the previous chapter, is based on cost-effective colloidal nanolithography, encompassing the following steps. Firstly, on top of the n-doped Si wafer (resistivity 1 Ohm·cm), arrays of positively charged polystyrene NPs of 500 nm diameter were self-assembled through electrostatic interaction and served as masks for defining the nanoneedles. Then the sample was subjected to isotropic Si etching via SF_6 gas, followed by the particle removal with an adhesive tape. This process resulted in Si nanoneedles, as shown in ***Figure 2***, with a height of ca. 300 nm. To remove potential leftovers of fluorine compounds, the nanostructured surface was treated with oxygen plasma. Finally, the samples were immersed in HF to remove the native SiO_2 layer right before Pt film deposition by e-beam evaporation, for ensuring a proper contact between Si and Pt to form the Schottky barrier.

Different thicknesses of platinum (3, 5, and 10 nm) were deposited on the Si nanoneedles to optimize the opto-electric response. This simple, fast, and low-cost method establishes an alternative to the pn junction, offering an easier and faster process that eliminates the need for three costly steps: implantation of p or n layer, annealing step, and removal of oxides.

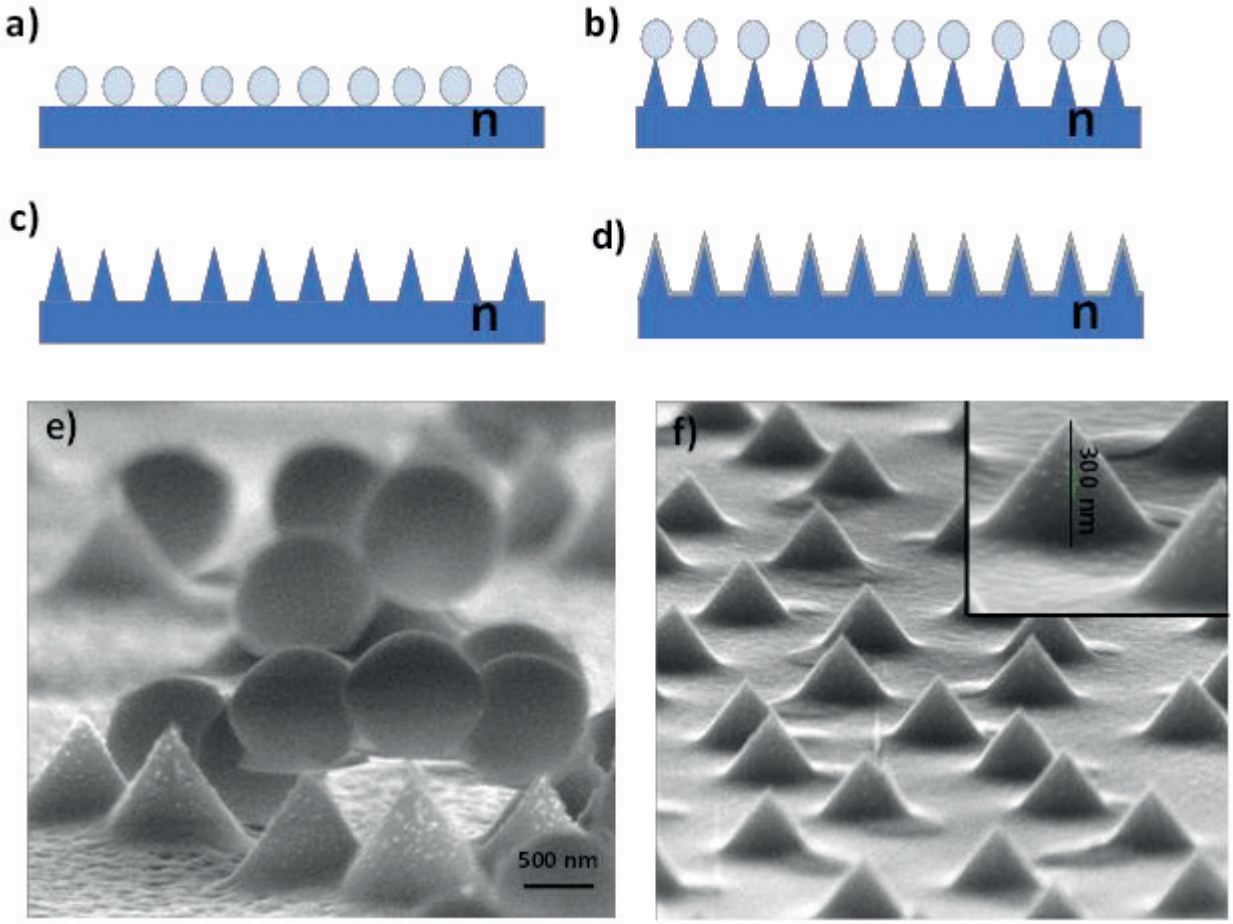


Figure 2 Schematic illustrations of Si/Pt nanoneedles fabrication processes. a) Electrostatic self-assembly of 0,2% amidine latex beads of size 500 nm on a Si wafer of n-type. b) Nanoneedles structures formed as a result of Si isotropic RIE etching using SF_6 gas with latex beads as mask. c) Nanoneedles structure after removal of the beads using adhesive tape. d) Nanoneedles covered with a thin platinum layer. e) SEM image of the nanoneedles capped with the beads. f) SEM image of the nanoneedles after beads removal.

3.2.2 Opto-Electric Analysis

In the proposed device, the combination of silicon and platinum is expected to create a Schottky junction at the interface, which produces photogenerated electrical responses upon NIR illumination. To prove the effect of the Schottky junction and the surface nano-structuration, we first compared the opto-electric response of a flat n-doped Si wafer (Si-flat), a flat n-Si with 5 nm of Pt (SiPt-flat) and the nanoneedles covered with 5 nm of Pt (SiPt-nanoneedles) with light incident on the Pt film side. As ***Figure 3*** shows, the PVs generated by the SiPt-nanoneedles Schottky junctions were much higher (ca. 2.5-fold) than that in the Si-flat, in both the first (810 nm) and second (1050 nm) biological windows. In addition, the SiPt-nanoneedles enabled the generation of a remarkable 2.5-fold higher PC than the SiPt-flat sample. Therefore, the Schottky junction and the nanoneedles provided a large enhancement of the opto-electric response. Overall, the PV and PC were slightly lower in the second biological window, as expected from the lower energy of the photons and their proximity to the bandgap energy.

Compared to the pn junction, the obtained PVs were ca. 40% smaller than in the Schottky junctions and the PCs were ca. 3-fold smaller. Nevertheless, the PV can reach values in the 200-250 mV range, which could be sufficient for cell electrical stimulation.

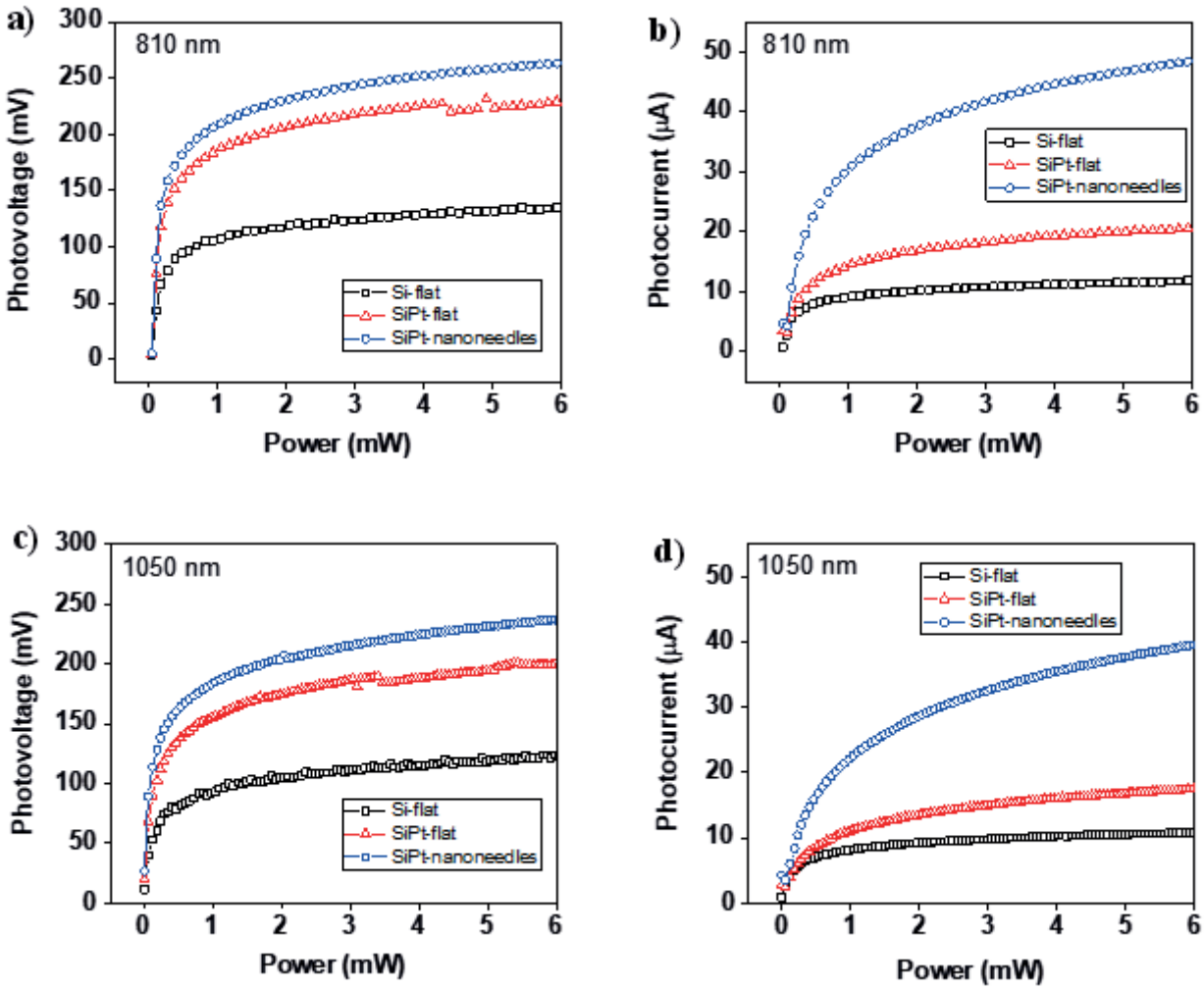


Figure 3 Comparison of the PV and PC for the Si-flat, the SiPt-flat and the SiPt-nanoneedles when samples were illuminated from the Pt side, using light in the first and second biological windows.

Considering the high transparency of Si for light in the second biological window, to analyze the opto-electric response we used two configurations with illumination (810 nm and 1050 nm) on the Pt side in contact to the electrolyte (PBS 1X) and illumination from the Si side (***Figure 4).***

To optimize the opto-electric response of the Schottky junction, we next studied the impact of the metal thickness on the performance of the Schottky junction under exposure to NIR light at 810 nm from the top side and under different light intensities. The metal thicknesses used were: 3 nm, 5 nm, and 10 nm. Results showed that the highest PV was obtained with the 5 nm

thickness (***Figure 5a***), while the highest PC was obtained with the 10 nm thickness (***Figure 5b***) with a slight difference with respect to the 5 nm sample. Since the difference in PC was not significant different between 5 and 10 nm, and considering the higher PV with 5 nm thickness, as well as the potential improvement in light absorption (less reflection) with decreasing metal thicknesses [155], a Pt thickness of 5 nm was chosen to proceed with the subsequent measurements and biological applications.

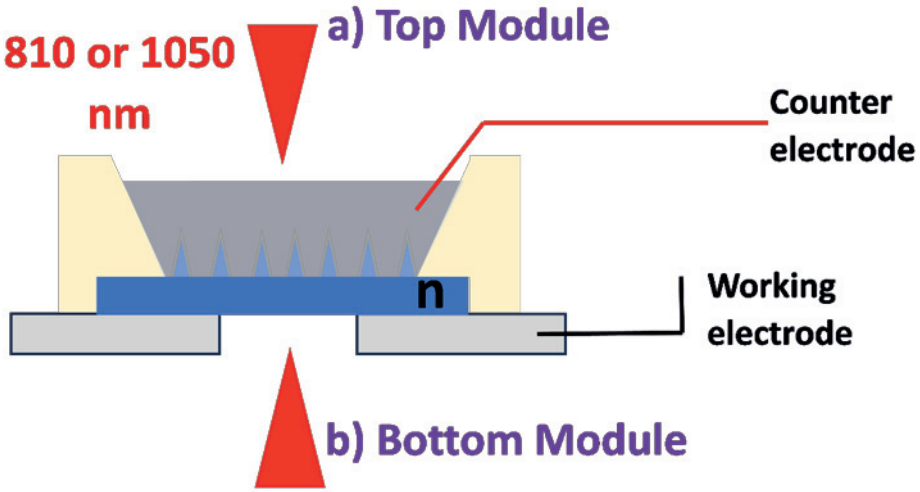


Figure 4 Scheme depicting opto-electric measurements (PV and PC). a) Scheme showing the exposure of the sample to NIR light from top. b) Scheme of NIR exposure from bottom side of the sample.

After optimizing the thickness of Pt, the characterization of the device under NIR illumination with 810 and 1050 nm at the different sides of the sample was assessed. When the light was exposed from the top (i.e., targeting the nanoneedles), a higher PV was generated at 810 nm wavelength compared to 1050 nm (***Figure 5c***). This could be explained by the absorption of silicon which decreases at higher wavelengths. In the case of the second configuration where light was exposed from the bottom (i.e., hitting the bare flat silicon surface), the PV at 810 nm dropped significantly. Conversely, at 1050 nm, the PV generated was almost the same whether the light came from the top or the bottom. The generation of the same PV at 1050 nm from both sides is due to the high transparency of Si in this range, thereby allowing a comparable number of photons reaching the active Si/Pt interface from both sides. Therefore, at this wavelength range, the samples can be illuminated from both sides producing similar opto-electric effects, which is an advantage with respect to the pn junction devices presented in the previous chapter. Moreover, the higher penetration depth and safeness of the NIR in the second biological window also favor its application over the first biological window. Regarding the PC, ***Figure 5d*** displays the PC produced under the same conditions as for PV, and it shows the same pattern as PV in terms of efficiency order. The PC generation displays that the NIR stimulus was able to cause a flow of electrons from the metal to the semiconductor side overcoming the Schottky barrier[62].

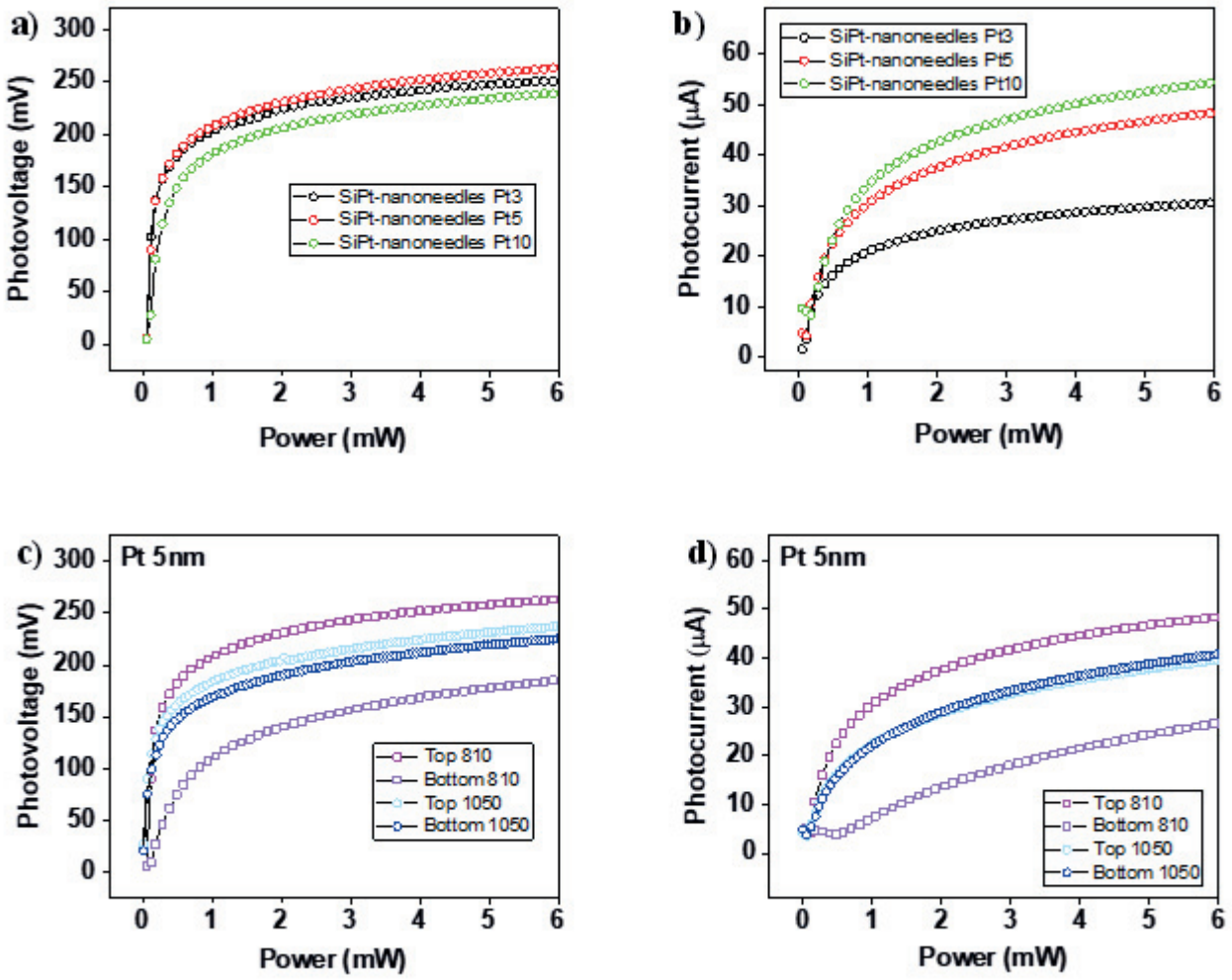


Figure 5 Opto-electric analysis of nanoneedles structures. a) PV and b) PC measurements of nanoneedles covered with different thicknesses of platinum upon illumination with 810 nm from the top side. c) PV and d) PC obtained by illumination of nanoneedles/Pt 5 nm with 810 nm and 1050 nm NIR light from top and bottom sides of the samples.

Even though the PV and PC produced are not as high as those produced by the Si/Au NWs with pn junctions obtained in the previous chapter, this device still exhibits promising results that can exploited for use in the second biological window of NIR light. As the light absorption in silicon at 1050 nm is low, its high transparency gives flexibility and more options for light illumination and for culturing cells on both sides of the device in the biological applications, in addition to the capacity to stimulate deeper tissues.

3.2.3 Biocompatibility and Interaction of Si/Pt Nanoneedles with Cells

To examine whether the nanoneedles surface presents a suitable substrate for cells to adhere and grow properly, a biocompatible test was performed. It was found that 48 h after seeding, 98% of osteoblast-like Saos-2 cells were alive (green cells) with only 2% of dead ones (red cells) (***Figure 6a***). These results confirm the biocompatibility of the Si/Pt nanoneedles interface, which is also in line with other reported studies[71,149]. In addition, it agrees with the study conducted by *Hansel et al.* which demonstrated the growth of HUVECs[j] and hMSCs on nanoneedles structures[162]. The adhesion of cells was analyzed by the detection of the actin filaments (***Figure 6b***). This image depicts the actin filaments spanning the cytoplasm of the cells in a parallel orientation, reflecting the proper and complete adhesion of cells on the nanoneedle surface.

Moreover, for a deeper analysis of the interaction of Saos-2 cells with the nanoneedle substrate at the level of morphology alterations, SEM images taken 48 h after cell seeding showed that cells were well attached and spread on top of the nanoneedles (***Figure 6c***), presenting a shape similar to the cells grown on bare silicon wafer previously studied by our group[71]. This provides evidence that the nanoneedle shape and the topology of the device forms a good substrate for cells growth. Moreover, the SEM images distinctly exhibited the presence of filopodia, which play a crucial role in cell adhesion processes. The filopodia were extending from the cellular membrane, connecting to the apex of multiple needles, and firmly adhering to them as shown in ***Figure 6d***.

-

[j] HUVECs: Human Umbilical Vein Endothelial Cells

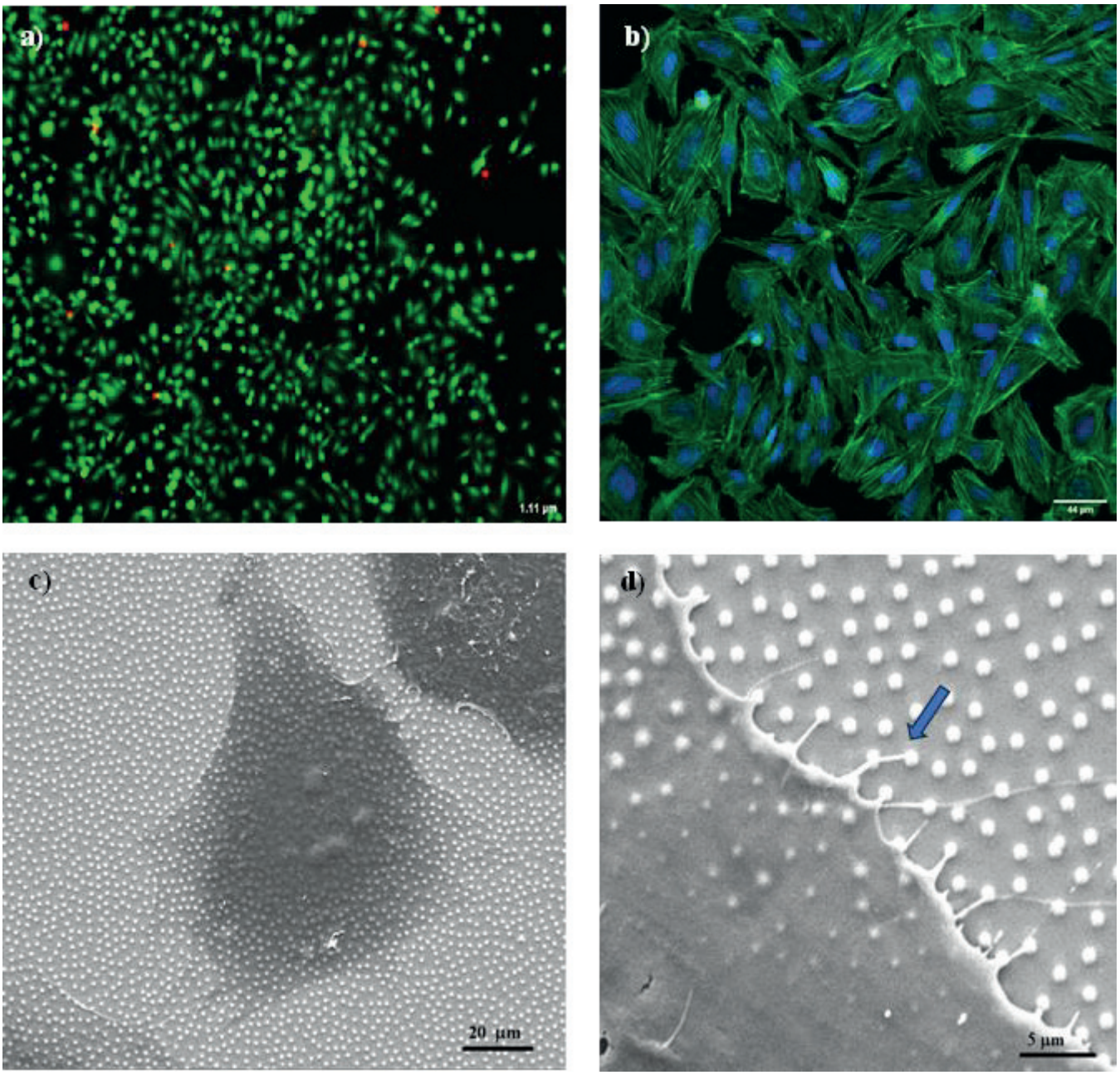


Figure 6 Biocompatibility and cell adhesion of Saos-2 cells 48 h post-seeding on top of the nanoneedles structures. a) Live (green) and dead (red) cells. b) Actin (green) filament distribution in a parallel orientation. Nucleus: blue. c) Scanning Electron Microscopy of cells adhered on the nanoneedles. d) Different filipodia could be observed connecting the cells to the nanoneedles.

3.2.4 Osteoblast -like Cells Response to Stimulation

After confirming the photogeneration of PV and PC with 1050 nm light and the biocompatibility of the Si/Pt nanoneedle device and its good interaction with cells, our focus turned to understanding the cellular response to such opto-electrical stimulation. According to the PV and PC measurements, illuminating the device from the needles surface or from the opposite side of the device, resulted in approximately equal values of the opto-electronic signals due to the high transparency of Si in the second biological window. Therefore, two sample configuration systems can be considered with the aim of stimulating the opening of the voltage gated Ca^{2+}channels and the consequent influx of Ca^{2+} in the cytoplasm. Following the same procedure as in chapter 2, the calcium flow into the cell was examined using the fluorescent calcium indicator Fluo4-AM in a confocal microscope. In the first experiment, Saos-2 cells were seeded on top of the nanoneedles but unfortunately very few cells survived after staining them with the Fluo4-AM. Thus, in the second experiment, cells were seeded on the other side of the device, that is, on the flat side of the wafer and NIR light was illuminating the nanoneedles from top (***Figure 7a***). Upon simulation with 1050 nm at 2.6 mW (spot size 1 cm^2, intensity 26 $\mu W/mm^2$, frequency 50 Hz with 10 ms on/off cycles), only 17% of the cells were activated, compared to 5% in dark conditions (***Figure 7b***). This suggests that at these conditions, the generated PV and PC were probably not high enough to trigger the efficient opening of the voltage gated Ca^{2+}channels and, consequently, the flow of calcium ions may not be sufficient for cell activation. These results are preliminary and there is still ample room to improve the performance of these devices. For instance, higher light intensity could be used to enhance the impact of the stimulation and direct cell culture on the nanoneedles interface.

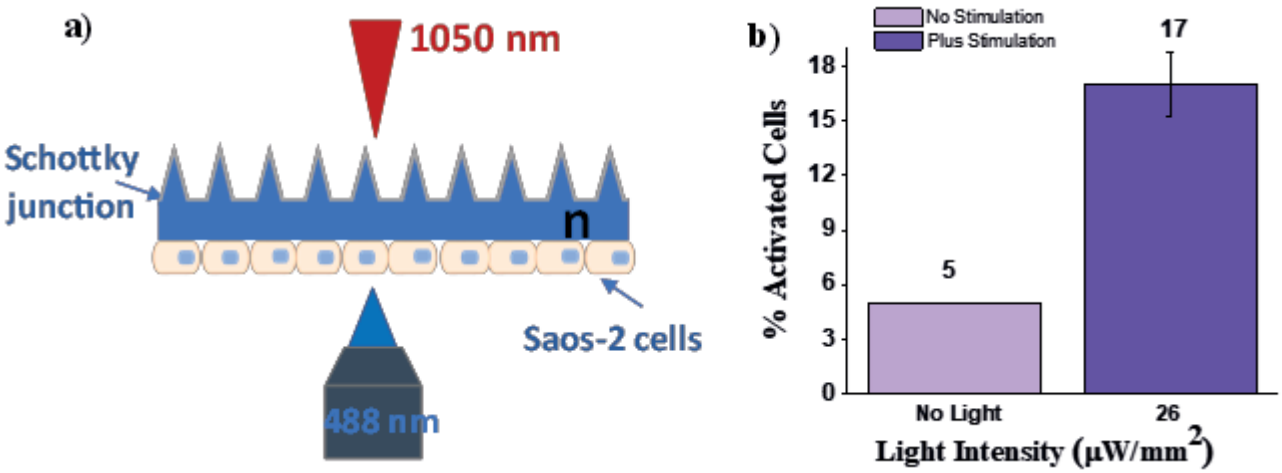


Figure 7 Response of Saos-2 cells to opto-electrical stimulation. a) Schematic representation of sample stimulation. b) Graph reflecting the percentage of activated cells upon exposure to opto-electrical stimulation using NIR light in the second biological window in comparison to the same sample in dark conditions. Stimulation conditions are light intensity of 26 $\mu W/mm^2$, 50 Hz frequency, 10 ms on/off cycles.

3.3 Conclusion

In conclusion, we have developed a cost-effective, easy, and fast strategy for an opto-electric powering system based on the fabrication of nanoneedle arrays integrating Schottky junctions, intended mainly for use in the second biological window of the NIR light stimulation. The Si/Pt nanoneedle device has shown good PV and PC production in the second biological window with the additional versatility to be activated by illumination either from the nanoneedle top side or from the flat bottom part due to the high transparency of silicon in this wavelength range compared to the first biological window. This characteristic is beneficial for biological applications, as it enables higher penetration depth and renders the final orientation of the device not relevant. This device has displayed a good interaction with the cultured cells. Moreover, it showed a 3.4-fold increase in the percentage of stimulated cells compared to dark conditions. These preliminary results are promising and further studies, along with modifications of the assay parameters, such as light intensity, cell culture on the nanoneedles interface, or increase of the density and aspect ratio of the nanostructures to maximize the Si/Pt interfacial interaction, could be performed to exert a more pronounced opto-electric stimulation on the cells.

3.4 Materials and Methods

3.4.1 Fabrication and Characterization of Si/Pt Nanoneedles

To fabricate the nanoneedles, a solution of 0.2% positively charged amidine latex beads (Thermo Fischer Scientific, 4% w/v, 500 nm in size) was dropped on the n-type wafer surface for 5 min. Then the wafer was cleaned by rinsing it in milli Q water to remove extra nanoparticles and blown gently by N_2 gas to be dried. In the next step, silicon was isotropically etched using SF_6 gas at a flow rate of 40 sccm for 4 min and with the following conditions: high frequency power (HF):30W, Pressure: 25 mTorr. The nanopatterned Si was treated by oxygen plasma (500 W, 5 min) to remove any possible fluorine residues. Next, the wafer was treated with buffered fluorhydric acid for 1 min in a concentration of 1:7 (mixing ratio between the hydrofluoric acid and the ammonium fluoride) to remove the native SiO_2 layer and washed with milli Q water for 2 min. Subsequently, platinum of different thicknesses: 3, 5 and 10 nm was deposited on top of the needles using physical vapor deposition (AJA International Inc.). SEM (FEI Magellan 400L XHRSEM) was used to characterize the nanoneedles in terms of size and structure.

3.4.2 Opto-Electric Tests

Same as in chapter 2 of nanowires. Here, the set up was modified to enable light exposure from both sides of the wafer as depicted in ***Figure 4.***

3.4.3 Osteoblast Cell Culture

Human osteoblast-like cells Saos-2 purchased form ATCC were used as tumoral cell line and maintained in a growth medium consisting of high-glucose Dulbecco´s Modified Eagle´s Medium (DMEM) (Gibco) supplemented with 10% Fetal Bovine Serum (FBS) (Gibco). Cells were maintained at 37 ^{0}C in a 5% CO_2 humidified incubator.

3.4.4 Cell Viability Analysis

The cytotoxicity of cells grown on Si/Pt nanoneedles was analyzed by live/dead viability/cytotoxicity kit for mammalian cells (Invitrogen), according to manufacturer´s instructions. A cell viability assay was performed 48 h after seeding. Samples were sterilized with UV-light and 2.8*10^5 Saos-2 cells were seeded on SiPt-nanoneedles in 35 mm petri dishes. 48 hours later, samples were transferred into glass-bottom dishes (Ibidi) with the cells facing the glass part of the petri dish and 3 images from different sites were taken by Olympus inverted microscope equipped with epifluorescence.

3.4.5 Cell Attachment Analysis

Attachment of cells on SiPt-nanoneedles was also analyzed 48 h after seeding. Cells were washed gently with 0.1 M cacodylate buffer then fixed with 2.5% of Glutaraldehyde for 15 min at RT. Then, dehydration was carried with a series of ethanol (50%, 70% and 90%, and twice of 100%) for 8 min each. Then, samples were dried with hexamethyldisilane reagent (Electron Microscopy Science) for 15 min at RT. Finally, samples were mounted on stubs, sputtered with a 5 nm layer of Au/Pt and visualized with SEM, (FEI Magellan 400L XHRSEM).

3.4.6 Actin Cytoskeleton Distribution

Cell cytoskeleton analysis of Saos-2 cells attachment to the Si/Pt nanoneedles was performed by actin filaments staining. A total of 2.8*10^5 cells were seeded on the nanoneedles for 48 h, followed by washing with 1x PBS twice. Then, cells were fixed by 4% PFA in PBS for 20 min at RT, followed by two washes with PBS. Next, cells were permeabilized with 1% tween-20 in PBS for 20 min at RT. A mixture of Phalloidin-Atto 488 (Sigma-Aldrich, Merck, Burlington, MA, USA) and Hoechst 33258 (Sigma-Aldrich) was prepared and incubated with the sample for 45 min in darkness. Then, cells were washed with PBS, air-dried, and mounted on 35 mm glass-bottom dishes (Ibidi, Germany) using prolong anti-fade mounting solution (Life technologies, CA, USA). Samples were visualized with confocal laser scanning microscopy

(CLSM, Confocal Olympus FluoView FV1000) and images were taken from different sites of the sample.

3.4.7 Intracellular Calcium Detection

At approximately 90% confluence, cells were washed with 2 ml of Hanks balanced salt solution (Gibco) followed by detachment with 1 ml of 1X trypsin/EDTA. In 35 mm petri dishes, UV-sterilized Si/Pt nanoneedles samples were placed with their opposite surface facing upwards and cells seeded at a density of $2.8*10^5$ cells/petri. 48 h later, cells were washed with warm complete media and then stained with Fluo-4 AM (Invitrogen) (λexcitation= 494 nm, λemission= 506 nm) (3 µl in 1500 µl of media without FBS) for 40 min inside the incubator. After incubation time, cells were washed with media and the wafer transferred into a 35 mm glass-bottom petri (Ibidi) containing warm DMEM (without FBS and phenol red) with cells facing the bottom of the petri and nanoneedles facing upwards. Then, the petri dish was transferred carefully into the pre-warmed chamber of Leica SP5 at 37 ^{0}C for 10 min. Videos were recorded for 20 min: 10 min without light, and 10 min with light. Surface was exposed to NIR light in the second biological window at 1050 nm wavelength. Light intensity was 26 $\mu W/mm^2$ and frequency was set at 50 Hz. A 488 nm Argon laser was used to visualize the cells. Videos recorded using the xyt mode of CLSM at a rate of 2 frames per second. Pinhole was set at 2 Airy disk units and image size at 512*512. Analysis was done in Image J (Fiji)12 and Microsoft Office-Excel.

4. Silica/MoS_2/Cu_2O Nanoreactors for Photodynamic Therapy with NIR Light in the First Biological Window

The goal of this chapter is to introduce innovative nanoreactors designed to generate lethal ROS for cancer photodynamic therapies with safe and high penetration NIR light. The hybrid nanoreactors combine mesoporous silica nanoparticles (MSN) with 2D layered MoS_2 and Cu_2O to induce localized and lethal ROS in cancer cells under NIR light illumination. The nanoreactors leverage the unique properties of MoS_2, such as low bandgap, efficient visible-NIR conversion, and high photocatalytic activity enhanced by the strategic copper deposition. This chapter details the fabrication process of the nanoreactors, including sol-gel methods and hydrothermal synthesis, the ROS identification, and their in vitro application in biological system. The application of these nanoreactors immobilized on a silicon support at a considerable distance from the cells (ca. 120 μm) has demonstrated a substantial decrease in cancer cell viability under NIR light at low intensity (100 mW/cm^2), i.e., substantially lower than the typical intensities used in photothermal applications. Illumination within the first biological window of NIR (808 nm) induced apoptosis as the main mechanism for cell death. In addition, cell internalization of dispersed nanoreactors in media was analyzed showing very low internalization rates. This highlights the potential need to functionalize the nanoreactors surface to enhance their internalization and improve further their therapeutic efficiency, especially considering that both MSN and MoS_2 can be easily functionalized. However, the demonstrated strong therapeutic effect by ROS generation outside the cells can also be promising advantage, as it minimizes the potential cytotoxicity that cell internalization could involve. The findings of this study position the MoS_2/Cu_2O nanoreactor system as highly promising for diverse ROS biomedical applications.

4.1 Introduction

This chapter focuses on the development of novel multicomponent nanoparticles designed to generate ROS with the objective of becoming promising candidates in the field of cancer photodynamic therapy. ROS exhibit a dual role in cancer, manifesting both pro-tumorigenic and anti-tumorigenic effects. ROS can activate signaling pathways promoting cell proliferation, a key process in tumorigenesis[95]. Elevated ROS levels can lead to DNA damage and genetic mutations, potentially causing cells to acquire cancerous characteristics[95,96]. Additionally, ROS can stimulate angiogenesis, i.e., the formation of new blood vessels crucial for supplying nutrients and supply oxygen to growing tumors. However, increasing the ROS levels over a certain threshold can induce programmed cell death (apoptosis) or irreversible cell cycle arrest, eliminating damaged or cancerous cells[97,99]. Given the dual role of ROS in cancer, the approach described in this chapter aims to induce localized and lethal ROS in cancer cells through apoptosis, while minimizing side effects often associated with conventional therapies.

The ROS-induced nanoreactors were made by combining MSN with 2D layered MoS_2, a transition metal dichalcogenide with significant potential in photocatalysis[112,114]. MSN have served as versatile support structures characterized by their high surface area, large pore volume, and stability, making them applicable in catalysis, biomedicine, energy storage, and environmental remediation[163,164]. The synthesis of mesoporous nanoparticles with tunable properties, such as pore size, particle size, and surface functionalities, has been a focus of extensive research efforts[165,166]. The unique properties of MSN including biocompatibility, low toxicity, and easy surface modification, have made them excellent candidates in biomedical applications for drug delivery, imaging, and diagnostic purposes[167,168]. In this study the high surface area was exploited to enhance the surface area of the MoS_2 and, subsequently, the photocatalytic process. On the other hand, the active element composed of MoS2 imparts distinctive attributes to the nanoreactor. These include a low bandgap for efficient conversion of visible-NIR light, fast and extensive photon absorption owing to their large surface area, adjustability of opto-electronic properties based on the number of stacked layers, exceptional physicochemical properties for forming heterojunctions with other materials to promote charge transfer, high capacity for surface tailoring to leverage edge effects for heightened catalytic efficacy, and an appropriate energy band structure relative to redox potentials for generating ROS[114,115]. These characteristics make these materials versatile and adaptable for use as photocatalysts sensitive to visible/NIR light or as co-catalysts to improve photocatalytic performance.

Specifically, 3D MSN were coated with 2D MoS_2 and interfaced with Cu_2O, created through a meticulous combination of sol-gel methods (silica), hydrothermal synthesis (MoS_2), and e-beam deposition methods (Cu). Serving as a high-surface-area structural support, the MSN transferred their large surface area to the MoS_2 deposits, enhancing their chemical reactivity. The strategic deposition of copper onto MoS_2 formed a heterojunction, improving the photoconversion process by leveraging enhanced light absorption properties and charge separation processes.

Under this context, the primary goal of this study was to demonstrate the effective generation of lethal ROS levels when exposing these multicomponent nanostructures to light, using only water and oxygen from the electrolyte. This chapter provides a comprehensive exploration of this hybrid system, covering the chemical synthesis of the MSN and the fabrication process of the multicomponent nanoreactors. Subsequent sections delve into the evaluation and identification of ROS generation using benchmark ROS quenchers. The synthesis of the nanoreactors and the identification of ROS was conducted in collaboration with Gubakhanim Shahnazarova (Magnetic Nanostructure group at ICN2) and more details about such processes can be found in her thesis[169]. Finally, the application of these nanoreactors to generate ROS in cellular environments was assessed. The photocatalytic activity of MoS_2/Cu_2O nanoreactors was evaluated in vitro on cancer cells, revealing a substantial decrease in cell viability under low intensity of different NIR light actuation wavelengths. This promising outcome sets the MoS_2/Cu_2O nanoreactor system as highly promising nanomaterials for photodynamic biomedical therapies.

4.2 Results and Discussion

4.2.1 Fabrication and Characterization of the Nanoreactors

The fabrication of the nanoreactors consisted of the following steps: 1) fabrication of the mesoporous silica by a sol-gel method, 2) self-assembly of silica NPs on silicon wafers, 3) synthesis of 2D layered MoS_2 onto the silica NPs by hydrothermal processes and 4) deposition of Cu by electron beam deposition. These nanoreactors were either immobilized on a silicon wafer (immobilized nanoreactors) or released from such platform to form a colloidal dispersion (dispersed nanoreactors), although most of the experiments were performed with the immobilized nanoreactors. The size, morphology, and surface properties of the nanoreactors play a crucial role in influencing their interactions with biological systems, impacting cellular internalization, trafficking, biodistribution, and tumor penetration. In the dispersed form, it is crucial to target smaller NPs within the range of 100-250 nm, as they are more readily endocytosed compared to larger NPs. Consequently, synthetic routes were specifically designed to achieve a NP size in the range of 200-250 nm.

4.2.2 Synthesis of Mesoporous Silica Nanoparticles

The synthesis of MSN involves a sol-gel process, encompassing specific steps aimed at creating a controlled porous structure with high surface area using a soft template. The process is based on the hydrolysis using a catalyst (e.g. ammonia) and condensation of a silica alkoxide (e.g. tetraethyl orthosilicate (TEOS))[170,171]. Such reaction takes place on a previously formed micelle template, which provides the mesoporous structure with hexagonal pattern. The micelles are made from a cationic surfactant, cetyltrimethylammonium bromide (CTAB) in ethanol. The reaction temperature, and the precursor concentration play an important role in the particle diameter. The pore size, which is controlled by the micelle template, can be additionally tuned by the introduction of pore-expanding agents[172,173]. After the synthesis, the template is removed by using a solvent extraction method. The process is depicted in ***Figure 1***, along with a schematic representation of the reaction pathway. In this particular case and in order to obtain larger porous size NPs, trimethyl benzene (TMB) was introduced as a pore-expanding agent during the silica synthesis. ***Figure 2a*** shows typical large porous silica NPs with sizes around 230 nm and pore sizes of about 35 nm.

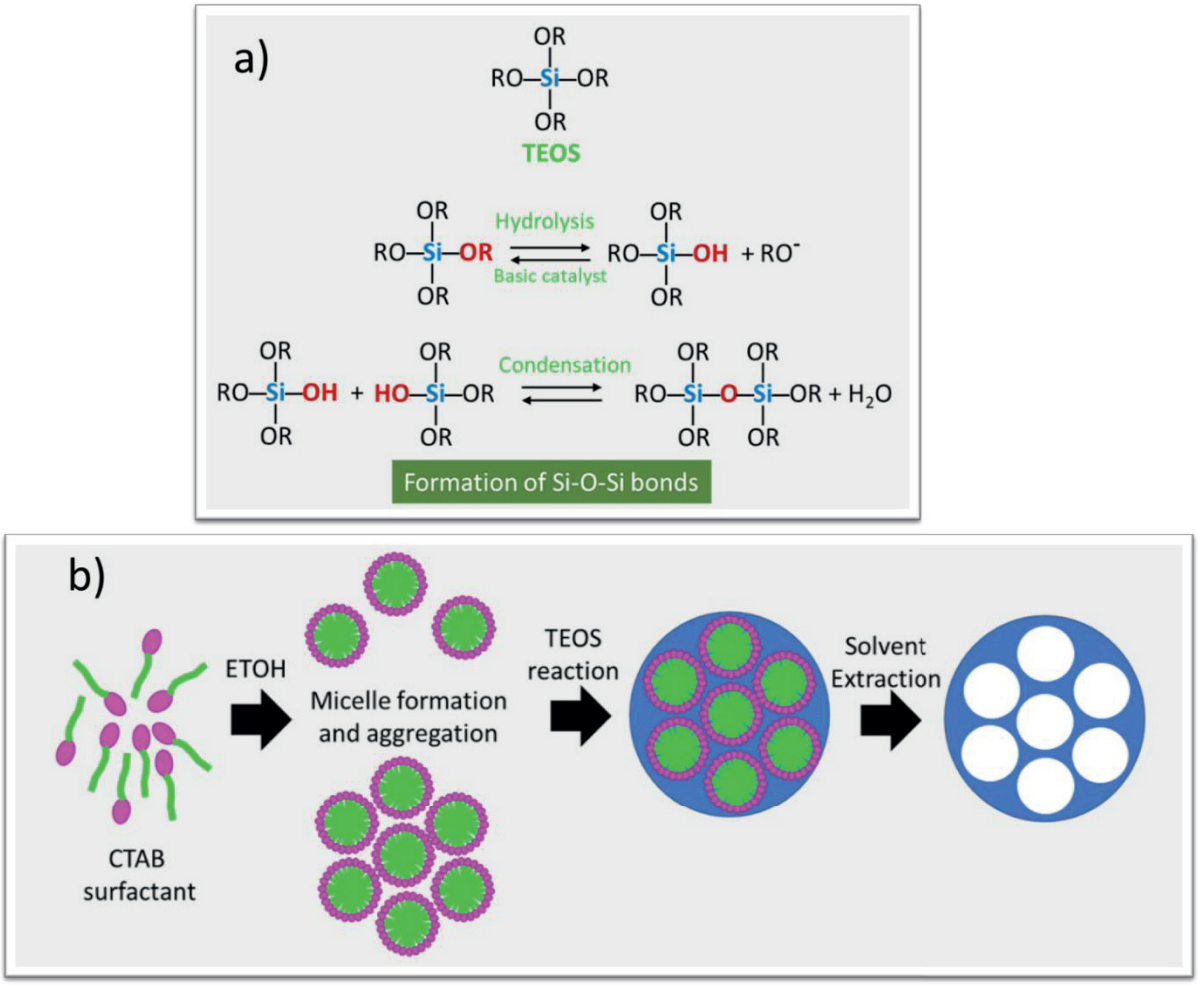


Figure 1 a) Reaction pathway scheme based on a catalyzed hydrolysis of TEOS and condensation. b) Formation of the micelle template in a hexagonal manner and subsequently the TEOS reaction to coat the micelle assembly with silica and then the solvent extraction process to remove the micelles to define the mesoporous silica structure.

4.2.3 Self-assembly of the Silica Nanoparticles

To fabricate nanoreactors, it was necessary to preassemble monolayer arrays of colloidal silica NPs on silicon wafers. To accomplish that the silica NPs were firstly self-assembled at the liquid/air interface and then transferred to the silicon substrate. The self-assembly at the liquid/interface was driven by lateral capillary forces, which were basically triggered by the liquid surface tension. The interplay between the cohesive forces within the liquid and the adhesive forces between the liquid and the nanoparticles lead to the formation of organized structures. Surface tension of water, acting as a key driving force, influences the spreading and organization of nanoparticles, affecting their final arrangement and morphology. This approach allowed the production of large-area, close-packed arrays of nanoparticles on the air/water interface. Then the NPs formed at the liquid interface were transferred onto a silicon wafer immersed in the water by draining the liquid in a controlled way with a pump. ***Figure 2b*** shows a schematic of the particle self-assembly driven by lateral capillary forces at the liquid/air

interface and the process of transfer of such assembly onto silicon by draining out the liquid. ***Figure 2c*** shows the self-assembly of silica NPs on the silicon wafer.

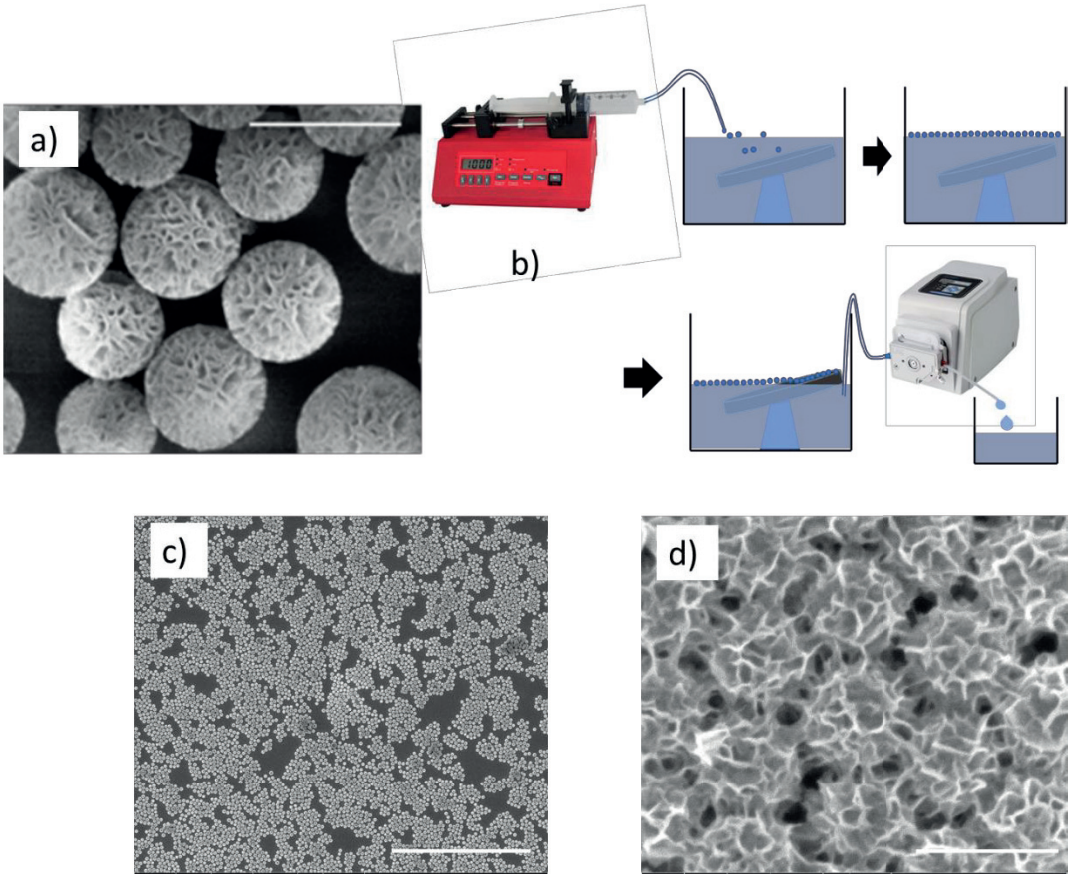


Figure 2 SEM images of large porous silica, scale bar 200 nm (a). Schematics of the colloidal self-assembly on silicon wafers (b) together with a SEM image of the wafer (c), scale bar 10 µm. (d) SEM image of the MSN coated with MoS_2/Cu_2O, scale bar 400 nm.

4.2.4 Modification of Silica Nanoparticles with MoS_2/Cu_2O

Following the self-assembly of the NPs, oxygen plasma cleaning was applied to eliminate any residues from the soft template. To customize the size of the NPs, RIE with CHF_3 gas can also be performed, followed by a rapid oxygen plasma treatment. At this stage, the assembled NPs were prepared for the subsequent MoS_2 modification. The fabrication process of hydrothermal MoS_2/Cu_2O entailed the following steps: 1) silanization of silica NPs to generate positive surface charges, 2) hydrothermal growth of MoS_2, and 3) Cu deposition. As known, MSN are negatively charged. Therefore, a silanization with positively charge silanes was needed to grow the MoS_2 flakes on the silica surface. For this purpose, the substrate was immersed in (3-Aminopropyl) triethoxysilane (APTES). Then the hydrothermal process took place in an autoclave using as precursor tetrathiomolybdate ($(NH_4)_2MoS_4$). After a reaction time of 18 h with a temperature of 180 °C, MoS_2 flakes were grown on the silica NPs. Subsequently 3 nm of copper was deposited onto the MoS_2 nanoreactors via e-beam deposition. ***Figure 2d*** shows

the synthesized nanoreactors, where the MoS_2 flakes formed a high density and uniform 3D network on the MSN.

MoS_2 is a van der Waals layered material, comprising an intercalated Mo atomic plane between two sulfur atomic planes. These 3 atomic planes conform a MoS_2 monolayer. Bulk and multilayered MoS_2 are constructed by vertically stacking monolayer units through van der Waals forces[174]. In turn, MoS_2 can adopt different polymorphic phases with different physical and chemical properties depending on the growth methodology. For instance, it can adopt a trigonal prismatic phase (1 H MoS_2, for a monolayer or 2 H-phase for MoS_2 multilayer), an octahedral phase (1T- MoS_2) or a distorted octahedral phase (1 T′-MoS_2)[174]. An exhaustive characterization analysis of the multicomponent nanoreactors can be found in the thesis of Gubakhanim Shahnazarova[169]. X-ray diffraction, XPS, Raman spectroscopy and UV/visible spectra provided hints to better understand the structure and properties of the hydrothermally grown MoS_2. The characterization techniques revealed that under hydrothermal synthesis, a mixture of phases coexisted, wherein the phase with a very small bandgap dominated the overall performance. That was supported by the absence of strong absorption/photoluminescence peaks, aligning more with a metallic character or small bandgap material. X-ray diffraction indicated poor crystallinity, and Raman spectroscopy revealed the presence of a defective phase alongside a certain proportion of the 2H phase. Further insights from XPS enabled evaluating the oxidation states of the components and assessing the valence band maximum of the material. Two distinct phases were distinguishable: an n-type 2H MoS_2 phase and another more defective phase. The latter phase could be attributed to a defective small gap octahedral phase. A pure metallic phase was ruled out, as the Fermi level did not coincide with the valence band maximum, exhibiting a 0.25 eV difference between them. In summary, these results collectively suggested a hybrid structure of 2H phase with a significant presence of a low bandgap distorted T'-phase, ultimately dominating the overall response of the material.

XPS measurements were also performed on the copper deposited on the MoS_2, concluding the presence of copper in oxidation state of +1, that was in the form Cu_2O.

4.2.5 Evaluation of ROS Generation

Generally, hydroxyl radicals (·OH) and superoxide radicals ($\cdot O_2^-$) are the main ROS that can be produced under light illumination of the nanoreactors. Consequently, ROS quenching experiments were conducted to identify the generated active species[175–177]. ROS quenching experiments typically employ substances or agents capable of neutralizing or quenching the activity of ROS. These experiments were carried out in the presence of molecules known to be degraded by ROS species, for instance an organic pollutant. If the added quencher does not affect the degradation performance of the pollutant, it indicates that the ROS generated is insensitive to the quencher. Conversely, if the quencher hinders the degradation of the pollutant, it implies that the ROS is reacting with the quencher rather than with the pollutant. In this study p-benzoquinone (p-BQ) was used as a quenching agent for $\cdot O_2^-$, isopropyl alcohol (IPA)

as a quenching agent for radical ·OH, and triethanolamine (TEA) as a quenching agent of h+. The experiments were conducted in presence of a typical pollutant benchmark, the antibiotic tetracycline, with 0.39 µg of the photocatalyst. ***Figure 3*** shows that, in absence of the quenchers, 90 % of the antibiotic was degraded at both pHs, 6 and 8. However, the removal efficiency of tetracycline was significantly affected by IPA and p-BQ after 180 min at the different pHs[169]. At pH=8, only 16.3 % and 34.5 % of the antibiotic was degraded in the presence of IPA and p-BQ respectively. At pH=6, in the presence of IPA and p-BQ, the photocatalyst decomposed 23.1 % and 21.2 % of tetracycline, respectively. In contrast, when TEA was added, the removal rate was of 81.5 % and 72.3 % at pH=6 and pH=8, which implies that ·OH and $\cdot O_2^-$ were the main active species for tetracycline removal.

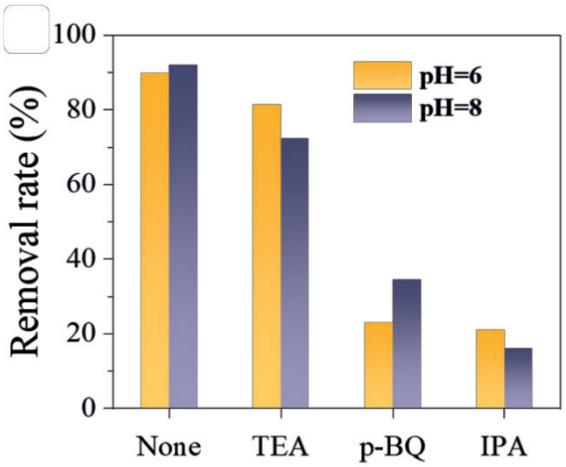


Figure 3 ROS quenching experiments in the presence of tetracycline with the quenchers p-BQ, IPA and TEA. The samples were illuminated with light visible light with 24.2 mW/cm^2. Graph is adapted from the thesis of Gubakhanim Shahnazarova[169].

.

4.2.6 Cell Viability Analysis

Immobilized nanoreactors (size 1 cm^2) were UV-sterilized to avoid any contamination before placing them inside the cell media. Then, they were placed on top of the cells, maintaining a separation of 120 µm between the immobilized nanoreactors and the cells as depicted in ***Figure 4.*** Two different NIR illumination wavelengths were used to trigger the production of ROS by the nanoreactors system: 660 nm LED and 808 nm laser, both with an intensity of 100 mW/cm^2. The effect of the immobilized nanoreactors on the viability of Saos-2 cells was evaluated using a live/dead test 48 h after seeding the cells and reaching confluency of 90%.

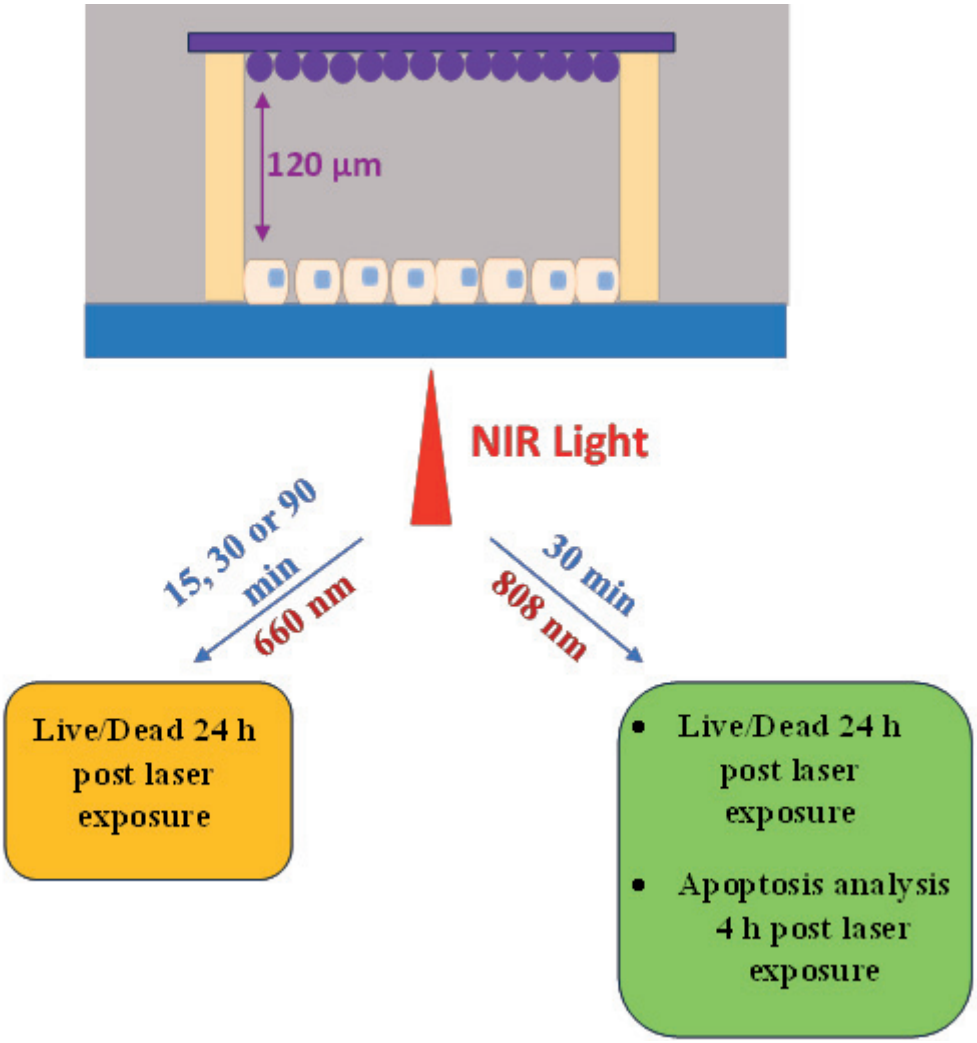


Figure 4 Scheme representing the setup for treatment of Saos-2 cells with immobilized nanoreactors and the assays performed after. The immobilized nanoreactor was placed in proximity with the cells at a 120 µm distance.

a) Cell Viability with 660 nm NIR light

Firstly, two controls were tested as shown in ***Figure 5a-b***, respectively. In the first control, cells were exposed to 660 nm NIR light for 90 min, which is the maximum time used in the assay. In the second control, cells were incubated with a chip of immobilized nanoreactors for 90 min but in absence of light. Quantification of the results showed that 96 ± 2 % and 99,5 ± 0,05 % of cells in controls 1 and 2, respectively, were stained green which means that these cells were alive and exhibited esterase activity. These findings corroborate that the 660 nm NIR light used was safe and did not interfere with the cytotoxic effect observed later, which agrees with a previous study that confirmed the safety of 660 nm light at higher light intensity[178]. In addition, these results confirm the biocompatibility of the silica nanoparticles, MoS_2 and Cu_2O when the immobilized nanoreactors are outside the cells.

In the next step, cells were incubated with the immobilized nanoreactors and exposed to NIR at 660 nm for different periods of time. After 90 min, most of the cells (94 ± 3,6 %) were stained

red, indicating that propidium iodide bound to DNA, which indicates that the membrane of cells is no longer intact, and cells are dead. To check the effectiveness of this strategy at shorter times, the process time was reduced to 30 and 15 min. Upon exposure of 30 min, 57% of cells remained alive and 43% died. Decreasing the time to 15 min resulted in a weak reduction in dead cells (37 ± 7 %). ***Figure 5f*** depicts a graph illustrating the percentages of live and dead cells at the different conditions. Therefore, the NIR LED at 660 nm with an intensity of 100 mW/cm^2 proved high efficiency in triggering the reaction for ROS production, leading to cell death in a time-dependent manner.

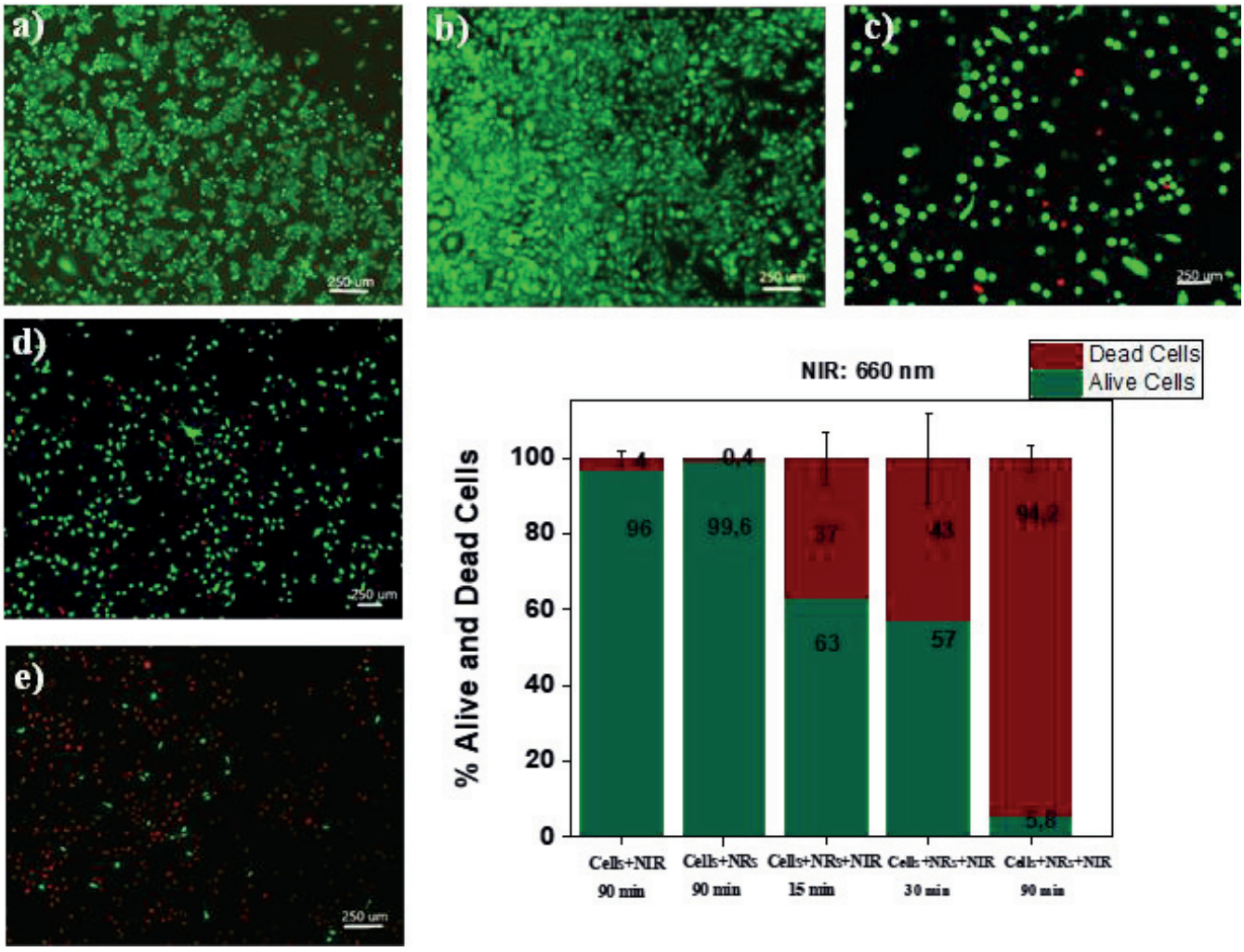


Figure 5 Viability of Saos-2 cells under different conditions. a) Cells exposed to NIR at 660 nm and 100 mW/cm^2 for 90 min, b) Cells exposed to immobilized nanoreactors for 90 min without light. Cells incubated with immobilized nanoreactors and exposed to NIR at 660 nm and 100 mW/cm^2 for different times c)15, d) 30 and e) 90 min. f) Percentages of alive (green) and dead (red) cells in the different conditions. NRs in the graph refers to nanoreactors.

b) Cell Viability with 808 nm NIR light

To assess the clinical applicability of this therapy with light showing deeper penetration into the tissues and higher maximum exposure levels, the same assay was carried out using NIR at 808 nm wavelength. As a control, cells were exposed to the 808 nm light for 30 min and, as expected, almost 99 ± 0,14 % of cells were alive (***Figure 6a***), which confirms once again the safety of NIR light at this intensity. This agrees with previous study showing the safety of 808 nm light, in a study in which SiO_2/MoS_2 was used as photothermal agent at 808 nm[179]. Given the previously confirmed biocompatibility of immobilized nanoreactors, such control was not repeated. Then, cells were incubated with immobilized nanoreactors and irradiated at 808 nm at the same intensity of 100 mW/cm^2 for 30 min. After 24 h, the live/dead assay showed that 37% of cells were found to be dead as shown in ***Figure 6b***. Compared to 660 nm irradiation at 30 min in which 41% of cells died, a slightly lower percentage of cells died with the longer wavelength. This result was expected as shorter wavelengths are more efficient for ROS generation. To achieve a more pronounced effect, increasing the irradiation time or intensity could result in higher cell death.

To the best of our knowledge, there are no studies using MoS_2 as a photodynamic agent for biomedical therapies. In general, due to the high photothermal conversion efficiency displayed by MoS_2, most studies have focused on its application as a photothermal agent[179,180]. Some studies have explored combined photothermal and photodynamic capabilities involving MoS_2 but using other materials as photosensitizers. For instance, Yang et al has synthesized MSN coated with MoS_2 nanosheets and loaded with the photosensitizer Chlorine e6 (Ce6). This system resulted in a combined photothermal and photodynamic therapy, achieving higher cell mortality when both 660 nm and 808 nm lights were applied[178]. In another study, taking advantage of the loading capacity of the MSN, up conversion nanoparticles using MSN loaded with a photosensitizer were employed for photodynamic therapy[181]. The photodynamic efficiency was also enhanced when combined with photothermal effects using p-MoS_2-n-rGo-MnO_2-PEG[182]. In general, in the reported studies, MoS_2 was mainly used as photothermal agent, unlike our system where it plays a clear and intense photodynamic role, resulting in a good mortality rate at 660 nm and 808 nm wavelengths under low light intensity. This approach could offer a promising alternative to the use of the conventional photosensitizers, thereby enhancing photodynamic performance through the efficient generation of cytotoxic ROS on cancer cells[183]. Moreover, by increasing the 808 nm light intensity (for example at 300 mW/cm^2, which remains well below the maximum permissible exposure level), combined photothermal and photodynamic effects could also be obtained with a single light source, thereby enabling a considerable reduction of the light exposure times to kill the cancer cells.

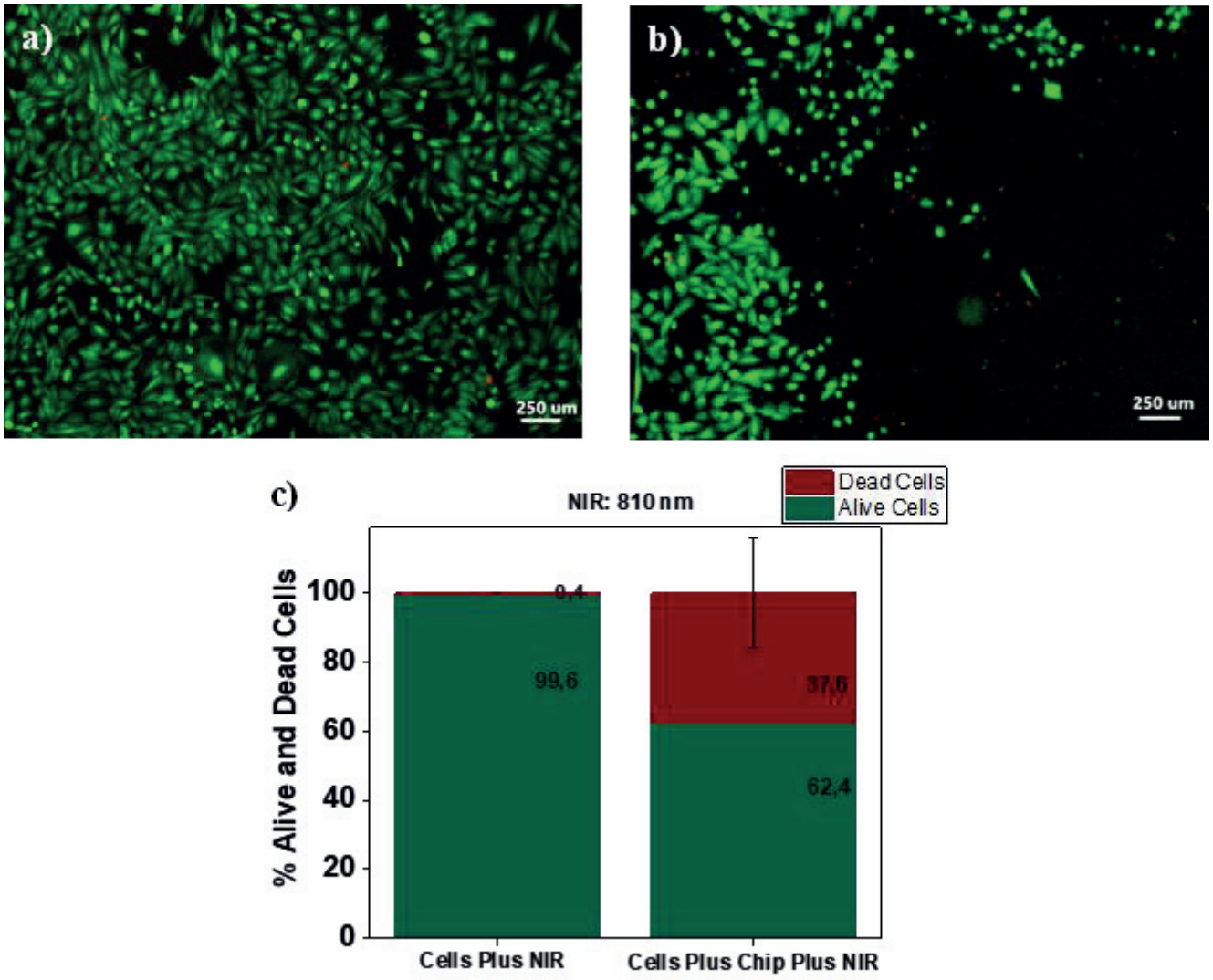


Figure 6 Viability of Saos-2 cells under different conditions. a) Cells exposed to NIR at 808 nm and 100 mW/cm^2 for 30 min, b) Cells incubated with immobilized nanoreactors and exposed to NIR at 808 nm and 100 mW/cm^2 for 30 min. c) Percentages of alive (green) and dead (red) cells in both conditions.

4.2.7 Apoptosis Detection

Among the cellular events triggered by photodynamic therapy, it is relevant to investigate the type of cell death. Apoptosis emerges as the preferred programmed cell death, as it holds the potential for therapeutic benefits while minimizing the adverse effects associated with alternative forms of cell demise, such as necrosis. Apoptosis has been detected via Annexin V - propidium iodide (PI) protocol through confocal microscopy. During apoptosis, certain events occur. For instance, phosphatidyl serine (PS) translocate from the inner to the outer leaflet of the plasma membrane. Fluorescent Annexin V exhibits a high affinity to PS, binding to it and consequently serving as a marker for the initial stages of apoptosis. Additional hallmarks of apoptosis encompass DNA fragmentation and the compromised integrity of the cellular

membrane. These events occur in the late stage of cell apoptosis. In this case, PI enters the cells and binds to the nucleic acid. Therefore, the presence of red fluorescence in the nucleus is an indicator of late-stage apoptosis. In our study, Saos-2 cells incubated with immobilized nanoreactors and illuminated with 808 nm laser for 30 min, exhibited typical features present in apoptotic cells as presence of blebs and condensed nucleus as indicated in ***Figure 7a.*** These features suggest apoptosis as a possible cell death mechanism.

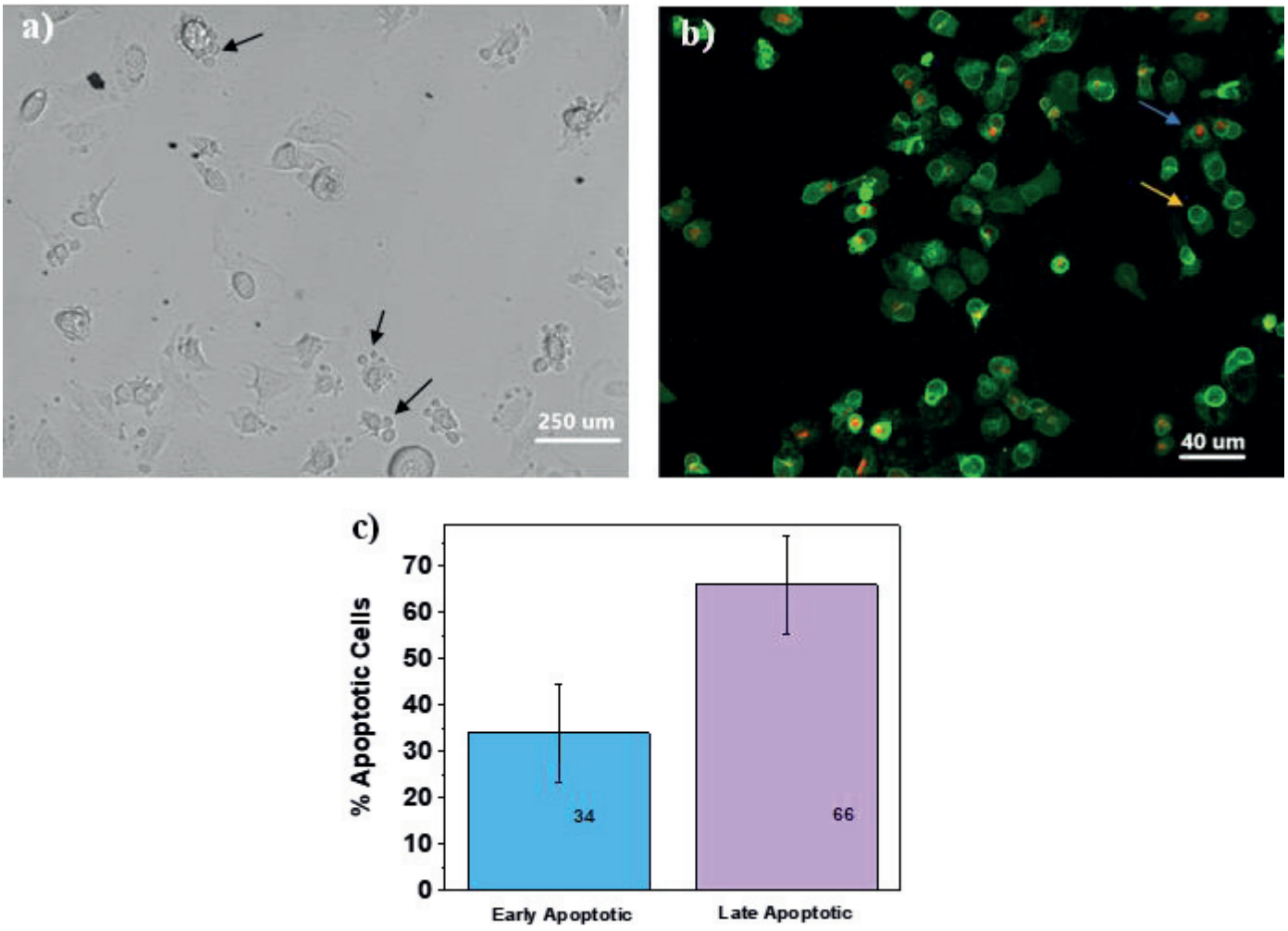


Figure 7 Apoptosis detection in Saos-2 cells via Annexin/PI assay. Saos-2 cells incubated with immobilized nanoreactors and exposed to NIR at 808 nm wavelength and intensity of 100 mW/cm^2 for 30 min. a) Bright filed image captured directly after 30 min of light exposure. Black arrows point to the blebs formed. b) Fluorescence image showing apoptotic cells, Annexin V binds to the translocated PS (green) and PI binds to DNA (red). Orange arrow shows early apoptotic cells and blue arrow shows late apoptotic cells. c) Quantitative analysis of early and late apoptotic cells obtained from three different regions.

For further confirmation, annexin V/PI analysis was performed. ***Figure 7b*** depicts early apoptotic cells (orange arrow). These cells were positively stained with annexin V, which means that PS was translocated to the outer leaflet of the cell membrane, an event that

characterizes cells undergoing apoptosis. At the same time, 34% of these cells were negatively stained to PI (***Figure 7c***), reflecting intact membranes where PI was not yet bound to nucleic acids. In the same figure, blue arrows point to cells that stained positively for both annexin V and PI, which corresponds to 66 % of the apoptotic cells. Such cells are defined in the late apoptosis stage. Therefore, the developed system was able to induce apoptosis of the Saos-2 cells through the generation of ROS triggered by the NIR illumination at a relatively low light intensity.

4.2.8 Nanoreactors Internalization Assessment

In the previous section, we have displayed a special nanoreactor configuration where the nanoreactors were incubated with cells while they were still immobilized on a solid support (immobilized nanoreactors), with a 120 μm distance separating them. Despite this distance, the nanoreactors still exhibited high efficiency in inducing cell death through the photocatalytic reaction in which ROS were produced. However, considering that the NIR photodynamic efficiency would be more pronounced when the nanoreactors are in direct contact or inside the cells, we decided to study the uptake of dispersed nanoreactors by the cells. The $SiO_2/MoS_2/Cu_2O$ NPs were easily dispersed in media through sonication, and they were incubated with the cells for 24 h at a concentration of 2.34 μg/ml. ***Figure 8*** shows some cells with internalized nanoreactors (yellow circles). The image indicates a low cellular uptake of nanoreactors. It is known that several parameters influence the internalization process, including the size of the nanoreactors, the charge and functionalization of the surface, in addition to the cell type that is a key factor in the process as well[12]. In our case, the nanoreactors were weakly charged. Measurements of the zeta potential of the nanoreactors have resulted in small surface charge values of around 10 mV. Therefore, probably there is a certain trend to form aggregates after dispersion, hindering their internalization. Although it has been reported that positively charged nanoparticles are more likely to be internalized by non-phagocytic cells[13], the positive charge values of the nanoreactors still remain relatively low to have a pronounced effect. Functionalization of the nanoreactors could help to reduce aggregation and to enhance the internalization through binding to certain receptors on targeted cells, hence facilitating their entry. Alternatively, the choice of the cell line, Saos-2, might not be optimal for efficiently internalizing these nanoreactors. Therefore, further work is required to improve internalization of our nanoreactors towards a higher potency in inducing cell death.

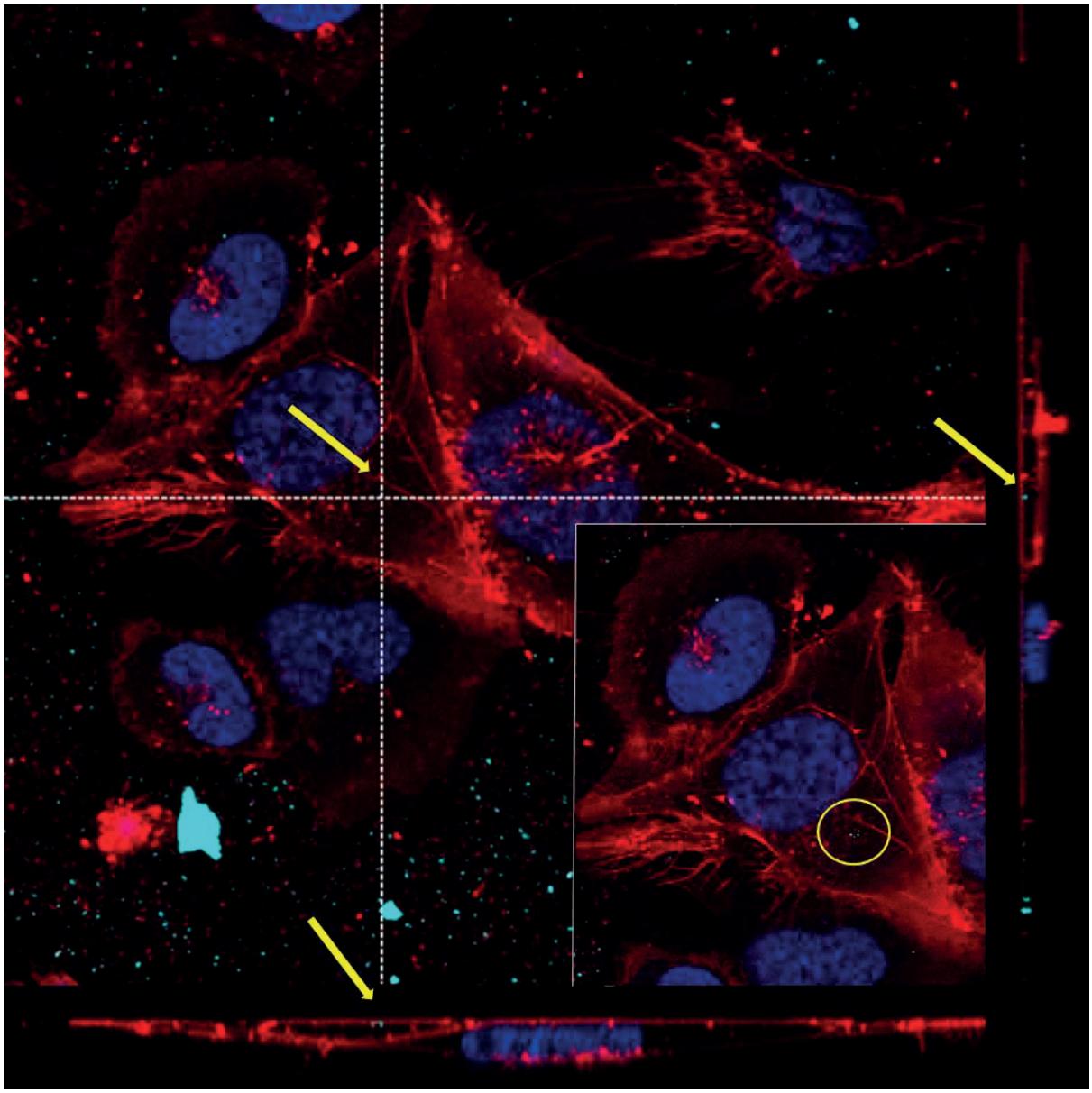


Figure 8 Saos-2 cells incubated with $SiO_2/MoS_2/Cu_2O$ nanoreactors at a concentration of 2.34 μg/ml for 24 h. The image obtained by z-stacks. Cell membrane (red) was stained by cell mask orange, nucleus (blue) stained by Hoechst and nanoparticles (cyan) were visualized by reflection mode. Orthogonal projection mode allows the detection and the confirmation of the nanoreactors entry into the cells (yellow arrows). Yellow circles include the internalized nanoreactors.

However, the powerful photodynamic effect that were observed when the nanoreactors were outside the cells and at a considerable distance (ca. 120 μm) can also be an advantage, as cell internalization is not mandatory to generate the therapeutic effect. The external actuation and low internalization levels can also prevent potential long-term cytotoxic effects that can be induced when nanoparticles are internalized.

4.3 Conclusion

In summary, this chapter has analysed the potential of the supported MoS_2/Cu_2O nanoreactors as photodynamic agents working in the first biological window. The MSN were successfully used as a support for 2D MoS_2 growth and subsequently decorated with Cu_2O nanostructures. The resulting nanoreactors were utilized either as assembled nanoparticle arrays (immobilized nanoreactors) on silicon wafers at a significant distance (ca. 120 μm) from the cells, or as released and dispersed hybrid nanoreactors in media for cell internalization. Characterization of the nanoreactors was done at different aspects concerning the NPs and pore size, MoS_2 structure and ROS production. The hybrid nanoreactors exhibited cell biocompatibility in the absence of light, and exposure of cells in absence of NPs to NIR light (660 nm and 808 nm) displayed safety towards cells. The photo-induced therapy efficiency of the supported nanoreactors exhibited a time-dependent decrease in the Saos-2 cells viability under light intensities considerably lower (100 mW/cm^2) than photothermal therapies. Moreover, apoptosis was observed as predominant cell death caused by the generated ROS upon illumination with 808 nm laser. The internalization of the nanoreactors was low and could be improved by surface functionalization. One way is through surface modification with polymers or certain antigens targeting them towards cells of interest and facilitating their entry. However, the strong external photodynamic effects can be exploited to prevent long-term cytotoxic effects triggered by NPs internalization. Hence, these cost-effective $Silica/MoS_2/Cu_2O$ nanoreactors present a promising model for biomedical applications, especially in NIR photodynamic therapies for cancer treatment.

4.4 Materials and Methods

4.4.1 Synthesis of Mesoporous Silica Nanoparticles

A surfactant-template method based on the Stöber approach was chosen to synthesize the mesostructured silica spherical NPs. The process begins by dissolving 1.02 g of CTAB surfactant in 340 ml of distilled water in a 500 ml Erlenmeyer flask, followed by sonication until the solution becomes transparent. The reagents are then maintained at a temperature between 30-35 °C in an oil bath, and 120 ml of absolute ethanol (EtOH) and NH_3 (1.5 ml 35%) are added under vigorous stirring. EtOH leads to the formation of uniform micelles with spherical morphology. Subsequently, the silica precursor, tetraethyl orthosilicate (TEOS), is introduced and undergoes hydrolysis catalyzed by NH_3. Typically, 1.5 mL of TEOS is added dropwise once the reagent temperature reaches 80°C, leading to hydrolysis and condensation around the CTAB micelles. 1 ml of TMB was also introduced as a pore-expanding agent. The reaction is maintained at 80 °C for 2 h. At the end of the reaction, the solution turns white due to light scattering by the synthesized silica nanoparticles. Particle sizes around 230 nm with pore sizes of about 35 nm were achieved.

The suspension was taken out of the heater and cooled down to RT. The solution was then poured into falcon tubes and centrifuged for 15 min at 10,000 rpm to separate the NPs from the solvent. After centrifugation and removal of the solvent, EtOH was added to the pellets, sonicated for homogenization, and centrifuged again. This EtOH washing process is repeated for three times in order to obtain a clean solution of NPs in EtOH and eliminate as much as possible the compounds of the reaction. To eliminate the CTAB template, a solvent extraction strategy is implemented. The NP dispersion is subjected to an ethanolic solution of ammonium nitrate (0.0038 M). The colloidal dispersion is heated at 80°C and maintained for 1 h under constant stirring. Following this step, the colloidal dispersion is centrifuged for 15 min at 10,000 rpm, the solvent is discarded, and the pellet containing the NPs is re-dispersed in ethanol. Subsequently, the NPs undergo washing in ethanol and centrifugation, repeating this washing step three times to ensure complete surfactant extraction. This solvent extraction method preserves the silanol groups at the particle surface, facilitating good dispersion of the NPs in water and preventing aggregation while maintaining the pore size of the mesoporous network. This approach stands out as a favorable strategy compared to the typical calcination method for CTAB removal, which may result in the destruction of silanol groups and structural shrinkage, leading to pore deformation.

4.4.2 Self-assembly Process

The colloidal dispersion of NPs previously sonicated was filtrated using 1200 and 800 nm hydrophilic filters to separate possible aggregates. Then, 4 ml of the colloidal dispersion was transferred into two 3 ml syringes (2ml in each one). After that, a previously clean silicon wafer was carefully placed in a slanted support inside a tank. Then, the tank was filled with distilled water until covering the wafer placed in the support. At that point, the colloidal dispersion of silica contained in the syringes was injected directly at the air-liquid interface with the syringes connected to a high precision peristaltic pump. The two needles attached to each 3 ml syringes were placed in the extremes of the wafer placed in the support, making sure the needles were on the air liquid interface. The pump device was used to get a flow of the solution placed in the syringes of 10 μl/min.

After injection of the NPs, they become irreversibly trapped at the interface and stack together by capillary forces. The area density of the NPs and therefore their separation was controlled by the number of NPs injected at the interface, leading to smaller NP distance for more crowded interfaces. For that reason, the NP flow was only stopped when no movement was seen in the floating particle monolayer, which denoted that the interface was totally filled with a particle monolayer and further NP addition would cause the three-dimensional aggregation due to steric effects.

To ensure a clean transfer of the floating monolayer to the wafer placed under the water, the tank was slowly drained at a controllable rate between 0.25 and 5.5 $ml \cdot s^{-1}$, in order to prevent turbulences, which would have resulted in destructive shear forces.

The assembled NPs were further subjected to oxygen plasma cleaning (400 W, 60 sccm O_2, 4 min). In some cases, an extra step of RIE was followed to tailor the size of the silica nanoparticles. That was made using CF_3 gas for 45 s. Once the process had finished, the NP substrate was again cleaned with O_2 plasma for 3 min in order to remove the leftovers of fluorine species from the surface.

4.4.3 Synthesis of MoS_2/Cu_2O on Silica

To initiate the growth of MoS2 flakes on the silica surface, a silanization process is first required. For this purpose, the substrate was immersed in a 4% APTES solution in toluene for 2 hours at 80 °C. Subsequently, the substrate was rinsed with toluene and then immersed in DI water for 2 hours to remove excess APTES. In the third step, 0.3 mg of ammonium tetrathiomolybdate ((NH4)2MoS4) was dissolved in 10 ml of dimethylformamide (DMF), and the solution was sonicated for 30 minutes. Following this, the substrate was submerged in the DMF solution, transferred to a stainless-steel autoclave, and hydrothermally treated for 18 hours at 180 °C. After 18 hours, the as-prepared sample was rinsed with water and dried using a nitrogen gun. Finally, a 3 nm layer of copper (Cu) was deposited onto the MoS2 nanoreactors via e-beam deposition.

4.4.4 ROS Quenchers

Tetracycline solutions (5 ppm) at pH 6 and 8 were prepared. The quenchers (TEA, p-BQ and IPA) were also independently added in each experiment at 1 mM concentration. Then the nanoreactors/silicon substrate (2 x 3 cm^2) were immersed in the TC/quencher solution. Subsequently, the mixture was continuously stirred in the dark for 60 min to reach the adsorption equilibrium. Once the equilibrium was achieved, the nanoreactors were irradiated under visible light (24.2 mW/cm^2).

4.4.5 Cell Viability Analysis

To check the biocompatibility of the nanoreactors and NIR light separately, a live/dead viability/cytotoxicity assay was performed. In a 35 mm petri dish, a thin double-sided adhesive spacer was placed. Saos-2 cells were seeded only inside the spacer at a density of 10,000 cells. After 48 h, different conditions were tested: i) cells exposed to 660 nm LED for 90 min, ii) cells exposed to 808 nm laser for 30 min, iii) cells incubated with immobilized nanoreactors for 90 min, iv) cells incubated with immobilized nanoreactors and exposed to 660 nm LED for 15, 30 or 90 min, v) cells incubated with immobilized nanoreactors and exposed to 808 nm laser for 30 min. In the next step, wafers were removed, and cells were kept at standard conditions (37 ^{0}C, 5% CO_2) for 24 h. Then the cells were analyzed with the live/dead kit

according to manufacturer´s instructions. Images from different sites were taken by Olympus inverted microscope equipped with epifluorescence. Note that the wafer size is 1 cm^2 with an amount of 0.26 μg/cm^2 nanoreactors.

4.4.6 Apoptosis Detection

Annexin V/PI assay was employed to determine the nature of cell death, specifically focusing on apoptosis. In a 35 mm petri dish, a thin double-sided adhesive spacer was placed. Saos-2 cells were seeded only inside the spacer at a density of 10,000 cells. After 48 h, cells were incubated with UV-sterilized immobilized nanoreactors (wafer size: 1 cm^2, 0.26 μg/cm^2 nanoreactors amount) and exposed to 808 nm laser for 30 min. Then, the wafer was removed, and cells were kept in standard conditions (37 ^{0}C, 5% CO_2) for 4 h. In the last step, cells were stained with a mix of annexin V and PI according to manufacturer´s instructions. Images from different sites were taken by Olympus inverted microscope equipped with epifluorescence.

4.4.7 Internalization Assessment

To assess the uptake of dispersed nanoreactors by cells, Saos-2 cells were seeded in 35 mm glass-bottom dishes (Ibidi, Germany) at a density of 10^5 cells/petri and incubated under standard conditions (37 ^{0}C, 5% CO_2) for 48 h. Then, nanoreactors were dispersed from the wafer (wafer size: 3 x 3 cm^2) in cell culture media through sonication and added to the cells for 24 h at a concentration of 2,34 μg/ml. On the next day, cells were washed 3 times with saline solution and 1 ml of fresh media was added. Finally, cells were stained with a mix of 1 μl of Hoechst 33258 (Sigma-Aldrich) to show the nucleus and 1 μl of cell mask orange to reveal the cell membrane. Images were captured using Confocal TCS SP5 (Leica, Switzerland). Three different lasers were used: 405, 488 and 635 to visualize the cell nucleus, the nanoreactors, and the cell membrane, respectively. Images were acquired in stacks along the z-axis using the xyz mode, and nanoreactors were visualized by reflection property. Image J (Fiji) was used to confirm the internalized nanoparticles through orthogonal projection.

5. Conclusions

In this thesis, different light-activated nanoplatforms have been designed and characterized for wireless opto-electric cell stimulation and controlled generation of therapeutic ROS, opening new avenues in potential biomedical applications. The current research has primarily focused on developing light-targeted therapies by combining nanofabrication strategies with low-power, safe, and high penetration NIR light within the first and second biological windows for precision treatments. The key elements for achieving this goal include the utilization of low-bandgap biocompatible semiconductor materials, plasmonic metal nanomaterials, and nano-structuration.

Concerning opto-electronic devices, two types of platforms were developed. The first one was based on nanostructured silicon in a NW array capped with Au and integrating pn junctions as light-powering actuators to induce the opto-electric stimulation of bone cells with NIR light within the first biological window. The second device relied on nanostructured silicon in the shape of an array of nanoneedles capped with Pt forming Schottky junctions as opto-electrical powering sources for cell electro-stimulation with NIR light within the second biological window.

In the case of the nanoreactors for therapeutic ROS generation, the combination of MSN and low-band gap MoS_2 interfaced with Cu_2O has formed an efficient system for the generation of ROS with NIR light within the first biological window for cancer therapy.

Below, the main conclusions concerning the three different devices discussed in the thesis are listed.

Si/Au NWs with pn junctions for opto-electronic cell stimulation

1. From the design point of view, the incorporation of silicon nano-structuration and gold nanostructures can significantly enhance NIR light absorption through effective light trapping and local enhancement of the electromagnetic field, assisted by the hybrid plasmonic-dielectric resonances of the gold/silicon nanostructures. The presence of the silicon pn junction enables more efficient separation of generated photocarriers, optimizing the opto-electronic response. Furthermore, the gold capping can also enable more efficient charge injection into the solution.

2. Short and long Si/Au NW were successfully fabricated through a cost-effective and scalable process based on colloidal self-assembly and RIE using colloidal NPs as masks for generating the NW array with the integrated pn junction.

3. In the case of short Si/Au NW with a pn junction, buried in the silicon material and, therefore, not exposed to the electrolyte, the exhibited PVs were slightly higher compared to the flat Si wafer with pn-junction. Moreover, the PCs were greatly enhanced with the short Si/Au NWs in both biological windows. These findings highlight the capabilities of the short Si/Au NW to induce faradaic and capacitive electrical signals.

4. The opto-electric performance of the short Si/Au NWs was better in the first biological window (810 nm) than in the second window (1050 nm) due to the decrease of silicon absorbance at higher wavelengths.

5. The short Si/Au NW displayed a suitable substrate for cell attachment and proliferation. Its biocompatibility was exhibited through the adhesion and survival of osteoblast Saos-2 cells on the NW surface. Moreover, NIR safety was confirmed, with 98,5% of cells remaining alive after 24 h of continuous exposure to NIR light at 810 nm.

6. The opto-electric actuation produced by the short Si/Au NW in response to NIR illumination (810 nm) was proved on osteoblast cultured in vitro. The opto-electric stimulation was demonstrated through the induction of calcium influx into the cells, via activation of the voltage-gated Ca^{2+} channels. Interestingly, this was achieved at very low light intensities (with significantly higher cell activation observed above 1 $\mu W/mm^2$ and below 11 $\mu W/mm^2$, compared to the flat pn Si wafer). Remarkably, very low light intensity (4.5 $\mu W/mm^2$) was enough to enhance cell proliferation over 21 days compared to dark conditions. Furthermore, the formation of calcium deposits and ALP activity were both enhanced with opto-electrical stimulation over the same 21 days period. The enhanced effects compared to the flat Si wafer could be attributed to the enhanced PCs generated by the short Si/Au NW devices.

7. In the case of the long Si/Au NW, a significant decrease in both PV and PC was observed, attributed to electrical shortcuts by the liquid electrolyte since the unprotected pn junction was exposed to the electrolyte. Protection strategies of the NW walls and hence of the pn interface were developed, which helped to increase the PV and PC. Preliminary results showed promising perspectives especially with 500 nm diameter NW covered with a protected SiO_2 layer in the side walls. Although charge trapping at the interface remains a challenging factor to improve, particularly in the PC response of NW with small diameters (200 nm).

8. Long Si/Au NW portrayed the advantage of their easy dispersion in water, self-assembly in solid surfaces, and transfer into soft elastic polymeric films. Preliminary results of a fabrication strategy for the easy transfer of dispersed NW into PDMS was developed, opening new avenues for developing soft implantable devices. On the other hand, this strategy could be exploited to produce dispersed protected NW that could be injected into the tissues, to induce a more pronounced stimulation effect.

Si/Pt nanoneedles with Schottky junctions for opto-electronic cell stimulation

9. A simple Si/Pt nanoneedle device featuring a Schottky junction was attained through an easy, cost-effective, and fast approach based on colloidal self-assembly and RIE isotropic Si etching. Integration of Schottky junction at the Si/Pt interface enabled a relatively good efficiency of the device at the level of PV and PC generation in the first and second biological window, although the obtained values were lower than in the case of the short Si/Au NWs with pn junction.

10. The successful use of NIR light in the second biological window conferred the additional versatility of light activation by illumination from either the nanoneedle side or flat back surface, resulting in similar PC and PV, due to the high transparency of silicon in this wavelength range as compared to the first biological window.

11. The developed device showed biocompatibility and a suitable surface for cells growth, as evidenced by 98% of cells remaining alive and well attached cells 48 h after seeding. Moreover, the demonstrated presence of filopodia connecting the nanoneedles apices underscores the good cell interaction and adhesion to this nanostructured surface. Preliminary results of opto-electrical stimulation of Saos-2 cells for calcium ion influx at low light intensity in the second biological window exhibited a 3,4-fold increase in activated cells compared to dark condition. Although these preliminary results are encouraging, further exploration and optimization of the key parameters of these devices should be undertaken to achieve a more pronounced stimulation performance.

SiO_2/MoS_2/Cu_2O for ROS generation

12. Novel SiO_2/MoS_2/CuO_2 nanoreactors for ROS generation has been analyzed as potential NIR photodynamic agents. These nanoreactors were either immobilized on a silicon support or dispersed in the culture medium. The immobilized nanoreactors exhibited nearly no cytotoxicity with 99,5% of cells remaining alive. In parallel, NIR light displayed its safety, with 96% and 99% of cells remaining alive when exposed to 660 nm and 808 nm for 90 and 30 min respectively, in absence of the nanoreactors.

13. The immobilized nanoreactors demonstrated high efficiency as NIR photodynamic agents in cancer treatment. Under 660 nm illumination and at a relatively low intensity (100 mW/cm^2) as compared to photothermal treatments, a time-dependent decrease in Saos-2 cells viability was observed, reaching a 94% of tumoral cell death after 90 min. Moreover, at 808 nm of the same intensity, a 37% of cell death was obtained after 30 min of illumination. The photo-induced activity at 808 nm produced an apoptotic mechanism of cell death. These results highlight the powerful photodynamic effect of

the immobilized nanoreactors, considering that they were outside the cells and at a considerable distance from them (ca. 120 μm).

14. Saos-2 cells internalized a low quantity of the dispersed nanoreactors, probably due to their low colloidal stability, thereby showing the importance of exploring functionalization strategies of the nanoreactors to achieve better colloidal stability and cell uptake to enhance even further the photodynamic effects inside the cells.

6. Future Perspectives

The designed silicon based opto-electronic devices have shown encouraging results at low light intensities, making them promising candidates in the field of wireless ES of cells. On one side, short Si/Au NW with pn junctions displayed a very good opto-electrical response, especially within the first biological window. In the case of the Si/Pt nanoneedles with Schottky junctions, although the response in PV and PC was lower than in the previous case, their opto-electrical output is still promising with good perspectives for measurements within the second biological window. On the other hand, the $SiO_2/MoS_2/CuO_2$ nanoreactors in their immobilized form, showed an outstanding photocatalytic activity reflected in the efficient ROS generation using light in the first biological window. However, more improvements for the three developed nano-systems could be done to enhance their efficiency. Additionally, further experiments are needed to assess the impact of opto-electrical signals on cellular processes.

- Further investigation into the cellular stimulation processes with the Si/Au NW device is required. It is necessary to analyze additional osteoblast differentiation markers, such as the expression of certain proteins involved in the process, including osteocalcin and osteopontin. Collagen I should be explored at an earlier stage when it is highly secreted. On the other hand, the same assays of biomarker differentiation could be performed at longer periods, reaching for example 28 days, especially considering that studies at long time are relatively rare.

- In an approach to confirm the activation and opening of the voltage-gated Ca^{2+} channels in response to the opto-electrical signals, blockers of these channels could be used.

- Considering the opto-electric response of the short Si/Au NW in the second biological window, the stimulation of the voltage-gated Ca^{2+} channels in these wavelength range could be explored.

- With the support of the protective strategies presented in this thesis, there exists considerable potential to enhance the opto-electrical response of Si/Au NW, by tuning their length and width and avoiding electrical shortcuts at the pn junctions. The intricate interplay of hybrid Si/Au resonances and their influence on light absorption enhancement underscores the critical importance of nanostructure size and diameter. Delving into these aspects not only paves the way for refining the fundamental

characteristics of Si/Au NW but also sets the stage for innovative applications in opto-electronic devices.

- Under the same context, the preliminary findings regarding the opto-electronic response of side wall-protected long Si/Au NWs provide a promising foundation for advancing cellular stimulation methodologies. These results present exciting prospects, suggesting the potential integration of these NW into flexible implants or their application in less invasive strategies through the injection of dispersed entities into cells. The encouraging outcomes highlight the importance of a deeper study into these protective strategies and exploring their viability for practical implementation.

- To improve the performance of Si/Pt nanoneedles, one approach could involve maximizing the Si/Pt interaction by achieving higher density of the nanoneedles. This, in turn, would result in higher PC generation and consequently, a more pronounced outcome in the stimulation of cells. Moreover, implementing other Schottky nanostructures, such as NWs, can be explored for improving the opto-electronic performance. In addition, modifying other parameters such as using higher light intensity or optimizing the conditions for preserving attachment of cells on the nanoneedles during calcium detection, are possible approaches towards obtaining better response in terms of cells stimulation. The stimulation with light in the first biological window could also be a strategy to increase the percentage of stimulated cells.

- The effectiveness of the $SiO_2/MoS_2/CuO_2$ nanoreactors as photodynamic agents in their immobilized form could be further improved at 808 nm by increasing the incubation time above 30 min or by increasing the concentration of the nanoreactors on the chip, as well as testing other TMD layered materials of low bandgap. To achieve higher internalization, surface functionalization of the nanoreactors is necessary. The use of charged polymers, antigens or lipids will definitely increase the colloidal stability and facilitate the uptake of these nanoreactors by the cells. Moreover, nanoreactors could be employed as drug carriers as well benefiting from the porosity of the silica NPs.

7. References

1. Kim JA, Wales DJ, Yang GZ. Optical spectroscopy for in vivo medical diagnosis — A review of the state of the art and future perspectives. *Progress in Biomedical Engineering*. 2020;2(4). doi:10.1088/2516-1091/abaaa3

2. Gudkov S V., Andreev SN, Barmina E V., et al. Effect of visible light on biological objects: Physiological and pathophysiological aspects. *Physics of Wave Phenomena*. 2017;25(3):207-213. doi:10.3103/S1541308X17030074

3. Vojisavljevic V, Pirogova E, Cosic I. The effect of electromagnetic radiation (550 - 850 nm) on l-Lactate dehydrogenase kinetics. *Int J Radiat Biol*. 2007;83(4):221-230. doi:10.1080/09553000701227565

4. Yun SH, Kwok SJJ. Light in diagnosis, therapy and surgery. *Nat Biomed Eng*. 2017;1(1). doi:10.1038/s41551-016-0008

5. Roca AG, Lopez-Barbera JF, Lafuente A, et al. Iron oxide nanoparticles (Fe3O4, γ-Fe2O3 and FeO) as photothermal heat mediators in the first, second and third biological windows. *Phys Rep*. 2023;1043:1-35. doi:10.1016/j.physrep.2023.10.003

6. Pujals S, Albertazzi L. Super-resolution Microscopy for Nanomedicine Research. *ACS Nano*. 2019;13(9):9707-9712. doi:10.1021/acsnano.9b05289

7. Zhang X, Wang S, Cheng G, Yu P, Chang J. Light-Responsive Nanomaterials for Cancer Therapy. *Engineering*. 2022;13:18-30. doi:10.1016/j.eng.2021.07.023

8. Overchuk M, Weersink RA, Wilson BC, Zheng G. Photodynamic and Photothermal Therapies: Synergy Opportunities for Nanomedicine. *ACS Nano*. 2023;17(9):7979-8003. doi:10.1021/acsnano.3c00891

9. Abrahamse H, Hamblin MR. New photosensitizers for photodynamic therapy. *Biochemical Journal*. 2016;473(4):347-364. doi:10.1042/BJ20150942

10. Busquets MA, Fernández-Pradas JM, Serra P, Estelrich J. Superparamagnetic Nanoparticles with Efficient Near-Infrared Photothermal Effect at the Second Biological Window. *Molecules*. 2020;25(22). doi:10.3390/MOLECULES25225315

11. Ghezzi D, Antognazza MR, MacCarone R, et al. A polymer optoelectronic interface restores light sensitivity in blind rat retinas. *Nat Photonics*. 2013;7(5):400-406. doi:10.1038/nphoton.2013.34

12. Azadgoli B, Baker RY. Laser applications in surgery. *Ann Transl Med*. 2016;4(23). doi:10.21037/atm.2016.11.51

13. Feng Z, Tang T, Wu T, et al. Perfecting and extending the near-infrared imaging window. *Light Sci Appl*. 2021;10(1). doi:10.1038/s41377-021-00628-0

14. Hemmer E, Benayas A, Légaré F, Vetrone F. Exploiting the biological windows: Current perspectives on fluorescent bioprobes emitting above 1000 nm. *Nanoscale Horiz*. 2016;1(3):168-184. doi:10.1039/c5nh00073d

15. Izzetoglu M, Bunce S, Izzetoglu K, Onaral B, Pourrezaei A. Functional brain imaging using near-infrared technology. *IEEE Engineering in Medicine and Biology Magazine*. 2007;26(4):38-46. doi:10.1109/MEMB.2007.384094

16. Mckinnon D. *Physiology of Electrically Excitable Cells*.

17. Hammond C. Ionic gradients, membrane potential and ionic currents. In: *Cellular and Molecular Neurophysiology: Fourth Edition*. Elsevier Inc.; 2015:39-54. doi:10.1016/B978-0-12-397032-9.00003-0

18. Yang M, Brackenbury WJ. Membrane potential and cancer progression. *Front Physiol*. 2013;4 JUL. doi:10.3389/fphys.2013.00185

19. Sharma S, Chrysafides SM. *Physiology, Resting Potential*.

20. Kadir LA, Stacey M, Barrett-Jolley R. Emerging roles of the membrane potential: Action beyond the action potential. *Front Physiol*. 2018;9(NOV). doi:10.3389/fphys.2018.01661

21. Bordes SJ, Murray I V, Chrysafides SM, Bordes S, Sandeep ;, Affiliations S. *Physiology, Resting Potential Anatomical Study of Ulnar Nerve Subluxation View Project Are Electronic Cigarettes Safer ? View Project Physiology, Resting Potential*.; 2020. https://www.researchgate.net/publication/342378191

22. Roux B. Ion channels and ion selectivity. *Essays Biochem*. 2017;61(2):201-209. doi:10.1042/EBC20160074

23. Vacher H, Mohapatra DP, Trimmer JS. Localization and Targeting of Voltage-Dependent Ion Channels in Mammalian Central Neurons. Published online 2008. doi:10.1152/physrev.00002.2008.-The

24. Becchetti A, Resta C Di. *Chapter 2 Introduction to Ion Channels*.

25. Litalien C, Beaulieu P. Molecular Mechanisms of Drug Actions: From Receptors to Effectors. In: *Pediatric Critical Care: Expert Consult Premium Edition*. Elsevier; 2011:1553-1568. doi:10.1016/B978-0-323-07307-3.10117-X

26. Dolphin AC. Voltage-gated calcium channels and their auxiliary subunits: physiology and pathophysiology and pharmacology. *Journal of Physiology*. 2016;594(19):5369-5390. doi:10.1113/JP272262

27. Yu FH, Yarov-Yarovoy V, Gutman GA, Catterall WA. Overview of molecular relationships in the voltage-gated ion channel superfamily. *Pharmacol Rev*. 2005;57(4):387-395. doi:10.1124/pr.57.4.13

28. Fiske JL, Fomin VP, Brown ML, Duncan RL, Sikes RA. Voltage-sensitive ion channels and cancer. *Cancer and Metastasis Reviews*. 2006;25(3):493-500. doi:10.1007/s10555-006-9017-z

29. Lipscombe D, Toro CP. Biophysics of Voltage-Gated Ion Channels. In: *From Molecules to Networks: An Introduction to Cellular and Molecular Neuroscience: Third Edition*. Elsevier Inc.; 2014:377-407. doi:10.1016/B978-0-12-397179-1.00013-0

30. Catterall WA. Voltage-gated calcium channels. *Cold Spring Harb Perspect Biol*. 2011;3(8):1-23. doi:10.1101/cshperspect.a003947

31. Dolphin AC. Voltage-gated calcium channels: Their discovery, function and importance as drug targets. *Brain Neurosci Adv*. 2018;2:239821281879480. doi:10.1177/2398212818794805

32. Fernández-Quintero ML, Ghaleb Y El, Tuluc P, Campiglio M, Liedl KR, Flucher BE. Structural determinants of voltage-gating properties in calcium channels. *Elife*. 2021;10. doi:10.7554/eLife.64087

33. Pelletier L, Moreau M. Cav1 channels is also a story of non excitable cells: Application to calcium signalling in two different non related models. *Biochim Biophys Acta Mol Cell Res*. 2021;1868(6). doi:10.1016/j.bbamcr.2021.118996

34. Pitt GS, Matsui M, Cao C. The Annual Review of Physiology is online at. *Annual Review of Physiology Annu Rev Physiol 2021*. 2020;83:183-203. doi:10.1146/annurev-physiol-031620

35. Golovynska I, Golovynskyi S, Stepanov Y V., Stepanova LI, Qu J, Ohulchanskyy TY. Red and near-infrared light evokes Ca2+ influx, endoplasmic reticulum release and membrane depolarization in neurons and cancer cells. *J Photochem Photobiol B*. 2021;214. doi:10.1016/j.jphotobiol.2020.112088

36. Parameswaran R, Koehler K, Rotenberg MY, et al. Optical stimulation of cardiac cells with a polymer-supported silicon nanowire matrix. *Proc Natl Acad Sci U S A*. 2019;116(2):413-421. doi:10.1073/pnas.1816428115

37. Yang SN, Berggren PO. The role of voltage-gated calcium channels in pancreatic β-cell physiology and pathophysiology. *Endocr Rev*. 2006;27(6):621-676. doi:10.1210/er.2005-0888

38. Blair HC, Larrouture QC, Li Y, et al. Osteoblast differentiation and bone matrix formation in vivo and in vitro. *Tissue Eng Part B Rev*. 2017;23(3):268-280. doi:10.1089/ten.teb.2016.0454

39. Rutkovskiy A, Stensløkken KO, Vaage IJ. Osteoblast Differentiation at a Glance. *Med Sci Monit Basic Res*. 2016;22:95-106. doi:10.12659/msmbr.901142

40. Xia G, Song B, Fang J. Electrical Stimulation Enabled via Electrospun Piezoelectric Polymeric Nanofibers for Tissue Regeneration. *Research*. 2022;2022. doi:10.34133/2022/9896274

41. Sahm F, Freiin Grote V, Zimmermann J, et al. Long-term stimulation with alternating electric fields modulates the differentiation and mineralization of human pre-osteoblasts. *Front Physiol*. 2022;13. doi:10.3389/fphys.2022.965181

42. Katoh K. Effects of Electrical Stimulation of the Cell: Wound Healing, Cell Proliferation, Apoptosis, and Signal Transduction. *Med Sci (Basel)*. 2023;11(1). doi:10.3390/medsci11010011

43. Chen C, Bai X, Ding Y, Lee IS. Electrical stimulation as a novel tool for regulating cell behavior in tissue engineering. *Biomater Res*. 2019;23(1). doi:10.1186/s40824-019-0176-8

44. Tsui CT, Lal P, Fox KVR, Churchward MA, Todd KG. The effects of electrical stimulation on glial cell behaviour. *BMC Biomed Eng*. 2022;4(1). doi:10.1186/s42490-022-00064-0

45. Wang H, Tian J, Jiang Y, et al. *A P P L I E D S C I E N C E S A N D E N G I N E E R I N G A 3D Biomimetic Optoelectronic Scaffold Repairs Cranial Defects*.; 2023. https://www.science.org

46. Shannon R V. Advances in auditory prostheses. *Curr Opin Neurol*. 2012;25(1):61-66. doi:10.1097/WCO.0b013e32834ef878

47. Eickenscheidt M, Jenkner M, Thewes R, Fromherz P, Zeck G. Electrical stimulation of retinal neurons in epiretinal and sub retinal configuration using a multi capacitor array. *J Neurophysiol*. 2012;107(10):2742-2755. doi:10.1152/jn.00909.2011

48. Famm K, Litt B, Tracey K, Boyden E, Slaoui M. A jump-start for electroceuticals. *Nature*. 2013;496:159-161.

49. Lozano AM, Lipsman N, Bergman H, et al. Deep brain stimulation: current challenges and future directions. *Nat Rev Neurol*. 2019;15(3):148-160. doi:10.1038/s41582-018-0128-2

50. Stingl K, Bartz-Schmidt KU, Besch D, et al. Artificial vision with wirelessly powered subretinal electronic implant alpha-IMS. *Proceedings of the Royal Society B: Biological Sciences*. 2013;280(1757). doi:10.1098/rspb.2013.0077

51. Tjong FVY, Koop BE. The modular cardiac rhythm management system: the EMPOWER leadless pacemaker and the EMBLEM subcutaneous ICD. *Herzschrittmachertherapie und Elektrophysiologie*. 2018;29(4):355-361. doi:10.1007/s00399-018-0602-y

52. Wells J, Kao C, Jansen ED, Konrad P, Mahadevan-Jansen A. Application of infrared light for in vivo neural stimulation. *J Biomed Opt*. 2005;10(6):064003. doi:10.1117/1.2121772

53. Ouyang W, Teng F, He JH, Fang X. Enhancing the Photoelectric Performance of Photodetectors Based on Metal Oxide Semiconductors by Charge-Carrier Engineering. *Adv Funct Mater*. 2019;29(9). doi:10.1002/adfm.201807672

54. Jiang Y, Tian B. Inorganic semiconductor biointerfaces. *Nat Rev Mater*. 2018;3(12):473-490. doi:10.1038/s41578-018-0062-3

55. Streetman BG, Banerjee SK. *Solid State Electronic Devices*. Pearson edition.; 2016.

56. Sze SM, Ng KK. Frontmatter. In: *Physics of Semiconductor Devices*. Wiley; 2006. doi:10.1002/9780470068328.fmatter

57. Neamen DA. *Semiconductor Physics and Devices : Basic Principles*. McGraw-Hill; 2012.

58. Wilson J, Hawkes J. *Optoelectronics an Introduction*. Third edition.; 1998.

59. Žerjav G, Zavašnik J, Kovač J, Pintar A. The influence of Schottky barrier height onto visible-light triggered photocatalytic activity of TiO2 + Au composites. *Appl Surf Sci*. 2021;543. doi:10.1016/j.apsusc.2020.148799

60. Jeon B, Lee C, Park JY. Electronic control of hot electron transport using modified Schottky barriers in metal−semiconductor nanodiodes. *ACS Appl Mater Interfaces*. 2021;13(7):9252-9259. doi:10.1021/acsami.0c22108

61. Sun Z, Fang Y. Electrical tuning effect for Schottky barrier and hot-electron harvest in a plasmonic Au/TiO2 nanostructure. *Sci Rep*. 2021;11(1). doi:10.1038/s41598-020-79746-5

62. Kishore Ravi S, Sun W, Krishna Nandakumar D, Zhang Y, Ching Tan S. *Optical Manipulation of Work Function Contrasts on Metal Thin Films*.; 2018.

63. Fajrina N, Tahir M. A critical review in strategies to improve photocatalytic water splitting towards hydrogen production. *Int J Hydrogen Energy*. 2019;44(2):540-577. doi:10.1016/j.ijhydene.2018.10.200

64. Wang A, Wu S, Dong J, et al. Interfacial facet engineering on the Schottky barrier between plasmonic Au and TiO2 in boosting the photocatalytic CO2 reduction under ultraviolet and visible light irradiation. *Chemical Engineering Journal*. 2021;404. doi:10.1016/j.cej.2020.127145

65. Li Z, Fang Y, Wang Y, Jiang Y, Liu T, Wang W. Visualizing the bidirectional electron transfer in a Schottky junction consisting of single CdS nanoparticles and a planar gold film. *Chem Sci*. 2017;8(7):5019-5023. doi:10.1039/c7sc00990a

66. Tung RT. The physics and chemistry of the Schottky barrier height. *Appl Phys Rev*. 2014;1(1). doi:10.1063/1.4858400

67. Dimitrijev S. *Principles of Semiconductor Devices*. Second.

68. Tomsen-Melero J, Passemard S, García-Aranda N, et al. Impact of chemical composition on the nanostructure and biological activity of α-galactosidase-loaded nanovesicles for Fabry disease treatment. *ACS Appl Mater Interfaces*. 2021;13(7):7825-7838. doi:10.1021/acsami.0c16871

69. Savchenko A, Cherkas V, Liu C, et al. *B I O P H Y S I C S Graphene Biointerfaces for Optical Stimulation of Cells*.; 2018. https://www.science.org

70. Di Bartolomeo A. Graphene Schottky diodes: An experimental review of the rectifying graphene/semiconductor heterojunction. *Phys Rep*. 2016;606:1-58. doi:10.1016/j.physrep.2015.10.003

71. Vargas-Estevez C, Blanquer A, Murillo G, et al. Electrical stimulation of cells through photovoltaic microcell arrays. *Nano Energy*. 2018;51:571-578. doi:10.1016/j.nanoen.2018.07.012

72. Yitzhak-David SL, Rotenberg MY. Emerging optoelectronic technologies for next-generation leadless bioelectronic modulation. *Cell Rep Phys Sci*. 2023;4(5). doi:10.1016/j.xcrp.2023.101414

73. Tian B, Xu S, Rogers JA, et al. Roadmap on semiconductor-cell biointerfaces. *Phys Biol*. 2018;15(3). doi:10.1088/1478-3975/aa9f34

74. Parameswaran R, Carvalho-De-Souza JL, Jiang Y, et al. Photoelectrochemical modulation of neuronal activity with free-standing coaxial silicon nanowires. *Nat Nanotechnol*. 2018;13(3):260-266. doi:10.1038/s41565-017-0041-7

75. Jiang Y, Li X, Liu B, et al. Rational design of silicon structures for optically controlled multiscale biointerfaces. *Nat Biomed Eng*. 2018;2(7):508-521. doi:10.1038/s41551-018-0230-1

76. Prominski A, Shi J, Li P, et al. Porosity-based heterojunctions enable leadless optoelectronic modulation of tissues. *Nat Mater*. 2022;21(6):647-655. doi:10.1038/s41563-022-01249-7

77. Lorach H, Goetz G, Smith R, et al. Photovoltaic restoration of sight with high visual acuity. *Nat Med*. 2015;21(5):476-482. doi:10.1038/nm.3851

78. Tang J, Qin N, Chong Y, et al. Nanowire arrays restore vision in blind mice. *Nat Commun*. 2018;9(1). doi:10.1038/s41467-018-03212-0

79. Pappas TC, Wickramanyake WMS, Jan E, Motamedi M, Brodwick M, Kotov NA. Nanoscale engineering of a cellular interface with semiconductor nanoparticle films for photoelectric stimulation of neurons. *Nano Lett*. 2007;7(2):513-519. doi:10.1021/nl062513v

80. Ghezzi D, Antognazza MR, Dal Maschio M, Lanzarini E, Benfenati F, Lanzani G. A hybrid bioorganic interface for neuronal photoactivation. *Nat Commun*. 2011;2(1). doi:10.1038/ncomms1164

81. Rand D, Jakešová M, Lubin G, et al. Direct Electrical Neurostimulation with Organic Pigment Photocapacitors. *Advanced Materials*. 2018;30(25). doi:10.1002/adma.201707292

82. Jakešová M, Silverå Ejneby M, Đerek V, et al. *Optoelectronic Control of Single Cells Using Organic Photocapacitors*. Vol 5.; 2019. http://advances.sciencemag.org/

83. Airaghi Leccardi MJI, Chenais NAL, Ferlauto L, Kawecki M, Zollinger EG, Ghezzi D. Photovoltaic organic interface for neuronal stimulation in the near-infrared. *Commun Mater*. 2020;1(1). doi:10.1038/s43246-020-0023-4

84. Deisseroth K. Optogenetics: 10 years of microbial opsins in neuroscience. *Nat Neurosci*. 2015;18(9):1213-1225.

85. Bruegmann T, Malan D, Hesse M, et al. Optogenetic control of heart muscle in vitro and in vivo. *Nat Methods*. 2010;7(11):897-900. doi:10.1038/nmeth.1512

86. Shapiro MG, Homma K, Villarreal S, Richter CP, Bezanilla F. Infrared light excites cells by changing their electrical capacitance. *Nat Commun*. 2012;3. doi:10.1038/ncomms1742

87. Wells J, Kao C, Konrad P, et al. Biophysical mechanisms of transient optical stimulation of peripheral nerve. *Biophys J*. 2007;93(7):2567-2580. doi:10.1529/biophysj.107.104786

88. Bedard N, Shope T, Hoberman A, et al. Light field otoscope design for 3D in vivo imaging of the middle ear. *Biomed Opt Express*. 2017;8(1):260. doi:10.1364/boe.8.000260

89. Migliori B, Ventra M Di, Kristan W. Photoactivation of neurons by laser-generated local heating. *AIP Adv*. 2012;2(3). doi:10.1063/1.4748955

90. Yong J, Needham K, Brown WGA, et al. Gold-Nanorod-Assisted Near-Infrared Stimulation of Primary Auditory Neurons. *Adv Healthc Mater*. 2014;3(11):1862-1868. doi:10.1002/adhm.201400027

91. Wang Y, Guo L. Nanomaterial-enabled neural stimulation. *Front Neurosci*. 2016;10(MAR). doi:10.3389/fnins.2016.00069

92. Fang Y, Jiang Y, Acaron Ledesma H, et al. Texturing Silicon Nanowires for Highly Localized Optical Modulation of Cellular Dynamics. *Nano Lett*. 2018;18(7):4487-4492. doi:10.1021/acs.nanolett.8b01626

93. Shi L, Jiang Y, Fernandez FR, et al. Non-genetic photoacoustic stimulation of single neurons by a tapered fiber optoacoustic emitter. *Light Sci Appl*. 2021;10(1). doi:10.1038/s41377-021-00580-z

94. Perillo B, Di Donato M, Pezone A, et al. ROS in cancer therapy: the bright side of the moon. *Exp Mol Med*. 2020;52(2):192-203. doi:10.1038/s12276-020-0384-2

95. Reczek CR, Chandel NS. The two faces of reactive oxygen species in cancer. *Annu Rev Cancer Biol*. 2017;1:79-98. doi:10.1146/annurev-cancerbio-041916-065808

96. Juránek I, Nikitovic D, Kouretas D, Hayes AW, Tsatsakis AM. Biological importance of reactive oxygen species in relation to difficulties of treating pathologies involving oxidative stress by exogenous antioxidants. *Food and Chemical Toxicology*. 2013;61:240-247. doi:10.1016/j.fct.2013.08.074

97. Yokoyama C, Sueyoshi Y, Ema M, Mori Y, Takaishi K, Hisatomi H. Induction of oxidative stress by anticancer drugs in the presence and absence of cells. *Oncol Lett*. 2017;14(5):6066-6070. doi:10.3892/ol.2017.6931

98. Dayem AA, Hossain MK, Lee S Bin, et al. The role of reactive oxygen species (ROS) in the biological activities of metallic nanoparticles. *Int J Mol Sci*. 2017;18(1). doi:10.3390/ijms18010120

99. Elsayed Azab A, A Adwas Almokhtar, Ibrahim Elsayed AS, A Adwas A, Ibrahim Elsayed Ata Sedik, Quwaydir FA. Oxidative stress and antioxidant mechanisms in human body. *Journal of Applied Biotechnology & Bioengineering*. 2019;6(1):43-47. doi:10.15406/jabb.2019.06.00173

100. Ye H, Zhou Y, Liu X, et al. Recent Advances on Reactive Oxygen Species-Responsive Delivery and Diagnosis System. *Biomacromolecules*. 2019;20(7):2441-2463. doi:10.1021/acs.biomac.9b00628

101. Graceffa V. Therapeutic Potential of Reactive Oxygen Species: State of the Art and Recent Advances. *SLAS Technol*. 2021;26(2):140-158. doi:10.1177/2472630320977450

102. Li Z, Zhou Z, Wang Y, et al. Activatable nano-photosensitizers for precise photodynamic cancer therapy. *Coord Chem Rev*. 2023;493. doi:10.1016/j.ccr.2023.215324

103. Gunaydin G, Gedik ME, Ayan S. Photodynamic Therapy—Current Limitations and Novel Approaches. *Front Chem*. 2021;9. doi:10.3389/fchem.2021.691697

104. Escudero A, Carrillo-Carrión C, Castillejos MC, Romero-Ben E, Rosales-Barrios C, Khiar N. Photodynamic therapy: Photosensitizers and nanostructures. *Mater Chem Front*. 2021;5(10):3788-3812. doi:10.1039/d0qm00922a

105. Chitgupi U, Qin Y, Lovell JF. Targeted nanomaterials for phototherapy. *Nanotheranostics*. 2017;1(1):38-58. doi:10.7150/ntno.17694

106. Wang D, Zhu Y, Wan X, Zhang X, Zhang J. Colloidal semiconductor nanocrystals for biological photodynamic therapy applications: Recent progress and perspectives. *Progress in Natural Science: Materials International*. 2020;30(4):443-455. doi:10.1016/j.pnsc.2020.08.016

107. Corbitt TS, Sommer JR, Chemburu S, et al. Conjugated polyelectrolyte capsules: Light-activated antimicrobial micro “roach Motels.” *ACS Appl Mater Interfaces*. 2009;1(1):48-52. doi:10.1021/am800096q

108. Kumar Sahu M. *Semiconductor Nanoparticles Theory and Applications*. Vol 14.; 2019. http://www.ripublication.com

109. Li H, Wei M, Lv X, et al. Cerium-based nanoparticles for cancer photodynamic therapy. *J Innov Opt Health Sci*. 2022;15(6). doi:10.1142/S1793545822300099

110. Shah Z, Nazir S, Mazhar K, Abbasi R, Samokhvalov IM. PEGylated doped- and undoped-TiO2 nanoparticles for photodynamic Therapy of cancers. *Photodiagnosis Photodyn Ther*. 2019;27:173-183. doi:10.1016/j.pdpdt.2019.05.019

111. Uprety B, Abrahamse H. Semiconductor quantum dots for photodynamic therapy: Recent advances. *Front Chem*. 2022;10. doi:10.3389/fchem.2022.946574

112. Wang L, Xu D, Jiang L, et al. Transition Metal Dichalcogenides for Sensing and Oncotherapy: Status, Challenges, and Perspective. *Adv Funct Mater*. 2021;31(5). doi:10.1002/adfm.202004408

113. Presutti D, Agarwal T, Zarepour A, et al. Transition Metal Dichalcogenides (TMDC)-Based Nanozymes for Biosensing and Therapeutic Applications. *Materials*. 2022;15(1). doi:10.3390/ma15010337

114. Zhou X, Sun H, Bai X. Two-Dimensional Transition Metal Dichalcogenides: Synthesis, Biomedical Applications and Biosafety Evaluation. *Front Bioeng Biotechnol*. 2020;8. doi:10.3389/fbioe.2020.00236

115. Diaz-Diestra D, Gholipour HM, Bazian M, Thapa B, Beltran-Huarac J. Photodynamic Therapeutic Effect of Nanostructured Metal Sulfide Photosensitizers on Cancer Treatment. *Nanoscale Res Lett*. 2022;17(1). doi:10.1186/s11671-022-03674-8

116. Sarkar D, Mondal B, Som A, et al. Holey MoS2 Nanosheets with Photocatalytic Metal Rich Edges by Ambient Electrospray Deposition for Solar Water Disinfection. *Global Challenges*. 2018;2(12). doi:10.1002/gch2.201800052

117. Islam MA, Church J, Han C, et al. Noble metal-coated MoS2 nanofilms with vertically-aligned 2D layers for visible light-driven photocatalytic degradation of emerging water contaminants. *Sci Rep*. 2017;7(1). doi:10.1038/s41598-017-14816-9

118. Dou X, Zhang Q, Shah SNA, Khan M, Uchiyama K, Lin JM. MoS2-quantum dot triggered reactive oxygen species generation and depletion: Responsible for enhanced chemiluminescence. *Chem Sci*. 2019;10(2):497-500. doi:10.1039/c8sc03511c

119. Yu Y, Lu L, Yang Q, Zupanic A, Xu Q, Jiang L. Using MoS2Nanomaterials to Generate or Remove Reactive Oxygen Species: A Review. *ACS Appl Nano Mater*. 2021;4(8):7523-7537. doi:10.1021/acsanm.1c00751

120. Mathieson K, Loudin J, Goetz G, et al. Photovoltaic retinal prosthesis with high pixel density. *Nat Photonics*. 2012;6(6):391-397. doi:10.1038/nphoton.2012.104

121. Jiang Y, Carvalho-De-Souza JL, Wong RCS, et al. Heterogeneous silicon mesostructures for lipid-supported bioelectric interfaces. *Nat Mater*. 2016;15(9):1023-1030. doi:10.1038/nmat4673

122. Parameswaran R, Carvalho-De-Souza JL, Jiang Y, et al. Photoelectrochemical modulation of neuronal activity with free-standing coaxial silicon nanowires. *Nat Nanotechnol*. 2018;13(3):260-266. doi:10.1038/s41565-017-0041-7

123. Jiang Y, Li X, Liu B, et al. Rational design of silicon structures for optically controlled multiscale biointerfaces. *Nat Biomed Eng*. 2018;2(7):508-521. doi:10.1038/s41551-018-0230-1

124. Carvalho-de-Souza JL, Treger JS, Dang B, Kent SBH, Pepperberg DR, Bezanilla F. Photosensitivity of neurons enabled by cell-targeted gold nanoparticles. *Neuron*. 2015;86(1):207-217. doi:10.1016/j.neuron.2015.02.033

125. Ghezzi D, Antognazza MR, MacCarone R, et al. A polymer optoelectronic interface restores light sensitivity in blind rat retinas. *Nat Photonics*. 2013;7(5):400-406. doi:10.1038/nphoton.2013.34

126. Weissleder R. A clearer vision for in vivo imaging. *Nat Biotechnol*. 2001;19(4):316-317.

127. C.P. Richter, A.I. Matic, J.D. Wells, E.D. Jansen JTWJr. Neural stimulation with optical radiation.pdf. *Laser Photonics Rev*. 2011;5(1):68-80.

128. Delori FC, Webb RH, Sliney DH. Maximum permissible exposures for ocular safety (ANSI 2000), with emphasis on ophthalmic devices. *Journal of the Optical Society of America A*. 2007;24(5):1250. doi:10.1364/josaa.24.001250

129. Smith MH, Fork RL, Cole ST. *Safe Delivery of Optical Power from Space*. Vol 5.; 1999. http://www.opticsexpress.org/oearchive/source/14181.htm.

130. Lavoie-Cardinal F, Salesse C, Bergeron É, Meunier M, De Koninck P. Gold nanoparticle-assisted all optical localized stimulation and monitoring of Ca2+ signaling in neurons. *Sci Rep*. 2016;6. doi:10.1038/srep20619

131. Fang Y, Jiang Y, Acaron Ledesma H, et al. Texturing Silicon Nanowires for Highly Localized Optical Modulation of Cellular Dynamics. *Nano Lett*. 2018;18(7):4487-4492. doi:10.1021/acs.nanolett.8b01626

132. Parameswaran R, Koehler K, Rotenberg MY, et al. Optical stimulation of cardiac cells with a polymer-supported silicon nanowire matrix. *Proc Natl Acad Sci U S A*. 2019;116(2):413-421. doi:10.1073/pnas.1816428115

133. Mathieson K, Loudin J, Goetz G, et al. Photovoltaic retinal prosthesis with high pixel density. *Nat Photonics*. 2012;6(6):391-397. doi:10.1038/nphoton.2012.104

134. Lorach H, Goetz G, Smith R, et al. Photovoltaic restoration of sight with high visual acuity. *Nat Med*. 2015;21(5):476-482. doi:10.1038/nm.3851

135. Ghezzi D, Antognazza MR, Dal Maschio M, Lanzarini E, Benfenati F, Lanzani G. A hybrid bioorganic interface for neuronal photoactivation. *Nat Commun*. 2011;2(1):164-167. doi:10.1038/ncomms1164

136. Rand D, Jakešová M, Lubin G, et al. Direct Electrical Neurostimulation with Organic Pigment Photocapacitors. *Advanced Materials*. 2018;30(25):1-11. doi:10.1002/adma.201707292

137. Jakešová M, Silverå Ejneby M, Đerek V, et al. Optoelectronic control of single cells using organic photocapacitors. *Sci Adv*. 2019;5(4):eaav5265. doi:10.1126/sciadv.aav5265

138. Eom K, Kim J, Choi JM, et al. Enhanced Infrared Neural Stimulation using Localized Surface Plasmon Resonance of Gold Nanorods. *Small*. 2014;10(19):3853-3857. doi:10.1002/smll.201400599

139. Yong J, Needham K, Brown WG a., et al. Gold-Nanorod-Assisted Near-Infrared Stimulation of Primary Auditory Neurons. *Adv Healthc Mater*. 2014;3(11):1862-1868. doi:10.1002/adhm.201400027

140. Gentemann L, Kalies S, Coffee M, et al. Modulation of cardiomyocyte activity using pulsed laser irradiated gold nanoparticles. *Biomed Opt Express*. 2017;8(1):177. doi:10.1364/boe.8.000177

141. Tang J, Qin N, Chong Y, et al. Nanowire arrays restore vision in blind mice. *Nat Commun*. 2018;9(1):1-13. doi:10.1038/s41467-018-03212-0

142. Jiang Y, Li X, Liu B, et al. Rational design of silicon structures for optically controlled multiscale biointerfaces. *Nat Biomed Eng*. 2018;2(7):508-521. doi:10.1038/s41551-018-0230-1

143. Pitt GS, Matsui M, Cao C. The Annual Review of Physiology is online at. *Annual Review of Physiology Annu Rev Physiol 2021*. 2020;83:183-203. doi:10.1146/annurev-physiol-031620

144. Xia G, Song B, Fang J. Electrical Stimulation Enabled via Electrospun Piezoelectric Polymeric Nanofibers for Tissue Regeneration. *Research*. 2022;2022. doi:10.34133/2022/9896274

145. Sahm F, Freiin Grote V, Zimmermann J, et al. Long-term stimulation with alternating electric fields modulates the differentiation and mineralization of human pre-osteoblasts. *Front Physiol*. 2022;13. doi:10.3389/fphys.2022.965181

146. Jiang Y, Tian B. Inorganic semiconductor biointerfaces. *Nat Rev Mater*. 2018;3(12):473-490. doi:10.1038/s41578-018-0062-3

147. Walter MG, Warren EL, McKone JR, et al. Solar water splitting cells. *Chem Rev*. 2010;110(11):6446-6473. doi:10.1021/cr1002326

148. Zhang Y. *Opto-Magneto-Electrical Nanoactuators for Wireless Cell Stimulation*. Universitat de Barcelona (UB); 2020.

149. Jiang Y, Carvalho-De-Souza JL, Wong RCS, et al. Heterogeneous silicon mesostructures for lipid-supported bioelectric interfaces. *Nat Mater*. 2016;15(9):1023-1030. doi:10.1038/nmat4673

150. Okumura A, Goto M, Goto T, et al. *Substrate a!Ects the Initial Attachment and Subsequent Behavior of Human Osteoblastic Cells (Saos-2)*. Vol 22.; 2001.

151. Leppik L, Oliveira KMC, Bhavsar MB, Barker JH. Electrical stimulation in bone tissue engineering treatments. *European Journal of Trauma and Emergency Surgery*. 2020;46(2):231-244. doi:10.1007/s00068-020-01324-1

152. Ercan B, Webster TJ. The effect of biphasic electrical stimulation on osteoblast function at anodized nanotubular titanium surfaces. *Biomaterials*. 2010;31(13):3684-3693. doi:10.1016/j.biomaterials.2010.01.078

153. Dos Santos MPS, Marote A, Santos T, et al. New cosurface capacitive stimulators for the development of active osseointegrative implantable devices. *Sci Rep*. 2016;6. doi:10.1038/srep30231

154. Portan D V., Deligianni DD, Papanicolaou GC, Kostopoulos V, Psarras GC, Tyllianakis M. Combined Optimized Effect of a Highly Self-Organized Nanosubstrate and an Electric Field on Osteoblast Bone Cells Activity. *Biomed Res Int*. 2019;2019. doi:10.1155/2019/7574635

155. Casalino M. Silicon meets graphene for a new family of near-infrared schottky photodetectors. *Applied Sciences (Switzerland)*. 2019;9(18). doi:10.3390/app9183677

156. Dai X, Wu L, Liu K, et al. A Silicon Sub-Bandgap Near-Infrared Photodetector with High Detectivity Based on Textured Si/Au Nanoparticle Schottky Junctions Covered with Graphene Film. *Sensors*. 2023;23(13). doi:10.3390/s23136184

157. Roca AG, Lopez-Barbera JF, Lafuente A, et al. Iron oxide nanoparticles (Fe3O4, γ-Fe2O3 and FeO) as photothermal heat mediators in the first, second and third biological windows. *Phys Rep*. 2023;1043:1-35. doi:10.1016/j.physrep.2023.10.003

158. Wen L, Chen Y, Liang L, Chen Q. Hot Electron Harvesting via Photoelectric Ejection and Photothermal Heat Relaxation in Hotspots-Enriched Plasmonic/Photonic Disordered Nanocomposites. *ACS Photonics*. 2018;5(2):581-591. doi:10.1021/acsphotonics.7b01156

159. Sakurai Y, Itou M, Barbiellini B, et al. Imaging doped holes in a cuprate superconductor with high-resolution compton scattering. *Science (1979)*. 2011;332(6030):698-702. doi:10.1126/science.1199391

160. Lin K Te, Chen HL, Lai YS, Yu CC. Silicon-based broadband antenna for high responsivity and polarization-insensitive photodetection at telecommunication wavelengths. *Nat Commun*. 2014;5. doi:10.1038/ncomms4288

161. Wu Q, Cen G, Liu Y, Ji Z, Mai W. A simple-structured silicon photodetector possessing asymmetric Schottky junction for NIR imaging. *Physics Letters, Section A: General, Atomic and Solid State Physics*. 2021;412. doi:10.1016/j.physleta.2021.127586

162. Hansel CS, Crowder SW, Cooper S, et al. Nanoneedle-Mediated Stimulation of Cell Mechanotransduction Machinery. *ACS Nano*. 2019;13(3):2913-2926. doi:10.1021/acsnano.8b06998

163. Wu SH, Lin HP. Synthesis of mesoporous silica nanoparticles. *Chem Soc Rev*. 2013;42(9):3862-3875. doi:10.1039/c3cs35405a

164. Stevens WJJ, Lebeau K, Mertens M, Van Tendeloo G, Cool P, Vansant EF. Investigation of the morphology of the mesoporous SBA-16 and SBA-15 materials. *Journal of Physical Chemistry B*. 2006;110(18):9183-9187. doi:10.1021/jp0548725

165. Chao MC, Wang DS, Lin HP, Mou CY. Control of single crystal morphology of SBA-1 mesoporous silica. *J Mater Chem*. 2003;13(12):2853-2854. doi:10.1039/b313028m

166. Shinde PS, Suryawanshi PS, Patil KK, et al. A brief overview of recent progress in porous silica as catalyst supports. *Journal of Composites Science*. 2021;5(3). doi:10.3390/jcs5030075

167. Knežević N, Durand JO. Large pore mesoporous silica nanomaterials for application in delivery of biomolecules. *Nanoscale*. 2015;7(6):2199-2209. doi:10.1039/c4nr06114d

168. Li Z, Barnes JC, Bosoy A, Stoddart JF, Zink JI. Mesoporous silica nanoparticles in biomedical applications. *Chem Soc Rev*. 2012;41(7):2590-2605. doi:10.1039/c1cs15246g

169. Shahnazarova G. *Silica-Supported Multicomponent Materials for Environmental Remediation, Biomedical and Energy Applications* . Universitat Autonoma de Barcelona (UAB); 2023.

170. Sahoo B, Devi KSP, Dutta S, Maiti TK, Pramanik P, Dhara D. Biocompatible mesoporous silica-coated superparamagnetic manganese ferrite nanoparticles for targeted drug delivery and MR imaging applications. *J Colloid Interface Sci*. 2014;431:31-41. doi:10.1016/j.jcis.2014.06.003

171. Vazquez NI, Gonzalez Z, Ferrari B, Castro Y. Synthesis of mesoporous silica nanoparticles by sol-gel as nanocontainer for future drug delivery applications. *Boletin de la Sociedad Espanola de Ceramica y Vidrio*. 2017;56(3):139-145. doi:10.1016/j.bsecv.2017.03.002

172. Meng Q, Xiang S, Zhang K, et al. A facile two-step etching method to fabricate porous hollow silica particles. *J Colloid Interface Sci*. 2012;384(1):22-28. doi:10.1016/j.jcis.2012.06.043

173. Moon DS, Lee JK. Tunable synthesis of hierarchical mesoporous silica nanoparticles with radial wrinkle structure. *Langmuir*. 2012;28(33):12341-12347. doi:10.1021/la302145j

174. He Z, Que W. Molybdenum disulfide nanomaterials: Structures, properties, synthesis and recent progress on hydrogen evolution reaction. *Appl Mater Today*. 2016;3:23-56. doi:10.1016/j.apmt.2016.02.001

175. Vital-Grappin AD, Ariza-Tarazona MC, Luna-Hernández VM, et al. The role of the reactive species involved in the photocatalytic degradation of hdpe microplastics using c,n-tio2 powders. *Polymers (Basel)*. 2021;13(7). doi:10.3390/polym13070999

176. Hayyan M, Hashim MA, Alnashef IM. Superoxide Ion: Generation and Chemical Implications. *Chem Rev*. 2016;116(5):3029-3085. doi:10.1021/acs.chemrev.5b00407

177. Ma HY, Zhao L, Guo LH, Zhang H, Chen FJ, Yu WC. Roles of reactive oxygen species (ROS) in the photocatalytic degradation of pentachlorophenol and its main toxic intermediates by TiO2/UV. *J Hazard Mater*. 2019;369:719-726. doi:10.1016/j.jhazmat.2019.02.080

178. Yang L, Wang J, Yang S, Lu Q, Li P, Li N. Rod-shape MSN@MoS2 nanoplatform for FL/MSOT/CT imaging-guided photothermal and photodynamic therapy. *Theranostics*. 2019;9(14):3992-4005. doi:10.7150/thno.32715

179. Wang J, Li Z, Yin Y, et al. Mesoporous silica nanoparticles combined with MoS2 and FITC for fluorescence imaging and photothermal therapy of cancer cells. *J Mater Sci*. 2020;55(31):15263-15274. doi:10.1007/s10853-020-04950-7

180. Wang S, Li K, Chen Y, et al. Biocompatible PEGylated MoS2 nanosheets: Controllable bottom-up synthesis and highly efficient photothermal regression of tumor. *Biomaterials*. 2015;39:206-217. doi:10.1016/j.biomaterials.2014.11.009

181. Ding B, Shao S, Yu C, et al. Large-Pore Mesoporous-Silica-Coated Upconversion Nanoparticles as Multifunctional Immunoadjuvants with Ultrahigh Photosensitizer and Antigen Loading Efficiency for Improved Cancer Photodynamic Immunotherapy. *Advanced Materials*. 2018;30(52). doi:10.1002/adma.201802479

182. Kapri S, Bhattacharyya S. Molybdenum sulfide-reduced graphene oxide p-n heterojunction nanosheets with anchored oxygen generating manganese dioxide nanoparticles for enhanced photodynamic therapy. *Chem Sci*. 2018;9(48):8982-8989. doi:10.1039/c8sc02508h

183. Sahoo D, Behera SP, Shakya J, Kaviraj B. Cost-effective synthesis of 2D molybdenum disulfide (MoS2) nanocrystals: An exploration of the influence on cellular uptake, cytotoxicity, and bio-imaging. *PLoS One*. 2022;17(1 January). doi:10.1371/journal.pone.0260955

Appendix

In addition to the work developed in this thesis with respect to the opto-electronic properties and wireless stimulation of cells with np Si/Au NWs, the efficiency of these devices was assessed in other applications. Two collaborative studies were undertaken with other research groups.

In the first work, similar short np Si/Au NWs with Pt coatings at the flat back side were developed. The device was successfully used to show the first example of wireless photoelectrochemical device for generating electrochemiluminescence under NIR light illumination (Article 1), which might have promising sensing applications.

In the second work (Article 2), a novel wireless pulsed nanophotoelectrochemical (nPEC) cell was developed for the ultrafast degradation of organic pollutants. The nPEC cell consisted of a nanostructured Si pn photodiode that monolithically integrates: (i) a nanostructured photocathode composed of Si-n/Au nanowires for the efficient light absorption and generation of photovoltages at low light intensities of near infrared (NIR) and visible light, and (ii) a Si-p/mesoporous Ni-rich NiPt photoanode as catalyst to produce sulfate radicals. These devices enabled a drastic increase in the catalytic reaction of peroxymonosulfate (PMS) to generate highly reactive sulfate radicals under illumination with low intensity NIR light to degrade organic pollutants. Remarkably, this work showed that illumination with a pulsed light beam (with half of the average power) can amplify even further the production of sulfate radicals and, therefore, the degradation rate of the organic pollutants.

JACS
JOURNAL OF THE AMERICAN CHEMICAL SOCIETY
pubs.acs.org/JACS
Article

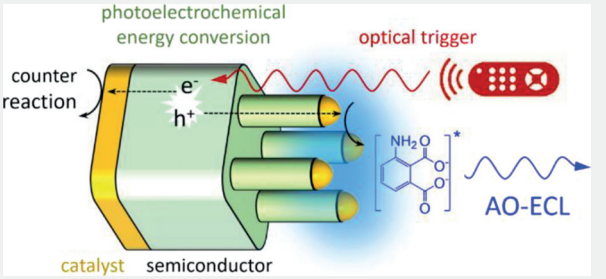
All-Optical Electrochemiluminescence

Yiran Zhao, Julie Descamps, Nour al Hoda Al Bast, Marcos Duque, Jaume Esteve, Borja Sepulveda, Gabriel Loget,* and Neso Sojic*

Cite This: https://doi.org/10.1021/jacs.3c05856
Read Online

ACCESS | Metrics & More | Article Recommendations | Supporting Information

ABSTRACT: Electrochemiluminescence (ECL) is widely employed for medical diagnosis and imaging. Despite its remarkable analytical performances, the technique remains intrinsically limited by the essential need for an external power supply and electrical wires for electrode connections. Here, we report an electrically autonomous solution leading to a paradigm change by designing a fully integrated all-optical wireless monolithic photoelectrochemical device based on a nanostructured Si photovoltaic junction modified with catalytic coatings. Under illumination with light ranging from visible to near-infrared, photogenerated holes induce the oxidation of the ECL reagents and thus the emission of visible ECL photons. The blue ECL emission is easily viewed with naked eyes and recorded with a smartphone. A new light emission scheme is thus introduced where the ECL emission energy (2.82 eV) is higher than the excitation energy (1.18 eV) via an intermediate electrochemical process. In addition, the mapping of the photoelectrochemical activity by optical microscopy reveals the minority carrier interfacial transfer mechanism at the nanoscale. This breakthrough provides an all-optical strategy for generalizing ECL without the need for electrochemical setups, electrodes, wiring constraints, and specific electrochemical knowledge. This simplest ECL configuration reported so far opens new opportunities to develop imaging and wireless bioanalytical systems such as portable point-of-care sensing devices.



Downloaded via UNIV AUTONOMA DE BARCELONA on August 4, 2023 at 14:48:49 (UTC).
See https://pubs.acs.org/sharingguidelines for options on how to legitimately share published articles.

INTRODUCTION

Among the luminescence techniques, electrochemiluminescence (ECL) is an ultrasensitive analytical technique[1] that is widely applied in biosensing[2−4] and imaging.[5] The ECL light emission is triggered by electrochemistry.[6] The electrochemical reactions initiated at the electrode surface generate the excited state of the luminophore that relaxes by emitting light. Its intrinsic remarkable features are nicely exploited in biosensing, especially for clinical diagnostics with successfully commercialized immunoassays.[7−10] In addition, since ECL offers an optical readout, it evolves progressively from a pure analytical technique to a powerful microscopy.[11,12] For example, Feng and co-workers resolved spatially a single photon emitted by an individual ECL reaction.[5,13,14] Moreover, single entities such as nanoparticles, cells, or mitochondria have been imaged by ECL microscopy.[15−22]

In spite of its exceptional analytical capabilities, ECL requires the use of an external source of electricity (typically, a potentiostat) powered by the local electrical network and an electrochemical setup involving reference and counter electrodes, connectors, and electrical wires. This considerably limits the applicability of ECL, especially for non-specialists and for on-site and portable analysis. In all the approaches documented so far, potentiostats or comparable electrical powering devices are necessary to produce ECL emission. Recent advances in photoinduced ECL have shown the possibility to reduce the potential needed to achieve ECL at an illuminated semiconductor electrode;[23−25] however, external power sources were still required hitherto. Here, we report an original approach for true wireless ECL generation that only requires an all-integrated monolithic device and a light source. The approach, named all-optical ECL (AO-ECL), is based on a nanostructured *pnn*$^{++}$Si photovoltaic junction, modified with catalytic Au and Pt coatings to generate ECL and the associated counter reaction at each device side under illumination with a low-cost light-emitting diode. This electrically autonomous strategy was inspired by research on monolithic water splitting photoelectrochemical devices,[26−35] in which the light absorbed by an immersed photovoltaic junction generates charge carriers that are directly employed at integrated catalytic interfaces for water electrolysis. It requires neither an electrical power supply nor additional electrodes but only a single all-optical device immersed in a standard ECL solution, thus constituting the simplest ECL configuration reported so far.

Received: June 5, 2023

© XXXX American Chemical Society

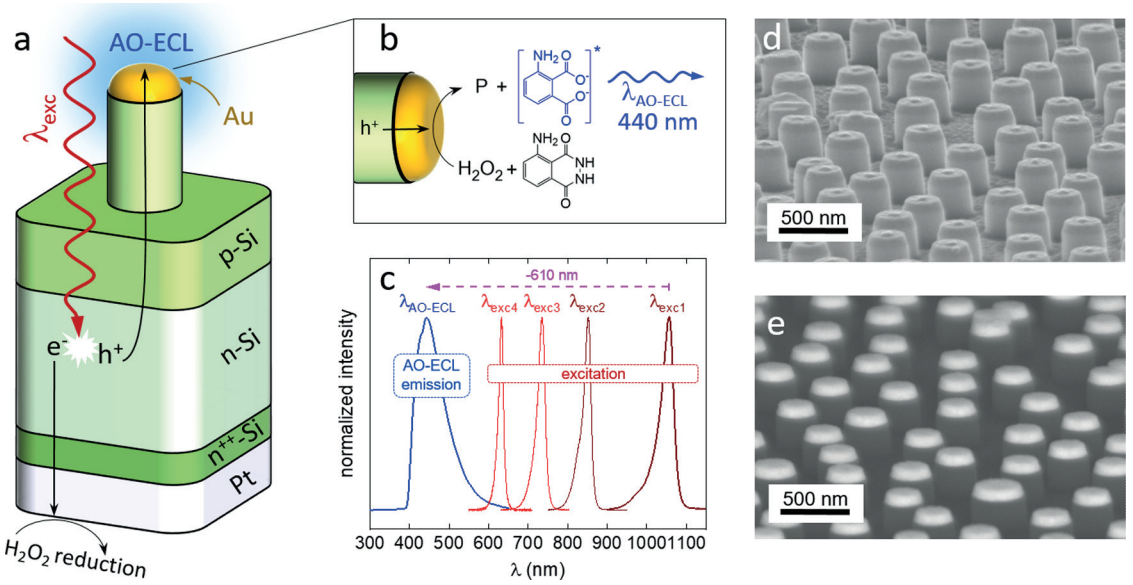


Figure 1. Description of the monolithic ECL device and light emission schemes. (a) Scheme of monolithic AO-ECL at a nanostructured Au-*pnn*$^{++}$Si-Pt junction under illumination. (b) Hole transfer mechanism leading to visible photons generation at the solid−liquid interface, P represents reaction products. (c) Normalized spectra of the incident excitation light-emitting diodes (brown/red curves) and the resulting AO-ECL emission of luminol/H_2O_2 at Au-*pnn*$^{++}$Si-Pt (blue curve); the largest anti-Stokes shift is represented by a pink dashed arrow. (d and e) Secondary (d) and backscattered (e) electron microscopy images of the frontside of Au-*pnn*$^{++}$Si-Pt.

RESULTS AND DISCUSSION

The reported approach is based on photoelectrochemical Au-*pnn*$^{++}$Si-Pt devices that were manufactured on Si wafers by a combination of dopant implantation, nanosphere lithography, and reactive ion etching (Section Manufacturing of the Au-*pnn*$^{++}$Si-Pt Junction in Supporting Information). As shown in Figure 1a, they are composed of a *pn*-Si photovoltaic junction interfaced at both sides with noble metal contacts, enabling efficient electrochemical reactions (Figure 1a,b). The implantation of a highly doped n^{++}Si layer between *n*Si and the Pt thin film (Figure S1) ensured the formation of an ohmic contact and optimal charge collection at the metal. The frontside (i.e., the illuminated side in Figure 1a) of the device comprised an array of randomly distributed Au-capped nanopillars with a diameter of ∼275 nm and a total height of 265 nm, which comprises 190 nm of the silicon nanopillar and 75 nm of the Au nanodisk, as shown in Figure 1d (secondary electrons image), Figure 1e (backscattered electron image), and Figure S2. X-ray photoelectron spectroscopy (XPS, Figure S3) confirmed the expected chemical composition at each side of the device (Section Description of the XPS Spectra in Supporting Information) and scanning electron microscopy (SEM) revealed the geometry of the nanostructures at the frontside. Figure 1d,e shows the entire nanopillars' morphology and the geometrical features of the Au nanodisks (a diameter of ∼275 nm and a height of 75 nm). The nanopillar geometry was designed for operating from the visible to the near-IR absorption and avoiding the shortcut of the *pn* junction when the electrolyte solution is exposed to both *n*- and *p*-doped regions. The Si-Au nanopillars exhibit enhanced absorption at 850 nm due to the excitation of a hybrid plasmonic-dielectric resonance (Figure S4a,c Section Optical Simulation in Supporting Information). Note that the pure plasmonic resonance of the Au nanodisk is located at 1.5 μm, i.e., much higher than the silicon bandgap 1.1 μm (Figure S4b,d). Due to its electrocatalytic performance for the H_2O_2 reduction,[36] a 50 nm-thick Pt (Figure S1) thin film was deposited at the backside (i.e., the non-illuminated side in Figure 1a) of the junction. In our studies, the Au-*pnn*$^{++}$Si-Pt device was immersed in a standard ECL aqueous system containing 3-aminophthalhydrazide (i.e., luminol) as the luminophore and H_2O_2.[1] These reagents constitute a model ECL system widely used in different fields such as biosensing, forensic science, and imaging.[1,37] The mechanism for the wireless AO-ECL generation occurring at the monolithic Au-*pnn*$^{++}$Si-Pt device during frontside illumination is depicted in Figure 1a,b. Under irradiation with photons having a higher energy than the Si bandgap (i.e., $\lambda_{exc} < 1.1$ μm), electron/hole pairs are generated at the photoactive Si *pn* junction, as it was confirmed by the photovoltaic solid-state measurements in Figure S5. Driven by the induced photovoltage (band diagram presented in Figure S6), the photogenerated electrons diffuse to the Pt surface where they trigger the H_2O_2 reduction, and the holes diffuse to the Au contacts where they afford simultaneous oxidation of H_2O_2 and luminol.[36,37] The concomitant oxidation of H_2O_2 and luminol, depicted in Figure 1b, is a well-known ECL process that produces blue light through a bond-breaking mechanism where the 3-aminophthalate* excited state relaxes to the ground state by emitting a photon at λ_{ECL} = 440 nm.[1,38−40] In the case of the Au-*pnn*$^{++}$Si-Pt device, the illumination leads to an anti-Stokes process where low-energy photons (from 1.18 eV) are converted into high-energy photons (2.82 eV), resulting in an anti-Stokes shift, which can be higher than 600 nm (Figure 1c). Such a large shift allows us to easily separate illumination from the AO-ECL emission.

To understand the wireless AO-ECL processes, the electrochemical properties of the frontside (the Au-*pnn*$^{++}$Si photoanode) and the backside (the Pt cathode) were independently investigated in the presence of the ECL electrolyte using a conventional three-electrode setup (Section Photoelectrochemical Measurements and Figure S7 in Supporting Information). We first discuss the photoanode

https://doi.org/10.1021/jacs.3c05856
J. Am. Chem. Soc. XXXX, XXX, XXX−XXX

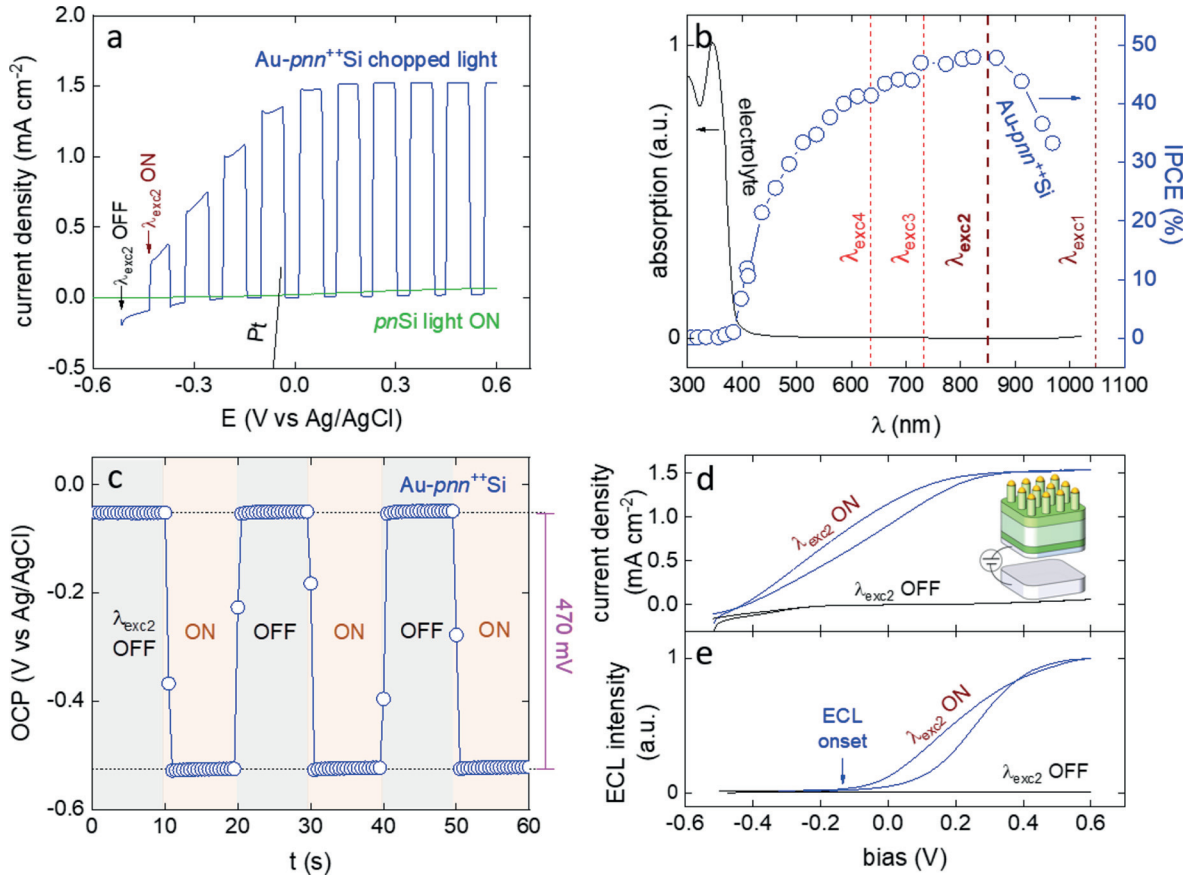


Figure 2. Electrochemical characterization of the involved surfaces. (a) Linear sweep voltammograms (50 mV s^{-1}) recorded with a three-electrode setup under intermittent IR light illumination at Au-*pnn*$^{++}$Si (blue curve), under IR light illumination at *pn*Si (green curve), and in the dark at Pt (gray curve). (b) IPCE spectrum recorded with a three-electrode setup at Au-*pnn*$^{++}$Si (blue curve) at 0.6 V vs Ag/AgCl, overlaid with the electrolyte absorption (black curve). The excitation wavelengths are represented by dashed lines. (c) OCP recorded with a three-electrode setup at Au-*pnn*$^{++}$Si under intermittent IR light illumination. The photovoltage is indicated by a pink line. (d and e) Cyclic voltammograms (50 mV s^{-1}) (d) and corresponding ECL intensity (e) measured with a two-electrode setup comprising an Au-*pnn*$^{++}$Si anode and a Pt cathode under IR light illumination (blue curves) and in the dark (black curves). Inset: Scheme of the two-electrode setup. Electrolyte composition: 10 mM luminol, 33 mM H_2O_2 (pH = 12.8), 0.1% Triton X-100. λ_{exc2} = 850 nm, P_{LED} = 5 mW cm^{-2}.

behavior. The blue voltammogram of Figure 2a, recorded on the Au-*pnn*$^{++}$Si under intermittent 850 nm irradiation (power density P_{LED} = 5 mW cm^{-2}), displays a pronounced photoactivity, which is characterized by a negligible dark current, a high photocurrent generation under near-IR irradiation (maximum current density, j_{max} = 1.5 mA cm^{-2}), and a low onset potential (−0.52 V vs Ag/AgCl, Figure S8a). This measurement demonstrates that the photogenerated holes efficiently participate in oxidation processes at the solid−liquid interface. As a comparison, an Au-free and flat *pn*Si junction studied in the same illumination conditions only produced a 30-fold lower photocurrent density (50 μA cm^{-2}) (Figure 2a, green curve) due to the poor hole transfer at the SiO_x interface impeding the electrochemical reactivity.[41−43] This effect reveals the essential role of the nanostructured Au metal contacts to promote an efficient interfacial Faradaic process by protecting the underlying Si from electrical passivation.[44−46]

The incident photon-to-current efficiency (IPCE) spectrum (Figure 2b, blue curve) recorded at 0.6 V vs Ag/AgCl at Au-*pnn*$^{++}$Si confirmed the strong photoactivity of the electrode in the visible-to-near-IR region with a maximum value of 48% at λ_{exc2} = 850 nm (note that the inactivity in the UV is caused by electrolyte absorption, Figure 2b, black curve). The open-circuit potential (OCP) measurements, performed under intermittent IR illumination (Figure 2c), allowed measuring a photovoltage value of 0.47 V, which is in good agreement with the 0.46 V estimated by voltammetry (Figure S8b). On the other hand, the gray voltammogram of Figure 2a, recorded at the Pt thin film in the dark (i.e., the backside of the Au-*pnn*$^{++}$Si-Pt junction, Figure 1a), displays a cathodic activity at an onset potential of −0.07 V vs Ag/AgCl, corresponding to H_2O_2 reduction (a cyclic voltammogram study is provided in Figure S9). The fact that the cathode onset potential is more positive than that of the illuminated photoanode indicates that the two shorted electrodes (Au-*pnn*$^{++}$Si-Pt) should spontaneously generate photocurrent in this medium.

This behavior was tested using a two-electrode electrochemical setup (depicted in the inset of Figure 2d, details in Section Photoelectrochemical Measurements, and Figure S10 in Supporting Information), which allows monitoring the current flow between the two surfaces as a function of bias. While negligible current was measured in the dark (Figure 2d, black curve), a considerable photocurrent was produced under the illumination of the Au-*pnn*$^{++}$Si photoanode with λ_{exc2} = 850 nm (Figure 2d, blue curve), with a short-circuit current density (i.e., at a bias of 0 V) of 1 mA cm^{-2}. If this proves that the system can spontaneously promote redox reactions at both faces, the possibility for AO-ECL generation was also assessed

https://doi.org/10.1021/jacs.3c05856
J. Am. Chem. Soc. XXXX, XXX, XXX−XXX

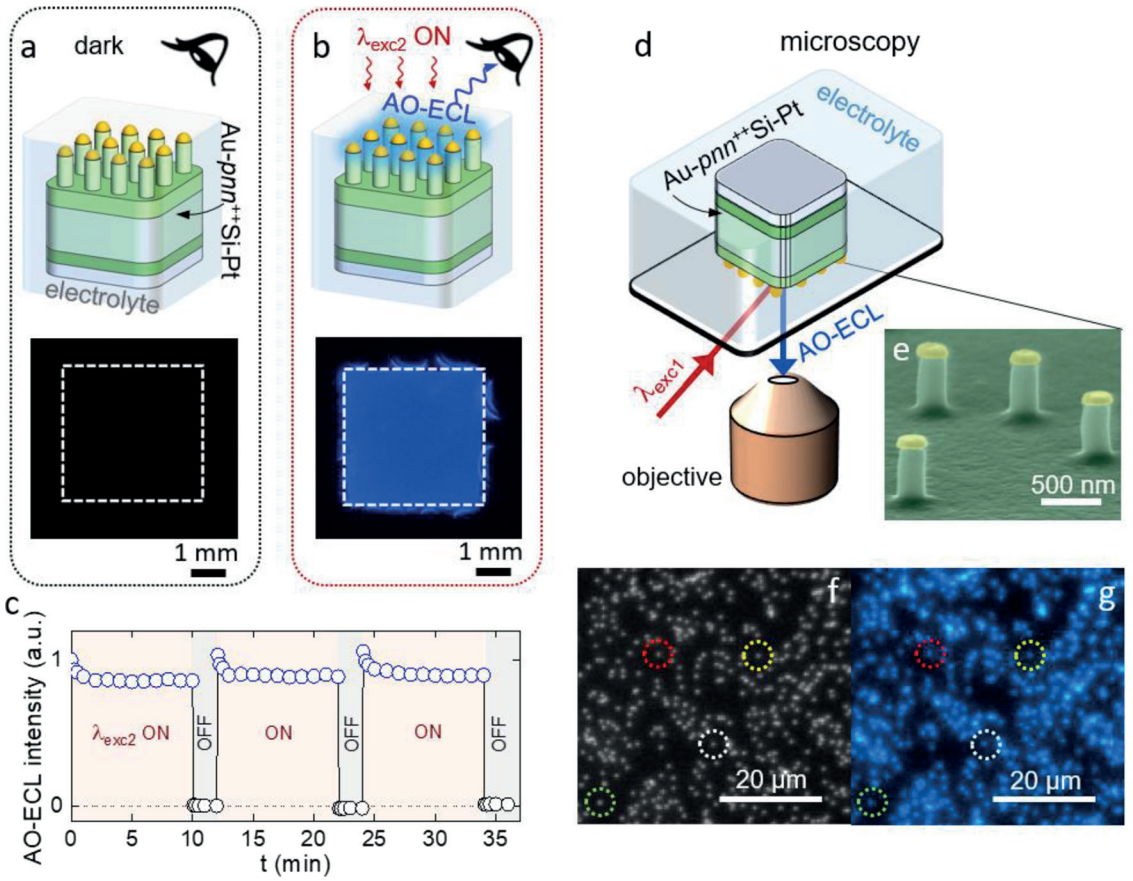


Figure 3. Monolithic photoelectrochemical emission resolved at the macroscopic and the single nanopillar scale. (a and b) Schemes (top) and corresponding smartphone photographs (bottom) showing Au-*pnn*$^{++}$Si-Pt immersed in the electrolyte in the dark (a) and under 850 nm illumination (b). (c) Graph showing the AO-ECL intensity emitted at the Au-*pnn*$^{++}$Si-Pt frontside as a function of time under intermittent IR illumination (λ_{exc2} = 850 nm, P_{LED} = 18 mW cm^{-2}). (d) Scheme showing the ECL imaging setup. (e) Colored SEM image showing the Au-*pnn*$^{++}$Si-Pt frontside, structured with a low nanopillar density, studied by AO-ECL microscopy. (f and g) Optical microscopy images of the Au-*pnn*$^{++}$Si-Pt frontside (low nanopillar density) measured under white light (f) and IR (λ_{exc1} = 1050 nm, P_{LED} = 7 mW cm^{-2}) illumination (g). For clarity, four individual nanodisks are localized by colored dashed circles. Electrolyte composition: 10 mM luminol, 33 mM H_2O_2 (pH = 12.8), 0.1% Triton X-100.

by measuring emission at the photoanode with a spectrometer (details in Section Photoelectrochemical Measurements and Figure S10a in Supporting Information). Figure 2e presents the ECL intensity signal recorded during the bias sweep and shows that the ECL emission starts at negative bias, demonstrating the possibility for ECL generation in short-circuit conditions. This was further confirmed by monitoring the short-circuit ECL emission (Figure S11a,b presents the setup and the control experiments that are discussed in Section Description of Control Experiments in Supporting Information) as a function of time (Figure S11c) and P_{LED} (Figure S11d).

The Au-*pnn*$^{++}$Si-Pt monolithic device was then studied by immersing the entire surface in the ECL electrolyte without any contact and recording the blue light emission first with a smartphone camera (details in Section Macroscale Measurements of AO-ECL and Figure S12 in Supporting Information). Indeed, the emitted AO-ECL light was bright enough to be easily viewed with naked eyes. As schematized in Figure 3a,b and demonstrated by the corresponding photographs, blue color light was observable only when λ_{exc2} = 850 nm was applied at the device frontside. The emission signal responded instantaneously to the IR stimulus, its intensity depended on the applied irradiation power density (Figure S13), and it was stable for 30 min without a decrease in intensity, as shown in Figure 3c. Similar behavior was observed with visible excitation (λ_{exc} = 733 and 633 nm, Figure S14). In other words, illumination wavelengths ranging from the visible to the near-IR can generate bright AO-ECL emission. The incident light can be conveniently tuned, and the spectral limits are imposed at low and high wavelengths by the emission of the selected ECL system (to easily differentiate λ_{exc} from $\lambda_{AO\text{-}ECL}$) and the bandgap of Si, respectively. Finally, the phenomenon was investigated by microscopy experiments (depicted in Figure 3d, details in Section Microscopy Measurements of AO-ECL and Figure S15 in Supporting Information) where the frontside of Au-*pnn*$^{++}$Si-Pt junctions, specifically tailored with a low density of nanopillars (Figures 3e and S16), was observed under different illumination conditions. Under white light illumination, the gold-capped nanopillars appeared as white dots due to light reflection (Figure 3f). In contrast, under near-IR illumination with λ_{exc1} = 1050 nm (Figure 3g), individual AO-ECL-emitting spots appeared that colocalize with a good correlation with the white light image (Figure S17). The spatial distribution of AO-ECL emission spots (Figure 3g) matches perfectly the pattern observed by white light (Figure 3f). This experiment allowed the direct visualization of the light emission process at the single nanopillar level (four randomly chosen individual Si-Au nanopillars are identified by dotted

https://doi.org/10.1021/jacs.3c05856
J. Am. Chem. Soc. XXXX, XXX, XXX−XXX

circles in Figure 3f,g). In addition, this imaging approach demonstrates that the photogenerated solid−liquid charge transfer specifically occurs at the surface of the Au nanodisks, thereby enabling direct visualization of the photoelectrochemical activity, which is essential to optimize catalytic photoelectrodes.[47]

CONCLUSIONS

To conclude, our results highlight a novel all-optical strategy for the generation of ECL emission in a wireless manner without any electrical power supply, any electrochemical setups, any additional electrodes, and the constraints related to the electrode connections. The ability to produce electrically autonomous ECL using the simplest configuration reported so far is in marked contrast to current methods that are limited by the requirement of such specific electrochemical setups and knowledge. Using immersed Au-*pnn*$^{++}$Si-Pt fully integrated monolithic devices, comprising a nanostructured photovoltaic junction interfaced with electroactive conductive coatings, we were able to directly exploit photogenerated carriers for wireless and stable ECL emission. In this process, the light absorption by the nanostructured surface triggers electrochemical activity, which, in turn, induces the generation of blue light ($\lambda_{AO\text{-}ECL}$ = 440 nm). This blue ECL was produced efficiently with excitation wavelengths ranging from the visible (633 nm) to the near-IR (1050 nm). Microscopy experiments allowed us to correlate the emission spots with the nanoscale architecture of the device, demonstrating that interfacial charge transfer specifically occurs at the Au nanodisk−liquid interface. This process is remarkable in several aspects. As such, it constitutes an unprecedented direct light emission process reminiscent of light upconversion (among rare examples such as two-photon absorption or triplet−triplet annihilation)[48] working at low light intensities, where the emission energy (2.82 eV) is higher than the excitation energy (down to 1.18 eV). This represents an ultimate anti-Stokes shift of −610 nm. From an analytical point of view, although we have demonstrated it on these specifically tailored Au-*pnn*$^{++}$Si-Pt devices, this strategy should be also effective with other photoelectrochemical devices, such as nanostructured photoelectrodes,[49−51] semiconductor photocatalysts,[52,53] or artificial leaves,[54,55] and can play a relevant role in elucidating energy conversion mechanisms at the nanoscale. Finally, due to its all-optical nature, the simplicity and versatility of the reported approach should extend this powerful technique to non-specialists. Given the importance of ECL technologies for biosensing and medical diagnosis,[1−3] this phenomenon has a strong potential for the development of a new generation of sensitive and portable biosensing devices and imaging strategies.

ASSOCIATED CONTENT

Supporting Information

The Supporting Information is available free of charge at https://pubs.acs.org/doi/10.1021/jacs.3c05856.

Experimental section and additional surface characterization and electrical and optical data (PDF)

AUTHOR INFORMATION

Corresponding Authors

Gabriel Loget − *Univ Rennes, CNRS, ISCR (Institut des Sciences Chimiques de Rennes)-UMR6226, Rennes 35000, France; Institute of Energy and Climate Research, Fundamental Electrochemistry (IEK-9), Jülich 52425, Germany;* orcid.org/0000-0003-4809-5013; Email: gabriel.loget@cnrs.fr

Neso Sojic − *University of Bordeaux, Bordeaux INP, ISM, UMR CNRS 5255, Pessac 33607, France;* orcid.org/0000-0001-5144-1015; Email: sojic@u-bordeaux.fr

Authors

Yiran Zhao − *Univ Rennes, CNRS, ISCR (Institut des Sciences Chimiques de Rennes)-UMR6226, Rennes 35000, France*

Julie Descamps − *University of Bordeaux, Bordeaux INP, ISM, UMR CNRS 5255, Pessac 33607, France*

Nour al Hoda Al Bast − *Catalan Institute of Nanoscience and Nanotechnology (ICN2), CSIC and BIST, Barcelona 08193, Spain;* Present Address: Universitat Autonoma de Barcelona, Campus UAB, 08193 Barcelona, Spain

Marcos Duque − *Instituto de Microelectrónica de Barcelona (IMB-CNM, CSIC), Barcelona 08193, Spain*

Jaume Esteve − *Instituto de Microelectrónica de Barcelona (IMB-CNM, CSIC), Barcelona 08193, Spain*

Borja Sepulveda − *Instituto de Microelectrónica de Barcelona (IMB-CNM, CSIC), Barcelona 08193, Spain;* orcid.org/0000-0002-1562-7602

Complete contact information is available at: https://pubs.acs.org/10.1021/jacs.3c05856

Author Contributions

The manuscript was written through contributions of all authors. All authors have given approval to the final version of the manuscript.

Funding

The research was funded by ANR (LiCORN - ANR-20-CE29-0006), Nouvelle Aquitaine-Euskadi-Navarre Euroregion (project ECLiCare), and the Spanish Ministerio de Ciencia, Innovación y Universidades (MICINN) through the PID2019-106229RB-I00 and PCI2019-111896-2 (Euronanomed 2019) projects funded by MCIN/AEI/10.13039/501100011033. NHB acknowledges the financial support of the UMBM Scholarship from Lebanon.

Notes

The authors declare no competing financial interest.

ACKNOWLEDGMENTS

Loic Joanny and Francis Gouttefangeas (ScanMat/CMEBA) are acknowledged for SEM. The XPS platform and Dr. Corinne Lagrost (Univ Rennes, CNRS, ScanMat), UAR2025, are acknowledged. Prof. Alexander Kuhn (Univ. Bordeaux, ISM), Prof. Francisco Javier del Campo (BCMaterials), Dr. Lionel Santinacci and Dr. Yoan Léger from CNRS are acknowledged for valuable discussions.

REFERENCES

(1) Liu, Z.; Qi, W.; Xu, G. Recent Advances in Electrochemiluminescence. *Chem. Soc. Rev.* **2015**, *44*, 3117−3142.

(2) Yang, H.; Leland, J. K.; Yost, D.; Massey, R. Electrochemiluminescence: A New Diagnostic and Research Tool. *Nat. Biotechnol.* **1994**, *12*, 193−194.

(3) Zanut, A.; Fiorani, A.; Canola, S.; Saito, T.; Ziebart, N.; Rapino, S.; Rebeccani, S.; Barbon, A.; Irie, T.; Josel, H.-P.; Negri, F.; Marcaccio, M.; Windfuhr, M.; Imai, K.; Valenti, G.; Paolucci, F. Insights into the Mechanism of Coreactant Electrochemiluminescence

Facilitating Enhanced Bioanalytical Performance. *Nat. Commun.* **2020**, *11*, 2668.
(4) Ma, X.; Gao, W.; Du, F.; Yuan, F.; Yu, J.; Guan, Y.; Sojic, N.; Xu, G. Rational Design of Electrochemiluminescent Devices. *Acc. Chem. Res.* **2021**, *54*, 2936−2945.
(5) Dong, J.; Lu, Y.; Xu, Y.; Chen, F.; Yang, J.; Chen, Y.; Feng, J. Direct Imaging of Single-Molecule Electrochemical Reactions in Solution. *Nature* **2021**, *596*, 244−249.
(6) Ding, Z.; Quinn, B. M.; Haram, S. K.; Pell, L. E.; Korgel, B. A.; Bard, A. J. Electrochemistry and Electrogenerated Chemiluminescence from Silicon Nanocrystal Quantum Dots. *Science* **2002**, *296*, 1293−1297.
(7) Faatz, E.; Finke, A.; Josel, H.-P.; Prencipe, G.; Quint, S.; Windfuhr, M. Automated Immunoassays for the Detection of Biomarkers in Body Fluids. In *Analytical Electrogenerated Chemiluminescence: From Fundamentals to Bioassays*; The Royal Society of Chemistry: 2019; pp. 443−470.
(8) Wang, Y.; Zhao, G.; Chi, H.; Yang, S.; Niu, Q.; Wu, D.; Cao, W.; Li, T.; Ma, H.; Wei, Q. Self-Luminescent Lanthanide Metal−Organic Frameworks as Signal Probes in Electrochemiluminescence Immunoassay. *J. Am. Chem. Soc.* **2021**, *143*, 504−512.
(9) Wang, Y.; Ding, J.; Zhou, P.; Liu, J.; Qiao, Z.; Yu, K.; Jiang, J.; Su, B. Electrochemiluminescence Distance and Reactivity of Coreactants Determine the Sensitivity of Bead-Based Immunoassays. *Angew. Chem., Int. Ed.* **2023**, *62*, No. e202216525.
(10) Zhu, W.; Dong, J.; Ruan, G.; Zhou, Y.; Feng, J. Quantitative Single-Molecule Electrochemiluminescence Bioassay. *Angew. Chem., Int. Ed.* **2023**, *62*, No. e202214419.
(11) Zhang, J.; Arbault, S.; Sojic, N.; Jiang, D. Electrochemiluminescence Imaging for Bioanalysis. *Annu. Rev. Anal. Chem.* **2019**, *12*, 275−295.
(12) Rebeccani, S.; Zanut, A.; Santo, C. I.; Valenti, G.; Paolucci, F. A Guide Inside Electrochemiluminescent Microscopy Mechanisms for Analytical Performance Improvement. *Anal. Chem.* **2022**, *94*, 336−348.
(13) Dong, J.; Xu, Y.; Zhang, Z.; Feng, J. Operando Imaging of Chemical Activity on Gold Plates with Single- Molecule Electrochemiluminescence Microscopy. *Angew. Chem., Int. Ed.* **2022**, *61*, No. e202200187.
(14) Zhou, Y.; Dong, J.; Zhao, P.; Zhang, J.; Zheng, M.; Feng, J. Imaging of Single Bacteria with Electrochemiluminescence Microscopy. *J. Am. Chem. Soc.* **2023**, *145*, 8947−8953.
(15) Zhao, W.; Chen, H.-Y.; Xu, J.-J. Electrogenerated Chemiluminescence Detection of Single Entities. *Chem. Sci.* **2021**, *12*, 5720−5736.
(16) Zhu, M.-J.; Pan, J.-B.; Wu, Z.-Q.; Gao, X.-Y.; Zhao, W.; Xia, X.-H.; Xu, J.-J.; Chen, H.-Y. Electrogenerated Chemiluminescence Imaging of Electrocatalysis at a Single Au/Pt Janus Nanoparticle. *Angew. Chem., Int. Ed.* **2018**, *130*, 4047−4078.
(17) Ding, H.; Guo, W.; Su, B. Imaging Cell-Matrix Adhesions and Collective Migration of Living Cells by Electrochemiluminescence Microscopy. *Angew. Chem., Int. Ed.* **2020**, *59*, 449−456.
(18) Chen, M.-M.; Xu, C.-H.; Zhao, W.; Chen, H.-Y.; Xu, J.-J. Super-Resolution Electrogenerated Chemiluminescence Microscopy for Single-Nanocatalyst Imaging. *J. Am. Chem. Soc.* **2021**, *143*, 18511−18518.
(19) Valenti, G.; Scarabino, S.; Goudeau, B.; Lesch, A.; Jović, M.; Villani, E.; Sentic, M.; Rapino, S.; Arbault, S.; Paolucci, F.; Sojic, N. Single Cell Electrochemiluminescence Imaging: From the Proof-of-Concept to Disposable Device-Based Analysis. *J. Am. Chem. Soc.* **2017**, *139*, 16830−16837.
(20) Voci, S.; Goudeau, B.; Valenti, G.; Lesch, A.; Jović, M.; Rapino, S.; Paolucci, F.; Arbault, S.; Sojic, N. Surface-Confined Electrochemiluminescence Microscopy of Cell Membranes. *J. Am. Chem. Soc.* **2018**, *140*, 14753−14760.
(21) Liu, Y.; Zhang, H.; Li, B.; Liu, J.; Jiang, D.; Liu, B.; Sojic, N. Single Biomolecule Imaging by Electrochemiluminescence. *J. Am. Chem. Soc.* **2021**, *143*, 17910−17914.
(22) Descamps, J.; Colin, C.; Tessier, G.; Arbault, S.; Sojic, N. Ultrasensitive Imaging of Cells and Sub-Cellular Entities by Electrochemiluminescence. *Angew. Chem., Int. Ed.* **2023**, *62*, No. e202218574.
(23) Zhao, Y.; Yu, J.; Xu, G.; Sojic, N.; Loget, G. Photoinduced Electrochemiluminescence at Silicon Electrodes in Water. *J. Am. Chem. Soc.* **2019**, *141*, 13013−13016.
(24) Zhao, Y.; Descamps, J.; Ababou-Girard, S.; Bergamini, B.; Bergamini, L.; Léger, Y.; Sojic, N.; Loget, G. Metal-Insulator-Semiconductor Anodes For Ultrastable And Site-Selective Upconversion Photoinduced Electrochemiluminescence. *Angew. Chem., Int. Ed.* **2022**, *61*, No. e202201865.
(25) Vogel, Y. B.; Darwish, N.; Ciampi, S. Spatiotemporal Control of Electrochemiluminescence Guided by a Visible Light Stimulus. *Cell Rep. Phys. Sci.* **2020**, *1*, No. 100107.
(26) Fujishima, A.; Honda, K. Electrochemical Photolysis of Water at a Semiconductor Electrode. *Nature* **1972**, *238*, 37−38.
(27) Prévot, M. S.; Sivula, K. Photoelectrochemical Tandem Cells for Solar Water Splitting. *J. Phys. Chem. C* **2013**, *117*, 17879−17893.
(28) Khaselev, O.; Turner, J. A. A Monolithic Photovoltaic Photoelectrochemical Device for Hydrogen Production via Water Splitting. *Science* **1998**, *280*, 425−427.
(29) Sun, K.; Liu, R.; Chen, Y.; Verlage, E.; Lewis, N. S.; Xiang, C. A Stabilized, Intrinsically Safe, 10% Efficient, Solar Driven Water-Splitting Cell Incorporating Earth-Abundant Electrocatalysts with Steady-State PH Gradients and Product Separation Enabled by a Bipolar Membrane. *Adv. Energy Mater.* **2016**, *6*, No. 1600379.
(30) Sivula, K.; Van De Krol, R. Semiconducting Materials for Photoelectrochemical Energy Conversion. *Nat. Rev. Mater.* **2016**, *1*, 15010.
(31) Wang, Y.; Schwartz, J.; Gim, J.; Hovden, R.; Mi, Z. Stable Unassisted Solar Water Splitting on Semiconductor Photocathodes Protected by Multifunctional GaN Nanostructures. *ACS Energy Lett.* **2019**, *4*, 1541−1548.
(32) Fu, H.-C.; Varadhan, P.; Lin, C.-H.; He, J.-H. Spontaneous Solar Water Splitting with Decoupling of Light Absorption and Electrocatalysis Using Silicon Back-Buried Junction. *Nat. Commun.* **2020**, *11*, 3930.
(33) Zhou, P.; Navid, I. A.; Ma, Y.; Xiao, Y.; Wang, P.; Ye, Z.; Zhou, B.; Sun, K.; Mi, Z. Solar-to-Hydrogen Efficiency of More than 9% in Photocatalytic Water Splitting. *Nature* **2023**, *613*, 66−70.
(34) Ager, J. W.; Shaner, M. R.; Walczak, K. A.; Sharp, I. D.; Ardo, S. Experimental Demonstrations of Spontaneous, Solar-Driven Photoelectrochemical Water Splitting. *Energy Environ. Sci.* **2015**, *8*, 2811−2824.
(35) Lewis, N. S.; Nocera, D. G. Powering the Planet: Chemical Challenges in Solar Energy Utilization. *Proc. Natl. Acad. Sci. U. S. A.* **2006**, *103*, 15729−15735.
(36) Katsounaros, I.; Mayrhofer, K. J. J. The Influence of Non-Covalent Interactions on the Hydrogen Peroxide Electrochemistry on Platinum in Alkaline Electrolytes. *Chem. Commun.* **2012**, *48*, 6660.
(37) Liu, Y.; Shen, W.; Li, Q.; Shu, J.; Gao, L.; Ma, M.; Wang, W.; Cui, H. Firefly-Mimicking Intensive and Long-Lasting Chemiluminescence Hydrogels. *Nat. Commun.* **2017**, *8*, 1003.
(38) Haapakka, K. E.; Kankare, J. J. The Mechanism of the Electrogenerated Chemiluminescence of Luminol in Aqueous Alkaline Solution. *Anal. Chim. Acta* **1982**, *138*, 263−275.
(39) Shi, M. J.; Cui, H. Electrochemiluminescence of Luminol in Dimethyl Sulfoxide at a Polycrystalline Gold Electrode. *Electrochim. Acta* **2006**, *52*, 1390−1397.
(40) Zhang, X.; Lu, W.; Ma, C.; Wang, T.; Zhu, J. J.; Zare, R. N.; Min, Q. Insights Into Electrochemiluminescence Dynamics by Synchronizing Real-time Electrical, Luminescence, and Mass Spectrometric Measurements. *Chem. Sci.* **2022**, *13*, 6244−6253.
(41) Zhang, X. G. *Electrochemistry of Silicon and Its Oxide*; Kluwer Academic Publishers, 2007.
(42) Walter, M. G.; Warren, E. L.; McKone, J. R.; Boettcher, S. W.; Mi, Q.; Santori, E. A.; Lewis, N. S. Solar Water Splitting Cells. *Chem. Rev.* **2010**, *110*, 6446−6473.

https://doi.org/10.1021/jacs.3c05856
J. Am. Chem. Soc. XXXX, XXX, XXX−XXX

(43) Bae, D.; Seger, B.; Vesborg, P. C. K.; Hansen, O.; Chorkendorff, I. Strategies for Stable Water Splitting via Protected Photoelectrodes. *Chem. Soc. Rev.* **2017**, *46*, 1933−1954.
(44) Hill, J. C.; Landers, A. T.; Switzer, J. A. An Electrodeposited Inhomogeneous Metal−Insulator−Semiconductor Junction for Efficient Photoelectrochemical Water Oxidation. *Nat. Mater.* **2015**, *14*, 1150−1155.
(45) Kenney, M. J.; Gong, M.; Li, Y.; Wu, J. Z.; Feng, J.; Lanza, M.; Dai, H. High-Performance Silicon Photoanodes Passivated with Ultrathin Nickel Films for Water Oxidation. *Science* **2013**, *342*, 836−840.
(46) Loget, G.; Mériadec, C.; Dorcet, V.; Fabre, B.; Vacher, A.; Fryars, S.; Ababou-Girard, S. Tailoring the Photoelectrochemistry of Catalytic Metal-Insulator-Semiconductor (MIS) Photoanodes by a Dissolution Method. *Nat. Commun.* **2019**, *10*, 3522.
(47) Sambur, J. B.; Chen, T.-Y.; Choudhary, E.; Chen, G.; Nissen, E. J.; Thomas, E. M.; Zou, N.; Chen, P. Sub-Particle Reaction and Photocurrent Mapping to Optimize Catalyst-Modified Photoanodes. *Nature* **2016**, *530*, 77−80.
(48) Zhu, X.; Su, Q.; Feng, W.; Li, F. Anti-Stokes Shift Luminescent Materials for Bio-Applications. *Chem. Soc. Rev.* **2017**, *46*, 1025−1039.
(49) Liu, C.; Tang, J.; Chen, H. M.; Liu, B.; Yang, P. A Fully Integrated Nanosystem of Semiconductor Nanowires for Direct Solar Water Splitting. *Nano Lett.* **2013**, *13*, 2989−2992.
(50) Laskowski, F. A. L.; Oener, S. Z.; Nellist, M. R.; Gordon, A. M.; Bain, D. C.; Fehrs, J. L.; Boettcher, S. W. Nanoscale Semiconductor/Catalyst Interfaces in Photoelectrochemistry. *Nat. Mater.* **2020**, *19*, 69−76.
(51) Fabre, B.; Loget, G. Silicon Photoelectrodes Prepared by Low-Cost Wet Methods for Solar Photoelectrocatalysis. *Acc. Mater. Res.* **2023**, *4*, 133−142.
(52) Takata, T.; Jiang, J.; Sakata, Y.; Nakabayashi, M.; Shibata, N.; Nandal, V.; Seki, K.; Hisatomi, T.; Domen, K. Photocatalytic Water Splitting with a Quantum Efficiency of Almost Unity. *Nature* **2020**, *581*, 411−414.
(53) Teitsworth, T. S.; Hill, D. J.; Litvin, S. R.; Ritchie, E. T.; Park, J.-S.; Custer, J. P.; Taggart, A. D.; Bottum, S. R.; Morley, S. E.; Kim, S.; McBride, J. R.; Atkin, J. M.; Cahoon, J. F. Water Splitting with Silicon p−i−n Superlattices Suspended in Solution. *Nature* **2023**, *614*, 270−274.
(54) Nocera, D. G. The Artificial Leaf. *Acc. Chem. Res.* **2012**, *45*, 767−776.
(55) Reece, S. Y.; Hamel, J. A.; Sung, K.; Jarvi, T. D.; Esswein, A. J.; Pijpers, J. J. H.; Nocera, D. G. Wireless Solar Water Splitting Using Silicon-Based Semiconductors and Earth-Abundant Catalysts. *Science* **2011**, *334*, 645−648.

https://doi.org/10.1021/jacs.3c05856
J. Am. Chem. Soc. XXXX, XXX, XXX−XXX

Wireless pulsed nanophotoelectrochemical cell for the ultrafast degradation of organic pollutants

Albert Serrà[1,2,*], Elvira Gómez [1,2], Nour al Hoda al Bast[3], Yue Zhang[3], Marcos Duque[4], María José Esplandiu[3], Jaume Esteve[4], Josep Nogués[3,5] and Borja Sepúlveda[4*]

[1] Grup d'Electrodeposició de Capes Primes i Nanoestructures (GE-CPN), Departament de Ciència de Materials i Química Física, Universitat de Barcelona, Martí i Franquès, 1, E-08028, Barcelona, Spain.

[2] Institute of Nanoscience and Nanotechnology (IN^{2}UB), Universitat de Barcelona, Barcelona, Spain.

[3] Catalan Institute of Nanoscience and Nanotechnology (ICN2), CSIC and BIST, Campus UAB, E-08193 Bellaterra, Barcelona, Spain

[4] Institut de Microelectrònica de Barcelona (IMB-CNM, CSIC), Campus UAB, 08193 Bellaterra, Barcelona, Spain

[5] ICREA, Pg. Lluís Companys 23, 08010 Barcelona, Spain

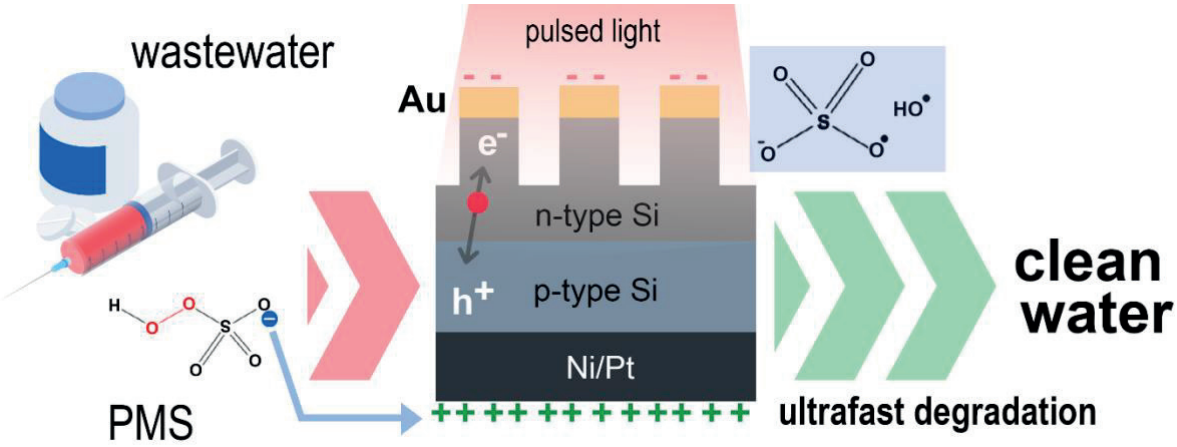
*Corresponding authors. E-mail: a.serra@ub.edu (A.S.), borja.sepulveda@csic.es (B.S.)

Abstract

An urgent demand exists for advanced technologies to efficiently remove persistent organic pollutants from water, while minimizing energy consumption. Here, we introduce an innovative wireless nanophotoelectrochemical (nPEC) cell using pulsed light for the ultrafast degradation and mineralization of organic pollutants. The nPEC cell comprises a nanostructured Si pn photodiode that monolithically integrates: (i) a Si-n/Au nanowire-based photocathode for effective light absorption and photovoltage generation, even at low light intensities in the safe near-infrared or visible spectrum, and (ii) a Si-p/mesoporous-NiPt photoanode serving as catalyst to wirelessly amplify the sulfate radical production by low-intensity light without any bias voltage. The efficacy of the proposed nPEC cell was shown by the ultrafast degradation (>99%) and mineralization (>98%) of three emerging pollutants (tetracycline, levofloxacin, and anatoxin-

A). Notably, reaction kinetics were boosted by more than one order of magnitude when exposed to light intensities ca. 5-fold lower than sunlight. Remarkably, pulsed light beams in the 100-500 Hz range provided an additional enhancement in the degradation and mineralization efficiencies, reducing energy input by half, while enhancing the NiPt catalyst's oxidation state and durability. The wireless activation, low energy consumption using safe NIR light, and compatibility with industrial photovoltaic technology position this pulsed nPEC approach as a promising solution for efficient water treatment.

Graphical abstract



Keywords: nanophotoelectrochemical cell, wireless, heterogeneous catalysis; water decontamination; advanced oxidation process; Peroxymonosulfate; antibiotics; biotoxins

1. Introduction

To ensure safe and clean drinking water, various methods can be applied to remove contaminants from water, such as advanced oxidation processes (AOPs), biological treatment, adsorption, membrane filtration, or chemical treatments [1–4]. However, most conventional methods are inadequate to effectively eliminate emerging organic pollutants due to their low concentrations, with certain cyanotoxins exhibiting harmful effects even at parts per billion (ppb) levels [5,6].

Advanced oxidation processes have garnered interest for their ability to simultaneously remove inorganic and organic pollutants from water. Operating through radical-mediated mechanisms, AOPs break down – or even mineralize (i.e., total oxidation) – complex organic compounds into harmless byproducts and inorganic forms that can be utilized by living organisms [7–9]. Radical-mediated mineralization of organic matter is a complex process that relies on the effective formation of highly reactive species. The formation of these radicals is a critical factor in chemical and photochemical reactions that can occur through various mechanisms, enabling a broad range of chemical transformations. One mechanism to form radicals is electron transfer, where a catalyst enhances the charge exchange with the species, allowing the generated radical to participate in chemical reactions [10,11]. Therefore, in order to optimize radical-mediated mineralization, it is crucial to carefully consider the selection of the radical initiator and the environmental conditions to ensure the highest possible yield of radicals [12–14].

Peroxymonosulfate (PMS) is an effective oxidizing agent that can produce highly reactive radicals under specific conditions. To activate PMS, reducing agents are typically required, which can come from oxidized compounds of transition metals such as Fe, Co, Mn, or Ni [15–18]. The reducing agent reacts with PMS to form a complex that undergoes a series of reactions leading to the formation of highly reactive sulfate radicals ($SO_4^{\bullet-}$). The sulfate radical, with its high redox potential (2.6-3.1 V), generated through PMS activation, can be utilized for a wide range of chemical and environmental applications, including the oxidation and transformation of organic contaminants into harmless carbon dioxide and water [19,20]. Compared to the hydroxyl radical, it

exhibits advantages such as effective operation across a broader pH range and longer lifespan. Sulfate radical-based advanced oxidation processes have gained attention in recent decades due to their high reactivity and ability to oxidize a broad group of toxic and non-biodegradable emerging organic pollutants [20,21].

On the other hand, photoelectrochemical (PEC) oxidation of organic pollutants is an intriguing and emerging advanced oxidation process that can overcome the limitations associated to photocatalysis, such as catalyst recovery and electron-hole recombination, as well as those of conventional electrocatalysis [22–26]. In PEC cells, photons generate photocarriers, which are efficiently separated via an applied bias potential. However, in the case of photoelectrochemical oxidation, both light and applied potential are employed to generate strong oxidants that indiscriminately oxidize organic compounds in wastewater. Despite potential of PEC cells, current research efforts primarily focus on other processes like water splitting [27–29].

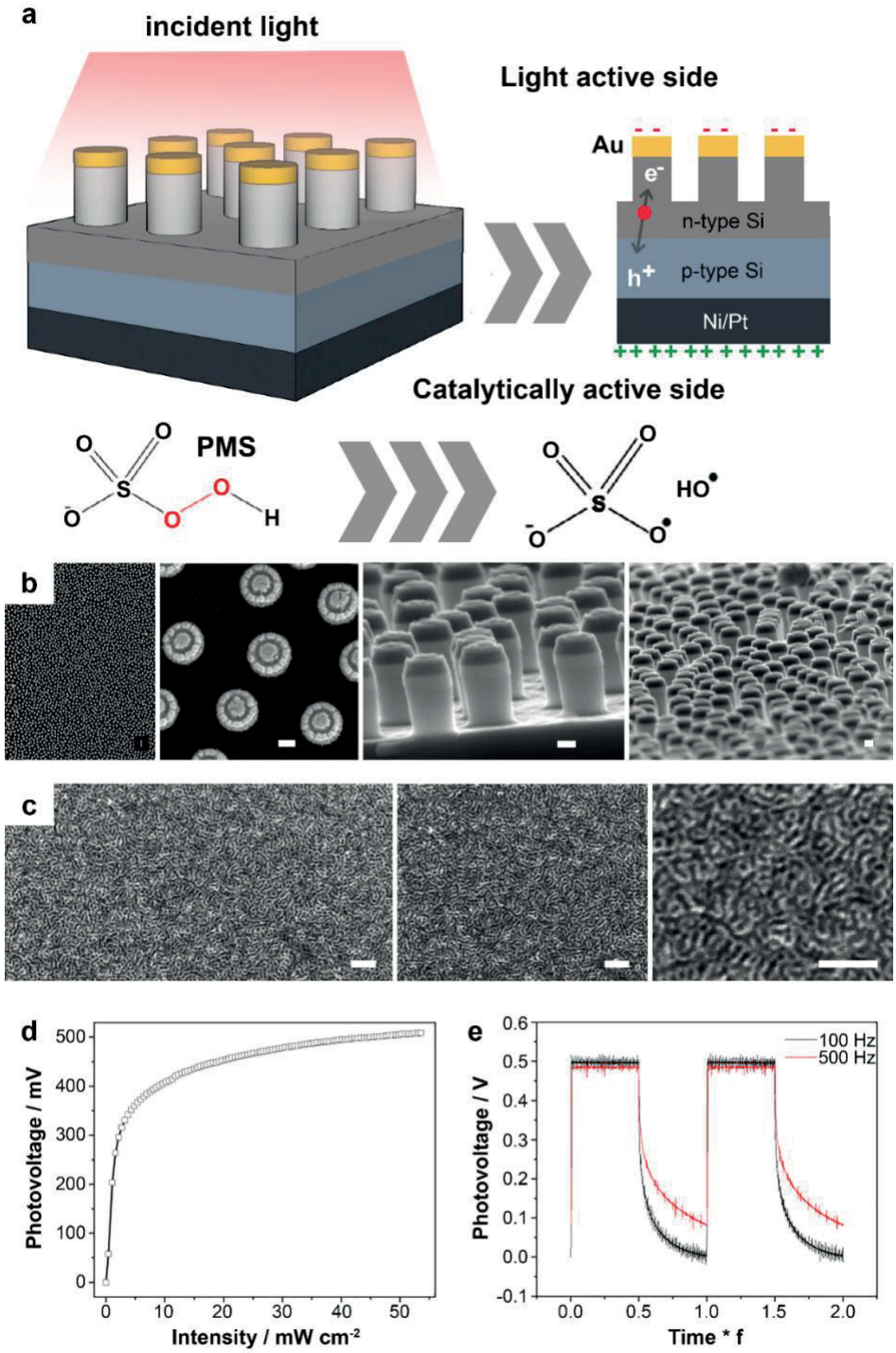
This study proposes a wireless pulsed nanophotoelectrochemical (nPEC) cell using PMS for the ultrafast degradation of organic pollutants, which is demonstrated by the mineralization of two different antibiotics and a biotoxin. The nPEC cell monolithically integrates a Si pn photodiode with a nanostructured Si-n/Au photocathode and a Si-p/mesoporous-NiPt photoanode to drastically amplify the generation of sulfate radicals with low intensity light beams without any external wiring or application of bias voltage. Strikingly, we demonstrate that illumination with a pulsed light beam with a frequency in the 100-500 Hz range enables an additional amplification of the pollutant degradation efficiency with a 2-fold reduction of the required average light intensity (ca. 10-fold lower than that of the sunlight) and, therefore, of the necessary energy input. Understanding the light triggered catalytic and photovoltaic effects in the nPEC structure that amplify the generation of radicals opens the path to the mineralization of organic pollutants in water bodies with very high energy efficiency.

2. Results and discussion

2.1. Characterization of the wireless nanophotoelectrochemical cell

Figure 1 shows the schematic of the wireless nanophotoelectrochemical (nPEC) cell, which is composed of two differentiated functional parts: (i) the light active side with a pn-junction, in which the n doped layer is formed by an array of Si/Au nanowires (NW) homogeneously distributed across the surface (average diameter and height 270 nm and 460 nm, respectively, surface density of 12 NW μm^{-2}, gold nanodiscs thickness 70 nm) acting as photocathode, and (ii) the catalytically active layer on the p-doped Si side, acting as photoanode, formed by a Ni-rich mesoporous NiPt film.

The fabrication nPEC cells was carried out following the following steps: (i) implantation and activation of the n dopants on the polished side of 4-inch Si wafers, (ii) deposition of the Au layers (75 nm) on both sides of the wafers, (iii) large scale colloidal nanolithography on the implanted n-doped side to form the Si/Au nanowires in the whole wafer surface (**Figure 1b**), (iv) wafer dicing in chips of 7 mm x 14 mm, and (v) deposition of the catalytic mesoporous NiPt film (between 130 µg and 160 µg per nPEC cell) on the p-doped side of the chips (**Figure 1c**) via a simple potentiostatic block-copolymer templated electrodeposition process, in which the block–copolymer micelles acted as porogen agents (more details can be found in the experimental section).



111

112 **Figure 1: The wireless nanophotoelectrochemical cell.** a) Schematic illustration of the wireless
113 nanophotoelectrochemical cell and the working principle. b) FE-SEM images of the arrays of
114 Au/Si nanowires in the n doped side of the wafer. c) Mesoporous NiPt films prepared at –1000
115 mV on the unpolished p doped side of the wafer. Scale bars: 100 nm; d) Generated photovoltages
116 vs light intensity for continuous wave light beam, and e) Photovoltage changes under squared-
117 pulsed light with 100 Hz and 500 Hz frequencies, under a light intensity of 50 $mW \cdot cm^{-2}$.

The nanostructured light active side has been designed to maximize the absorption of the NIR radiation (wavelength 810 nm) used in this work, and to maximize the generated photovoltages. The enhanced light absorption is due to the excitation of hybrid plasmonic/dielectric resonances in the Si/Au nanowires [30]. Note that the spectral position of the pure plasmonic resonance of the Au nanodiscs is located over 1.5 μm wavelength. This light active side is able to generate open circuit photovoltages up to 500 mV, for a continuous wave light intensity of ca. 50 $mW \cdot cm^{-2}$. (**Figure 1d**). The photovoltage versus intensity curve exhibited an initial steep increase for light intensities up to 4 $mW \cdot cm^{-2}$, and slower increment over this intensity. If instead of a continuous light source, the light is pulsed with a square shape pattern, the photovoltage shows also a square pattern with an initial sharp increase and slower decrease when the light intensity is turned to zero (**Figure 1e**). In the case of 100 Hz square modulation, the photovoltage was able to drop up to zero before the next light pulse was on. However, the nPEC cell, which acts as a capacitor, was not able to fully discharge when the square-pulsed light had a frequency of 500 Hz. Therefore, in this case, an average higher photovoltage can be obtained compared to the 100 Hz light modulation, which has an important effect in the opto-electric amplification of the catalytic effects, as will be shown below.

On the other hand, the catalytically active mesoporous Ni-rich NiPt layer, whose morphology and architecture are shown in **Figure 1c**, was first optimized to maximize its catalytic activity in the transformation of the peroxymonosulfate (PMS) into highly reactive sulfate and hydroxyl radicals in the absence of illumination. The morphology and composition were fine-tuned by selecting the applied potential [31,32]. **Table S1** summarizes the elemental composition of each electrodeposit as a function of the applied potential. The content of nickel increased as the applied potential became more negative, but the quality of the porosity and the film thickness diminished. Therefore, a compromise between nickel content and porosity integrity was necessary to maximize the catalytic activity. The high porosity is particularly relevant in the heterogeneous catalytic

transformation of PMS because it provides a larger surface area and more active centers, thus becoming more reactive.

The chemical composition and oxidation state of the NiPt films is also especially relevant to efficiently activate the PMS. It is very important to have an oxidized Ni surface, as it is known that Ni(0) frequently generates a competing reaction with PMS in which no sulfate or hydroxyl radicals are formed, thereby forcing the increase in the PMS concentration [33]. To analyze the composition of the deposited films, XPS analysis of Ni 2p and Pt 4f was performed, and the obtained binding energies were calibrated using the C 1s peak (284.60 eV). As shown in **Figure S1**, for the three deposition voltages, the Ni 2p spectra revealed that Ni(II) oxides were the most abundant superficial species. This is especially important because Ni^{2+}, among other transition metal ions (e.g., Co^{2+}, Mn^{2+}, Fe^{2+}, and Ru^{3+}), has proven to be an exceptional activator of PMS [34–37]. The relative amount of metallic nickel was more relevant at less negative potentials, because the pH variation at the electrode's interface, enhanced by the presence of Pt, caused the chemical precipitation of nickel hydroxides. The contribution of metallic nickel also increased after Ar ion sputtering, thus demonstrating the formation of a highly oxidized Ni surface. At the same time, the Pt 4f spectra of the surfaces revealed the predominant presence of metallic Pt at 71.4 eV and Pt(I) at 72.3 eV, possibly due to the formation of some Pt hydroxide.

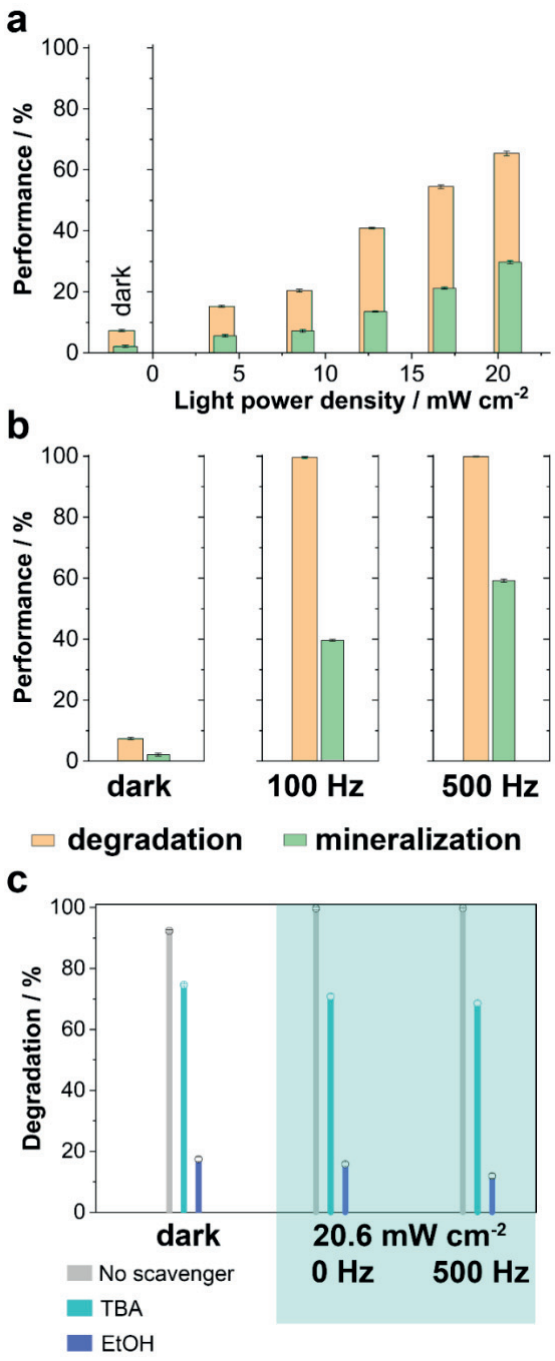
To determine and optimize the catalytic activity towards PMS activation of the mesoporous NiPt layers deposited at different voltages, their efficiency to degrade and mineralize the antibiotic tetracycline was analyzed under dark conditions (see **Table S2**). As can be observed in **Figure S2**, the catalytic efficiency of the mesoporous pure Pt film was very low, showing poor tetracycline degradation and negligible mineralization. The degradation/mineralization efficiencies clearly improved when de Ni/Pt ratio increases, i.e., for higher deposition potentials. Degradation rates exceeding 90% were observed when the Ni-to-Pt ratio was 19 after 10 min reaction. Therefore, Pt did not facilitate the catalytic process, but it is nevertheless necessary to attain the mesoporous architecture. Therefore, although Pt does not directly affect the activation of PMS, the maximization of the surface area was pivotal to increase catalytic efficiency. The

mineralization values were slightly lower, as can be expected, but the same tendency was observed as a function of the Ni/Pt ratio. As a result, for all the subsequent experiments under illumination conditions the optimal deposition of the mesoporous NiPt films at -1000 mV was fixed.

We also assessed the tetracycline degradation efficiency in the presence of PMS by the nanostructured Si/Au interface with and without illumination, showing a negligible effect, as expected from the low activity of both materials to activate the PMS.

2.2. Degradation and mineralization amplification by the wireless nPEC cell

We now show the capacity to drastically accelerate the activation of the PMS with the light illumination in the monolithically integrated nPEC cell, under wireless actuation, i.e., without applying any bias voltage. We analyzed the effect of the light intensity for continuous wave illumination, and the ability to amplify even further the PMS activation under pulsed actuation at different frequencies by reducing the net amount of incident NIR photons (and the input energy) by half, using the tetracycline degradation and mineralization as model. The nPEC cell was totally immersed in the polluted aqueous media for all the experiments. The experiments were conducted with a short contact time of 3 min to clearly capture the amplification of the tetracycline degradation kinetics (**Figure 2**). The first interesting observation is that, even for low light intensities (*e.g.*, 4 $mW \cdot cm^{-2}$), there was a clear amplification of both the degradation of mineralization values **Figure 2a,** and this amplification steadily increased with the light intensity. After only 3 min of reaction, a degradation exceeding 65% and nearly 30% mineralization were achieved when the nPEC cell was irradiated with a light intensity of 20.6 mW cm^{-2}, which corresponds to a remarkable 8.6-fold and 14.1-fold amplifications of the degradation and mineralization efficiencies, respectively with respect to the dark condition. It is worth highlighting that such light intensity is ca. 5-fold lower than sunlight.



195

196 **Figure 2: Demonstration of the continuous and pulsed light amplification of degradation**
197 **and mineralization of tetracycline**. a) Tetracycline degradation and mineralization after 3 min
198 of treatment as a function of the continuous wave light intensity. b) Tetracycline degradation and
199 mineralization of nPEC cell, after 3 min, in dark and under pulsed (i.e., 100 Hz and 500 Hz) light
200 irradiation (20.6 mW cm^{-2}). The error bars indicate the standard deviations from three replicate
201 experiments. c) Effect of tert-butyl alcohol (TBA) and ethanol (EtOH), as radical quenchers, on

the degradation of tetracycline after 10 min in the dark and under continuous and pulsed light irradiation (highlighted area). Experimental conditions: 20 ppm of tetracycline, [PMS] = 0.3 mM, T = 20 °C, and pH 7.0.

Even more striking was the effect of the pulsed light on the tetracycline degradation and mineralization efficiencies. Even though the amount of incident photons was twice lower, the pulsed light was able to amplify even further both the tetracycline degradation and mineralization. In these cases, the degradation of the antibiotic was practically completed with the light pulsed at 100 Hz and 500 Hz frequencies (see **Figure 2b** and **Table S4**), and achieved outstanding values of mineralization of 39.5% and 59.2% after only 3 min of reaction, i.e., 18-fold and 28-fold amplification, respectively, with respect to the dark conditions. Importantly, the mineralization efficiency could be fully completed by just increasing the reaction time up to 10 min, as can be observed in **Figure S3-4,** for the illumination at 20.6 $mW \cdot cm^{-2}$ and 500 Hz modulation. Again, it should be emphasized that these results were obtained with an average light intensity that was ca. 10-fold lower than the sunlight, and with safe low energy NIR light, using nPEC cells with light and catalytic active cross-sections of only 1 cm^2 and 0.5 cm^2, respectively, and without applying any bias voltage.

The nPEC system exhibited notably superior performance for the degradation and mineralization of tetracycline compared to various other strategies employing catalytically activated PMS with heterogeneous systems [38–45], particularly considering the low amount of catalyst (between 45 µg/mL and 55 µg/mL). For example, Cu-doped CoOOH achieved tetracycline degradation rates as high as 97.7% in 10 min, yet their mineralization rates reached only 51.5% [38]. In other examples, around 90% degradation could be obtained in 40 min for single-atom Fe-g-C_3N_4 catalysts [39], ca. 98% in 60 min for WO_3/BiOBr [40], roughly 80% in 40 min with CoO@Co-N-GC [41], about 94% in 60 min in Ag/MoS_2@Fe-CS catalysts[42], 98% in 12 min in Ca-Co bimetallic catalyst[44], and a remarkable degradation of 99.6% in 24 min, but with mineralization rates below 56% with Co–Zn–N–C catalysts [45]. In the case of $SrTiO_3$/$BaFe_{12}O_{19}$ catalysts stimulated with

visible light, approximately 96% degradation was obtained in just 1 min, but the mineralization rates were less than 40% [43]even at much linger reaction times, and the quantity of employed catalyst was ca. 20-fold higher. Hence, none of the previously mentioned PMS catalysts approached the mineralization rates achieved by the proposed nPEC system, underscoring its remarkable competitiveness, especially considering the low quantity of catalyst per nPEC cell. As additional advantage, the NiPt catalyst is supported on the nPEC cells, thereby avoiding the need of any filtration steps to remove and recover the catalyst.

To investigate the role of reactive species formed by the PMS activation process, free radical quenching experiments using EtOH and TBA as scavengers were performed (**Figure 2c**). In general, hydroxyl and sulfate radicals are quenched by EtOH, whereas hydroxyl radicals are quenched by TBA. The reaction constant between hydroxyl radicals and TBA ($3.8\cdot10^8$–$7.6\cdot0^8$ M^{-1} s^{-1}) is significantly larger than that between TBA and sulfate radicals ($4.0\cdot10^5$–$9.1\cdot10^5$ M^{-1} s^{-1}), while the kinetic constant between hydroxyl and TBA and sulfate and TBA are quite similar[46–48]. A comparison of the degradation values in the presence of these quenching agents clearly distinguishes the effects of both radical species. **Figure 2c** shows that regardless of the irradiation conditions, degradation was governed by the formation of sulfate radicals. The capture of sulfate and hydroxyl radicals led drastic decrease of the tetracycline degradation rates, dropping from approximately 92% and 100% to approximately 12% and 17%. By contrast, when a hydroxyl quencher was used, degradation rates between 69% and 74% were obtained. Thus, though the formation of hydroxyl has a non-negligible effect on the degradation, sulfate radicals play the predominant role.

2.3. Understanding the degradation amplification by the wireless nPEC cell

We hypothesize that the strong amplification efficacy of the nPEC cells is due to two main opto-electric effects. The first is the efficient accumulation of the photogenerated holes in the mesoporous Ni-rich NiPt network, which enables maintaining the adequate oxidized state of the Ni surface. The second effect is the photovoltaic induced increase in the PMS mass transport in

the mesoporous structure. When the nPEC cell is illuminated, it acts as a capacitor in which the photogenerated holes are concentrated in the mesoporous NiPt layer (Figure 1a), thereby generating positive surface potential. This potential electrostatically attracts the negatively charged PMS molecules to the catalytic surface and, therefore, drastically increases the PMS activation rate to generate the radical species. However, when the light illumination is constant, the formation of the dielectric double layer and the accumulation of negatively charge species inside the mesoporous NiPt matrix can hamper the adequate access of new PMS molecules to the active surface and the exit of the also negatively charged sulfate radicals. This adverse effect can be minimized by using the pulsed light beam. In this case, a dynamic double layer is formed at the NiPt surface, which enables simultaneously enhancing the access of the PMS molecules to the catalytic surface, and the efficient release of the generated negatively charged sulfate radicals, thus maximizing the tetracycline degradation efficiency. This effect can be confirmed by the additional improvement of the degradation and mineralization efficiencies when the pulse frequency increases, thereby maximizing the dynamic mass transport rate of reactants and products. This effect is probably also aided by the average higher photovoltage at 500 Hz (**Figure 1e**), as a consequence of the slow capacitive discharge at this frequency.

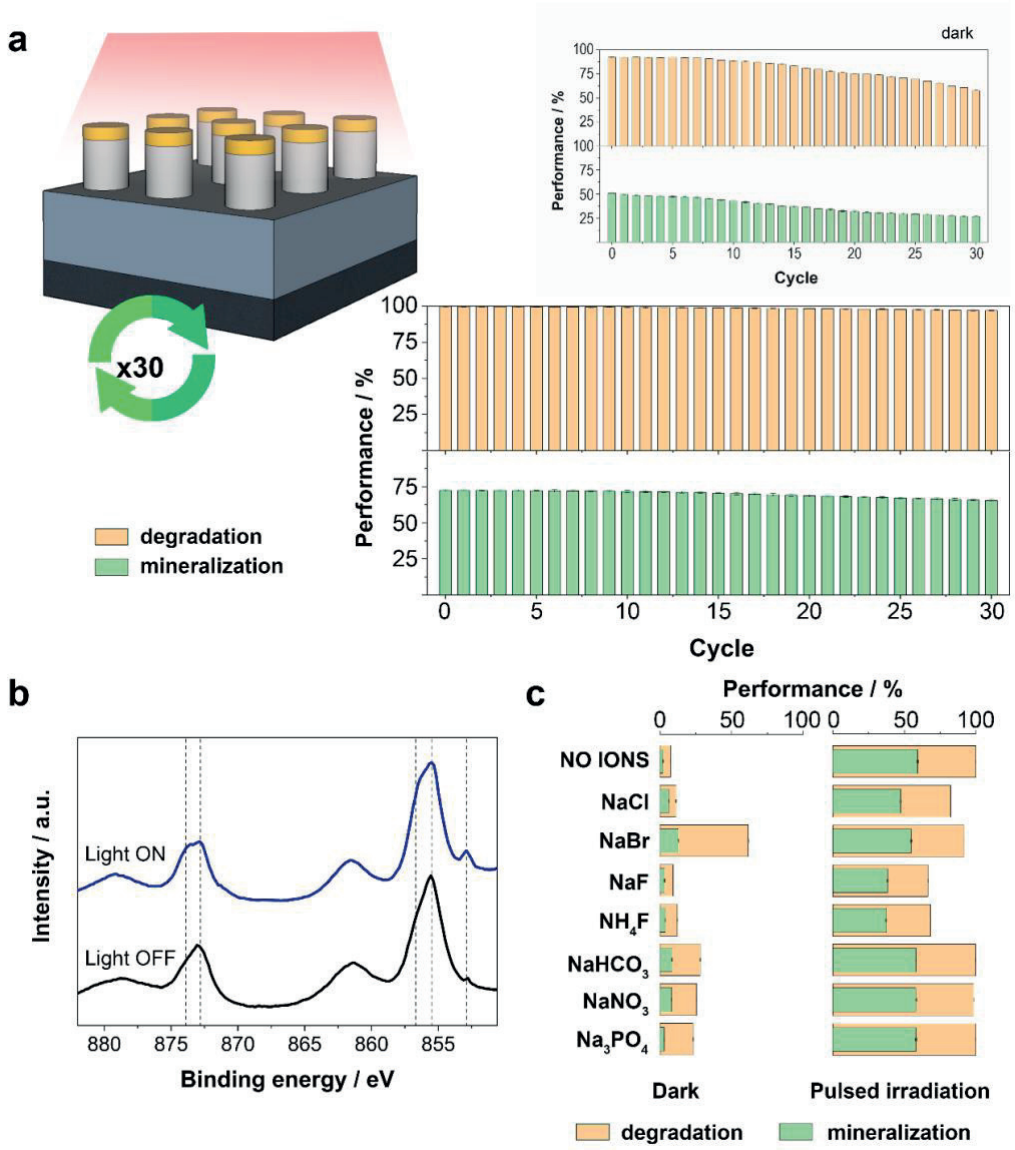


Figure 3: Analysis of the photo-electrochemical effects. a) Reusability of the nPEC cells during 30 consecutive 10-min reaction cycles for degrading and mineralizing tetracycline in dark and under irradiation with a constant light intensity of 20.6 mW cm^{-2}. Experimental conditions: 20 ppm of tetracycline, $[PMS]_0$ = 0.3 mM, T = 20 °C, and pH 7.0. b) XPS spectra of Ni 2p for Si(n)-Au/Si(p)@NiPt after 30 reusability cycles in the dark or under light irradiation. c) Influence of different ions on the PMS-catalyzed degradation and mineralization in dark and pulsed light irradiation (20.6 mW cm^{-2} and 500 Hz) conditions. Salt concentration: 10 mM. Experimental conditions: 20 ppm of tetracyclines, $[PMS]_0$ = 0.3 mM, T = 20 °C, and pH 7.0.

To demonstrate the first hypothesis, we analyzed the catalytic efficiency and the oxidation state of the NiPt films after 30 consecutive cycles of 10 min reaction in the dark and under constant light irradiation conditions (**Figures 3a**). In the absence of light, the degradation and mineralization rates showed a clear and monotonic drop after the seventh cycle. By contrast, under light irradiation, the degradation maintained relatively similar values across the 30 cycles, whereas the mineralization only showed a slight decrease after 12 runs. The PMS activation and formation of sulfate radicals normally exhibit the following mechanism when transition metals are used as activators [33,49]:

$$M(OH)^{(n-1)+} + HSO_5^- \rightarrow M(OH)^{n+} + OH^- + SO_4^{-\bullet} \quad (1)$$

$$M(OH)^{n+} + HSO_5^- \rightarrow M(OH)^{(n-1)+} + H^+ + SO_5^{-\bullet} \quad (2)$$

Therefore, it seems that the electron–hole pair formed during irradiation not only affected the kinetics of degradation and mineralization, but also significantly improved the reusability of the catalyst by maintaining a robust oxidized Ni surface. To confirm it, the chemical nature of the NiPt film after the 30 cycles in the dark and under light irradiation was further investigated by XPS. In dark conditions, the Ni 2p spectra (**Figure 3b**) revealed that Ni(II) was the dominant species, whereas the amount of Ni(III) was significantly lower, as evidenced by the intensity of the binding energies at 855.5 eV (Ni $2p_{3/2}$) and 873.0 eV (Ni $2p_{1/2}$) for Ni^{2+} and 856.7 eV (Ni $2p_{3/2}$) and 874.2 eV (Ni $2p_{1/2}$) for Ni^{3+}. In contrast, under irradiation, the amount of Ni(III) was significantly higher than in dark conditions. It should be noted that, in the mechanism proposed above, Ni(II) is oxidized upon reacting with PMS, which results in the formation of sulfate radicals. Moreover, Ni(III) is also reduced to Ni(II) upon reacting with PMS, which results in the formation of peroxymonosulfate anion radicals ($^-O_3SOO^{\bullet}$or $SO_5^{-\bullet}$). Therefore, the photogenerated holes favor the oxidation of Ni(II) to Ni(III) and thereby enhance the PMS activation.

In addition, to the effect of photogenerated holes in the oxidation state of the NiPt catalyst, the electrostatic interactions at the catalytic interface caused by the photovoltaic actuation on both

reactants and products can be a crucial factor to amplify the pollutant degradation efficiency. As discussed above, the NiPt layer is positively charged under irradiation conditions due to the accumulation of holes in this layer. Therefore, to confirm the relevance of the electrostatic interactions we exploited the capacity to tune the PMS charge with the pH. At low pH, PMS predominantly exists in its protonated neutral form. Conversely, at higher pH, the PMS is negatively charged. Several studies have reported that the optimal pH range for PMS activation lies between 7 and 9, where PMS undergoes partial dissociation, leading to the efficient production of sulfate radicals. However, at even higher pH values, the competition between PMS dissociation and sulfate radical scavenging reactions can reduce the sulfate radical yield. Taking this into consideration, we compared the tetracycline degradation and mineralization at pH 4.5, 7.0 and 8.0 when the nPEC cell was illuminated by the 500 Hz pulsed light with a peak intensity of 20.6 mW cm^{-2}. At pH 4.5, i.e., neutral PMS, the degradation and mineralization rates showed a drastic decrease by approximately 70% and 86%, respectively, compared to the values obtained at pH 7.0. On the other hand, at pH 8.0, values only slightly lower than pH 7.0 were obtained, with a reduction of approximately 11% and 15% in the degradation and mineralization, respectively. These results confirm that electrostatic interactions play a crucial role to amplify the catalytic performance of the system.

In this particular case, in which the tetracycline degradation is carried out by the released free sulfate and hydroxyl radicals in solution, as confirmed by the radicals quenching experiments (**Figure 2e**), the electrostatic interactions of the contaminant with the nPEC cell are not relevant. Actually, at pH=7.0, tetracycline exists primarily in its zwitterionic form, with more than 80% of molecules exhibiting no net charge and, consequently, with null electrostatic interaction with the NiPt interface. However, a non-negligible percentage of molecules have a negative global charge, leading to favorable electrostatic interactions under irradiation between the surface and the tetracycline molecules, which could also contribute in the degradation amplification.

Considering the relevance of the electrostatic interactions between PMS and the charged interfaces of the nPEC cell, it is important to determine the potential cross talk with other

inorganic ions that can be present in complex natural waters, including chlorides, nitrates, carbonates, sulfates, ammonium, and sodium. This motivated the analysis of the impact of these ions on the degradation processes due to their potential strong influence on both radical and non-radical degradation mechanisms [50]. Six different anions (chloride, bromide, fluoride, bicarbonate, nitrate, and phosphate) and two cations (sodium and ammonium) were analyzed used under pulsed light irradiation and in the dark. Bicarbonate, carbonate, and phosphate significantly increased the pH of the medium, while chloride, bromide, fluoride, and nitrate did not induce significant pH changes. The alkaline pH promotes the self-decomposition of PMS, but the sulfate and hydroxyl radicals generated can be rapidly consumed by the inorganic anions. Interestingly, after 3 minutes of reaction in the dark, the tetracycline degradation improved for all the ionic species, showing an enhancement of 1.5-fold for chloride, 8.3-fold for bromide, 1.2-fold for fluoride + sodium, 1.6-fold for fluoride + ammonium, 3.8-fold for bicarbonate, 3.5-fold for nitrate, and 3.1-fold for phosphate. However, the effect significantly differs depending on the type of ion, with the most relevant ones being bromide, bicarbonate, nitrate, and phosphate. Bicarbonate and phosphate anions can activate PMS, forming singlet oxygen through the nucleophilic attack of PMS, and transforming into peroxoanions that have moderate oxidative capacity [50–52]. On the other hand, chloride and fluoride ions have a much lower impact on the degradation rate. Chloride ions undergo a two-electron reaction with PMS, forming HOCl and binary mixtures (PMS/Cl^-) with oxidative capacity of electron-rich organic compounds [50,53]. Recent studies have shown that bicarbonate, nitrate, and phosphate have a significant effect during the initial steps of the reaction, mainly affecting the degradation, while the impact of chloride is less relevant at the beginning, but becomes more important at longer reaction times (**Figure 3c**) [50]. Regarding the mineralization, all ions also contributed to improve the mineralization rate, with approximately 3.0-fold increase for chloride, 6.1-fold for bromide, 1.5-fold for fluoride + sodium, 1.8-fold for fluoride + ammonium, 4.0-fold for bicarbonate, 3.9-fold for nitrate, and 1.4-fold for phosphate. At reaction times longer than 10 minutes, chlorides and bromides maintain higher mineralization rates, while the rest of the ions have less impact, resulting in nearly identical mineralization values.

In contrast, the impact of the inorganic ions is less significant in the case of the nPEC cells illuminated with pulsed light for 3 min (Figure 3b), showing similar tetracycline degradation rates for the nitrate, bicarbonate, and phosphate. However, a slight decrease of the degradation rate was observed for the chloride (1-2 fold), bromide (1.1- fold), and fluoride (1.5-fold). The same trend is observed in the mineralization rates, with only fluorides, chlorides, and bromides showing some negative influence at longer times, while negligible difference is observed with respect to sodium and ammonium. The effective impact of anions on the degradation and mineralization (with greater negative charges resulting in a more negative effect), confirms the importance of the effects between the light-induced positively charged NiPt interface and the anions competing with the negative PMS. Despite this negative influence, **Figure 3c** clearly shows that the pulsed light actuation can generate a large amplification of the tetracycline degradation rate, even in the presence of large concentrations of competing negative ions.

Finally, to further clarify the working principle of the wireless nPEC cells, we examined the tetracycline degradation and mineralization after blocking either the NiPt catalytic or the light active Si/Au interfaces, by depositing a non-permeable transparent acrylic resin (see **Table S2**). When the mesoporous NiPt was blocked, degradation and mineralization presented very low values. By comparison, when the active Si/Au surface, where the electrons are directed, was blocked, the catalytic activity only slightly decreased (ca. 20% in degradation and 10% the mineralization). In this case, as the resin is transparent electron-hole pairs can be still generated and the holes concentrated in the NiPt region. Therefore, the electrochemical reduction reactions that could be generated in the Si/Au region do not play a significant role in the tetracycline degradation.

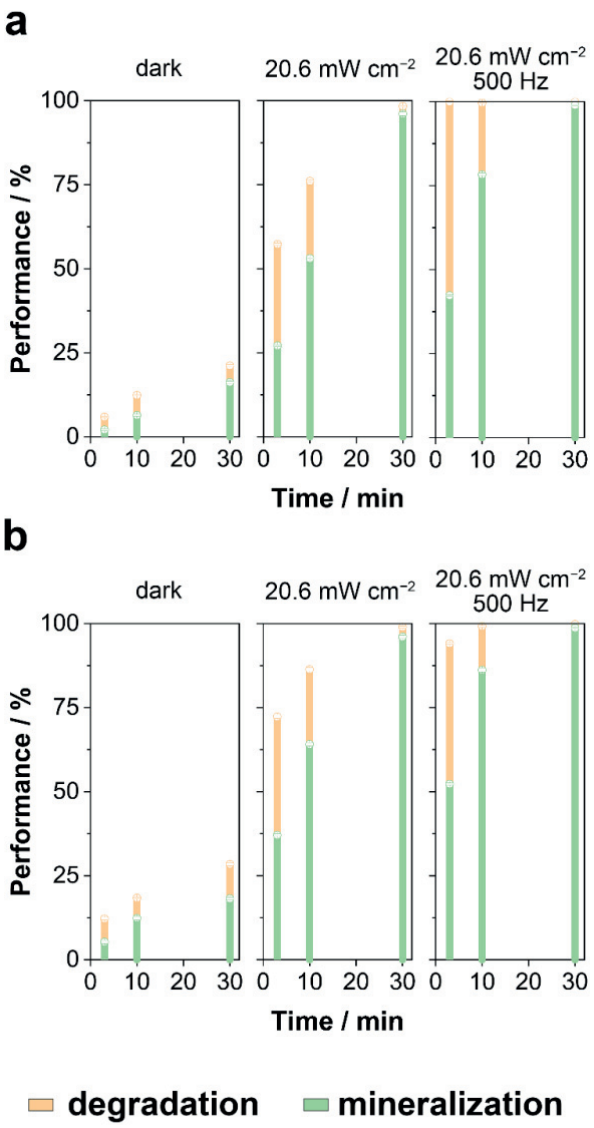
These results confirm that the NiPt layer is crucial to activate the PMS, whereas the photogenerated holes play the key synergistic role to amplify the reaction rates and enhance the durability of the device.

Although the nPEC cell has been designed to maximize the light absorption efficiency in the NIR, it is possible to use any light source with emission wavelength from the UV up to 1.1 μm, which

387 is the bandgap limit of the silicon [30]. Actually, white light sources can generate similar
388 photovoltages as those shown in **Figure 1d** (see **Figure S4** in **SI**), thus suggesting the same
389 capacity to enhance the PMS activation.

390 2.4. Amplification of the degradation and mineralization of other relevant organic
391 pollutants: levofloxacin and anatoxin-A

392 Finally, it is essential to explore whether the remarkably amplified catalytic activity of the
393 wireless pulsed nPEC cells exhibited in the degradation and mineralization of tetracycline can be
394 extended to other highly relevant contaminants. To prove the efficiency and versatility of the
395 nPEC cells, the degradation and mineralization of another widely extended antibiotic,
396 levofloxacin, and the biotoxin anatoxin-A, whose degradation with advanced oxidation processes
397 is much more difficult, were evaluated.



398

399 **Figure 4:** Degradation and mineralization of (a) levofloxacin and (b) anatoxin-A under different
400 conditions. Experimental conditions: 20 ppm of levofloxacin or 5 ppm of anatoxin-A, $[PMS]_0$ =
401 0.3 mM, T = 20 °C, and pH7.0.

402

403 **Figure 4** illustrates the impact of treatment time in the dark and under irradiation with continuous
404 (0 Hz) or pulsed (500 Hz) light for both organic pollutants (**Tables S5** and **S6)**. As can be
405 observed, the PMS activation was not as efficient as in the case of tetracycline, due to the different
406 chemical composition of the pollutants, showing low degradation and mineralization values in
407 the dark, even after 30 min of reaction. In contrast, a large amplification was again observed by

light illumination under constant intensity and, even more pronounced, for the pulsed illumination. The powerful amplification can be clearly seen in the case of levofloxacin pollutant. While the degradation and mineralization rates after 30 min reaction were below 25% in the dark, complete degradation and nearly 50% mineralization was achieved with the pulsed illumination after just 3 min reaction. A similar trend was observed for the anatoxin-A. Moreover, after 30 min reaction complete mineralization of both compounds was attained by the pulsed light illumination. These results indicate that this wireless pulsed nPEC cell approach can be applied to drastically enhance the degradation rate of other organic contaminants.

3. Conclusions

We have presented a novel concept of nanostructured photoelectrochemical cell for the highly amplified degradation of organic pollutants. The nPEC cell has been designed to monolithically integrate: (i) a photovoltaic cell with improved light absorption efficiency in the NIR, and (ii) an optimized catalytically active mesoporous NiPt layer for the activation of PMS to efficiently generate highly reactive sulfate and hydroxyl radical. This configuration enables wireless actuation without the need for any applied bias voltage, which drastically reduces the simplicity and cost of the device. The nPEC can be driven by low intensities (ca. 10-fold lower than sunlight) with light from the UV to the NIR (up to 1.1 μm wavelength) to generate photovoltages up to 500 mV, thus with minimal energy costs. In the three analyzed pollutants, over one order of magnitude amplification of the degradation and mineralization rates has been demonstrated after only 3 min of reaction. Such high amplification has been achieved by the synergistic effects of the photogenerated holes, which can preserve and even increase the oxidation state of the Ni surface to efficiency activate the PMS, and the electrostatic interactions between the positively charged NiPt network and the negatively charged PMS. The combination of both effects explains: (i) the even higher catalytic amplification observed with pulsed light due to the formation of a dynamic dielectric double layer that maximizes PMS mass transport and the release of the dominant sulfate radicals, and (ii) the enhanced durability of the nPEC cells under illumination.

This technology represents an important step towards improved advanced oxidation processes with minimal energy input requirements, particularly with pulsed light, which enables a 2-fold reduction of the actuation energy. The interest of the technology is also reflected by the simplicity of the wireless actuation, and the scalability of both the nanopatterning process based on large scale colloidal lithography and the electrochemical deposition of the Ni-rich mesoporous NiPt layer. This concept could be extended to other photovoltaic cells providing larger photovoltages than monocrystalline silicon photodiodes, and to other catalysts and chemicals, to amplify a wide range of chemical reactions.

Acknowledgements

We acknowledge the financial support of the projects PID2020-115663GB-C32, PCI2019-111896-2 (Euronanomed 2019), PID2021-124568NB-I00, PID2019-106229RB-I00 funded by MCIN/ AEI /10.13039/501100011033. Authors thank the CCiT-UB for the use of their equipment. The funding from Generalitat de Catalunya through the 2021-SGR-00651 project is also acknowledged. ICN2 is funded by the CERCA programme/Generalitat de Catalunya. The ICN2 is supported by the CEX2021-001214-S grant funded by MCIN/AEI/10.13039/501100011033

4. Experimental details

4.1. Fabrication and characterization of the wireless nanophotoelectrochemical cell

The fabrication of the nPEC cells on 4" p-doped silicon wafers (single side polished, resistivity 1 Ohm·cm) started with the implantation of phosphorous as n-dopant by a ion implanter EATON NV4206 (energy 50 KeV, density $4 \cdot 10^{15}$ cm^{-2}), followed by diffusion and activation of the dopants via thermal oxidation process (Tempress Furnace, TS-Series V) under atmospheric

pressure. This process generated a built-in pn junction at a depth of 500 nm. Next, the Ti (1 nm) and Au (75 nm) layers were deposited at both sides of the Si wafer by e-beam evaporation (OERLIKON UNIVEX 450B). To enable an efficient light absorption and photovoltage generation at low light intensity, the photo-active side of the wafer with the pn-juntion was nanopatterned by low cost and scalable colloidal nanolithography on the whole wafer surface. The Au surface on the n-doped region was activated by oxygen reactive ion etching (RIE, Alcatel AMS 110 DE) (HF 100W, 30 sccm, 3 Pa) and amide-functionalized polystyrene beads (diameters ca. 200 nm, Thermo Fisher Scientific) were self-assembled on the whole 4" Au surface by incubation the beads colloidal dispersion at 0.1% during 3 min. This was followed by thorough rinsing with deionized water and drying with N_2 airflow, yielding a randomly distributed monolayer of polystyrene spheres on the Au surface, which was used as mask to fabricate the Si-n/Au nanowires by a two-step RIE process. First, Ar RIE (ICP 1000 W, HF 50 W, 20 sccm, 1 Pa, 2 min, Alcatel AMS 110 DE) was used to etch the Au layer and leave Au discs under the polystyrene beads. Second, SF_6/C_4F_8 RIE (ICP 800 W, HF 15 W, SF_6 150 sccm, C_4F_8 100 sccm, 2.7 Pa, 40 s, Alcatel AMS 110 DE) formed the Si/Au nanowires with a height of around 460 nm. The leftovers of the polystyrene beads on the Si/Au nanowires were mechanically removed by a clean-room adhesive tape. The wafers were then cut into 7 mm x 14 mm chips to proceed with the electrodeposition of the mesoporous NiPt layer on the p-doped side of the Si wafer using the deposited Au layer as electrode.

The Ni-rich mesoporous NiPt deposits were potentiostatically electrodeposited with an Autolab PGSTAT30 equipment and a NOVA software. The electrochemical depositions were performed in a thermostatized three-electrode system using Ag|AgCl as the reference electrode and a platinum spiral as the counter-electrode. The electrochemical media was a block copolymer micellar solution composed of Na_2PtCl_6 (3 mM), $NiCl_2$ (200 mM), H_3BO_3 (200 mM), NH_4Cl (25 mM), and 10 g L^{-1} of the block copolymer poly(ethylene glycol)-*b*-poly(propylene glycol)-*b*-poly(ethylene glycol), Pluronic P-123. The pH was adjusted to 2.7 by adding HCl to the solution.

Before the experiments, solutions were deaerated with argon and maintained in an argon atmosphere during the electrochemical experiments. The temperature was kept at 30 ◦C [32,54].

The morphology of the Au/Si pillar and the porous NiPt deposits was examined with field-emission scanning microscopy (FE-SEM; JSM-7100F Analytical Microscope). The elemental composition of the NiPt deposits was determined by using coupled energy-dispersive spectroscopy (EDS) at 20 kV, calibrated using pure cobalt standard, and by inductively coupled plasma optical emission spectrometry (ICP-OES; Perkin Elmer Optima 3200 RL) after dissolving the NiPt layer using 4% nitric acid. Before and after the catalytic experiments, the chemical nature of NiPt deposits were further examined with X-ray photoelectron spectroscopy (XPS) in an ultra-high vacuum chamber with an XPS system (PHI 5600 MultiTechnique, Physical Electronics) using a monochromatic X-ray source (Al K_{α}line = 1486.6 eV, 350 W).

The optoelectrical measurements were performed on a custom-made 2-electrode set up. The nPECL cells were sealed in a well, with the bottom Ni/Pt surface acting a working electrode and a Pt wire as counter electrode. A water solution containing the same PMS concentration as the degradation experiments (0.3 mM) contacting only the optically active nanostructured Si/Au surface was used during the measurements. The samples were illuminated with a collimated fiber coupled LED sources with emission at 810 nm (Thorlabs M810F2) or white light (Thorlabs MWWHF2). The light intensity was controlled and pulsed with a LED controller (Thorlabs DC2200). The photovoltages were directly detected with a National Instruments data acquisition card (NI-6352) and processed with a Labview program. The photocurrents were measured with a transimpedance I/V amplifier (Thorlabs PDA200C).

4.2. Pollutant degradation experiments

Single-pollutant solutions of tetracycline (20 ppm), levofloxacin (20 ppm), and anatoxin-A (5 ppm) at a pH of 7.0 were used to investigate the potential of the wireless nanophotoelectrochemical cell. Degradation and mineralization experiments were performed in a 3 mL quartz cuvette at 20 ◦C.

Firstly, the persistence of the three contaminants in aqueous solution at a pH of 7 was analyzed over a period of 7 days without any actuation. Measurements of time-dependent UV–vis spectra and by high-performance liquid chromatography mass-spectroscopy (HPLC) chromatograms as well as the total organic content (TOC) values demonstrated the persistence of the contaminants and, thus, the maintained harmful potential of all three species.

In a typical degradation experiment, the catalyst was immersed in the pollutant solution for 3 min to achieve adsorption–desorption equilibrium. The solution was magnetically stirred throughout the process. Afterward, 0.3 mL of 3 mM PMS solution was added to the cuvette.

In addition, the impact of sodium chloride, sodium bromide, sodium fluoride, ammonium fluoride, sodium bicarbonate, sodium nitrate, and sodium phosphate, each at a concentration of 10 mM, on the degradation and mineralization of tetracycline was also studied under dark and infrared light illumination conditions.

A UV–vis spectrophotometer (UV-vis, UV-1800 Shimadzu) was used to measure the concentration of tetracycline and levofloxacin at different reaction times and under different irradiation conditions. In addition, tetracycline, levofloxacin anatoxin-A concentrations were also determined by high-performance liquid chromatography mass-spectroscopy (HPLC-MS, Waters Xevo G2-XS QToF system). The mobile phase comprised a 0.1% (v/v) formic acid aqueous solution, with elution at a flow rate of 0.2 mL min^{-1} and an injected volume of 2 μL. A linear gradient elution transitioned from 90% formic acid aqueous solution and 10% acetonitrile to a final composition of 10% formic acid aqueous solution and 90% acetonitrile over 4 minutes. Mass-spectroscopy analysis was performed using an electrospray ionization source in positive ion mode (capillary voltage: 4.0 kV; N_2 gas flow rate; gas temperature: 300 °C). The concentration of anatoxin-(A) at different times was determined using an ultra-high-performance liquid chromatography (UHPLC) system (Accela; Thermo Fisher Scientific) and a Kinetex HILIC column (Phenomenex) with a 100 mm × 2.1 mm inner diameter and particles 2.6 μm in size. A gradient elution solvent based on solvent A (i.e., 95% [v/v] of acetonitrile and 5% [v/v] 2 mM of ammonium formate + 3.6 mM of formic acid aqueous solution) and solvent B (i.e., 2 mM of

ammonium formate + 3.6 mM of formic acid aqueous solution) was used. The UHPLC system was coupled to a triple quadrupole mass spectrometer (TSQ Quantum Ultra AM, Thermo Fisher Scientific) equipped with a heated electrospray ionization source (HESI-I). Xcalibur software (version 2.0; Thermo Fisher Scientific) was used to control the LC–MS system and to process the data. Mineralization was examined by determining the total organic content (TOC) in the aqueous solution (TOC-VCSH, Shimadzu). The different irradiation conditions were applied using the collimated fiber coupled LED source with emission at 810 nm or white light controlled and pulsed with the LED controller.

Appendix A. Supplementary data

Supplementary data related to this article can be found, in the online version, at doi:

References

1. Oller, I., Malato, S. & Sánchez-Pérez, J. A. Combination of Advanced Oxidation Processes and biological treatments for wastewater decontamination-A review. *Sci. Total Environ.* **409**, 4141–4166 (2011).
2. Yang, Y., Ok, Y. S., Kim, K. H., Kwon, E. E. & Tsang, Y. F. Occurrences and removal of pharmaceuticals and personal care products (PPCPs) in drinking water and water/sewage treatment plants: A review. *Sci. Total Environ.* **596**–**597**, 303–320 (2017).
3. Gómez, E., Cestaro, R., Philippe, L. & Serrà, A. Electrodeposition of nanostructured Bi_2MoO_6@Bi_2MoO_{6-x} homojunction films for the enhanced visible-light-driven photocatalytic degradation of antibiotics. *Appl. Catal. B Environ.* **317**, 121703 (2022).
4. Esplandiu, M. J. *et al.* Interfacial phenomena in nanotechnological applications for water remediation. in (eds. Wandelt, K. & Bussetti, G. B. T.-E. of S.-L. I. (First E.) 465–484 (Elsevier, 2024). doi:https://doi.org/10.1016/B978-0-323-85669-0.00066-0.
5. Serrà, A., Philippe, L., Perreault, F. & Garcia-Segura, S. Photocatalytic treatment of natural waters. Reality or hype? The case of cyanotoxins remediation. *Water Res.* **188**, 116543 (2021).
6. Chae, S., Noeiaghaei, T., Oh, Y., Kim, I. S. & Park, J. S. Effective removal of emerging dissolved cyanotoxins from water using hybrid photocatalytic composites. *Water Res.* **149**, 421–431 (2019).
7. Miklos, D. B. *et al.* Evaluation of advanced oxidation processes for water and wastewater treatment – A critical review. *Water Res.* **139**, 118–131 (2018).
8. Sirés, I., Brillas, E., Oturan, M. A., Rodrigo, M. A. & Panizza, M. Electrochemical advanced oxidation processes: Today and tomorrow. A review. *Environ. Sci. Pollut. Res.* **21**, 8336–8367 (2014).

9. Serrà, A. *et al.* Hybrid Ni@ZnO@ZnS-Microalgae for Circular Economy: A Smart Route to the Efficient Integration of Solar Photocatalytic Water Decontamination and Bioethanol Production. *Adv. Sci.* **7**, 1902447 (2020).

10. Cañizares, P., Lobato, J., Paz, R., Rodrigo, M. A. & Sáez, C. Advanced oxidation processes for the treatment of olive-oil mills wastewater. *Chemosphere* **67**, 832–838 (2007).

11. Luo, S. *et al.* Kinetic and mechanistic aspects of hydroxyl radical–mediated degradation of naproxen and reaction intermediates. *Water Res.* **137**, 233–241 (2018).

12. Xiao, R. *et al.* Experimental and theoretical insight into hydroxyl and sulfate radicals-mediated degradation of carbamazepine. *Environ. Pollut.* **257**, 113498 (2020).

13. Cheng, S. *et al.* Coexposure Degradation of Purine Derivatives in the Sulfate Radical-Mediated Oxidation Process. *Environ. Sci. Technol.* **54**, 1186–1195 (2020).

14. Zhang, H. *et al.* Construction of cubic $CaTiO_3$ perovskite modified by highly-dispersed cobalt for efficient catalytic degradation of psychoactive pharmaceuticals. *J. Hazard. Mater.* **459**, 132191 (2023).

15. Wang, J. *et al.* Facile Synthesis of Atomic Fe-N-C Materials and Dual Roles Investigation of Fe-N4 Sites in Fenton-Like Reactions. *Adv. Sci.* **8**, 2101824 (2021).

16. Lim, J. & Hoffmann, M. R. Peroxymonosulfate (PMS) activation on cobalt-doped TiO2nanotubes: degradation of organics under dark and solar light irradiation conditions. *Environ. Sci. Nano* **7**, 1602–1611 (2020).

17. Li, X. *et al.* $FexCo_{3-x}O_4$ nanocages derived from nanoscale metal-organic frameworks for removal of bisphenol A by activation of peroxymonosulfate. *Appl. Catal. B Environ.* **181**, 788–799 (2016).

18. Gómez, E., Fons, A., Cestaro, R. & Serrà, A. Electrodeposition of CoNi alloys in a biocompatible DES and its suitability for activating the formation of sulfate radicals. *Electrochim. Acta* **435**, 141428 (2022).

19. Guo, S. *et al.* Scalable synthesis of Ca-doped α-Fe_2O_3 with abundant oxygen vacancies for enhanced degradation of organic pollutants through peroxymonosulfate activation. *Appl. Catal. B Environ.* **262**, 118250 (2020).

20. Yang, Q., Choi, H., Chen, Y. & Dionysiou, D. D. Heterogeneous activation of peroxymonosulfate by supported cobalt catalysts for the degradation of 2,4-dichlorophenol in water: The effect of support, cobalt precursor, and UV radiation. *Appl. Catal. B Environ.* **77**, 300–307 (2008).

21. Hu, L., Zhang, G., Liu, M., Wang, Q. & Wang, P. Enhanced degradation of Bisphenol A (BPA) by peroxymonosulfate with Co_3O_4-Bi_2O_3 catalyst activation: Effects of pH, inorganic anions, and water matrix. *Chem. Eng. J.* **338**, 300–310 (2018).

22. James, A., Rodney, J. D., Rao, L., Bhat, B. R. & Udayashankar, N. K. Bi-functional LaMxFe1-xO3 (M = Cu, Co, Ni) for photo-fenton degradation of methylene blue and photoelectrochemical water splitting. *Int. J. Hydrogen Energy* **48**, 17536–17552 (2023).

23. Huang, X., Wang, S., Zhu, S. & Ye, Z. Spectroscopic characteristics and disinfection byproduct formation during UV-assisted photoelectrochemical degradation of humic acid. *J. Clean. Prod.* **375**, 134171 (2022).

24. Alulema-Pullupaxi, P. *et al.* Fundamentals and applications of photoelectrocatalysis as an efficient process to remove pollutants from water: A review. *Chemosphere* **281**, 130821 (2021).

25. Divyapriya, G. *et al.* Treatment of real wastewater by photoelectrochemical methods: An overview. *Chemosphere* **276**, 130188 (2021).

26. Son, A. *et al.* Persulfate enhanced photoelectrochemical oxidation of organic pollutants using self-doped TiO_2 nanotube arrays: Effect of operating parameters and water matrix. *Water Res.* **191**, 116803 (2021).

27. Kaushik, R., Gandhi, S. & Halder, A. Photoelectrochemical Degradation of Organic Pollutants Coupled with Molecular Hydrogen Generation Using Bi_2O_3/TiO_2 Nanoparticle Arrays. *ACS Appl. Nano Mater.* **6**, 4297–4308 (2023).

28. Wang, R. *et al.* Cobalt-doped V_2O_5 hexagonal nanosheets for superior photocatalytic toxic pollutants degradation, Cr (VI) reduction, and photoelectrochemical water oxidation performance. *Environ. Res.* **217**, 114923 (2023).

29. Reddy, C. V., Kakarla, R. R., Shim, J., Zairov, R. R. & Aminabhavi, T. M. Hydrothermally derived Cr-doped SnO_2 nanoflakes for enhanced photocatalytic and photoelectrochemical water oxidation performance under visible light irradiation. *Environ. Res.* **217**, 114672 (2023).

30. Zhao, Y. *et al.* All-Optical Electrochemiluminescence. *J. Am. Chem. Soc.* **145**, 17420–17426 (2023).

31. Eiler, K., Krawiec, H., Kozina, I., Sort, J. & Pellicer, E. Electrochemical characterisation of multifunctional electrocatalytic mesoporous Ni-Pt thin films in alkaline and acidic media. *Electrochim. Acta* **359**, 136952 (2020).

32. Serrà, A., Artal, R., Philippe, L. & Gómez, E. Electrodeposited Ni-Rich Ni-Pt Mesoporous Nanowires for Selective and Efficient Formic Acid-Assisted Hydrogenation of Levulinic Acid to γ-Valerolactone. *Langmuir* **37**, 4666–4677 (2021).

33. Liu, F. *et al.* Degradation of sulfamethoxazole by cobalt-nickel powder composite catalyst coupled with peroxymonosulfate: Performance, degradation pathways and mechanistic consideration. *J. Hazard. Mater.* **400**, 123322 (2020).

34. Monteagudo, J. M., Durán, A., González, R. & Expósito, A. J. In situ chemical oxidation of carbamazepine solutions using persulfate simultaneously activated by heat energy, UV light, Fe^{2+} ions, and H2O2. *Appl. Catal. B Environ.* **176**–**177**, 120–129 (2015).

35. Dong, X. *et al.* Diatomite supported hierarchical 2D $CoNi_3O_4$ nanoribbons as highly efficient peroxymonosulfate catalyst for atrazine degradation. *Appl. Catal. B Environ.* **272**, 118971 (2020).

36. Li, J. *et al.* Core-shell structured cobalt–nickel bimetallic sulfide with dual redox cycles to activate peroxymonosulfate for glyphosate removal. *Chem. Eng. J.* **453**, 139972 (2023).

37. Wang, M. *et al.* Activating peroxydisulfate with $Co_3O_4/NiCo_2O_4$ double-shelled nanocages to selectively degrade bisphenol A – A nonradical oxidation process. *Appl. Catal. B Environ.* **282**, 119585 (2021).

38. Han, Y. *et al.* Cu-doped CoOOH activates peroxymonosulfate to generate high-valent cobalt-oxo species to degrade organic pollutants in saline environments. *Appl. Catal. B Environ.* **340**, 123224 (2024).

39. Peng, X. *et al.* Activation of peroxymonosulfate by single-atom Fe-g-C_3N_4 catalysts for high efficiency degradation of tetracycline via nonradical pathways: Role of high-valent iron-oxo species and Fe–Nx sites. *Chem. Eng. J.* **427**, 130803 (2022).

40. Liu, C. *et al.* Peroxymonosulfate-assisted for facilitating photocatalytic degradation

performance of 2D/2D WO_3/BiOBr S-scheme heterojunction. *Chem. Eng. J.* **430**, 132806 (2022).

41. Ma, S. *et al.* Maximally exploiting active sites on Yolk@shell nanoreactor: Nearly 100% PMS activation efficiency and outstanding performance over full pH range in Fenton-like reaction. *Appl. Catal. B Environ.* **316**, 121594 (2022).

42. Liu, C. *et al.* Construction of Ag/MoS_2@Fe-CS aerogel as excellent PMS activator via synergistic photocatalysis and photothermal effects. *Chem. Eng. J.* **455**, 140814 (2023).

43. Feng, S. *et al.* Photocatalytic activation of PMS over magnetic heterojunction photocatalyst $SrTiO_3$/$BaFe_{12}O_{19}$ for tetracycline ultrafast degradation. *Chem. Eng. J.* **470**, 143900 (2023).

44. Mao, X. *et al.* High atom utility of robust Ca-Co bimetallic catalyst for efficient Fenton-like catalysis in advanced oxidation processes. *Appl. Catal. B Environ.* **331**, (2023).

45. Li, X. *et al.* ZIF-derived non-bonding Co/Zn coordinated hollow carbon nitride for enhanced removal of antibiotic contaminants by peroxymonosulfate activation: Performance and mechanism. *Appl. Catal. B Environ.* **325**, 122401 (2023).

46. Lin, L. *et al.* Enhanced photocatalytic performance and persulfate activation properties by BiOBr supported waste rock wool fibers under LED blue light. *J. Environ. Chem. Eng.* **10**, 107963 (2022).

47. Li, R., Cai, M., Liu, H., Liu, G. & Lv, W. Thermo-activated peroxydisulfate oxidation of indomethacin: Kinetics study and influences of co-existing substances. *Chemosphere* **212**, 1067–1075 (2018).

48. Ding, Y., Zhu, L., Wang, N. & Tang, H. Sulfate radicals induced degradation of tetrabromobisphenol A with nanoscaled magnetic $CuFe_2O_4$ as a heterogeneous catalyst of peroxymonosulfate. *Appl. Catal. B Environ.* **129**, 153–162 (2013).

49. Zhang, L., Yang, X., Zhou, R., Lin, S. & Zhou, L. High-efficiency carbamazepine degradation using a Ni/Co-LDH as the peroxymonosulfate activator: Performance, mechanism and degradation pathway. *Appl. Surf. Sci.* **574**, 151580 (2022).

50. Sun, Y. *et al.* Disparate effects of four anions on the non-radical oxidation process of sulfamethoxazole by peroxymonosulfate: kinetics, mechanism and toxicity variation. *J. Environ. Chem. Eng.* **10**, 107572 (2022).

51. Jiang, M., Lu, J., Ji, Y. & Kong, D. Bicarbonate-activated persulfate oxidation of acetaminophen. *Water Res.* **116**, 324–331 (2017).

52. Lou, X. *et al.* Significantly enhanced base activation of peroxymonosulfate by polyphosphates: Kinetics and mechanism. *Chemosphere* **173**, 529–534 (2017).

53. Lente, G. *et al.* One- versus two-electron oxidation with peroxomonosulfate ion: reactions with iron(II), vanadium(II), halide ions, and photoreaction with cerium(III). *Inorg. Chem.* **48**, 1763–1773 (2009).

54. Eiler, K., Suriñach, S., Sort, J. & Pellicer, E. Mesoporous Ni-rich Ni–Pt thin films: Electrodeposition, characterization and performance toward hydrogen evolution reaction in acidic media. *Appl. Catal. B Environ.* **265**, 118597 (2020).